



**HAL**  
open science

# Nonlinear local behaviours and numerical modeling of damping in civil engineering structures in dynamic

Thomas Heitz

► **To cite this version:**

Thomas Heitz. Nonlinear local behaviours and numerical modeling of damping in civil engineering structures in dynamic. Civil Engineering. Université Paris Saclay (COmUE), 2017. English. NNT : 2017SACLN048 . tel-01684727

**HAL Id: tel-01684727**

**<https://theses.hal.science/tel-01684727>**

Submitted on 15 Jan 2018

**HAL** is a multi-disciplinary open access archive for the deposit and dissemination of scientific research documents, whether they are published or not. The documents may come from teaching and research institutions in France or abroad, or from public or private research centers.

L'archive ouverte pluridisciplinaire **HAL**, est destinée au dépôt et à la diffusion de documents scientifiques de niveau recherche, publiés ou non, émanant des établissements d'enseignement et de recherche français ou étrangers, des laboratoires publics ou privés.

# Comportements non-linéaires locaux et modélisation numérique de l'amortissement dans les structures de génie civil en dynamique

Thèse de doctorat de l'Université Paris-Saclay  
préparée à l'École Normale Supérieure de Cachan  
(École normale supérieure Paris-Saclay)

École doctorale n°579 : sciences mécaniques et énergétiques,  
matériaux et géosciences  
Spécialité de doctorat : génie civil

Thèse présentée et soutenue à Cachan, le 16 novembre 2017, par

**M. Thomas Heitz**

Composition du Jury :

M. Christian La Borderie	Président
Professeur, Université de Pau et des Pays de l'Adour	
Mme Katrin Beyer	Rapporteur
Professeure associée, École Polytechnique Fédérale de Lausanne	
M. Philippe Guéguen	Rapporteur
Directeur de recherche, Institut des Sciences de la Terre	
M. Pierre Léger	Examineur
Professeur, École Polytechnique Montréal	
M. Pierre-Alain Nazé	Examineur
Docteur-ingénieur, Géodynamique et Structure	
M. Frédéric Ragueneau	Directeur de thèse
Professeur, École normale supérieure Paris-Saclay	
M. Cédric Giry	Examineur
Maître de conférence, École normale supérieure Paris-Saclay	
M. Benjamin Richard	Examineur
Ingénieur-chercheur (HDR), Commissariat à l'Énergie Atomique et aux Énergies Alternatives	



# Résumé substantiel

Suite à l'accident nucléaire de Fukushima, des fonds supplémentaires ont été débloqués par le gouvernement français afin de renforcer la recherche dans le domaine du risque sismique qui reste aujourd'hui un enjeu majeur pour l'industrie nucléaire dédiée à la production d'énergie en France où 77 % de l'électricité était d'origine nucléaire en 2014. Dans ce contexte, le projet *SINAPS@* (Séismes et Installations Nucléaire : Assurer la Pérénité et la Sûreté) a été proposé par l'institut SEISM Paris-Saclay (constitué de l'École normale supérieure Paris-Saclay, CEA, EDF, Centrale Supélec; voir la page internet [De la faille à la structure](#) pour davantage d'informations) en collaboration avec huit autres partenaires académiques et industriels (IRSN, Areva, Egis, IFSTTAR, École Centrale Nantes, INP Grenoble, ISTerre, CEREMA). Ce projet multidisciplinaire a pour but d'évaluer les incertitudes liées au risque sismique, de la faille aux équipements. Ainsi, six volets ont été définis: (1) aléa sismique; (2) effets de site et interactions non linéaires entre le champ sismique lointain, proche et les structures; (3) comportement sismique des structures et des équipements; (4) évaluation du risque sismique; (5) contributions expérimentales et interaction bâtiment-bâtiment; (6) formation et dissémination des connaissances. Le travail entrepris dans cette thèse intervient au sein des volets 3 et 5, et vise plus particulièrement à l'amélioration de la calibration de modèles et la modélisation non-linéaire du comportement dynamique des structures.

La résistance d'une structure à un séisme dépend de sa capacité à stocker et/ou à dissiper l'énergie introduite sans que son intégrité ne soit compromise. Le niveau d'endommagement acceptable dépend de la classe structurale, telle que définie dans l'Eurocode 8 tableau 4.3 à la clause 4.2.5. Bien que les lois de comportement matériaux soient maintenant capables de fournir des résultats réalistes et précis concernant le comportement non-linéaire du béton armé (BA), les coûts de calcul associés dissuadent souvent les ingénieurs d'employer de telles lois de comportement. Les nombreuses sources d'incertitudes peuvent nécessiter un nombre important de simulations afin de mener des études de sensibilité. Pour ces raisons, les stratégies de modélisation simplifiées sont toujours populaires au sein des communautés d'ingénieurs et de chercheurs.

Dans l'Eurocode 8, clause 4.3.3.4.3 traitant de l'analyse temporelle non-linéaire, il est nécessaire que les dissipations survenant dans les éléments de structure lors de cycles post-élastiques soient correctement décrites pour les niveaux de déplacements attendus au cours du séisme de dimensionnement. De plus, il est intéressant de mener au moins sept analyses temporelles non-linéaires. En effet, l'Eurocode 8 autorise dans ce cas l'usage de la réponse moyenne aux sept signaux comme référence plutôt que la réponse la plus défavorable lorsque moins de sept analyses sont réalisées. Ainsi, la stratégie de modélisation des dissipations n'influencera pas seulement la qualité de la réponse inélastique, mais définira également les besoins de calcul pour mener à bien l'analyse.

En pratique, un amortissement visqueux additionnel est souvent utilisé pour représenter les dissipations qui ne sont pas prises en compte par le modèle structural (Ragueneau, 1999; Crambuer *et al.*, 2013), particulièrement dans le domaine linéaire où ce dernier ne dissipe *a priori* pas d'énergie. La quantité d'amortissement visqueux additionnel dépend des phénomènes inclus dans le modèle. En fait, le modèle de structure peut ne représenter qu'une partie des dissipations, à condition que le modèle d'amortissement visqueux additionnel soit capable de représenter les dissipations restantes. Les méthodes basées sur le déplacement sont devenues très populaires ces dernières décennies, principalement parce qu'elles ne nécessitent la connaissance que (i) d'une courbe force-déplacement monotone et (ii) d'une valeur d'amortissement visqueux. Tandis que cet amortissement a une influence importante sur la réponse maximale en déplacement, certaines études estiment qu'il s'agit de la seconde source d'incertitude après le mouvement du sol (Celik & Ellingwood, 2010; Lee *et al.*, 2004). De plus, il est démontré par Charney, 2008 et Hall, 2006 qu'il ne faut pas combiner directement ces deux types de dissipations (i.e. hysterétiques et visqueux) et qu'il est nécessaire de réduire l'amortissement visqueux une fois dans le domaine non-linéaire (Correia *et al.*, 2013). Dans cet optique, différents amortissements évolutifs de type Rayleigh ont été testés par Jehel *et al.*, 2014. Des observations expérimentales sur des bâtiments de grande hauteur indiquent que l'amortissement modal visqueux est un intermédiaire entre un amortissement constant sur chaque mode et un amortissement proportionnel à la raideur (Cruz & Miranda, 2016; Satake *et al.*, 2003).

La notion d'amortissement visqueux *équivalent* est plus adéquate : le coefficient d'amortissement visqueux équivalent  $c$  – ou le taux d'amortissement visqueux équivalent  $\xi^1$  – est calibré de sorte à dissiper la bonne quantité d'énergie par un champ de force visqueuse agissant dans la direction opposée et proportionnelle au champ de vitesse. Même si l'expérience montre que des forces visqueuses de faible intensité sont bien présentes dans le domaine de comportement linéaire, la plupart des chercheurs considèrent qu'il s'agit globalement d'une modélisation artificielle des dissipations dans les structures BA. Les phénomènes de frottement entre éléments différents, entre lèvres de fissures, ou à l'interface acier-béton sont plus proches d'un modèle de frottement de Coulomb que d'un modèle d'amortissement visqueux. La dépendance au taux de déformation du champ de force visqueuse ne coïncide pas avec un phénomène de type frottement sec et cela conduit à une dépendance irréaliste à la fréquence. Cependant, la stratégie la plus commune est d'assigner des valeurs de taux d'amortissement visqueux à chaque mode de vibration de la structure. Pour le modèle de Rayleigh, l'amortissement est calibré pour une ou deux fréquences propres, suivant qu'il est proportionnel à la masse, à la raideur, ou aux deux grandeurs. Une approche plus générale est possible grâce aux matrices de Caughey (Caughey, 1960; O'Kelly & Caughey, 1965) avec lesquelles les taux d'amortissement peuvent être calibrés pour un nombre arbitraire de modes, mais cette stratégie induit des variations très importantes d'amortissement pour les fréquences autres que celles de calibration. De plus, le terme proportionnel à la masse introduit un amortissement des mouvements de corps rigides qui n'est pas physique et qui peut affecter les simulations de structures sous-contraintes ou isolées en pied, selon Hall, 2006. Luco & Lanzani, 2017 ont proposé une méthode pour calibrer une matrice de Caughey de manière optimale dans un domaine de fréquence donné.

---

<sup>1</sup> $\xi$  est défini comme étant le rapport entre le coefficient d'amortissement visqueux  $c$  et le coefficient d'amortissement critique

Quoi qu'il en soit, l'évaluation du taux d'amortissement visqueux équivalent reste problématique. Différents essais existent dans la littérature, et ils ne donnent *a priori* pas les mêmes valeurs d'amortissement. Surtout, ils ne mettent pas forcément en jeu les mêmes phénomènes. Certains s'appuient sur des chargements quasi-statiques, d'autres dynamiques (aussi bien harmonique qu'à contenu fréquentiel plus riche). À quelle vitesse et à quelle fréquence devraient être réalisés ces essais ? De plus, les signaux sismiques ont un contenu fréquentiel à large bande : comment cela influence-t-il le taux d'amortissement visqueux équivalent ? Est-ce que des couplages existent entre les modes en terme d'amortissement ? Au delà de la nature du signal, les phénomènes en jeu peuvent aussi dépendre de l'amplitude des déplacements de la structure. Par exemple, un frottement entre deux éléments pourrait ne survenir qu'à partir d'une certaine amplitude. Un autre point à étudier est l'évolution des dissipations au cours de l'analyse temporelle non-linéaire. Pour ces raisons, le choix de la méthode expérimentale est primordial. Il faut néanmoins garder à l'esprit que l'essai idéal n'existe pas : soit il est possible d'effectuer différents essais de natures complémentaires, soit un compromis doit être fait sur les résultats attendus pour l'essai choisi.

Pour répondre aux questions précédentes, cette thèse s'articule autour de quatre chapitres. Dans le premier chapitre, les essais qui ont été choisis pour étudier la dépendance de l'énergie dissipée aux caractéristiques structurelles et aux signaux sont décrits. Pour cela, une revue de littérature se concentrant sur les modèles d'amortissement visqueux et les méthodes d'identification des paramètres associés est d'abord présentée. Cette étude doit permettre la formulation d'un cahier des charges pour la campagne expérimentale à mener.

Dans le second chapitre, la campagne expérimentale IDEFIX (acronyme pour Identification des dissipations et de la fissuration dans les éléments structuraux en béton armé) sera détaillée. Cette dernière s'appuie sur la table vibrante Azalée et le strong-floor de la plateforme expérimentale TAMARIS du Commissariat à l'Énergie Atomique et aux Énergies Alternatives (CEA). Le principal enjeu est la définition d'une procédure d'essai pour traiter, point par point, les questions concernant les relations entre la dissipation et les grandeurs d'intérêt.

Le troisième chapitre n'est pas une présentation exhaustive des résultats expérimentaux mais plutôt celle de quelques résultats remarquables et des techniques développées pour les obtenir. Cela concerne notamment des analyses qualitatives, par exemple l'influence des propriétés matériaux sur les courbes de capacité. Des analyses plus approfondies sont ensuite faites après avoir présenté les outils numériques utilisés. Une méthode basée sur la corrélation d'images numériques permet l'identification de l'évolution du taux d'amortissement visqueux équivalent. Un modèle de raideur est également formulé afin de décrire l'évolution de la raideur de l'oscillateur simple associé aux corps d'épreuves durant l'analyse temporelle non-linéaire.

Enfin, deux approches différentes de simulations numériques sont comparées aux résultats expérimentaux. La première est basée sur le modèle identifié susmentionné tandis que la seconde est basée sur un modèle éléments finis. Leurs performances et la pertinence d'un modèle d'amortissement visqueux additionnel sont étudiées.

Ces études ont montré qu'il est possible de reproduire de manière satisfaisante les déplacements d'un élément de structure assimilable à un oscillateur simple uniquement

à l'aide d'un amortissement hystérétique lorsque les autres sources de dissipations sont limitées. Cela est rendu possible pour IDEFIX par des conditions aux limites maîtrisées et des interactions avec l'environnement faibles. La formulation d'un modèle hystérétique représentant les principaux phénomènes dissipatifs est toutefois une condition nécessaire à une telle simulation. Cela pose deux difficultés : l'identification du modèle est indispensable mais peut-être rendue difficile par des paramètres peu sensibles aux données expérimentales, et le coût de calcul d'une simulation non-linéaire est plus élevé pour des structures plus complexes. Pour ces raisons, l'utilisation d'un modèle de dissipation visqueux équivalent se justifie toujours. La mise en évidence d'une dépendance directe entre demande en déplacement et déplacement maximal historique (assimilable à un niveau de ductilité) et sa formalisation par le biais d'une surface d'équation connue liant l'amortissement à ces deux grandeurs constitue une piste intéressante dans la poursuite d'études axées sur de tels modèles équivalents. L'utilisation de cette surface pour mener des calculs d'oscillateurs non-linéaires par le biais d'un schéma numérique de type Newmark implicite est donc envisagée. L'ensemble des résultats expérimentaux n'est pas présenté dans ce manuscrit. Un travail de classification, de formalisation et la rédaction d'une notice d'utilisation sont nécessaires pour pérenniser les connaissances acquises et les données encore inexploitées au cours de la campagne IDEFIX.

## *Acknowledgements*

The authors wish to express their most grateful thanks to CEA/DEN for its financial support. The work carried out under the SINAPS@ project has benefited from French funding managed by the National Research Agency under the program Future Investments (SINAPS@ reference No. ANR-11-RSNR-0022). The work reported in this thesis has also been supported by the SEISM Institute (<http://www.institut-seism.fr>).

# Contents

<b>Résumé substantiel</b>	<b>iii</b>
<b>Acknowledgements</b>	<b>vii</b>
<b>Introduction</b>	<b>1</b>
<b>1 Viscous damping models and experimental campaigns</b>	<b>5</b>
1.1 Various sources of dissipation . . . . .	5
1.1.1 Forewords . . . . .	5
1.1.2 External dissipation . . . . .	5
1.1.3 Internal sources . . . . .	6
1.1.4 Accounting for dissipations in the dynamic balance equation . . . . .	6
1.2 Viscous damping models . . . . .	7
1.2.1 Modeling scales and elements . . . . .	7
1.2.2 Dissipations included in the viscous damping model . . . . .	8
1.2.2.1 A viscous damping dichotomy . . . . .	8
1.2.2.2 Caughey’s damping models . . . . .	9
1.2.2.3 Global damping models: critical reviews . . . . .	11
a Physical interpretation . . . . .	11
b Calibration challenges . . . . .	12
1.3 Estimation of an equivalent viscous damping . . . . .	13
1.3.1 From quasi-static tests . . . . .	13
1.3.1.1 A particular case of nonlinear viscous damping . . . . .	13
1.3.1.2 Jacobsen’s areas method to estimate an equivalent viscous damping . . . . .	17
1.3.2 From free vibrations tests . . . . .	21
1.3.2.1 Theoretical aspects . . . . .	21
1.3.2.2 Application to experimental data . . . . .	24
1.3.3 From low-level dynamic excitations . . . . .	26
1.3.3.1 Obtaining a frequency response function (FRF) from hammer shock tests . . . . .	26
1.3.3.2 Half-power bandwidth method (HBM) . . . . .	30
1.3.3.3 Peak response method (PRM) . . . . .	34
1.4 Overview of experimental campaigns on RC specimens . . . . .	35
1.4.1 Quasi-static tests . . . . .	35
1.4.2 Free vibrations tests . . . . .	37
1.4.3 Low-level dynamic excitations . . . . .	37
1.4.4 High-level dynamic excitations . . . . .	38
1.5 Conclusions of the first chapter . . . . .	38

<b>2</b>	<b>IDEFIX experimental campaign: overview</b>	<b>41</b>
2.1	About the experimental needs	41
2.2	Experimental framework	42
2.3	Specimens	44
2.3.1	Dimensions	44
2.3.2	Reinforcement	45
2.3.3	Constitutive materials	46
2.3.3.1	Concrete	46
a	Compressive tests	46
b	Fracture energy measurement	48
2.3.3.2	Steel	49
2.3.3.3	Steel-concrete bond	50
2.4	Boundary conditions of the RC beams	52
2.4.1	Definition of the mechanical constraints	52
2.4.2	Intermediate supports	52
2.4.3	Beam-end supports	53
2.4.4	Modeling of the setup	54
2.5	Loadings	55
2.5.1	Quasi-static loadings	55
2.5.1.1	QSC1 and QSC2	55
2.5.1.2	SPS1 and SPS2	57
2.5.2	Dynamic loadings	57
2.5.2.1	White noise test (WN)	57
2.5.2.2	Band-passed white noise (SC)	58
2.5.2.3	Decreasing sinus sweep	59
2.5.3	Natural seismic signal SS1	60
2.5.4	Summary of the loadings	60
2.6	Measurements	61
2.6.1	Positioning	61
2.6.2	Displacements	61
2.6.3	Acceleration	62
2.6.4	Rotational velocity	63
2.6.5	Forces	63
2.6.6	Strains	64
2.7	Conclusions of the second chapter	64
<b>3</b>	<b>Experimental results analyses</b>	<b>67</b>
3.1	Identification strategy of the modal damping ratios	67
3.1.1	Forewords	67
3.1.2	Projection on the modal basis	69
3.1.2.1	Case of a simply supported beam	69
3.1.2.2	Case of a simply supported beam with additional masses	71
3.1.2.3	Seismic loading on shaking table	74
3.1.2.4	Evaluation of the modal displacements using full-field displacement measurement	76
3.1.3	Error evaluation and minimization strategy	77
3.1.4	About parametric and non-parametric identifications	79
3.1.4.1	Non-parametric identification	79

	3.1.4.2	Parametric identification . . . . .	79
3.2		Quasi-static tests . . . . .	80
	3.2.1	Capacity curves . . . . .	80
	3.2.1.1	Capacity curves deduced from QSC1 tests . . . . .	80
	a	Obtaining the capacity curves . . . . .	80
	b	Concrete influence . . . . .	80
	c	Reinforcement pattern influence . . . . .	81
	d	Reinforcement ribs influence . . . . .	81
	e	Conclusion regarding the capacity curves (from QSC1) . . . . .	81
	3.2.1.2	Capacity curve deduced from QSC2 test . . . . .	82
	3.2.2	Velocity sweep tests (SPS1 and SPS2) . . . . .	82
	3.2.3	Cyclic quasi-static tests (QSC1 and QSC2) . . . . .	86
	3.2.4	Formulation of a SDOF hysteretic model for the beam behavior . . . . .	92
	3.2.4.1	Objectives . . . . .	92
	3.2.4.2	Modeled phenomena . . . . .	92
	3.2.4.3	State potential . . . . .	95
	3.2.4.4	State laws . . . . .	96
	3.2.4.5	Flow rules . . . . .	96
	3.2.4.6	Dissipation . . . . .	97
	3.2.4.7	Model identification strategy . . . . .	98
	3.2.5	IDEFIX identification results . . . . .	99
3.3		Numerical experimentation campaign . . . . .	101
	3.3.1	Forewords . . . . .	101
	3.3.2	Equivalent viscous damping ratio evaluation using Jacobsen's method . . . . .	102
	3.3.2.1	Influence of the ductility level . . . . .	103
	3.3.2.2	Influence of the hysteresis loops width and slope . . . . .	103
	3.3.2.3	Influence of the closure displacement . . . . .	103
	3.3.2.4	Influence of the fragility coefficient . . . . .	103
	3.3.3	Equivalent viscous damping ratio evaluation using logarithmic decrement method . . . . .	109
	3.3.3.1	Loading procedure . . . . .	109
	3.3.3.2	Comparison with Jacobsen's area method conducted in dynamics . . . . .	109
	3.3.4	Further investigation on the influence of the ductility level and the displacement amplitude on the EVDR . . . . .	110
3.4		Hammer shock tests . . . . .	112
3.5		White noise on shaking table . . . . .	115
	3.5.1	General observations . . . . .	115
	3.5.2	Non-parametric identification of WN12 tests . . . . .	120
	3.5.2.1	Forewords . . . . .	120
	3.5.2.2	First vibration mode identification . . . . .	121
	3.5.2.3	Second vibration mode identification . . . . .	123
	3.5.2.4	Role of the relative variation constraint . . . . .	123
3.6		Decreasing sinus sweep on shaking table . . . . .	123
	3.6.1	Non-parametric identification of DSS52 tests . . . . .	123
3.7		Conclusions of the third chapter . . . . .	126

<b>4 Numerical simulations using simplified damping modeling</b>	<b>131</b>
4.1 Strategies of numerical modeling	131
4.2 Computation of a SDOF oscillator response	131
4.2.1 Newmark method	131
4.2.2 Hughes Hilber Taylor (HHT) method	134
4.2.3 Influence of the integration scheme on the identified damping	136
4.2.3.1 Reference problem	136
4.2.3.2 Validation of the numerical implementation of JAM	138
4.2.3.3 Newmark parameters influence on the computation error	138
4.2.4 Application of the Newmark implicit algorithm to the Niigata-ken Chuetsu Oki Earthquake (NCOE)	138
4.3 Finite element modeling	146
4.3.1 Forewords	146
4.3.2 Multifiber elements	146
4.3.3 IDEFIX numerical multifiber beam model	147
4.3.3.1 Discretization	147
a Axial discretization	147
b Cross-section discretization	148
4.3.3.2 Boundary conditions	148
4.3.3.3 Additional masses	149
4.3.3.4 Additional viscous damping	149
4.3.3.5 Materials models	150
a Concrete	150
b Steel	150
4.3.4 Validation of the FE model	151
4.3.4.1 Eigenfrequencies	151
4.3.4.2 Dissipated energy	152
4.4 Numerical results	152
4.5 Concluding remarks	155
<b>Conclusions and perspectives</b>	<b>157</b>
<b>A Experimental results</b>	<b>163</b>
A.1 Cyclic compressive tests results	163
A.2 Fracture energy measurement tests	166
A.3 Pull-out tests	169
<b>B Plans</b>	<b>171</b>
<b>C Miscellaneous</b>	<b>177</b>
<b>Bibliography</b>	<b>179</b>

# List of Abbreviations

<b>3PB</b>	<b>3-Point Bending</b>
<b>4PB</b>	<b>4-Point Bending</b>
<b>BF-LDM</b>	<b>Best-Fitting Logarithmic Decrement Method</b>
<b>C-LDM</b>	<b>Corrected Logarithmic Decrement Method</b>
<b>CEA</b>	<b>Commissariat à l'Énergie Atomique et aux énergies alternatives (French Alternative Energies and Atomic Energy Commission)</b>
<b>CEREMA</b>	<b>Centre d'Études et d'expertise sur les Risques, l'Environnement, la Mobilité et l'Aménagement</b>
<b>DIC</b>	<b>Digital Image Correlation</b>
<b>DOF</b>	<b>Degree Of Freedom</b>
<b>EDF</b>	<b>Electricity De France</b>
<b>EMSI</b>	<b>Études Mécaniques et Sismiques (Seismic Mechanic Studies)</b>
<b>ENS</b>	<b>École Normale Supérieure</b>
<b>EVDR</b>	<b>Equivalent Viscous Damping Ratios</b>
<b>FE</b>	<b>Finite Element</b>
<b>FFT</b>	<b>Fast Fourier Transform</b>
<b>FRF</b>	<b>Frequency Response Function</b>
<b>HBM</b>	<b>Half-power Bandwidth Method</b>
<b>IDEFIX</b>	<b>Identification des Dissipations et de la Fissuration dans les éléments structuraux en béton armé (Identification of Damping/Dissipation in RC structural elements)</b>
<b>I-DIC</b>	<b>Integrated Digital Image Correlation</b>
<b>IFSTTAR</b>	<b>Institut Français des Sciences et Technologies des Transports, de l'Aménagement et des Réseaux</b>
<b>IRSN</b>	<b>Institut de Radioprotection et de Sûreté Nucléaire</b>
<b>JAM</b>	<b>Jacobsen's Areas Method</b>
<b>LMT</b>	<b>Laboratoire de Mécanique et Technologie (Laboratory of Mechanics and Technology)</b>

<b>MDOF</b>	<b>Multi Degree Of Freedoms</b>
<b>NLTHA</b>	<b>NonLinear Time History Analysis</b>
<b>NPP</b>	<b>Nuclear Power Plant</b>
<b>NCOE</b>	<b>Niigataken Chuestu Oki Earthquake</b>
<b>PGA</b>	<b>Peak Ground Acceleration</b>
<b>PRM</b>	<b>Peak Response Method</b>
<b>PSD</b>	<b>Power Spectral Density</b>
<b>RC</b>	<b>Reinforced Concrete</b>
<b>REV</b>	<b>Representative Element of Volume</b>
<b>RPP</b>	<b>Rigid Perfectly Plastic</b>
<b>SDOF</b>	<b>Single Degree Of Freedom</b>
<b>SINAPS@</b>	<b>Séismes et Installations Nucléaires: Assurer la Pérénité et la Sûreté (Earthquake and Nuclear Facilities: Ensuring Safety and Sustaining)</b>
<b>SSI</b>	<b>Soil-Structure Interaction</b>
<b>VDM</b>	<b>Videometric®</b>



*À mes parents.*



# Introduction

Consequently to the Fukushima nuclear accident, additional financial supports have been made available by the French government to strengthen the research in the field of the seismic risk, which is a major issue for nuclear buildings devoted to energy production, in France where 77 % of the electricity was still produced by nuclear power plants (NPPs) in 2014. In this context, the *SINAPS@* project (Earthquake and Nuclear Facilities: Ensuring Safety and Sustaining) has been proposed by the SEISM Paris-Saclay Institute (constituted of École Normale Supérieure Paris–Saclay, CEA, EDF, Centrale Supélec; see the web page [De la faille à la structure](#) for more information) in association with eight other academic and industrial partners (IRSN, Areva, Egis, IFSTTAR, École Centrale Nantes, INP Grenoble, ISTerre, CEREMA). This multidisciplinary project aims to assess the uncertainties related to the seismic hazard from the fault to the secondary structures (i.e. equipments). Hence, six work packages have been defined: (1) seismic hazard; (2) nonlinear site effects and soil-structure interaction; (3) structural and components behaviors; (4) seismic risk analysis; (5) building to building interaction analysis and experimental campaigns; (6) training and dissemination of the knowledge. The work carried out during this Ph.D. thesis takes place in the work packages 3 and 5, and more specifically, in the improvement of the model calibration and the modeling of the nonlinear dynamic behavior of complex structures.

The ability of a structure to withstand a seismic event is driven by its capability to store and/or dissipate the input energy without compromising its integrity. The level of damage considered as acceptable depends on the structural class, as defined in the Eurocode 8, table 4.3 in section 4.2.5. Even though available material constitutive laws are now able to provide realistic and accurate results about the nonlinear behavior of reinforced concrete (RC), the computational cost is a strong counterpart that designers and engineers are rarely prone to pay for when dealing with full-scale structures. Overshadowing the uncertainties coming from external sources which are considered in the other work packages, and apart from the dimensional constraints leading to this need of computational resources, important uncertainties arise from the material properties and could sometimes require extensive numerical sensitivity studies. For these reasons, simplified modeling strategies are still popular among the engineering and research communities.

In Eurocode 8, section 4.3.3.4.3 dealing with the nonlinear time-history analysis, it is expected that the dissipation occurring in structural components for post-elastic cycles are properly described for the displacement amplitude expected in case of the design seismic loading. Furthermore, it may be advantageous to proceed to at least 7 nonlinear time-history analyses since the Eurocode 8 authorizes to use the mean response to these input signals rather than the most unfavorable when less than 7 analyses are performed. Hence, the strategy to model the dissipation will not only influence the quality of the post-elastic response, but will also define the necessary computational demand for the analysis.

In practice, an additional viscous damping is often used to represent the dissipations not taken into account by the structural model (Ragueneau, 1999; Crambuer *et al.*, 2013), particularly in its linear domain (Correia *et al.*, 2013). The amount of viscous damping depends on the phenomena included. In fact, the structural model can represent only a part of the energy dissipation, given that the additional viscous damping accounts for the remaining dissipated energy. For example, displacement-based methods have become popular for the past decades, mostly because they only require the knowledge of (i) a monotonous nonlinear force-displacement curve and (ii) a value of viscous damping. While this damping ratio has a key influence when assessing maximum structural responses, some studies show it is the second source of uncertainties after the ground motions (Celik & Ellingwood, 2010; Lee *et al.*, 2004). Furthermore, as shown in (Charney, 2008; Hall, 2006), combining both types of dissipation (i.e. hysteretic and viscous damping) should not be considered as a trade-off since it may compromise the validity of a study and could require a reduction of the viscous damping in the nonlinear range (Correia *et al.*, 2013). In order to weight this effect, several evolving Rayleigh-type viscous damping models have been compared by Jehel *et al.*, 2014. Experimental evidence on slender buildings tends to show that modal viscous damping can be thought to be an intermediate between constant viscous damping for all modes and stiffness-proportional damping (Cruz & Miranda, 2016; Satake *et al.*, 2003).

The notion of *equivalent* viscous damping (EVDR) is more accurate: the equivalent viscous damping coefficient  $c$  – or the equivalent viscous damping ratio  $\xi^2$  – is calibrated in order to dissipate the right amount of energy by a viscous force field, acting in opposition and proportionally to the velocity field. If some evidence shows that slight viscous effects exist in the linear range, most of researchers consider that it is an artificial modeling of the dissipations in RC structures. Friction phenomena between different components, crack surfaces or in the steel-concrete bond are closer to a solid damping (such as Coulomb's friction model) than to a viscous damping. The strain rate dependence on the viscous force field does not match with friction damping and this leads to an unrealistic dependence on the frequency. However, the traditional strategy is to assign damping ratio values to each eigenmode of the structure. For the classical Rayleigh model, the damping is calibrated on one or two eigenmodes, depending if the damping matrix is mass-proportional, stiffness-proportional, or both. A more general approach is possible through Caughey series (Caughey, 1960; O'Kelly & Caughey, 1965), with which modal damping ratios can be set for an arbitrary number of modes, but this strategy induce large variations to damping ratios other than those set by the user (Clough R.W., 2003). In addition, the mass-proportional term creates a spurious damping when rigid body motions are involved, as stated by Hall, 2006 for partially constrained structures and base-isolated buildings. Luco & Lanzani, 2017 proposed a method to calibrate an optimal Caughey matrix in order to set the damping ratios at a constant value, in a certain frequency range.

Still, the question of the assessment of the EVDR arises. Different tests can be found in the literature, and there is no reason for which they would all provide the same damping ratios values. Mostly, they do not necessarily involve the same phenomena. Some of them rely on quasi-static loadings, whereas others use dynamic signals which can in turn be either harmonic or broadband. Which velocity and frequency should be considered to evaluate the dissipated energy? Moreover, natural seismic signals have a broadband

---

<sup>2</sup> $\xi$  is defined as the ratio of the viscous damping coefficient  $c$  over the critical damping (see section 1.3.2.1)

frequency content: how does this influence the equivalent viscous damping ratio? Do the main eigenmodes interact with each other in terms of damping? Beyond the nature of the signal, the phenomena involved could also depend on the amplitude of the displacements exhibited by the structure. For example, a frictional contact between two nonstructural components may occur only for strong seismic motions. Another point which is worth to study is the evolution of the dissipation through a nonlinear time-history analysis. Hence, the choice of the experimental method to evaluate the EVDR is of primary importance, keeping in mind that the ideal test does not exist: either the possibility to carry out different complementary tests exist (i.e. tests that provide complementary information regarding the damping), or a compromise has to be found if only one test is possible.

To address the aforementioned questions, this thesis is split up into four chapters. In the first one, the choice of the testing procedure that will provide the key information regarding the dependency of the dissipated energy on structural and signal characteristics (i.e. material properties, structural design, signal content, response amplitude, etc.) is described. To this end, a literature review focused on the viscous damping models and the way to identify the related parameters is presented. This study will allow for the formulation of a testing procedure that will answer to identified specifications.

In the second chapter, the resulting IDEFIX experimental campaign (French acronym for *Identification of damping/dissipations in RC structural elements*) will be explained. It has been carried out with the support of the Azalée shaking table and the strong-floor of the TAMARIS experimental facility operated by the French Alternative Energies and Atomic Energy Commission (CEA). The main issue is to define the testing procedure in order to address, point-by-point, the questions regarding the relationships between the dissipation and the quantities of interest.

The third chapter is not a full review of the experimental results but rather a presentation of remarkable results and the associated post-processing methods. It mostly concerns qualitative analyses, regarding for example the influence of material properties over capacity curves. More in-depth analyses are performed after some necessary numerical tools are described. An identification method based upon digital image correlation (DIC) allows for the identification of the EVDR evolution. A stiffness model is formulated in order to describe the evolution of the stiffness of the single degree-of-freedom associated to the beam during the nonlinear time-history analysis.

Finally, two numerical simulations approaches are compared to the experimental results. The first one is based on the aforementioned identified model while the second one is based on a finite element model. Their performance and the relevance of an additional viscous damping model are assessed.



## Chapter 1

# Viscous damping models and experimental campaigns

### 1.1 Various sources of dissipation

#### 1.1.1 Forewords

The identification of the dissipation in RC structures is not straightforward because many sources may contribute in it. The complexity mainly arises from the fact that they act generally together and involve nonlinear phenomena at different scales. For these reasons, they are difficult to uncouple and this is why damping phenomena were, at the beginnings of earthquake engineering, gathered into one “do-it-all” damping term in the dynamic balance equation. However, researchers have quickly understood the importance of a proper and clear description of the energy dissipation and consequently, have worked since decades on the identification of the different sources leading to the clarification of this poorly understood term into an expanded one. A common way to sort the dissipation in case of RC structures is to consider separately internal and external sources (Smyrou *et al.*, 2011). This last statement motivates the organization of the next two sections.

#### 1.1.2 External dissipation

In external dissipations are included every phenomena that do not take place within the constitutive materials of the structural components. Indeed, the interaction between the structure and its surroundings leads to energy dissipation. In this case, fluids are often involved: viscous damping is physically observed, for example in the case of a fluid-structure interaction with surrounding water (dams (Hall, 1988), bridges, offshore structures, etc.), tanks (Livaoğlu & Doğangün, 2006; Ozdemir *et al.*, 2010) or air (slender buildings (Satake *et al.*, 2003), wind (Kareem & Gurley, 1996), etc.). Nonetheless, the environment also generates non-viscous dissipations such as the ones related to the soil-structure interaction (SSI) which has been a major research concern for the past decades. Also, equipments and aesthetic or functional parts such as filling masonry, plasterboards, doors, windows, pipes, electricity network, etc. are considered as external sources of dissipation since they are not necessary for ensuring the mechanical capacity of the structure. Hence, they play a major role in the overall damping of the structure, and

consequently, on its dynamic response. The nature of the damping is not viscous in this case.

Since the damping is difficult to assess at the designing step while it is often considered as beneficial, more predictable sources of damping can be added with real viscous dampers (Kareem *et al.*, 1999). Some damping devices are in fact not viscous, such as tuned mass dampers (Gutierrez Soto & Adeli, 2013), or hysteretic dampers (Skinner *et al.*, 1977). The latter use the yielding capability of the constitutive material as a source of energy dissipation. Defining these devices as external or internal dissipation sources is a matter of point-of-view and considerations. The literature witnesses these sources have been arbitrarily considered as external sources but this may be subjected to discussions.

### 1.1.3 Internal sources

The material behavior represents the main source of internal dissipation, at least when seismic excitation overcomes a given intensity. Indeed, the energy dissipated through the constitutive law highly depends on the phenomena which are activated. For instance, steel reinforcements yielding is more prone to occur in case of strong seismic motions, mostly at the joints. The resulting plastic hinges act as hysteretic dampers. The dissipation related to cracks in concrete is also of primary importance. The energy dissipated at the initiation and propagation stages is driven by the fracture energy  $G_f$  (RILEM TCS, 1985) and reaches relatively high levels but is dissipated only once. Then, frictional effects occurring between cracks surfaces becomes significant for high-duration and/or high-amplitude cyclic motions.

Similarly, friction occurs between concrete and reinforcements. This phenomenon is often called “bond-slipping”. Eligehausen *et al.*, 1982 have studied the mechanical properties of the steel-concrete bond by means of pull-out tests. It turned out that the bond strength and the residual bond friction were mainly driven by the confinement pressure (either active<sup>1</sup> or passive<sup>2</sup>) on the specimens. This means that the energy dissipated by friction between the steel and the concrete is proportional to the local confinement level around the bar reinforcement once the surrounding concrete has cracked. This local confinement depends on the stirrups design and on the external loading. Hence, the dissipations due to bond slipping in the case of a bent slender RC component tend to be lower than the ones occurring in massive components.

### 1.1.4 Accounting for dissipations in the dynamic balance equation

A general form of equilibrium equation for a single degree of freedom (SDOF) system can be written as:

$$m \cdot \ddot{u} + f_{int}(\dot{u}, u, \dots) = -m \cdot \ddot{u}_g \quad (1.1)$$

where  $u(t)$  is the relative displacement between the SDOF system and its foundations, and  $u_g(t)$  is the ground motion (the double dots stand for the second time derivative function). These two displacements are detailed on figure 1.1. In this equation, all the

---

<sup>1</sup>due to an external loading

<sup>2</sup>due to the stirrups

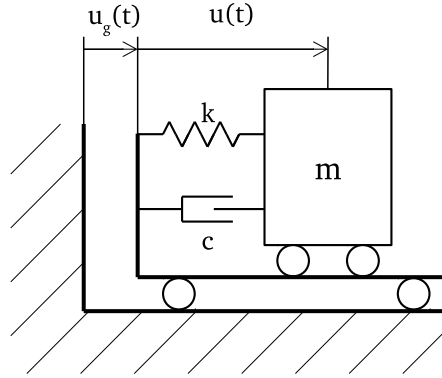


FIGURE 1.1: Notation of the SDOF system subject to a ground motion

dissipations are included in the so-called “internal force” term  $f_{int}$ , which may depend on many variables such as displacement or velocity but also on internal variables related to the chosen model (e.g. a damage variable). Hence, the oscillator response may depend on its loading history. Often, a viscous damping model is extracted from this internal force. Therefore, equation (1.1) is modified as follows:

$$m \cdot \ddot{u} + f_{vis}(\dot{u}) + f_{int}(u, \dots) = -m \cdot \ddot{u}_g \quad (1.2)$$

where  $f_{vis}$  is a viscous force (not necessarily linear). As emphasized in previous section 1.1.1, it is convenient to model as many dissipations as possible by viscous damping model(s). The most simplified equation (1.2) becomes:

$$m \cdot \ddot{u} + c \cdot \dot{u} + k \cdot u = -m \cdot \ddot{u}_g \quad (1.3)$$

The corresponding system is depicted in figure 1.1.

However, this practice may sometimes lead to unexpected results. Regarding SSI, Crouse & McGuire, 2001 reported that modal damping ratios greater than 10 % and up to 35 % are observed. These values are much higher than the common structural damping ratios (i.e. between 2 % and 7 %). Literature reviews on this topic can be found in (Dutta & Roy, 2002) or (Lou *et al.*, 2011).

## 1.2 Viscous damping models

### 1.2.1 Modeling scales and elements

The modeling scale depends on the values of the gradients involved (strain, stress, material properties, etc.). Hill, 1963 first introduced the notion of RVE as the smallest volume over which a measurement can be made that will yield a value representative of the whole. Hence, all the material dissipation should be observable within this RVE. The main difficulty when assessing energy dissipations occurring in RC structures is related to the fact several distinct phenomena may occur in a coupled way at different scales. Of course, the choice of a very fine modeling in case of the civil engineering structures (e.g. at the

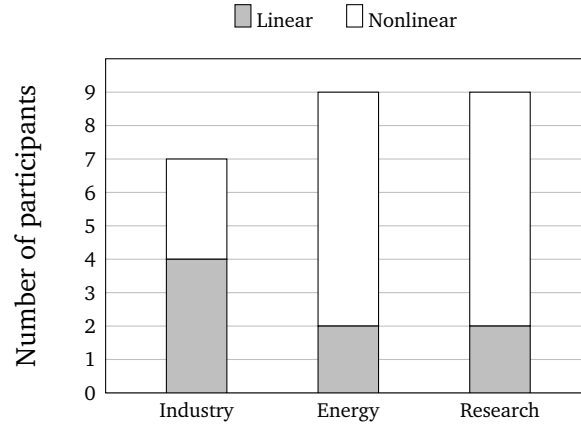


FIGURE 1.2: Linearity of the simulation of SMART 2008 participants depending on their work field (Richard *et al.*, 2016a)

aggregate scale as studied by Daoud, 2003) would be ideal but remains an utopia. One would rather use much coarser finite elements or components scale models.

Organized between 2008 and 2010, SMART 2008 international Benchmark (Richard *et al.*, 2016a) gathered 34 participating teams from 18 countries from different continents. An asymmetric three-story RC mock-up has been tested on a shaking table with both synthetic and natural seismic ground motions. This benchmark provides a representative overview of the state-of-the-art related to the nonlinear analyses in earthquake engineering, particularly regarding the structural modeling and constitutive laws implemented by the participants, as shown in figure 1.3. Only 20 % of participants have used exclusively solid elements. Therefore, it is still of interest to reduce the computational cost through the use of simplified finite elements, but it does not necessarily imply less realistic results. The use of nonlinear models tends to become more popular with the improvement of computing capabilities. However, the linear ones are still widely used among the civil engineering community when dealing with conventional buildings (i.e. not related to the nuclear energy production field) as it is shown in figure 1.2.

## 1.2.2 Dissipations included in the viscous damping model

### 1.2.2.1 A viscous damping dichotomy

The viscous damping ratio  $\xi_{eq}$  is often split up in two contributions, as proposed for example by Smyrou *et al.*, 2011:

$$\xi_{eq} = \xi_{el} + \xi_{hyst} \quad (1.4)$$

The term  $\xi_{hyst}$  accounts for dissipations related to hysteretic phenomena (i.e. related to non-viscous damping) and  $\xi_{eq}$  accounts for all other dissipative phenomena. This decomposition should be considered carefully in equation (1.2). Indeed, hysteretic dissipations are already taken into account in the internal forces  $f_{int}$ . However, it is still possible to model a part of the hysteretic dissipations through the viscous term  $\xi_{hyst}$  if and only if

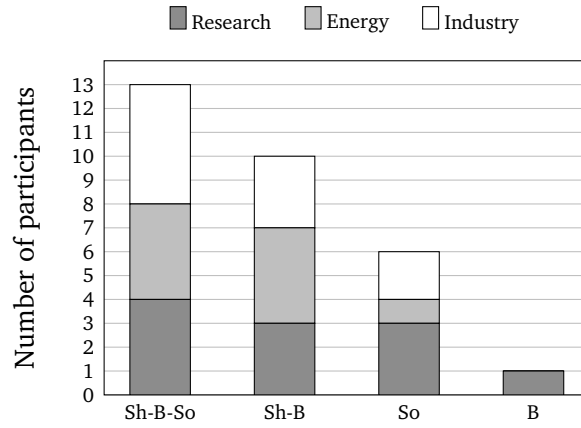


FIGURE 1.3: Type of elements used by SMART 2008 participants for the best-estimate analysis (Richard *et al.*, 2016a) — Sh: shells; B: beams; So: Solid

this part is excluded from the model  $f_{int}$ . If the aforementioned strategy is followed, the energy dissipations due to  $\xi_{hyst}$  remain small compared with the ones due to  $f_{int}$ .

The damping forces that act even when the structure behaves elastically (e.g. for small displacement amplitudes) are accounted in the term  $\xi_{el}$ . The origins of those forces are not easy to identify but they often come from external sources (see section 1.1.2). The choice of the common value of elastic damping  $\xi_{el} = 5\%$  (as prescribed in “Eurocode 8 Design of structures for earthquake resistance Part 1: General rules, seismic actions and rules for buildings”) has some experimental evidences, such as by Petrini *et al.*, 2008, but this observation is valuable only in the linear range. Indeed, the same authors — but also several others (Jehel *et al.*, 2014; Charney, 2008; Léger & Dussault, 1992) — emphasized the importance to update the damping ratio once in the nonlinear range, otherwise the dissipations may be overestimated. The value of 7% is also found in the guidelines established by the French Autorité de sûreté nucléaire, 2006 related to NPPs.

The values of damping ratios to choose are anyway a concern, as shown in figure 1.4. The values chosen by the participants of SMART 2008 international benchmark range from 0% to 9%. It is interesting to note that the lowest values of damping ratios are used in association with nonlinear models analogously to equation (1.2).

### 1.2.2.2 Caughey’s damping models

Considering a linear multi-degrees of freedom (MDOF) system, the dynamic equation is defined analogously to equation (1.3):

$$\mathbf{M} \cdot \ddot{\mathbf{u}}(t) + \mathbf{C} \cdot \dot{\mathbf{u}}(t) + \mathbf{K} \cdot \mathbf{u}(t) = \mathbf{F}(t) \quad (1.5)$$

where  $\mathbf{F}$  is the dynamic load vector,  $\mathbf{M}$  is the mass matrix and  $\mathbf{K}$  is the stiffness matrix. The mass and stiffness matrices are by definition diagonal and orthogonal when projected onto the modal basis. This allows for a more computationally efficient resolution of the MDOF equation since the number of equations is reduced to the number of DOFs if and only if the

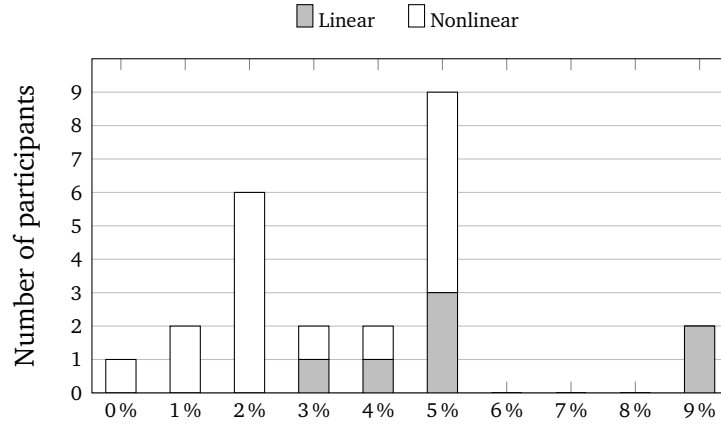


FIGURE 1.4: Values of damping ratios used by SMART2008 participants for the best-estimate analysis depending on the linear nature of the simulation (Richard *et al.*, 2016a)

damping matrix  $\mathbf{C}$  is also diagonal in the modal basis (in this case, the matrix is designated as “classical”). To ensure the latter assumption and not relying on any physical basis, a diagonal damping matrix is formulated with arbitrary damping coefficients associated to each mode, or is generated by Caughey’s series (Caughey, 1960):

$$\mathbf{C} = \mathbf{M} \cdot \sum_{n=0}^N a_n \cdot (\mathbf{M}^{-1} \cdot \mathbf{K})^n \quad (1.6)$$

In equation (1.6), the number of terms in the sum is generally taken equal to the number of vibration modes  $N_m$  considered, i.e.  $N = N_m - 1$ , but could theoretically be any integer. The damping ratios associated to each damping coefficients are given by:

$$\xi_i = \frac{1}{2 \cdot \omega_i} \cdot \sum_{n=0}^N a_n \cdot \omega_i^{2 \cdot n} \quad (1.7)$$

However, it is often necessary to compute  $\mathbf{K}^{-1}$  and  $\mathbf{M}^{-1}$ , the latter being possibly undefined because of zero masses degrees of freedoms. This problem disappears when the particular case of  $N = 1$  is used:

$$\mathbf{C} = a_0 \cdot \mathbf{M} + a_1 \cdot \mathbf{K} \quad (1.8)$$

which is also called Rayleigh damping, or proportional damping, because it is linearly proportional to both mass and stiffness. Equation (1.7) becomes:

$$\xi_i = \frac{1}{2 \cdot \omega_i} \cdot (a_0 + a_1 \cdot \omega_i^2) \quad (1.9)$$

In practice, it is often preferred to compute  $a_0$  and  $a_1$  for two prescribed damping ratios  $\xi_a$  and  $\xi_b$  corresponding to angular frequencies  $\omega_a$  and  $\omega_b$ :

$$\begin{pmatrix} a_0 \\ a_1 \end{pmatrix} = \frac{1}{\omega_b^2 - \omega_a^2} \cdot \begin{bmatrix} 2 \cdot \omega_a \cdot \omega_b^2 & -2 \cdot \omega_a^2 \cdot \omega_b \\ -2 \cdot \omega_a & 2 \cdot \omega_b \end{bmatrix} \cdot \begin{pmatrix} \xi_a \\ \xi_b \end{pmatrix} \quad (1.10)$$

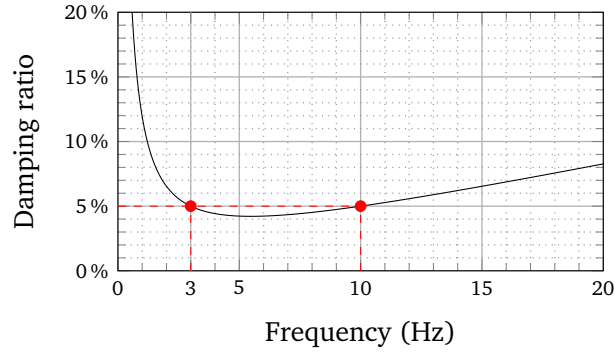


FIGURE 1.5: Rayleigh damping ratio function of the frequency for  $\xi = 5\%$  at 3 Hz and 10 Hz

This means that the damping ratio could only be chosen for two arbitrary frequency values (not necessarily corresponding to actual eigenmodes) which are often either the first two eigenfrequencies or the 1<sup>st</sup> and the 3<sup>rd</sup> eigenfrequencies. Since equation (1.9) is a second order polynomial expression, the damping value is fully constrained by these two frequency values, according to a function plotted on figure 1.5.

According to Hall, 2006, this procedure may be optimized if an acceptable damping ratio range  $[\xi_{min}; \xi_{max}] = [\xi - \Delta\xi; \xi + \Delta\xi]$  rather than two damping ratios is chosen using the following procedure:

$$a_0 = \xi \cdot \frac{4 \cdot \omega_b}{1 + \frac{\omega_b}{\omega_a} + 2 \cdot \sqrt{\frac{\omega_b}{\omega_a}}} \quad (1.11)$$

$$a_1 = \xi \cdot \frac{1}{\omega_a} \cdot \frac{4}{1 + \frac{\omega_b}{\omega_a} + 2 \cdot \sqrt{\frac{\omega_b}{\omega_a}}} \quad (1.12)$$

In this case, the damping ratio will be equal to  $\xi + \Delta\xi$  at  $\omega_a$  and  $\omega_b$  and equal to  $\xi - \Delta\xi$  at  $\omega_m = \sqrt{\omega_a \cdot \omega_b}$  with:

$$\Delta\xi = \xi \cdot \frac{1 + \frac{\omega_b}{\omega_a} - 2 \cdot \sqrt{\frac{\omega_b}{\omega_a}}}{1 + \frac{\omega_b}{\omega_a} + 2 \cdot \sqrt{\frac{\omega_b}{\omega_a}}} \quad (1.13)$$

The updating strategy of the damping ratio is a concern when structural parameters variations are observed. For instance, if the calibration angular frequency  $\omega_a$  is chosen equal to the 1<sup>st</sup> eigenmode and if the latter decreases because of damage in the structure, the damping ratio  $\xi$  for the 1<sup>st</sup> eigenmode increases. To prevent this effect, the parameters  $a_0$  and  $a_1$  can be updated during the nonlinear time-history analysis.

### 1.2.2.3 Global damping models: critical reviews

#### a Physical interpretation

The main criticism formulated about the Caughey's damping matrices is related to their physical interpretation. Taking the example of the Rayleigh damping, it is based

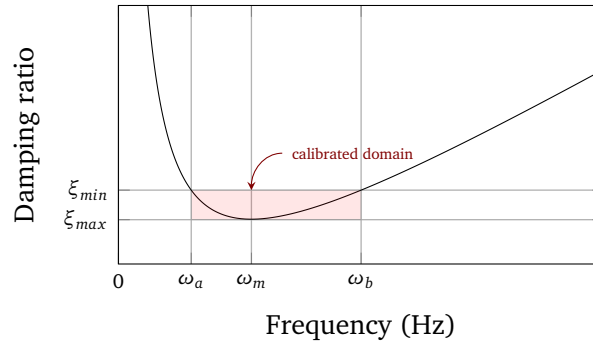


FIGURE 1.6: Calibration of Rayleigh damping with a range criterion

upon a mass proportional and a stiffness proportional term. The former can be viewed as viscous dampers (dashpots) connecting the masses of each DOF to a fixed support. This means that even an infinitely rigid mobile system subjected to a seismic load would dissipate energy if associated to a Rayleigh damping. Hall, 2006 pictures this dissipation as a “viscous penetrating ether in which the structure is immersed”. Even if this mass-proportional term is physically irrelevant, it is still convenient to control the constant part of damping, as explained in section 1.2.2.2. It is also the only part of the Rayleigh damping that could consistently model the damping of the non-structural components that are not involved in the stiffness matrix. Regarding the stiffness-proportional term, it acts as linear viscous dampers interconnecting the DOFs with each other. Even if this contribution has a more physically justifiable use, the choice of the initial stiffness matrix is questionable as discussed in paragraph b.

## b Calibration challenges

Whatever the Caughey’s damping model chosen is, the user has to calibrate it on the  $N + 1$  frequencies in equation (1.7) based on experimental evidences. This representation of the dissipations is global, and may lead to spurious damping forces when the actual stiffness of the structure decreases due to nonlinearities, for example, when the following nonlinear dynamic equation is considered:

$$\mathbf{M} \cdot \ddot{\mathbf{u}}(t) + \mathbf{C} \cdot \dot{\mathbf{u}}(t) + \mathbf{F}_{\text{int}} = \mathbf{F}(t) \quad (1.14)$$

with  $\mathbf{F}_{\text{int}}$  the vector representing the resisting forces. Some researchers advise to use the tangent stiffness  $\mathbf{K}_t$  matrix rather than the initial one in equations (1.6) or (1.8) to take into account these modifications when computing the damping matrix. This operation is not more expensive from a numerical point of view when the tangent stiffness matrix is computed during the time integration procedure to solve the nonlinear time-history analysis (NLTHA). In addition, one may wish to update the damping ratios with respect to the calibration frequencies which may have changed according to the new structural state. This can be done by modifying the coefficients  $a_n$ , which then evolve through the time-history analysis:

$$\mathbf{C} = a_0(t) \cdot \mathbf{M} + a_1(t) \cdot \mathbf{K}_t \quad (1.15)$$

Comparative studies that can be found in the literature (e.g. Jehel *et al.*, 2014, Hall, 2006, Charney, 2008, Léger & Dussault, 1992) suggest that initial stiffness can be used under certain conditions: if the coefficients  $a_n$  are modified accordingly and/or if the stiffness-proportional term is bounded arbitrarily, otherwise, the highest velocities in softening or yielding elements will produce unrealistic high viscous damping forces. According to Jehel, 2014 who introduces the concept of *discrepancy force*, a systematic comparison between the amplitudes of viscous damping forces and restoring forces may be a good indicator of the relevance of the damping model used in the simulation.

After having chosen whether initial or tangent stiffness is used, and if the coefficients  $a_n$  are updated or not during the simulation, the following questions still arise: how to estimate the equivalent viscous damping that will dissipate the right amount of energy? How to get distinct viscous damping values for the different calibration frequencies? How do these damping values evolve throughout the NLTHA? The first question is discussed in the following section 1.3, and the other questions are investigated in the next chapters.

## 1.3 Estimation of an equivalent viscous damping

### 1.3.1 From quasi-static tests

The two following methods (sections 1.3.1.1 and 1.3.1.2), initially proposed by Jacobsen in case of dynamic tests, have been adapted to analyze quasi-static cyclic reverse tests. If they should be considered with care for several reasons described in the aforementioned sections, they still provide uses with useful information regarding the equivalent damping ratio for SDOF systems during quasi-static tests which are often performed for the reasons recalled in section 1.4.1. This is probably one of the most suitable methods to date when dealing with the nonlinear range.

#### 1.3.1.1 A particular case of nonlinear viscous damping

This case is the one which motivated the work done by Jacobsen, 1930 which aimed at the development of a method to approximate nonlinear damping models by an equivalent linear damping model. The nonlinear viscous damping considered depends on the  $n^{\text{th}}$  power of the velocity and the *constant* viscous damping coefficient  $c_n$ . Considering an mono-harmonic excitation of angular frequency  $\omega$  and force amplitude  $F$ :

$$m \cdot \ddot{u}(t) + \frac{\dot{u}(t)}{|\dot{u}(t)|} \cdot c_n \cdot \dot{u}^n(t) + k \cdot u(t) = F \cdot \sin(\omega \cdot t + \varphi) \quad (1.16)$$

It was of interest, mostly when Jacobsen developed his method, to transform this equation to a linear one similar to the equation:

$$m \cdot \ddot{u}(t) + c \cdot \dot{u}(t) + k \cdot u(t) = F \cdot \sin(\omega \cdot t + \varphi) \quad (1.17)$$

To this end, a linear viscous coefficient  $c_1$  is assumed so that the energy dissipated by an oscillation is equal to the energy dissipated during a cycle of the system associated to

equation (1.16). Then, the work of the both damping forces should be equal:

$$W_d = \int_0^{\frac{2\pi}{\omega}} c_n \cdot \frac{\dot{u}}{|\dot{u}|} \cdot \dot{u}^n \cdot du = \int_0^{\frac{2\pi}{\omega}} c_1 \cdot \dot{u} \cdot du \quad (1.18)$$

In other words, it is assumed that the effect of the friction on the wave shape of the displacement is negligible. Then, the solution displacement and velocity fields can be expressed as follows:

$$u(t) = U \cdot \sin(\omega \cdot t) \quad (1.19)$$

$$\dot{u}(t) = U \cdot \omega \cdot \cos(\omega \cdot t) \quad (1.20)$$

the phase angle  $\varphi$  between the excitation and the response being included in the expression of the force  $F \cdot \sin(\omega \cdot t + \varphi)$  in equation 1.16. To overcome the discontinuity of  $\frac{\dot{u}(t)}{|\dot{u}(t)|}$ , the integral is computed over a quarter of the period (where this ratio is constant). Given a signal, the integral over the full period is four times the one on a quarter of the period:

$$4 \cdot c_n \int_0^{\frac{\pi}{2\omega}} \dot{u}^n \cdot du = 4 \cdot c_1 \int_0^{\frac{\pi}{2\omega}} \dot{u} \cdot du \quad (1.21)$$

Equations (1.19) and (1.20) in (1.21) give:

$$\int_0^{\frac{\pi}{2\omega}} c_n \cdot U^n \cdot \omega^n \cdot \cos(\omega \cdot t) \cdot dt = \int_0^{\frac{\pi}{2\omega}} c_1 \cdot U \cdot \omega \cdot \cos(\omega \cdot t) \cdot dt \quad (1.22)$$

Given that  $du = \dot{u} \cdot dt \implies du = U \cdot \omega \cdot \cos(\omega \cdot t) \cdot dt$ :

$$\int_0^{\frac{\pi}{2\omega}} c_n \cdot U^{n+1} \cdot \omega^{n+1} \cdot \cos(\omega \cdot t) \cdot dt = \int_0^{\frac{\pi}{2\omega}} c_1 \cdot U^2 \cdot \omega^2 \cdot \cos^2(\omega \cdot t) \cdot dt \quad (1.23)$$

This leads to:

$$c_n \cdot U^{n-1} \cdot \omega^{n-1} \cdot \int_0^{\frac{\pi}{2\omega}} \cos^{n+1}(\omega \cdot t) \cdot dt = c_1 \cdot \frac{\pi}{4 \cdot \omega} \quad (1.24)$$

An integration by parts gives the following equation:

$$A_{n+1} = \int_0^{\frac{\pi}{2\omega}} \cos^{n+1}(\omega \cdot t) \cdot dt = \int_0^{\frac{\pi}{2\omega}} \cos^n(\omega \cdot t) \cdot \cos(\omega \cdot t) \cdot dt \quad (1.25)$$

Then, a recursive relationship is established:

$$A_{n+1} = \frac{n}{n+1} \cdot A_{n-1} \quad (1.26)$$

$$\text{with } A_0 = \frac{\pi}{2 \cdot \omega} \quad (1.27)$$

$$\text{and } A_1 = \frac{1}{\omega} \quad (1.28)$$

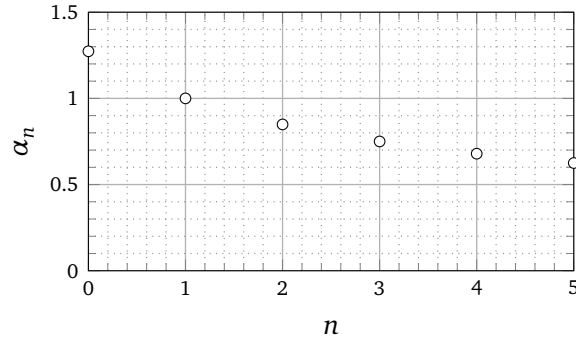


FIGURE 1.7: Equivalence coefficient between linear viscous damping and  $n^{\text{th}}$  order nonlinear viscous damping

It can be demonstrated that:

$$A_{n+1} = \begin{cases} \frac{\left(\left(\frac{n}{2}\right)! \cdot 2^{\left(\frac{n}{2}\right)}\right)^2}{(n+1)!} \cdot \frac{1}{\omega} & \text{if } n+1 \text{ is odd} \\ \frac{(n+1)!}{\left(\left(\frac{n+1}{2}\right)! \cdot 2^{\left(\frac{n+1}{2}\right)}\right)^2} \cdot \frac{\pi}{2\omega} & \text{else} \end{cases} \quad (1.29)$$

Hence:

$$c_1 = U^{n+1} \cdot \omega^n \cdot \left(\frac{4 \cdot A_{n+1}}{\pi}\right) \cdot c_n \quad (1.30)$$

which finally gives:

$$c_1 = U^{n-1} \cdot \omega^{n-1} \cdot \alpha_n \cdot c_n \quad (1.31)$$

$$\text{with } \alpha_n = \begin{cases} \frac{4}{\pi} \cdot \frac{\left(\left(\frac{n}{2}\right)! \cdot 2^{\left(\frac{n}{2}\right)}\right)^2}{(n+1)!} & \text{if } n \text{ is even} \\ \frac{2 \cdot (n+1)!}{\left(\left(\frac{n+1}{2}\right)! \cdot 2^{\left(\frac{n+1}{2}\right)}\right)^2} & \text{else} \end{cases} \quad (1.32)$$

These equations allow for plotting the values of  $\alpha_n$  with respect to  $n$  in figure 1.7.

The following observations are made:

- the case  $n = 1$  actually corresponds to a linear viscous damping because  $\alpha_1 = 1$ ;
- the case  $n = 0$  involves a constant friction force of amplitude  $c_0$  in the opposite direction of the motion. This gives an equivalent linear viscous force:

$$f_d(t) = \frac{4 \cdot c_0}{\pi} \cdot \cos(\omega \cdot t)$$

– the case  $n = 2$  gives an equivalent linear viscous force:

$$f_d(t) = \frac{8}{3 \cdot \pi} \cdot c_2 \cdot U^2 \cdot \omega^2 \cdot \cos(\omega \cdot t)$$

When establishing this equivalence, it is necessary to verify the pseudo-periodic regime condition, i.e.  $\xi < 1$ , which is equivalent to:

$$\frac{c_1}{2 \cdot m \cdot \omega_0} < 1 \quad (1.33)$$

which gives:

$$c_1^2 < 4 \cdot k \cdot m \quad (1.34)$$

Similarly for the equivalent viscous damping:

$$c_n^2 \cdot \alpha_n^2 \cdot U^{2 \cdot n - 2} \cdot \omega^{2 \cdot n - 2} < 4 \cdot k \cdot m \quad (1.35)$$

leads to:

$$U \cdot \tau < \frac{F}{k} \cdot \left( \frac{2}{f_n} \right)^{\frac{1}{n-1}} \quad (1.36)$$

$$\text{with } \tau = \frac{\omega}{\omega_0} \quad (1.37)$$

$$\text{and } f_n = c_n \cdot \alpha_n \cdot \omega_0^n \cdot k^{-n} \cdot Q^{n-1} \quad (1.38)$$

Contrary to the linear viscous damping case, the existence of oscillations depends not only on the structure but also on the excitation properties, i.e. (i) on the ratio  $\tau$  of angular frequency of the excitation over the one of the system and (ii) on the steady-state displacement amplitude  $U$ . Differently said, the linear viscous damping equivalence is valid if and only if the aforementioned conditions related to the excitation are fulfilled.

The well-known linear viscous damping response displacement has the form given in equation (1.19). Then, it can be shown that the steady-state amplitude is:

$$U = \frac{F}{\sqrt{(k - m \cdot \omega^2)^2 + c_1^2 \cdot \omega^2}} \quad (1.39)$$

Applying the equivalence with  $n^{\text{th}}$  order viscous damping:

$$U = \frac{F}{\sqrt{(k - m \cdot \omega^2)^2 + U^{2 \cdot n - 2} \cdot \omega^{2 \cdot n} \cdot \alpha_n^2 \cdot c_n^2}} \quad (1.40)$$

Injecting equation (1.40) in the limit condition for the existence of oscillations:

$$U \cdot \tau = \frac{F}{k} \left( \frac{2}{f_n} \right)^{\frac{1}{n-1}} \quad (1.41)$$

gives the following polynomial equation:

$$U^{2\cdot n} + \frac{(1 - \tau^2)^2}{f_n^2 \tau^{2\cdot n}} \cdot \left(\frac{F}{k}\right)^{2\cdot n - 2} \cdot U^2 - \frac{1}{f_n^2 \cdot \tau^{2\cdot n}} \cdot \left(\frac{F}{k}\right)^{2\cdot n} = 0 \quad (1.42)$$

As an example, the case of the Coulomb's friction damping is considered, i.e.  $n = 0$  in equation (1.42). Combining equations (1.42) and (1.36):

$$f_{n=0} \geq \frac{2 \cdot \tau}{\sqrt{(1 - \tau^2)^2 + 4 \cdot \tau^2}} \quad (1.43)$$

which gives the minimal response amplitude condition:

$$U_{min} = \frac{F/k}{\sqrt{(1 - \tau^2)^2 + 4 \cdot \tau^2}} \quad (1.44)$$

This means that the steady-state amplitude has to be above  $U_{min}$  in order to dissipate the right amount of energy when comparing the equivalent system with the original one.

To sum up, many restrictions have to be considered when attempting to model nonlinear viscous dissipations (proportional to the  $n^{\text{th}}$  power of the velocity) by a linear viscous model:

- the loops in the force-displacement curve have to be closed and symmetric;
- the size of the applicability domain of the equivalence depends on the frequency of the steady-state response;
- the steady-state response is assumed to be mono-harmonic;
- a minimal steady-state displacement amplitude is necessary to ensure the equivalence between linear and nonlinear viscous damping.

Hence, questions arise regarding the cases of the non-harmonic response, when loops are not closed and/or symmetric, and when a steady-state regime is never reached (e.g. when the loading is not stationary, or is not long enough). This is generally the case of seismic loadings.

### 1.3.1.2 Jacobsen's areas method to estimate an equivalent viscous damping

Consequently to the method described in section 1.3.1.1 applicable to the nonlinear viscous damping, Jacobsen, 1960 proposed another method to estimate an equivalent viscous damping for the more general case of the hysteretic damping. Considering once again the classical linear oscillator excited by a mono-harmonic force  $F(t) = F_0 \cdot \cos(\omega \cdot t)$ :

$$\ddot{u} + 2 \cdot \xi \cdot \omega_0 \cdot \dot{u} + \omega_0^2 \cdot u = \frac{F}{m} \quad (1.45)$$

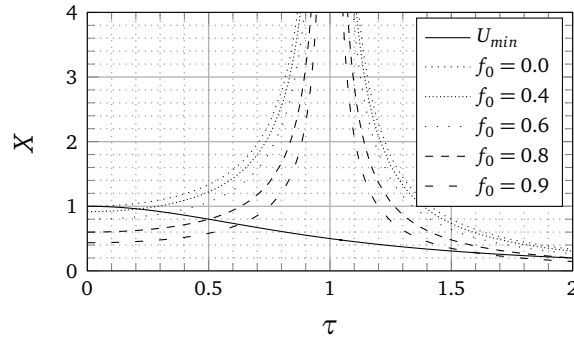


FIGURE 1.8: Domain on which the equivalence is valid (above  $U_{min}$  line) for different friction forces  $f_0$

Hence, when the steady-state regime is reached, the displacement, the velocity and the acceleration responses of the oscillator are:

$$u(t) = U \cdot \sin(\omega \cdot t + \phi) \quad (1.46)$$

$$\dot{u}(t) = U \cdot \omega \cdot \cos(\omega \cdot t + \phi) \quad (1.47)$$

$$\ddot{u}(t) = -U \cdot \omega^2 \cdot \sin(\omega \cdot t + \phi) \quad (1.48)$$

with  $U$  the displacement amplitude and  $\phi$  the phase angle. This allows for the calculation of the energies involved during one period  $T = \frac{2\pi}{\omega}$ : the kinetic energy  $E_c$ , the potential elastic energy  $E_{el}$  and the dissipated energy  $E_d$ .

$$E_c = \oint_T F_a \cdot du = \oint_T (-m \cdot \ddot{u}) \cdot du = \oint_T (-m \cdot \ddot{u}) \cdot \dot{u} \cdot du = 0 \quad (1.49)$$

$$E_{el} = \oint_T F_r \cdot du = \oint_T (-k \cdot u) \cdot du = 0 \quad (1.50)$$

$$E_d = \oint_T F_d \cdot du = \oint_T (-c \cdot \dot{u}) \cdot du = -\pi \cdot c \cdot U^2 \cdot \omega \quad (1.51)$$

The energy dissipated during one cycle can also be re-formulated (for the following, the dissipated energy is counted positively):

$$\begin{aligned} E_d &= \pi \cdot (2 \cdot \xi \cdot m \cdot \omega_0) \cdot U^2 \cdot \omega \\ &= \pi \cdot (2 \cdot \xi \cdot \sqrt{k \cdot m}) \cdot U^2 \cdot \omega \\ &= 4 \cdot \pi \cdot \frac{\omega}{\omega_0} \cdot \xi \cdot \left( \frac{1}{2} \cdot k \cdot U^2 \right) \\ &= 4 \cdot \pi \cdot \frac{\omega}{\omega_0} \cdot \xi \cdot E_s \end{aligned} \quad (1.52)$$

where  $E_s$  is the maximum stored elastic potential energy, which is depicted on figure 1.9b. Then, the damping ratio can be estimated as:

$$\xi = \frac{1}{4 \cdot \pi} \cdot \frac{\omega_0}{\omega} \cdot \frac{E_d}{E_s} \quad (1.53)$$

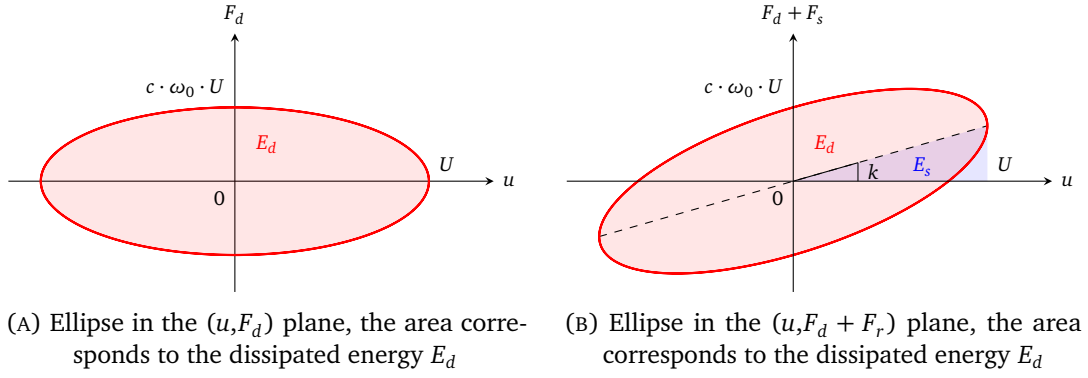


FIGURE 1.9: Representation of the dissipated and stored energy during one cycle of steady-state mono-harmonic response

If the excitation frequency is equal to the eigenfrequency of the oscillator, i.e.  $\omega = \omega_0$ , equation (1.53) is simplified:

$$\xi = \frac{1}{4 \cdot \pi} \cdot \frac{E_d}{E_s} \quad (1.54)$$

In steady-state, the input energy during one cycle is fully dissipated by the damper. To express this energy, a closed-form expression  $F(u)$  is needed. To this end, the velocity  $\dot{u}$  is re-written:

$$\begin{aligned} \dot{u}(t) &= \pm \omega \cdot \sqrt{U^2 \cdot \cos^2(\omega \cdot t)} = \pm \omega \cdot \sqrt{U^2 - U^2 \sin^2(\omega \cdot t)} \\ &= \pm \omega \cdot \sqrt{U^2 - u(t)^2} \end{aligned} \quad (1.55)$$

So, the damping force writes:

$$F_d = -c \cdot \dot{u} = \pm c \cdot \omega \cdot \sqrt{U^2 - u(t)^2} = \pm c \cdot \omega \cdot U \cdot \sqrt{1 - \frac{u^2}{U^2}} \quad (1.56)$$

Thus, the following equation of an ellipse in the plane  $(u, F_d)$  plotted on figure 1.9a is obtained:

$$\left( \frac{F_d}{c \cdot \omega \cdot U} \right)^2 + \left( \frac{u}{U} \right)^2 = 1 \quad (1.57)$$

If the resisting force of the spring, noted  $F_s$ , is added (figure 1.9b), the equation becomes:

$$F_d + F_s = \pm c \cdot \omega_0 \cdot U \cdot \sqrt{1 - \frac{u^2}{U^2}} - k \cdot u \quad (1.58)$$

The damping ratio given in equation (1.54) can be graphically interpreted in the force-displacement plane (in figure 1.9b) as the ratio between the area in the ellipse and the area of the triangle formed by the point of maximum displacement and the abscissas multiplied by a coefficient  $\frac{1}{4 \cdot \pi}$ . However, as shown in equation (1.53), the excitation frequency should be taken into account through the term  $\frac{\omega_0}{\omega}$ . Physically, this means that

the equivalent viscous damping ratio associated with one calibration frequency (in the sense of the Caughey's damping model described in section 1.2.2.2) should be adapted to the excitation frequency. Indeed, the higher the excitation frequency will be, the lower the equivalent viscous damping ratio is. In practice, this effect is almost never taken into account. For example, Chopra, 2007 (in section 3.9 of his book) states that it represents a satisfactory approximation for structures that respond mainly on their 1<sup>st</sup> eigenmode.

In summary, the two following assumptions should be checked so that the equivalent viscous damper works properly:

- the steady-state regime is reached;
- the response is mono-harmonic at a known angular frequency ( $\omega$ );

These two assumptions are challenging for the traditional Jacobsen's areas method (JAM): a seismic event is transient and has a wide frequency content by nature.

Authors	Expression of $\xi$	Remarks
Rosenblueth & Herrera, 1964	$\xi_0 + \frac{2}{\pi} \cdot \left[ \frac{(1-r)(\mu-1)}{\mu-r\mu+r\mu^2} \right]$ (1.59)	–
Gulkan & Sozen, 1974	$\xi_0 + 0.2 \cdot \left( 1 - \frac{1}{\sqrt{\mu}} \right)$ (1.60)	Based on Takeda model, for RC frames
Iwan & Gates, 1979	$\xi_0 + 0.0587 \cdot (\mu - 1)^{0.371}$ (1.61)	For elastic and Coulomb slip elements
Kowalsky, 1994	$\xi_0 + \frac{1}{\pi} \cdot \left( 1 - \frac{1-r}{\sqrt{\mu}} - r \cdot \sqrt{\mu} \right)$ (1.62)	Based on Takeda model with $\alpha = 0.5$ and $\beta = 0$
Priestley, 2003a	$\xi_0 + \frac{1.50}{\mu \cdot \pi} \cdot (\mu - 1)$ (1.63)	For steel members
Priestley, 2003b	$\xi_0 + \frac{1.20}{\pi} \cdot \left( 1 - \frac{1}{\sqrt{\mu}} \right)$ (1.64)	For concrete frames
Priestley, 2003c	$\xi_0 + \frac{0.95}{\pi} \cdot \left( 1 - \frac{1}{\sqrt{\mu}} \right)$ (1.65)	For concrete columns and walls
Priestley, 2003d	$\xi_0 + \frac{0.25}{\pi} \cdot \left( 1 - \frac{1}{\sqrt{\mu}} \right)$ (1.66)	For precast walls or frames with unbonded prestressing
Elmenschawi & Brown, 2009	$\xi_0 + 0.061 \cdot \ln \mu$ (1.67)	–
Rodrigues <i>et al.</i> , 2011	$\xi_0 + 0.0518 \cdot \ln \mu$ (1.68)	For RC columns
Rodrigues <i>et al.</i> , 2011	$0.2725 - \frac{0.2225}{\mu^{0.37}}$ (1.69)	For RC columns

TABLE 1.1: Overview of damping models based on ductility level in the literature ( $\mu$ : displacement ductility level —  $r$ : hardening stiffness for bilinear models)

Of course, JAM can be used on the basis of experiments as well as on theoretical hysteretic models as shown in table 1.1. Almost every equivalent damping ratio model listed in this table and represented in figure 1.10 increases with respect to the displacement ductility factor  $\mu = \frac{\delta_{max}}{\delta_y}$  with  $\delta_{max}$  the maximum seen displacement and  $\delta_y$  the elastic displacement limit. The two exceptions are Rosenblueth & Herrera, 1964 and Priestley, 2003, which show an asymptotically decreasing equivalent viscous damping ratio (EVDR) beyond a certain value of ductility.

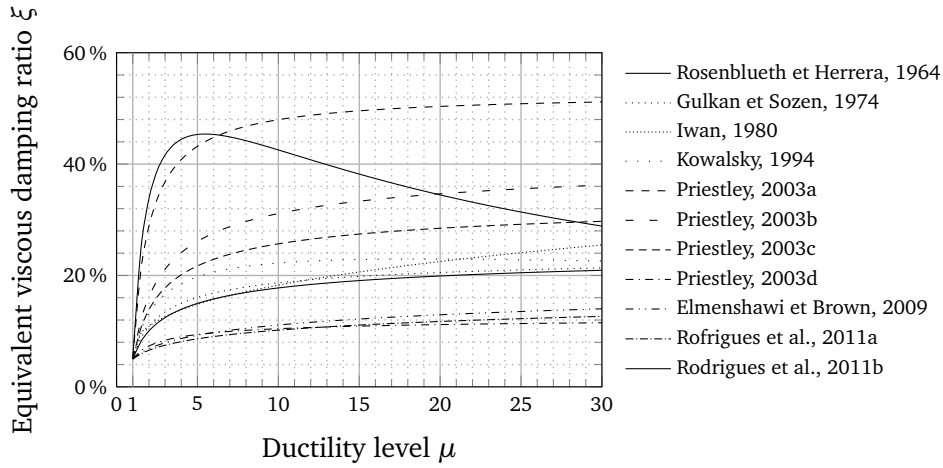


FIGURE 1.10: Comparative plots of models expressed in table 1.1 with  $\xi_0 = 5\%$  and  $r = 0.05$  for models requiring it

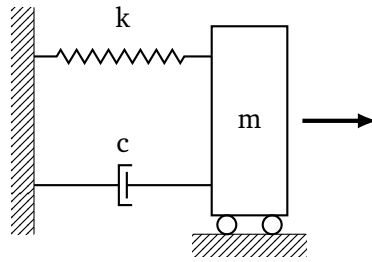


FIGURE 1.11: Conventional linear mass-spring-damper model

### 1.3.2 From free vibrations tests

#### 1.3.2.1 Theoretical aspects

The experimental aspects of the free vibrations tests are treated in section 1.4.2. The ideal linear SDOF system depicted in 1.11 is here studied from a theoretical point of view when it is freed from an unbalanced state at a prescribed displacement  $u_0$  with an initial velocity  $\dot{u}_0$  (which is often zero). Due to damping, the oscillations present a decay envelope. The nature of this envelope depends on the type of damping dissipating the energy. Hence, for a linear viscous damping, the decay envelope is an exponential function, as it will be demonstrated below. The free vibrations equation of a linear SDOF system writes:

$$m \cdot \ddot{u}(t) + c \cdot \dot{u}(t) + k \cdot u(t) = 0 \quad (1.70)$$

Its response may be expressed in the following complex form:

$$\underline{u}(t) = U \cdot \exp(j \cdot \omega \cdot t) \quad (1.71)$$

where underlining denotes the complex variables, and  $j = \sqrt{-1}$ . Injecting this expression in equation (1.70) gives:

$$(-m \cdot \omega^2 + j \cdot \omega \cdot c \cdot t + k) \cdot \underline{U} \cdot \exp(j \cdot \omega \cdot t) = 0 \quad (1.72)$$

which can be simplified in the following way:

$$-\omega^2 + j \cdot \omega \cdot 2 \cdot \xi \cdot \omega_0 + \omega_0^2 = 0 \quad (1.73)$$

with  $c = 2 \cdot m \cdot \xi \cdot \omega_0$  and  $\omega_0 = \frac{k}{m}$ . The characteristic equation associated to equation (1.73) has the following complex roots:

$$\underline{\omega}_{1,2} = j \cdot \xi \cdot \omega_0 \pm \omega_0 \cdot \sqrt{1 - \xi^2} \quad (1.74)$$

The viscous damping ratio  $\xi$  in case of a mono-harmonic oscillator may be interpreted as the ratio between the damping coefficient  $c$  and the so-called critical damping coefficient  $c_c = 2 \cdot m \cdot \omega_0$  below which the oscillations appear when a free vibrations test is carried out. The critical damping is a dynamic characteristic of the studied structure since it depends on both its mass  $m$  and *undamped* angular frequency  $\omega_0$  (also called eigenpulsation). Hence, three cases can be distinguished:

- when  $\xi \geq 1$ , the system is said “*over-damped*” (or “*critically damped*” if  $\xi = 1$ ) and returns to its equilibrium state without any oscillation;
- when  $0 < \xi < 1$ , the system is “*under-damped*” and returns to its equilibrium with oscillations;
- when  $\xi = 0$ , the system is “*undamped*” and oscillates indefinitely.

Considering the case of an under-damped system ( $\xi < 1$ ), the solutions of the equation (1.73) is built as the superposition of two terms (with  $j = \sqrt{-1}$ ):

$$\underline{u}(t) = U_1 \cdot \exp(j \cdot \underline{\omega}_1 \cdot t) + U_2 \cdot \exp(j \cdot \underline{\omega}_2 \cdot t) \quad (1.75)$$

which may be simplified as follows:

$$\underline{u}(t) = \exp(-\xi \cdot \omega \cdot t) \cdot \left( U_1 \cdot \exp(j \cdot \omega_0 \cdot \sqrt{1 - \xi^2}) + U_2 \cdot \exp(-j \cdot \omega_0 \cdot \sqrt{1 - \xi^2}) \right) \quad (1.76)$$

Then, the real displacement response  $u(t) = \text{Re}(\underline{u})$  is:

$$u(t) = \exp(-\xi \cdot \omega_0 \cdot t) \cdot (U_1 \cdot \cos(\omega_d \cdot t) + U_2 \cdot \sin(\omega_d \cdot t)) \quad (1.77)$$

where  $\omega_d = \omega_0 \cdot \sqrt{1 - \xi^2}$  is the pseudo-angular frequency. In fact, the pseudo-angular frequency is the one which is directly measured from the pseudo-period  $T_d$ , as shown in figure 1.12. The value of the damping ratio  $\xi$  is then necessary to calculate the undamped angular frequency  $\omega_0$  of the system. However, when the viscous damping ratio is rather low ( $\xi \ll 1$ ), it is often assumed that  $\omega_0 \approx \omega_d$ . Indeed, for  $\xi = 0.01$ , the relative difference between the two angular frequencies is approximately of 0.005 %.

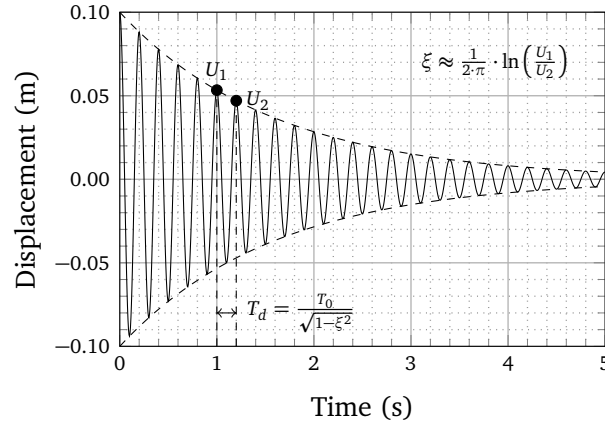


FIGURE 1.12: Logarithmic decrement method (LDM),  $T_0$  is the natural period of the undamped oscillations

The initial conditions are used to fully determine the solution:

$$\begin{cases} u(0) = u_0 = U_1 \\ \dot{u}(0) = \dot{u}_0 = -\xi \cdot \omega_0 \cdot U_1 + U_2 \cdot \omega_d \end{cases} \quad (1.78)$$

$$\Leftrightarrow \begin{cases} U_1 = u_0 \\ U_2 = \frac{\dot{u}_0 + \xi \cdot \omega_0 \cdot u_0}{\omega_d} \end{cases} \quad (1.79)$$

The exponential term  $\exp(-\xi \cdot \omega_0 \cdot t)$  in equation (1.77) corresponds to the decay envelope of the oscillations. Therefore, the decrease rate is directly linked to the damping ratio and the eigenfrequency of the SDOF oscillator. If  $\xi$  is interpreted as the *ratio* of dissipated energy over the maximum stored energy (per cycle), the multiplication  $\xi \cdot \omega_0$  is indeed the rate of energy dissipated per second in the free vibrations regime.

Provided the displacement response of a linear viscously damped SDOF system, the viscous damping ratio may be simply identified thanks to two different local maxima. Indeed, considering two displacement maxima at times  $t$  and  $t + n \cdot T_d$  ( $n \in \mathbb{N}$ ), denoted  $u_i$  and  $u_{i+n}$ :

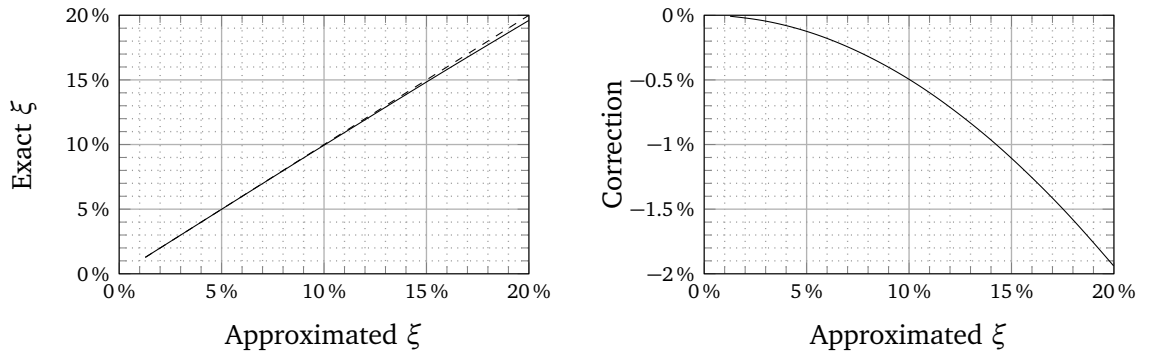
$$\frac{u_i}{u_{i+n}} = \frac{\exp(-\xi \cdot \omega_0 \cdot t)}{\exp(-\xi \cdot \omega_0 \cdot (t + n \cdot T_d))} = \exp(\xi \cdot \omega_0 \cdot n \cdot T_d) \quad (1.80)$$

The so-called logarithmic decrement (LDM) is defined as:

$$\delta_n = \ln\left(\frac{u_i}{u_{i+n}}\right) \quad (1.81)$$

Hence:

$$\xi = \frac{1}{n \cdot T_d \cdot \omega_0} \cdot \delta_n \quad (1.82)$$



(A) Exact versus approximated damping ratio evaluated by the LDM

(B) Relative correction to bring to the approximated  $\xi$ 

FIGURE 1.13: Comparison between the approximated damping ratio and the exact one

Due to theoretical considerations, for a perfect linear viscous damper, the value of  $\xi$  does not depend on  $n$ . The expression often seen in the literature (for  $n = 1$ ) is:

$$\xi = \frac{1}{2 \cdot \pi} \cdot \delta_1 \quad (1.83)$$

It is assumed that  $T_0 \approx T_d$  (which is acceptable for  $\xi \ll 1$ ), thus,  $\omega_0 \cdot T_0 = 2 \cdot \pi$ . However, it can be demonstrated from equation (1.82), using  $T_d = T_0 \cdot \sqrt{1 - \xi^2}^{-1}$ , that:

$$\xi = \frac{\delta}{\sqrt{4 \cdot \pi^2 + \delta^2}} \quad (1.84)$$

The results of these two expressions are compared in figure 1.13. Of course, it can be argued that the difference is negligible for the usual cases where  $\xi < 20\%$ , but since the expression (1.84) is quite simple, there is no reason not to use it rather than the approximated one for a perfect linear viscous damper.

### 1.3.2.2 Application to experimental data

It is of interest, as what is done with the JAM, to evaluate an EVDR for non-viscous or non-linear viscous damping phenomena. For this reason, the theory recalled in section 1.3.2.1 has to be adapted in order to be applied to experimental data. It is observed that the decay envelope is not an exponential function. The consequence is that the value of  $\xi$  identified with equation (1.82) will depend on  $n$  (not to mention it will also depend on the 1<sup>st</sup> maximum considered). Different strategies may be used for a decay motion presenting  $N + 1$  measured maxima:

- the damping is assumed linear and viscous between two successive maxima and is evaluated  $N$  times. In this case, one could either consider the damping as viscous but evolving along with the decay motion (label C-LDM for “consecutive logarithmic decrement method”);

- or compute the mean value of the EVDR during the test;
- otherwise, the best-fitting linear viscous damping model can be identified thanks to the method detailed below (labeled BF-LDM for “best-fitting logarithmic decrement method”).

This latter method is the one classically used to analyze free vibrations tests, for example Angela Salzmann, 2003:

1. obtain the coordinates of the successive local maxima of the oscillations;
2. normalize the value of the maxima by the value of the first one (the greatest);
3. compute the logarithmic values of the maxima;
4. identify the best-fitting affine function that approximate the logarithmic values along the time;
5. deduce the damping ratio from the slope of the best-fitting line which corresponds to  $-\xi \cdot \omega_0$  according to equation (1.82).

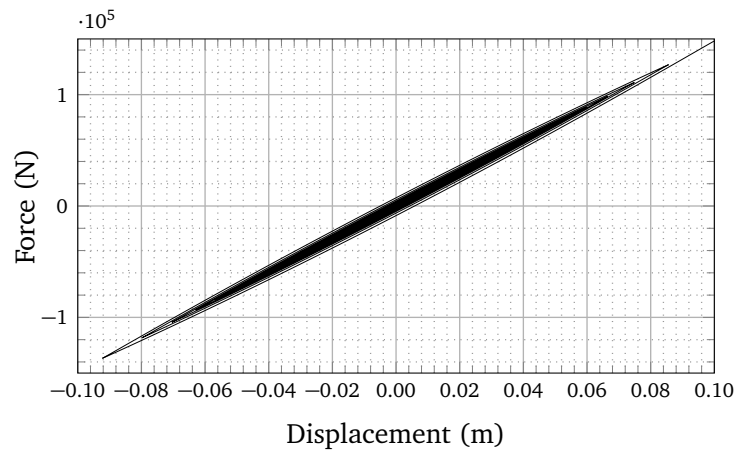
For the sake of clarity, an application case is generated synthetically. A free vibrations test is performed numerically (thanks to a converged Newmark’s explicit scheme) on a nonlinear viscous oscillator with quadratic viscous damping:

$$m \cdot \ddot{u} + c \cdot \text{sign}(\dot{u}) \cdot \dot{u}^2 + k \cdot u = 0 \quad (1.85)$$

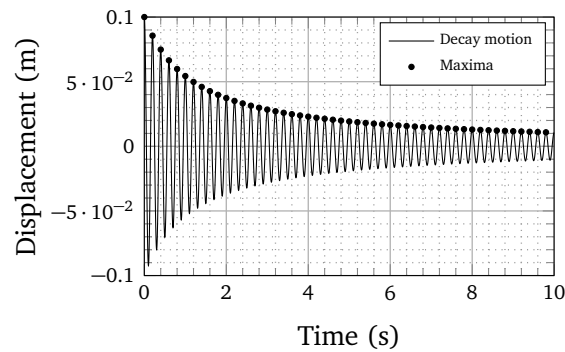
The resulting free vibrations motion is plotted on figure 1.14b and the reaction force will be used to compare the logarithmic decrement based methods with the JAM (applied on the force-displacement curve on figure 1.14a). The BF-LDM is applied as plotted on figure 1.15. The different EVDR are finally plotted on figure 1.16. The curve labeled “Mean C-LDM” corresponds to the time-integral mean value of the EVDR identified between successive maxima. The following observations are made:

- C-LDM and JAM are in perfect agreement;
- the mean of the C-LDM values differs from the only value identified by the slope of the best-fitting straight line (BF-LDM);
- the EVDR values decrease from 2.49 % to 0.29%, which makes a relative difference of +182 % to -67 % with the BF-LDM value.

Thus, the validity of the BF-LDM only value is challenged by the variations of the EVDR evaluated by JAM and C-LDM during the free vibrations. To assess the relevance of the EVDR estimation, the free vibrations motions of the different equivalent linear viscous oscillators identified are computed. The displacement responses are plotted on figure 1.17. The two one-value identifications (BF-LDM and Mean C-LDM) overestimate the displacement, BF-LDM being the better between both. On the contrary, the scalable EVDR identified by JAM allows for a good fit of the reference quadratic viscous damping model. The exact same observations are made regarding the forces (not represented here).



(A) Force-displacement response of a nonlinear oscillator



(B) Nonlinear and non-viscous free vibrations decay motion

FIGURE 1.14: Synthetic free vibrations test performed on a nonlinear SDOF oscillator

To sum up, due to the non-exponential shape of the decay envelope, it is impossible for a linear viscous damping model to fit any other decay motion. But, with a scalable EVDR (i.e. a nonlinear 1<sup>st</sup> order viscous damping), it seems possible to obtain an accurate estimation of the displacements of a quadratic viscously damped oscillation. If this conclusion can not be extended to any other type of damping, it is encouraging and motivates the development of model(s) of nonlinear 1<sup>st</sup> order viscous damping of the form  $F_d = c(\{p\}) \cdot \dot{u}$ , where  $\{p\}$  is a set of parameters that is still to investigate.

### 1.3.3 From low-level dynamic excitations

#### 1.3.3.1 Obtaining a frequency response function (FRF) from hammer shock tests

A typical hammer shock test takes place through the following steps:

- the structure is not loaded, a light shock is performed with the hammer;

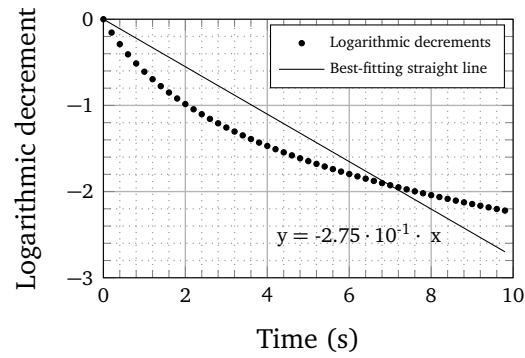


FIGURE 1.15: Best-fitting linear model for LDM

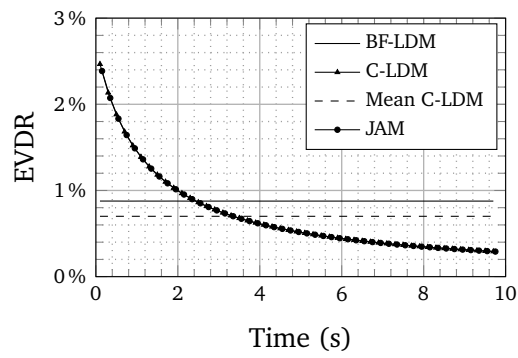


FIGURE 1.16: Comparison between LDM-based methods and JAM

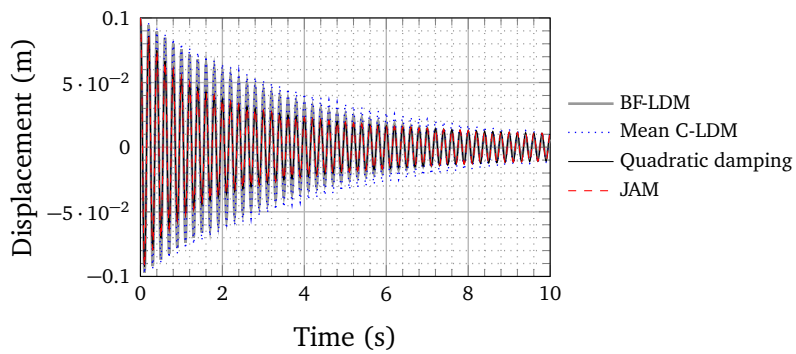


FIGURE 1.17: Comparison between LDM-based methods and JAM

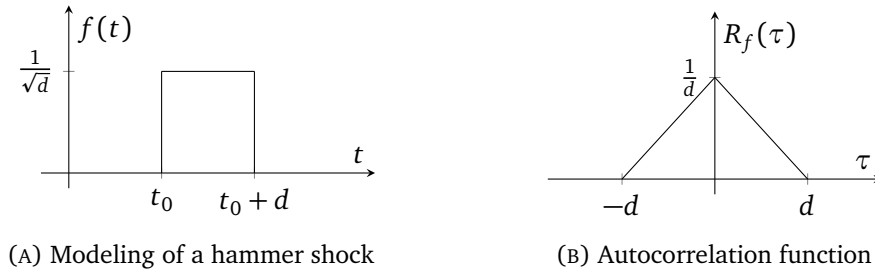


FIGURE 1.18: Hammer shock impulse and its autocorrelation function

- the time-signals of the force of the impact and of the acceleration of a point of the structure are recorded;
- the Fourier's transforms of these signals are computed;
- the FRF is deduced from the ratio between the two Fourier's transforms;
- a mean on several impacts is generally computed;
- these steps are repeated on each node of the experimental grid.

The quality of the shock strongly conditions the results: the direction of the impact should excite the sought modes, and the energy of the shock should be equally distributed on all the frequencies. To address this latter aspect, the shock has to be as brief as possible. In an ideal case, it can be modeled by a Dirac's impulse  $\delta(t)$ . The corresponding autocorrelation function is:

$$R_{\delta}(\tau) = \int_{-\infty}^{+\infty} \delta(t + \tau) \cdot \delta(t) \cdot dt = \delta(-\tau) \quad (1.86)$$

Then, the power spectral density (PSD) is:

$$\begin{aligned} S_{\delta}(\omega) &= \int_{-\infty}^{+\infty} R_{\delta}(\tau) \cdot \exp(-j \cdot \omega \cdot \tau) \cdot d\tau \\ &= \int_{-\infty}^{+\infty} \delta(-\tau) \cdot \exp(-j \cdot \omega \cdot \tau) \cdot d\tau \\ &= \exp(0) \\ &= 1 \end{aligned} \quad (1.87)$$

Hence, according to equation (1.87), all the frequencies are excited when the shock is a Dirac's impulse. A more realistic modeling of the hammer shock is a constant function  $f(t)$  of duration  $d$  and amplitude  $1/\sqrt{d}$ , as depicted on figure 1.18a, so that the energy of the signal  $\int_{-\infty}^{+\infty} f(t)^2 \cdot dt$  is equal to 1.

If  $H(t)$  denotes the Heaviside function:

$$f(t) = \frac{1}{\sqrt{d}} \cdot (H(t_0) - H(t_0 + d)) \quad (1.88)$$

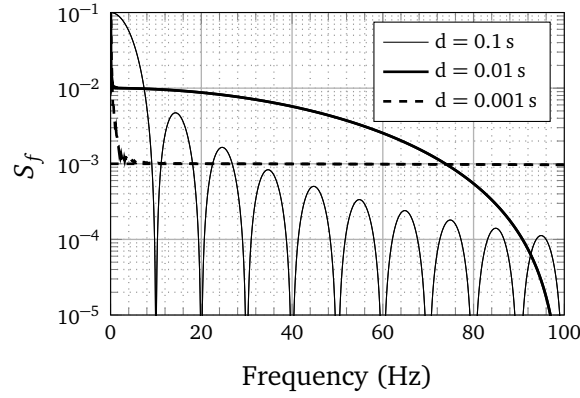


FIGURE 1.19: PSD of the hammer shock

Thus, the autocorrelation function is:

$$\begin{aligned}
 R_f(\tau) &= \int_{-\infty}^{\infty} f(t) \cdot f(t + \tau) \cdot dt = \frac{1}{d} \int_{-\infty}^{+\infty} f(t) \cdot f(t + \tau) \cdot dt \\
 &= \frac{1}{d} \cdot \langle d - |\tau| \rangle_+
 \end{aligned} \tag{1.89}$$

The PSD is finally computed:

$$\begin{aligned}
 S_f(\omega) &= \int_{-\infty}^{+\infty} R_f(\tau) \cdot \exp(-j \cdot \omega \cdot \tau) \cdot d\tau \\
 &= \int_{-\infty}^{+\infty} \underbrace{\frac{1}{d} \cdot \langle d - |\tau| \rangle_+}_{\text{even function}} \cdot \left( \underbrace{\cos(-\omega \cdot t)}_{\text{even function}} + j \cdot \underbrace{\sin(-\omega \cdot t)}_{\text{odd function}} \right) \cdot d\tau \\
 &= 2 \cdot \int_0^d \frac{1}{d} \cdot (d - \tau) \cdot \cos(-\omega \cdot \tau) \cdot d\tau \\
 &= \frac{2}{\omega^2 \cdot d} \cdot (1 - \cos(\omega \cdot d)) \quad \text{using an integration by parts}
 \end{aligned} \tag{1.90}$$

As observed on the PSD shown in figure 1.19, the frequency content of the impact signal highly depends on the duration  $d$  of the shock. The shorter it is, the wider is the frequency range on which the PSD is constant. As a rule of thumb, it is considered that the hammer shock excites equally the modes in a frequency range going from 0 to  $\frac{1}{5 \cdot d}$ .

The data recorded during the hammer-shock tests are also useful to get the frequency response function (FRF) of the tested structure. Then, this FRF can be used to assess an equivalent viscous damping ratio using for example the half-power bandwidth method, as explained in section 1.3.3.2.

### 1.3.3.2 Half-power bandwidth method (HBM)

This method is often applied on responses to low-level dynamic excitation because a linear behavior of the structure is assumed. A linear viscously damped SDOF system subjected to a mono-harmonic loading is driven by the following balance equation:

$$m \cdot \ddot{u}(t) + c \cdot \dot{u}(t) + k \cdot u(t) = F_0 \cdot \sin(\omega \cdot t) \quad (1.91)$$

The complex notation is used to find the steady-state solution of equation (1.91). A particular solution of the form  $\underline{u}(t) = U_0 \cdot \exp(i \cdot \omega \cdot t + i \cdot \phi)$  is sought:

$$(-\omega^2 + i \cdot \omega \cdot 2 \cdot \xi \cdot \omega_0 + \omega_0^2) \cdot U_0 \cdot \exp(i \cdot \omega \cdot t + i \cdot \phi) = \frac{F_0}{m} \cdot \exp(i \cdot \omega \cdot t) \quad (1.92)$$

The displacement FRF is defined as the ratio between the actual dynamic displacement and the equivalent static displacement that would produce the same force level as the force excitation, namely  $\frac{F_0}{k}$ :

$$H_d(\omega) = \frac{U_0 \cdot \exp(i \cdot \phi)}{F_0/k} = \frac{k}{m} \cdot \frac{1}{\omega_0^2 - \omega^2 + i \cdot 2 \cdot \xi \cdot \omega \cdot \omega_0} \quad (1.93)$$

$$\Leftrightarrow H_d(\omega) = \frac{1}{1 - \left(\frac{\omega}{\omega_0}\right)^2 + i \cdot 2 \cdot \xi \cdot \frac{\omega}{\omega_0}} \quad (1.94)$$

In a similar manner, the acceleration FRF modulus is the ratio between the acceleration  $\ddot{u}(t) = -\omega^2 \cdot U_0 \cdot \exp(i \cdot \omega \cdot t + i \cdot \phi)$  and the equivalent excitation acceleration  $\frac{F_0}{m} \cdot \exp(i \cdot \omega \cdot t)$ :

$$H_a(\omega) = \frac{-\omega^2 \cdot U_0 \cdot \exp(i \cdot \phi)}{F_0/m} \quad (1.95)$$

$$\Leftrightarrow H_a(\omega) = -\left(\frac{\omega}{\omega_0}\right)^2 \cdot H_d(\omega) \quad (1.96)$$

Hence, the dynamic displacement and acceleration amplification factors are respectively expressed by the following equations:

$$|H_d(\omega)| = \frac{1}{\sqrt{\left(1 - \left(\frac{\omega}{\omega_0}\right)^2\right)^2 + \left(2 \cdot \xi \cdot \frac{\omega}{\omega_0}\right)^2}} \quad (1.97)$$

$$|H_a(\omega)| = \frac{\left(\frac{\omega}{\omega_0}\right)^2}{\sqrt{\left(1 - \left(\frac{\omega}{\omega_0}\right)^2\right)^2 + \left(2 \cdot \xi \cdot \frac{\omega}{\omega_0}\right)^2}} \quad (1.98)$$

In the following study, the acceleration amplification factor will be used. The maximum acceleration is reached for:

$$\omega_{ra} = \frac{\omega_0}{\sqrt{1 - 2 \cdot \xi^2}} \quad (1.99)$$

which corresponds to a modulus:

$$|H_a(\omega)|_{max} = \frac{1}{2 \cdot \xi \cdot \sqrt{1 - \xi^2}} \quad (1.100)$$

The so-called half-power frequencies are the roots of equation 1.101:

$$|H_a(\omega)| = \frac{|H(\omega)|_{max}}{\sqrt{2}} \quad (1.101)$$

which are:

$$\frac{\omega_1}{\omega_0} = \left( \frac{1 - 2 \cdot \xi^2 - 2 \cdot \xi \cdot (1 - \xi^2)^{\frac{1}{2}}}{1 - 8 \cdot \xi^2 + 8 \cdot \xi^4} \right)^{\frac{1}{2}} \quad (1.102)$$

$$\frac{\omega_2}{\omega_0} = \left( \frac{1 - 2 \cdot \xi^2 + 2 \cdot \xi \cdot (1 - \xi^2)^{\frac{1}{2}}}{1 - 8 \cdot \xi^2 + 8 \cdot \xi^4} \right)^{\frac{1}{2}} \quad (1.103)$$

It is more convenient to work with the resonance angular frequency  $\omega_{ra}$  since it is the one measured experimentally. Using  $\omega_0 = \omega_{ra} \cdot \sqrt{1 - 2 \cdot \xi^2}$ :

$$\frac{\omega_1}{\omega_{ra}} = \left( \frac{1 - 4 \cdot \xi^2 - 2 \cdot \xi \cdot \sqrt{1 - \xi^2} + 4 \cdot \xi^4 + 4 \cdot \xi^3 \cdot \sqrt{1 - \xi^2}}{1 - 8 \cdot \xi^2 + 8 \cdot \xi^4} \right)^{\frac{1}{2}} \quad (1.104)$$

$$\frac{\omega_2}{\omega_{ra}} = \left( \frac{1 - 4 \cdot \xi^2 + 2 \cdot \xi \cdot \sqrt{1 - \xi^2} + 4 \cdot \xi^4 - 4 \cdot \xi^3 \cdot \sqrt{1 - \xi^2}}{1 - 8 \cdot \xi^2 + 8 \cdot \xi^4} \right)^{\frac{1}{2}} \quad (1.105)$$

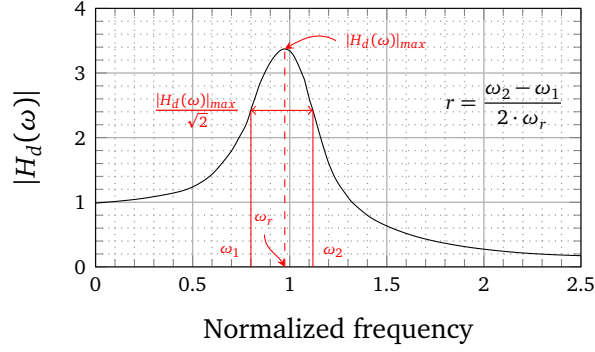
The half-power bandwidth is defined as the ratio:

$$r = \frac{\omega_2 - \omega_1}{2 \cdot \omega_{ra}} \quad (1.106)$$

Until this point, no approximation has been made yet. The common practice is to consider that the damping ratio is small ( $\xi \ll 1$ ). Then, higher-order terms are neglected. Taylor's series expansions of equations (1.104) and (1.105) give:

$$\frac{\omega_1}{\omega_{ra}} = 1 - \xi + \frac{3}{2} \cdot \xi^2 - 4 \cdot \xi^3 + \frac{71}{8} \cdot \xi^4 + O(\xi^5) \quad (1.107)$$

$$\frac{\omega_2}{\omega_{ra}} = 1 + \xi + \frac{3}{2} \cdot \xi^2 + 4 \cdot \xi^3 + \frac{71}{8} \cdot \xi^4 + O(\xi^5) \quad (1.108)$$

FIGURE 1.20: Illustration of the half-power bandwidth  $r$ 

Two different approximation strategies can be found out from the literature. The classical choice is to neglect terms for which the power is higher than 1, then:

$$\omega_0 \approx \omega_{ra} \quad (1.109)$$

$$\frac{\omega_1}{\omega_{ra}} \approx 1 - \xi \quad (1.110)$$

$$\frac{\omega_2}{\omega_{ra}} \approx 1 + \xi \quad (1.111)$$

and the damping ratio is estimated using both equations (1.110) and (1.111):

$$\xi \approx \frac{\omega_2 - \omega_1}{2 \cdot \omega_{ra}} = r \quad (1.112)$$

In other words, being provided a Frequency Response Function (FRF), a damping ratio can be estimated for each peak by measuring the frequency bandwidth of the domain where the amplification is higher than the peak amplification over  $\sqrt{2}$ , as pictured on figure 1.20.

Another choice, suggested by Wang, 2011, is to keep the 3<sup>rd</sup> order terms. The following equations arise:

$$\frac{\omega_1}{\omega_{ra}} \approx 1 - \xi + \frac{3}{2} \cdot \xi^2 - 4 \cdot \xi^3 \quad (1.113)$$

$$\frac{\omega_2}{\omega_{ra}} \approx 1 + \xi + \frac{3}{2} \cdot \xi^2 + 4 \cdot \xi^3 \quad (1.114)$$

and the damping ratio is also estimated using both equations (1.113) and (1.114):

$$\xi + 4 \cdot \xi^3 \approx \frac{\omega_2 - \omega_1}{2 \cdot \omega_{ra}} = r \quad (1.115)$$

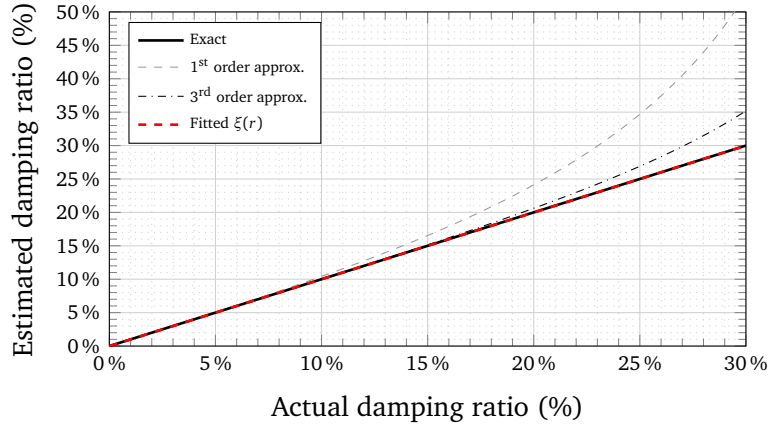


FIGURE 1.21: Comparison of the corrected damping ratio against the usual one (Fitted  $\xi(r)$  corresponds to equation (1.118))

The only real closed-form solution of equation (1.115) is:

$$\xi = \left( \frac{\sqrt{27 \cdot r^2 + 1}}{8 \cdot 3^{\frac{3}{2}}} + \frac{r}{8} \right)^{\frac{1}{3}} - \frac{1}{12 \cdot \left( \frac{\sqrt{27 \cdot r^2 + 1}}{8 \cdot 3^{\frac{3}{2}}} + \frac{r}{8} \right)^{\frac{1}{3}}} \quad (1.116)$$

This corresponds to the 3<sup>rd</sup> order approximation of the viscous damping of a linear viscously damped SDOF oscillator evaluated from the HBM.

To obtain the comparison plot presented in figure 1.21, the half-power bandwidth  $r$  is computed according to the exact damping ratio thanks to equations (1.104) and (1.105):

$$r = \frac{1}{2} \cdot \left( \frac{1 - 4 \cdot \xi^2 - 2 \cdot \xi \cdot \sqrt{1 - \xi^2} + 4 \cdot \xi^4 + 4 \cdot \xi^3 \cdot \sqrt{1 - \xi^2}}{1 - 8 \cdot \xi^2 + 8 \cdot \xi^4} \right)^{\frac{1}{2}} - \frac{1}{2} \cdot \left( \frac{1 - 4 \cdot \xi^2 + 2 \cdot \xi \cdot \sqrt{1 - \xi^2} + 4 \cdot \xi^4 - 4 \cdot \xi^3 \cdot \sqrt{1 - \xi^2}}{1 - 8 \cdot \xi^2 + 8 \cdot \xi^4} \right)^{\frac{1}{2}} \quad (1.117)$$

Then, the 1<sup>st</sup> and 3<sup>rd</sup> order approximations of the damping ratios are computed using equations (1.112) and (1.116) respectively (in a similar way to what is done by Wang, 2011). Wang, 2011 and Papagiannopoulos & Hatzigeorgiou, 2011 recommend to use the 3<sup>rd</sup> order HBM for damping ratios higher than 10 %.

In practice, it is necessary to use an approximation, whatever its order is, because equation (1.117) is not trivial to inverse to get the exact value of  $\xi$  depending on the half-power bandwidth  $r$ : formal computational softwares fail to provide a closed-form solution. However, it is still possible to fit the proper function with numerical optimization tools, e.g. MATLAB<sup>®</sup>. This operation is carried out for  $r \lesssim 0.5$  on figure 1.22, i.e. for  $\xi$  up to 30 % but this could have been performed for  $\xi > 30$  %. Moreover, equation (1.117) does not have real solution for  $\xi \gtrsim 0.382$  because of the sign of the argument of the square root in equation (1.117). The obtained expression:

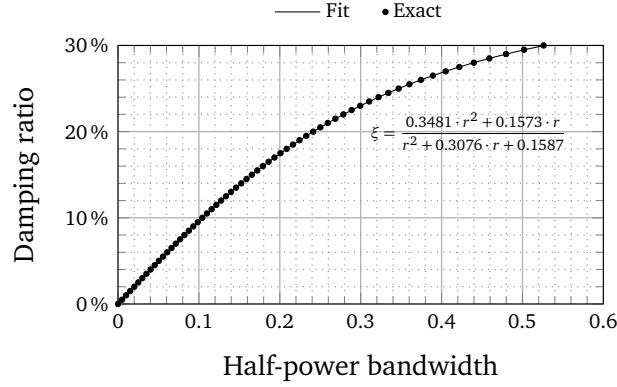


FIGURE 1.22: Fitting of a function  $\xi(r)$  for values of damping between 0 and 30 %

$$\xi = \frac{0.3481 \cdot r^2 + 0.1573 \cdot r}{r^2 + 0.3076 \cdot r + 0.1587} \quad (1.118)$$

allows for a better estimation as seen with the red dashed curve on figure 1.21, especially for higher damping values.

### 1.3.3.3 Peak response method (PRM)

Once again, this method is generally applied on low-level dynamic excitation responses because a linear behavior of the structure is assumed. It is possible to use the dynamic amplification factors given by equations (1.98) and (1.97) to get the viscous damping ratio using the peak response. Using the displacement resonance angular frequency:

$$\omega_{rd} = \arg \max_{\omega} (|H_d(\omega)|) = \omega_0 \cdot \sqrt{1 - 2 \cdot \xi^2} \quad (1.119)$$

$$\Rightarrow |H_d(\omega)|_{max} = \frac{1}{2 \cdot \xi} \cdot \frac{1}{\sqrt{1 - \xi^2}} \quad (1.120)$$

then, the damping ratio is expressed by:

$$\xi = \sqrt{\frac{1}{2} - \frac{\sqrt{|H_d(\omega)|_{max}^2 - 1}}{2 \cdot |H_d(\omega)|_{max}}} \quad (1.121)$$

The same method can be applied with the acceleration resonance frequency (which differs from the displacement acceleration frequency):

$$\omega_{ra} = \arg \max_{\omega} (|H_a(\omega)|) = \frac{\omega_0}{\sqrt{1 - 2 \cdot \xi^2}} \quad (1.122)$$

$$\Rightarrow |H_a(\omega)|_{max} = \frac{1}{2 \cdot \xi} \cdot \frac{1}{\sqrt{1 - \xi^2}} \quad (1.123)$$

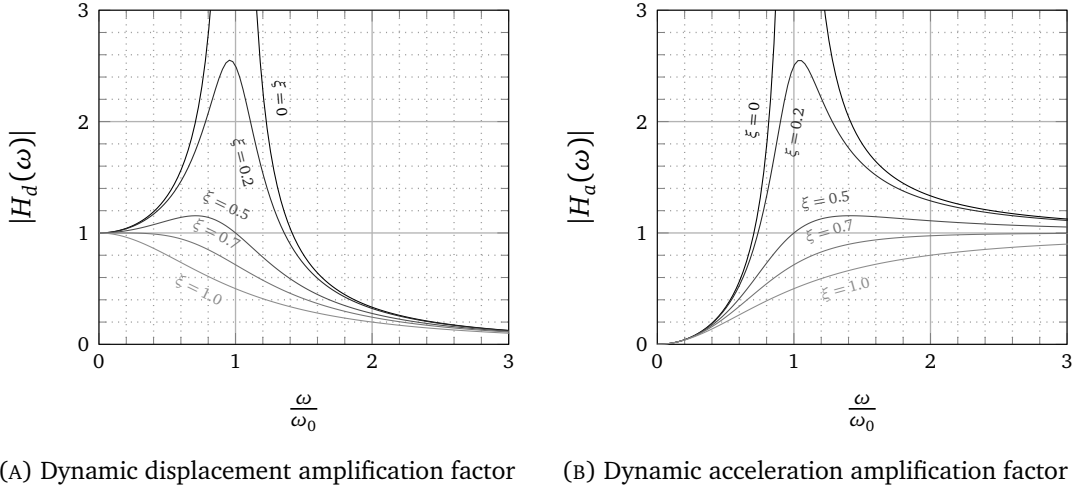


FIGURE 1.23: Dynamic amplification factors for different damping ratios

It is interesting to note that the maximum dynamic displacement and acceleration factors have exactly the same value. Then:

$$\xi = \sqrt{\frac{1}{2} - \frac{\sqrt{|H_a(\omega)|_{max}^2 - 1}}{2 \cdot |H_a(\omega)|_{max}}} \quad (1.124)$$

The maximum dynamic amplification factor can be measured experimentally. Such a measurement requires a device able to excite the SDOF oscillator with an input signal having a large frequency content. If so, results similar with the one shown in figure 1.23 can be obtained.

## 1.4 Overview of experimental campaigns on RC specimens

### 1.4.1 Quasi-static tests

Quasi-static tests are generally easier to set up since they do not bring issues related to inertial effects (e.g. spurious resonances or rattling phenomena), and allow for cancelling inertial effects that are inherent to seismic loadings. This characteristic makes them more convenient to identify the (material) dissipations which are independent on the velocity or on the acceleration, since both are negligible. However, there is a loss of information regarding the dependency of the damping on the excitation frequency. According to Jacobsen, 1960 (see also section 1.3.1.2), the approximation of structural damping by an equivalent viscous damping (i.e. proportional to the velocity) is realistic enough for structures exhibiting light to moderate nonlinear phenomena. As emphasized in section 1.3.1.1, the equivalent viscous damping ratio (EVDR)  $\xi_{eq}$  identified by Jacobsen's areas method (JAM) in quasi-static tests dissipates the right amount of energy when the

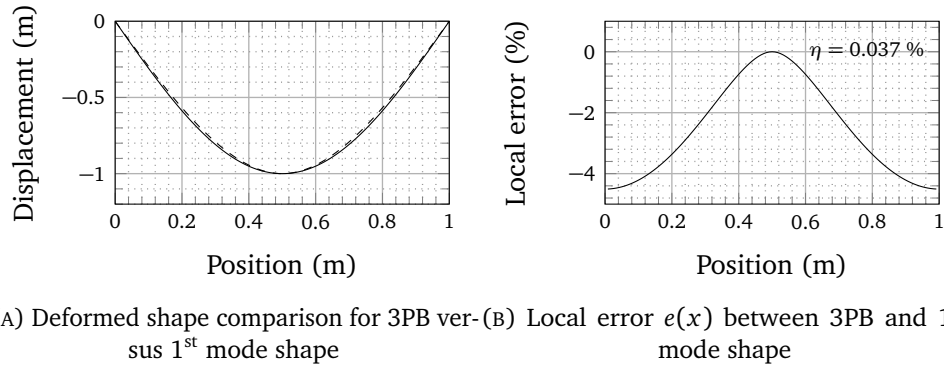


FIGURE 1.24: Comparison between 3-point bend deformed shape and 1<sup>st</sup> mode shape of the beam

SDOF system is excited exclusively at the associated eigenfrequency and when hysteretic loops in the force-displacement plane are full.

The tests carried out by Crambuer *et al.*, 2013 on RC beams subjected to quasi-static cyclic reverse three-point bend (3PB) loadings aimed to evaluate the EVDR for different damage levels and cycle amplitudes (force-controlled). The underlying hypothesis is that the recorded quasi-static response is the one of the associated SDOF in dynamics. However, due to inertial effects, the bending mode shape of the beam is sinusoidal in dynamics while the deformed shape during the quasi-static 3PB test is a 3<sup>rd</sup> degree polynomial function. This observation challenges the validity of the aforementioned assumption, but the difference remains small as shown in figure 1.24. The local error criterion used in figure 1.24b is defined in equation (1.125), with  $x$  the position along the beam,  $u$  the 3PB deformed shape normalized by the midspan displacement and  $\phi_1$  the 1<sup>st</sup> mode shape also normalized by its midspan value. The overall error criterion expressed in equation (1.126) indicates the good accordance of the 3PB deformed shape with the 1<sup>st</sup> mode shape.

$$e(x) = \frac{u(x) - \phi_1(x)}{\Phi_1(x)} \quad (1.125)$$

$$\eta = \frac{\int_0^L |u(x) - \phi_1(x)| \cdot dx}{\int_0^L |\phi_1(x)| \cdot dx} \quad (1.126)$$

with  $L$  the span length. Another experimental campaign consisting in quasi-static tests has been carried out by Rodrigues *et al.*, 2011 and focused on the assessment of dissipations in RC columns under biaxial cyclic loadings: an actuator pushes in the transverse direction at the top of the column. Several RC sections, reinforcement patterns and loading trajectories have been studied. The energy dissipated per cycle, the cumulative dissipated energy and the hysteretic damping ratio have been investigated (the latter being deduced from the two former by Jacobsen's equivalence, recalled in section 1.3 with equation (1.54)). Finally, two simplified expressions allowing for a rough estimation of the so-called biaxial damping in RC columns are proposed (equations (1.68) and (1.69) in table 1.1).

It is interesting to mention another study carried out by Elmenshawi & Brown, 2009 on RC beam-column connections which leads to a damping ratio evolution law, having exactly the same form as equation (1.67). However, Rodrigues *et al.*, 2011 state that these expressions should be corrected on the basis of nonlinear time-history analysis and dynamic shaking table tests.

### 1.4.2 Free vibrations tests

The principle of this test is to bring a structure away from its equilibrium state at a prescribed displacement (e.g. with an actuator) level, and to release it as suddenly as possible (generally without initial velocity) in order to record the decay envelope of the oscillations. It is possible to activate different vibration modes depending on the initial conditions: the higher order is the studied mode, the more complex it is to prescribe the initial conditions. A common method to evaluate an equivalent viscous damping ratio (EVDR) through this test is to apply the logarithmic decrement method (LDM). The theoretical background of this method is given in section 1.4.2. The main advantage of this type of test is that the instrumentation required is minimal since only the relative displacement is needed. However, this tests is also difficult to execute because it requires a good control over the initial conditions (position, velocity, acceleration). Indeed, the solution used load the structure from the initial displacement with the desired initial velocity (often zero) may be tricky. Carneiro *et al.*, 2005 tackle this challenge thanks to pseudo-dynamic tests allowing for a quasi-static experimental loading applied by an actuator at the tip of a RC beam deduced from a numerical dynamic simulation.

### 1.4.3 Low-level dynamic excitations

Among the low-level dynamic excitations, hammer shock tests are widely used by the researchers and engineers communities (Perera *et al.*, 2007; Baghiee *et al.*, 2009; Capozucca, 2009; Franchetti *et al.*, 2009). The three main advantages are that (i) they are easy to perform since they only require the dedicated hammer and at least one accelerometer, a measure only takes few seconds; (ii) consequently, they offer of portable solution to assess *in situ* the dynamic properties of a structure; (iii) they are not destructive and repeatable at will. The latter point counterbalances the fact that, according to Reynolds & Pavic, 2000, 10 to 20 % of the shocks are spoilt by a rattling phenomenon: the user makes the hammer bounce on the tested structure and hit it several times unintentionally in a short time period. However, the same authors found out that shaker excitation allows for higher quality measurements than hammer tests thanks to a more favorable signal/noise ratio. A similar study conducted by Ndambi *et al.*, 2000 shows that nonlinearities still have a major influence on the damping ratios scattering, whatever the method used is. Another practical issue of the method is the difficulty to excite the highest frequencies as explained in section 1.3.3.1 and depicted on figure 1.19: the shorter the duration of the impact is, the wider the excited frequency range is.

Ambient seismic noise monitoring are mostly used on existing structures (Ndambi *et al.*, 2000; Dunand, 2005). Some of them rely on the random decrement methodology, initially developed by Cole, 1973, or also on the frequency decomposition domain method

(FDD, Michel *et al.*, 2008). The result is a low amplitude free vibrations regime which has to be treated as described in section 1.4.2. Those ambient seismic noise records can also be post-treated by the so-called half bandwidth method (the reader can refer to Asmussen, 1997 for a literature review of the method and an uncertainty propagation study).

If the use of low-level dynamic excitations is convenient for the aforementioned reasons, the major issue is that they do not allow for a complete study of all the dissipative phenomena occurring during seismic events. When the crack opening is very small and that contacts between crack surfaces exist locally, the low-level excitations fail to fully open the cracks. This results in a higher stiffness than the one which would be measured in the case of fully opened cracks due to higher-level dynamic excitation. This problem is well-known for researchers developing crack detection techniques based on ultrasonic emitters (Hilloulin *et al.*, 2014).

#### 1.4.4 High-level dynamic excitations

Hydraulic jacks are commonly used as actuators for high level dynamic excitation. For economical or technical reasons, not all experimental facilities can afford a shaking table. When available, it is probably the best suited piece of equipment for studying complex structures such as for SMART 2008 (Richard *et al.*, 2016a) or SMART 2013 (Richard *et al.*, 2016b) international benchmarks on a scaled three-story RC building. The control quality is of first importance in this case, because the structure itself may disturb the actuators due to inertial effects. More reasonable setups can also provide rich information such as electromagnetic or mechanical shakers (Demarie & Sabia, 2010), mostly when simple SDOF-like structures of moderate size are studied. The damping evaluation during those tests is challenging because many phenomena are involved and the evolution of the sought properties during the loading: this motivates the choice of tests at the component scale. For this reason, consolidated intermediate low level dynamic tests are performed during the experimental campaign.

### 1.5 Conclusions of the first chapter

In this chapter, the different sources of dissipation have been described in section 1.1. Their variety explains the motivation of the development of a “unified” or “homogenized” simplified modeling through the equivalent viscous damping model which is traditionally split up in two contributions (section 1.2.2.1). However, the value of the elastic contribution is *a priori* unknown and the validity of the hysteretic contribution is always questionable regarding their viscous nature. Their variety also explains why so many viscous damping models have been developed through the last decades (section 1.2) and why there is still no consensus on the value(s) to consider for the hysteretic contribution of the damping ratio depending on the other modeling choices when performing a finite element computation.

If the latter problem is still relevant nowadays, it is partially due to the difficulty to evaluate the (equivalent) damping ratio despite the numerous methods available and non-exhaustively presented in section 1.3. The method to use depends on the nature of

the excitation (dynamic/quasi-static, low-level/high-level), and several methods can be used for a same excitation, which give in practice different results. In this case, which one is the one to consider?

In fact, a definitive answer to these questions probably does not exist, but different complementary partial answers may be obtained thanks to the use of different methods. This is the approach chosen for IDEFIX experimental campaign described and explained in the next chapter.



## Chapter 2

# IDEFIX experimental campaign: overview

### 2.1 About the experimental needs

To set up an experimental campaign, a clear identification of the needs and aims should be carried out. Indeed, it is necessary to define the phenomena of interest and what should be monitored. This section explains the choices that motivated the design of IDEFIX experiments. A focus is made on:

- the samples;
- the boundary conditions;
- the materials;
- the loadings;
- the measurements.

The main objectives are the identification and the estimation of the dissipations in RC components subjected to a seismic loading. According to these points are decided the design of tests and the types of measures (types and positions of the sensors, material characterization tests to perform, number of samples, loading procedures, experimental setup, etc.). It has been shown in chapter 1 that quasi-static tests allow for canceling the dynamic forces during the test. This characteristic is convenient to identify the hysteretic dissipations which do not depend on the velocity nor the acceleration. Nevertheless, the dynamic aspects should be considered to identify the type of damping occurring in the structure: experimental evidence shows that linear viscous damping, quadratic viscous damping (Franchetti *et al.*, 2009), or other types of non-hysteretic damping may still model satisfyingly a part of the dissipations in RC components, at least as long as material behavior laws implemented in computational softwares do not take into account the physical phenomena responsible for these types of damping.

A lack of quasi-static/dynamic experimental comparisons on the same specimens and experimental setup has been observed in this literature review. For these reasons, quasi-static and dynamic tests are both considered as essential in the search for experimental evidences and have been performed during IDEFIX experimental campaign.

Test	Advantages	Disadvantages
Cyclic reverse quasi-static	<ul style="list-style-type: none"> <li>■ Displacement/force amplitude control</li> <li>■ No inertial effect (good)</li> </ul>	<ul style="list-style-type: none"> <li>■ No inertial effect (bad)</li> </ul>
Hammer shocks	<ul style="list-style-type: none"> <li>■ Allow for a wide frequency range study</li> <li>■ Low-level excitation: “no” material nonlinearities</li> </ul>	<ul style="list-style-type: none"> <li>■ Hammer shocks require operator’s expertise</li> <li>■ Low-level excitation: not all dissipative phenomena are activated</li> </ul>
Free vibrations	<ul style="list-style-type: none"> <li>■ Easy to analyze</li> <li>■ Can provide quick information on the nature of the damping</li> </ul>	<ul style="list-style-type: none"> <li>■ May be tricky to perform experimentally</li> </ul>
Shaking table tests	<ul style="list-style-type: none"> <li>■ Possibility to generate representative seismic loading</li> <li>■ Possibility to perform sinusoidal loading</li> </ul>	<ul style="list-style-type: none"> <li>■ Requires a good online control of the table</li> <li>■ Complex loading implies complex analysis</li> </ul>
In-situ measurements	<ul style="list-style-type: none"> <li>■ Real structure</li> </ul>	<ul style="list-style-type: none"> <li>■ Boundary conditions difficult to model</li> <li>■ Small amplitudes: not all dissipative phenomena are activated</li> </ul>

TABLE 2.1: Non-exhaustive summary of the pros and cons associated to different tests

Another aspect that should be assessed is the coupling between modes in order to bring knowledge to address the following question: how does the damage due to a modal harmonic loading influence the dissipation (damping) of other modes? How is the dissipation spread out over vibration modes when they are excited at one time?

The advantages and disadvantages of some tests seen in the literature are given in table 2.1 and some references of various types of studies are given in table 2.2. It is utterly necessary to choose a type of specimen as a starting point for the design of the campaign. In their work, Crambuer *et al.*, 2013 have tested RC beams under 3-point quasi-static cyclic reverse tests. This choice was motivated by the variety of physical-wise models available to describe the stresses and strains within the specimen in such an experimental setup. For the same reason, beams are chosen as specimens for IDEFIX.

## 2.2 Experimental framework

The IDEFIX experimental campaign took place in the TAMARIS experimental facility at the French Alternative Energies and Atomic Energy Commission (CEA) from May to November 2016. Among the testing capabilities of the EMSI (Seismic Mechanic Studies) laboratory, a strong floor and a shaking table, *Azalée* (figure 2.1), have been selected as the best suited pieces of equipment for this work.

Test	Authors
Cyclic reverse quasi-static	<ul style="list-style-type: none"> <li>■ Rodrigues <i>et al.</i>, 2011</li> <li>■ Vintzileou <i>et al.</i>, 2006</li> <li>■ Elmenshawi &amp; Brown, 2009</li> <li>■ Crambuer <i>et al.</i>, 2013</li> </ul>
Hammer shocks	<ul style="list-style-type: none"> <li>■ Salzman, 2002</li> <li>■ Perera <i>et al.</i>, 2007</li> <li>■ Baghiee <i>et al.</i>, 2009</li> <li>■ Capozucca, 2009</li> <li>■ Franchetti <i>et al.</i>, 2009</li> </ul>
Free vibrations	<ul style="list-style-type: none"> <li>■ Angela Salzman, 2003</li> <li>■ Carneiro <i>et al.</i>, 2005</li> </ul>
Shaking table	<ul style="list-style-type: none"> <li>■ SEMT/EMSI/RT/98-066A, 1998</li> <li>■ Zembaty <i>et al.</i>, 2006</li> <li>■ Richard <i>et al.</i>, 2016a</li> <li>■ Richard <i>et al.</i>, 2016b</li> <li>■ Lestuzzi &amp; Bachmann, 2007</li> </ul>
In-situ measurement	<ul style="list-style-type: none"> <li>■ Dunand, 2005</li> <li>■ Mikael, 2011</li> </ul>

TABLE 2.2: Overview of experimental studies dedicated to the dissipations assessment in RC

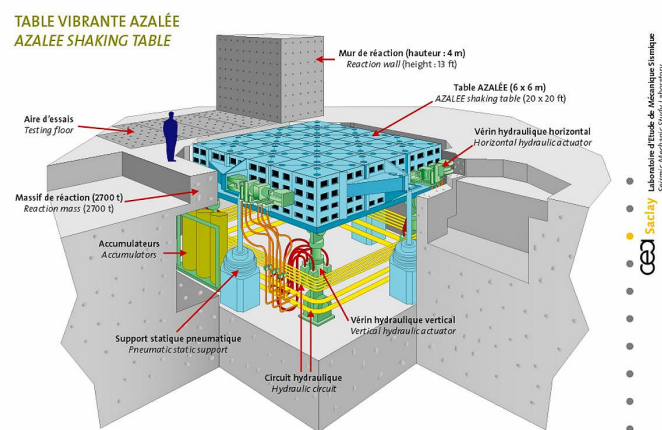


FIGURE 2.1: Description of Azalée shaking table (courtesy of EMSI laboratory)

The choice of this equipment is of primary importance because it conditions the designs of the specimens that are presented in section 2.3. Indeed, the shaking table measures  $6 \times 6 \text{ m}^2$  and the samples dimensions shall not exceed this limit for safety reasons but makes possible tests on full-scale specimens which prevent any representativeness problem related to size effects. The first studies really dedicated to these size effects in RC components have been made in the late 1990s. A study of Bažant, 1997 focuses on the influence of the size effect on the shear failure with the fracturing truss model and also gives a review of experimental campaigns that exhibited such an effect. Also, Bažant, 1999 gives an even more exhaustive review of studies dealing with size effect in the wider range of quasi-brittle materials. In the case of RC beams, the size effect shows up by a virtual increase of the beam resistance. According to Bažant, 1997, several explanations exist among which three are commonly found:

- a Weibull-type theory of random strength;
- the theory of the fracture energy release (Bazant, 1983; Bažant, 1984);
- the theory of fractal character of cracks surfaces or microcracks distributions (Carpinteri & Ferro, 1994; Carpinteri & Chiaia, 1995).

More details are given in the aforementioned article from Bažant.

The online control of the shaking table also plays a role in the design of the beams: the frequency range in which the actuators are able to reproduce in a relevant way the prescribed input signal goes from 0 Hz to 30 Hz. In order to bring answers to the questions regarding the mode coupling (see section 2.1), the specimens should have at least their first two eigenmodes in this frequency range.

For the quasi-static tests, two 25 kN capacity actuators allow for 4-point bending (4PB) tests. The advantage of such a test lies in the fact that the bending moment is constant between the two force application points, so the damage state is homogeneous in this area. Thus, it is possible to analyze the results per unit of volume. Crambuer *et al.*, 2013 has stated that dissipation occurred mainly at the mid-span, were the only actuator was mounted.

Due to the time schedule and space constraints, a maximum of 23 beams could be casted. To better overview the elements that will be detailed in the following section, a view of the two experimental setups (for quasi-static and dynamic tested) is presented in figure 2.2.

## 2.3 Specimens

### 2.3.1 Dimensions

The specimens have been designed to meet the needs and constraints expressed in sections 2.1 and 2.2. The beams are 6 m long: this respects the dimensions of the table and will also help to match the two first eigenfrequencies. A longer span could have been used (the diagonal of the table is about 8.48 m long), but there is in this case a higher risk of cracking under self-weight.

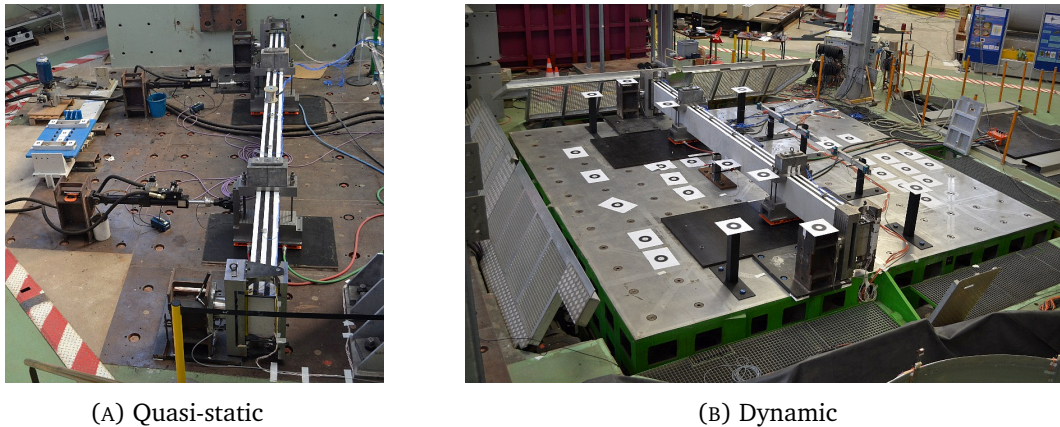


FIGURE 2.2: Experimental setups

These competing constraints were a strong concern: the beam had to be stiff enough to prevent significant cracking under self-weight (i.e. a significant reduction of the apparent bending stiffness), but slender enough to lower the two first eigenfrequencies. This problem is partially addressed by performing the test in the horizontal direction. In this way, the principal bending axis resists to gravity loads while the weak axis is the one excited during the tests. Hence, the cross section of the beams is 20 cm wide and 40 cm high.

### 2.3.2 Reinforcement

The influence of the steel-concrete bond on the dissipations has been addressed in section 1.1.3 (see the reference paper of Eligehausen *et al.*, 1982). To provide data regarding this issue at the member scale, different reinforcement patterns that are presented in table 2.3 have been chosen. Three parameters are investigated:

- the reinforcement ratio: 4HA12, 4RL12 (1.41 % both) and 4HA20 (1.57 %) have approximately the same reinforcement ratio defined as the ratio between cross section surface of steel over concrete while 8HA16 has a significantly higher reinforcement ratio of 2.01 %.
- The steel concrete bond surface (per meter): 4HA12, 4RL12 (37.7 cm<sup>2</sup>/m) have comparable bond surfaces while 4HA20 has a significantly lower bond surface (25.1 cm<sup>2</sup>/m).
- The steel reinforcement bars are all standard except for the pattern 4RL12 which uses round bars (without ribs). This will allow to evaluate qualitatively the influence of the friction between steel and concrete on the dissipated energy. It is to note that such reinforcement bars (rebars) are prohibited in the European construction code “Eurocode 2: Design of concrete structures - Part 1-1: General rules and rules for buildings”.

Past experience showed that the higher the number of longitudinal rebars is, the more cracks initiate. More cracks implies a greater cracking surface and lower crack opening. Consequently, the crack friction is more important. This point is also to investigate with the experimental results.

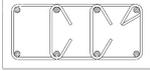
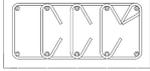
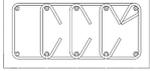
Pattern design				
Pattern label	4HA20	8HA16	4HA12	4RL12
Reinforcement ratio (%)	1.57	2.01	1.41	1.41
Bond surface (cm <sup>2</sup> /m)	25.1	40.2	37.7	37.7

TABLE 2.3: Summary of the reinforcements designs

Detailed plans of the reinforcement designs are given in appendix (figures B.2, B.3, B.4). The frames are distant of 10 cm and stirrups are used for beams 8HA16 and 10HA12.

### 2.3.3 Constitutive materials

#### 2.3.3.1 Concrete

##### a Compressive tests

Two concrete formulations were initially chosen to estimate the influence of the concrete strength on the dissipations: a C25/30 (for 21 beams) and a C45/55 (for 2 beams) (see section 3.1 of “Eurocode 2: Design of concrete structures - Part 1-1: General rules and rules for buildings” for the definition of the concrete class). Due to the high number of beams, two concrete casts were considered for the concrete C25/30 which appeared to be quite different in terms of strength (-10.6 %), Young’s modulus (+7.25 %) and fracture energy (-17.3 %). Therefore, the choice has been made to distinguish the two casts (labeled respectively with the indices *A* and *B*).

A first series of standard compressive tests (i.e. non-cyclic) has been carried out after 28 days of cure, following the guidelines *NF-EN-12390-1: Testing hardened concrete. Shape, dimensions and other requirements for specimens and moulds* on 16 cm of diameter by 32 cm of height cylinders. The results obtained from these tests are gathered in table 2.6. Then, a new series of tests has been performed after 6 months of cure at the LMT on the same types of samples, not following the norm but being cyclic in compression (the actuator velocity is 10  $\mu\text{m}/\text{m}$ ). A photo of the experimental setup is shown on figure 2.3. These cyclic tests allowed to estimate the energy dissipated by opening/closing of cracks in compression as plotted for example on figure 2.4. The loading/unloading is manually triggered by the operator when the maximum stress is reached, which explains the high standard deviations given in table 2.6. The dissipated energy seems mostly correlated with the concrete strength. The maximum aggregate size also plays a major role in the energy dissipation, this parameter has been set at 10 mm following the standard formulation proposed by the supplier of the concrete (see the delivery forms in appendix figures C.1 and C.2). The stress-strain curves of these tests are all given in appendix A.1. A summary

of the cyclic compressive tests is made in table 2.4, and the mean values are reported in table 2.6.



FIGURE 2.3: Experimental setup for the compressive cyclic test

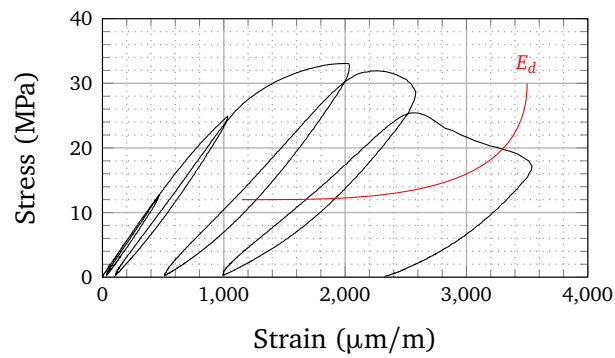


FIGURE 2.4: Cyclic compressive test on concrete C1B-2 after 6 months of cure,  $E_d$  shows the loop used for the assessment of the dissipated energy

Concrete	C1A			C1B			C2		
Test ref.	C1A-1	C1A-2	C1A-3	C1B-1	C1B-2	C1B-3	C2-1	C2-2	C2-3
$f_c$	35.9	37.6	37.2	32.7	33.1	33.2	44.1	49.6	48.6
Std dev. MPa	0.9 (2.5 %)			0.3 (0.8 %)			3.0 (6.2 %)		
Mean	36.9			33.0			47.4		
E	25.1	26.3	27.2	28.4	27.9	27.9	28.8	27.5	28.4
Std dev. GPa	1.1 (4.0 %)			0.3 (1.0 %)			0.7 (2.4 %)		
Mean	26.2			28.1			28.2		
$G_f$	3781	5391	3403	3170	3915	3318	5046	3872	4048
Std dev. J	1056 (25.2 %)			395 (11.4 %)			633 (14.6 %)		
Mean	4192			3467			4322		

TABLE 2.4: Summary of the cyclic compressive tests

### b Fracture energy measurement

The fracture energy, commonly noted  $G_f$  (in  $J/m^2$ ), is estimated after monotonic three-point bending tests on prismatic  $84\text{ cm} \times 10\text{ cm} \times 10\text{ cm}$  beams notched at mid-span on the half of their height (see figure 2.5 or B.1 in appendix), following the recommendations of the RILEM TCS, 1985. An example of the response obtained for concrete C1A is given in figure 2.6 and the other curves are given in appendix A.2. A summary table of the  $G_f$  measurements is made in table 2.5, and the mean results are added in table 2.6.

Concrete	C1A			C1B			C2		
Test ref.	C1A-1	C1A-2	C1A-3	C1B-1	C1B-2	C1B-3	C2-1	C2-2	C2-3
$G_f$	89.2	85.5	80.2	77.0	79.0	83.9	85.3	72.6	85.1
Std dev. $J/m^2$	4.5 (5.3 %)			3.5 (4.4 %)			7.3 (9.0 %)		
Mean	84.9			80.0			81.1		

TABLE 2.5: Summary of fracture energies measurements

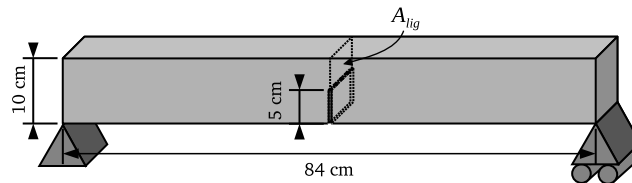


FIGURE 2.5: Single edge notched sample

The fracture energy is the one dissipated by the initiation and the propagation of a crack. Its value is generally given per unit of crack surface. By convention, it is evaluated as the total area under the force-deflection curve of the aforementioned specimen during a 3-point bending test. Thus, it also includes the elastically stored energy. This energy is eventually relieved through different nonlinear mechanisms at the end of the test (friction, sound, heat, etc.).

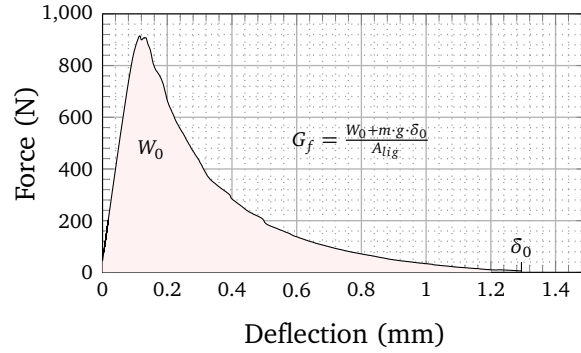


FIGURE 2.6: Example of fracture energy measurement for concrete C1A

Concrete label	C1A	C1B	C2
Concrete class	C25/30	C25/30	C45/55
$f_{c,28d}^{(1)}$ (MPa)	35.0	29.7	45.4
$f_{c,6m}^{(1)}$ (MPa)	36.9	33.0	47.4
$E_{c,28d}^{(1)}$ (GPa)	26.4	28.7	29.2
$E_{c,6m}^{(1)}$ (GPa)	26.2	28.1	28.2
$E_{d,6m}^{(1)}$ (J)	4192	3467	4322
$G_{f,6m}^{(1)}$ (J/m <sup>2</sup> )	84.9	80.0	81.0
$f_{t,G_f,6m}^{(1)}$ (J/m <sup>2</sup> )	2.09	2.22	2.47

<sup>(1)</sup>  $f_{c,28d}$ : concrete strength at 28 days —  $f_{c,6m}$ : concrete strength at 6 months —  $E_{c,28d}$ : concrete Young's modulus at 28 days —  $E_{c,6m}$ : concrete Young's modulus at 6 months —  $E_{d,6m}$ : energy dissipated for the loading/unloading cycle at maximum stress —  $G_{f,6m}$ : concrete fracture energy —  $f_{t,G_f,6m}$ : concrete tensile strength deduced after  $G_f$  measurement tests.

TABLE 2.6: Concretes' mechanical properties

This value of the fracture energy is useful when performing computations at the structural scale as it allows to dissipate the right amount of energy during the degradation of the material (see for example Matallah *et al.*, 2013). The 3-point bend tests also allow for the computation of the tensile strength, denoted  $f_{t,G_f,6m}$  in table 2.6. However, these values are not normative and are generally higher than the ones obtained after the normative wedge splitting tests since the crack is arbitrarily located at the tip of the notch. Therefore, the measured tensile strength is less sensitive to the randomness of the material properties fields which tends to minimize the force necessary to initiate and propagate a crack (weakest link theory).

The results of the three types of concrete are shown in appendix A.2. The force-displacement responses are roughly the same. The only noticeable difference is the highest peak for concrete C2 due to a higher strength.

### 2.3.3.2 Steel

The reinforcements have been classically tested in traction with an hydraulic jack (norm "EN 10080 - Steel for the reinforcement of concrete — Weldable reinforcing steel — General"). Due to the maximum capacity of the clamping system, the 20 mm diameter



FIGURE 2.7: Experimental setup of the fracture measurement tests (RILEM TCS, 1985)

bars (HA20) were not tested, but their minimal guaranteed properties were given by the supplier, and the Young's modulus is not expected to be highly scattered. The smooth and round bars RL12 have a lower yield limit because of their different manufacturing process.

Steel	HA12	HA16	HA20	RL12
Elastic limit (MPa)	528	568	>560 <sup>(2)</sup>	468
Young's modulus (GPa)	206	217	210 <sup>(2)</sup>	218

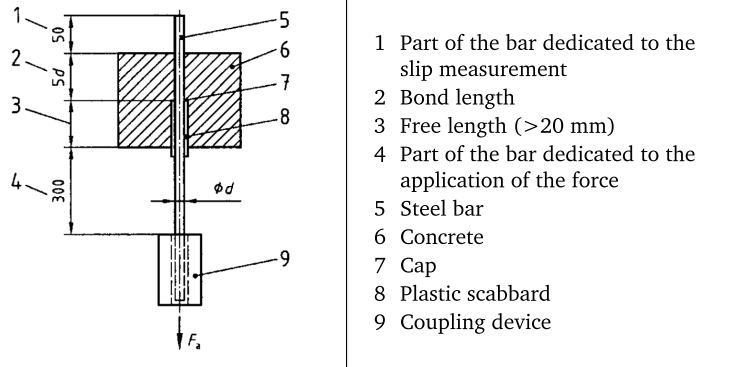
<sup>(2)</sup> clamping claw not available, values chosen from the manufacturer data

TABLE 2.7: Steel's mechanical properties

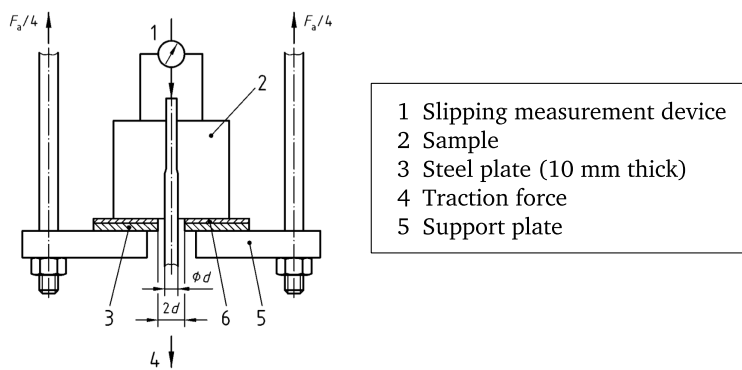
### 2.3.3.3 Steel-concrete bond

The strength of the steel-concrete bonds has been evaluated by pull-out tests, following the recommendation of the Appendix D of EN 10080. This test consists in applying a tension force in a steel bar sealed on a prescribed length in a concrete cube. Then, the traction force and the relative slipping displacement between the steel and the concrete are measured. The bar is placed at the middle of the cube, and the steel-concrete bond has a length of five times the diameter of the bar as depicted on figures 2.8. The device used for these tests is the one developed by Torre-Casanova *et al.*, 2013.

For the sake of clarity, only mean results are given in figure 2.9. For complete results, please refer to figure A.7 in the appendix. The scattering of the results is high because the strength of the steel-concrete bond is highly dependent on the local stress state and on the manufacturing defects. Two out of three samples with HA20 steel bars failed because of a macro-crack passing by the bar's axis. Other samples failed by progressive slipping of the bond. The bond tends to have a brittle behavior for larger bar diameters. Nevertheless, such a failure mode is not expected to happen with IDEFIX beams because of the transversal reinforcement which prevent the concrete from splitting away.



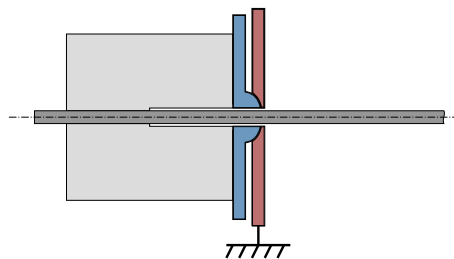
(A) Pull-out sample (from Appendix D of EN 10080)



(B) Pull-out experimental setup (from Appendix D of EN 10080)



(C) Photo of the experimental setup



(D) Pull-out experimental setup corresponding to the photo

FIGURE 2.8: Pull-out test description

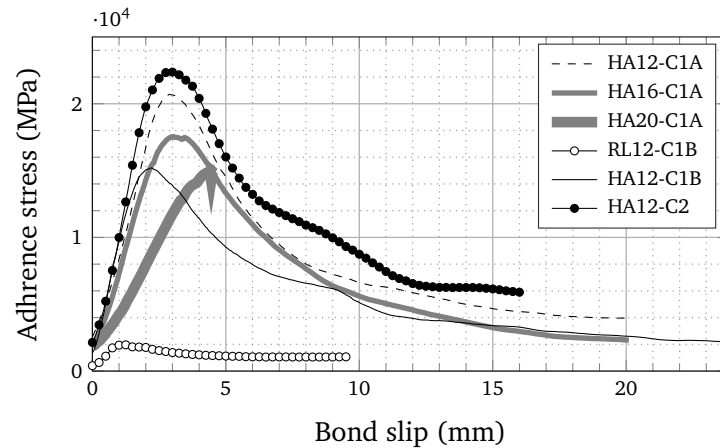


FIGURE 2.9: Mean results of the pull-out tests

Among the C1A concretes, the smaller the bars' diameter is, the more energy dissipated during the pull-out test will be. However, the difference is rather small and does not allow for general conclusions. The stronger concrete C2 does not exhibit a significantly better strength of the steel-concrete bond than with concrete C1A (see HA12-C1A versus HA12-C2). As expected, the round bars provide almost no strength to the concrete bond in which the sealing is mostly chemical.

## 2.4 Boundary conditions of the RC beams

### 2.4.1 Definition of the mechanical constraints

The boundary conditions are a critical point in the design of IDEFIX experimental campaign. They drive the eigenfrequencies of the tested structure and should behave as predictable as possible. When considering a problem in mechanics, the modeling of the boundary conditions is a strong concern, especially for the study of components embedded in complex structures. For example, the modeling of beam-column connections in RC frames is always questionable, depending on the geometries of the joints and of the reinforcement patterns.

In order to propose a consistent design for the boundary conditions, preliminary numerical studies have been carried out with Cast3M finite element code. The complete finite element model and numerical results will be presented in chapter 4. In this chapter, only the method used for the design of intermediate supports (section 2.4.2) and the beam-end supports (section 2.4.3) will be presented.

### 2.4.2 Intermediate supports

As explained in section 2.3.1, cracking may occur under self-weight loading. To prevent this problem, intermediate supports are necessary to reduce the maximum bending moment under self-weight which is reached at mid-span and would otherwise equal  $\frac{\rho \cdot S \cdot g \cdot L^2}{8}$  where



(A) Air-cushions (Courtesy of AV-T®)

(B) Air-cushions mounted under the intermediate supports

FIGURE 2.10: Air-cushion system

$\rho$  is the volumic mass (in  $\text{kg}/\text{m}^3$ ),  $S$  is the cross section of the beam and  $L$  is the span length. With pre-design values and a regulatory load safety coefficient equal to 1.35, this corresponds to a maximum tensile strength at the lowest fiber of the beam of 2.06 MPa which gives a reasonable safety margin.

The intermediate supports have been placed at the quarter-spans in order to bear the additional masses of 310 kg each or to mount the actuators for the tests on the strong-floor as represented in figures 2.13 and 2.14. They are constituted of three parts detailed in figure 2.11a. The hydraulic jacks adaptation plates are removed during the dynamic tests on shaking table.

The supports rely on air cushions devices that bear the whole self-weight of the beam and almost cancel the friction with the table upper surface. Hence, the beam-end supports described in section 2.4.3 do not withstand any vertical load. The intermediate supports are mounted on the beam by clamping on the upper and lower beam surfaces.

### 2.4.3 Beam-end supports

The beam-end supports are designed to withstand only horizontal loads mainly directed perpendicularly to the axis of the beam, i.e. in the loading direction. The system relies on elastic blades seen in figure 2.11b made of high performance steel (Marval 18 X2NiCoMo18-8-5 with a yield stress of 1780 MPa and a Young's modulus of 186 GPa) and is inspired from a setup from La Borderie, 1991. This material has been chosen for its high yield stress. The motivation of the steel blade design is to resist to high axial loads while having a comparatively negligible stiffness in bending to allow for the rotation of the beam-ends with almost no resisting moment. Hence, the chosen solution for the steel blades is to have a significant cross-section surface while reducing as much as possible the moment of inertia around the bending axis corresponding to the rotation axis of the beam (z-axis on figures 2.12a and 2.13). The design load has been computed numerically for the quasi-static most critical loading, QSC1 (see the description in section 2.5.1.1). Because of the limitation of the hydraulic jacks whose maximum load capacity is 25 kN, the maximum

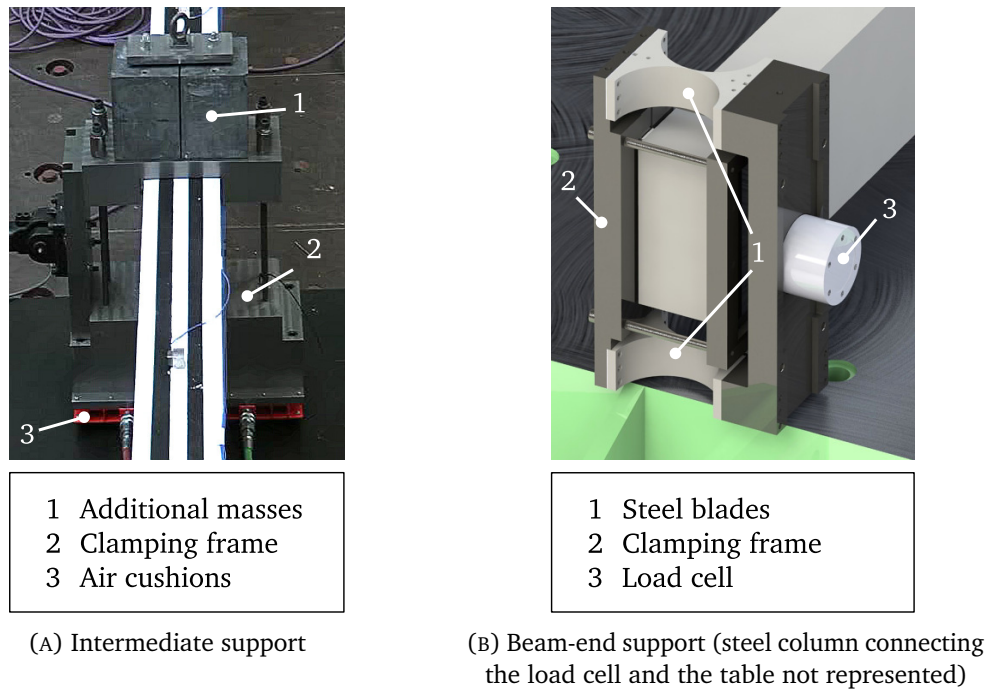


FIGURE 2.11: Supports description

load expected at each beam-end is also 25 kN (see figure 2.14a). A safety coefficient of 1.8 has been used, corresponding to a design load of 45 kN.

As figure 2.11b shows, there are two steel blades per beam-end support. For this reason, the finite element model used to validate the design of the blades consists in two steel blades placed concomitantly as if they were one unique part. However, the axial load noted  $F$  on figure 2.12b is not the only constraint to consider: because of the bending of the beam, the beam-end supports can reach a rotation of  $0.6^\circ$  during QSC1 test, under the hypothesis that the beam remains elastic. But this hypothesis is not true and nonlinear hinges are expected to appear (more probably where the hydraulic jacks are mounted on the beam). These hinges will allow for higher rotation at the beam-ends. Nonlinear computations carried out on Cast3M with pre-design material properties have shown that this maximum rotation can reach  $1.7^\circ$ . With a safety coefficient of 3.6, the elastic blades are design to withstand a  $6^\circ$  rotation around z-axis. The combination of an important compressive force, an imposed rotation and a very low moment of inertia around z-axis makes the blades susceptible to buckling. A finite element computation taking into account large strains have been used to ensure that the risk of instability is negligible. The buckling test case is presented on figure 2.12b.

#### 2.4.4 Modeling of the setup

The IDEFIX tests can be modeled in two different planes (see the axes definition on figure 2.13): the vertical plane ( $y, z$ ), in which the weight acts and the horizontal plane ( $x, y$ ), in which the loading is applied. The design has been realized in order to reduce

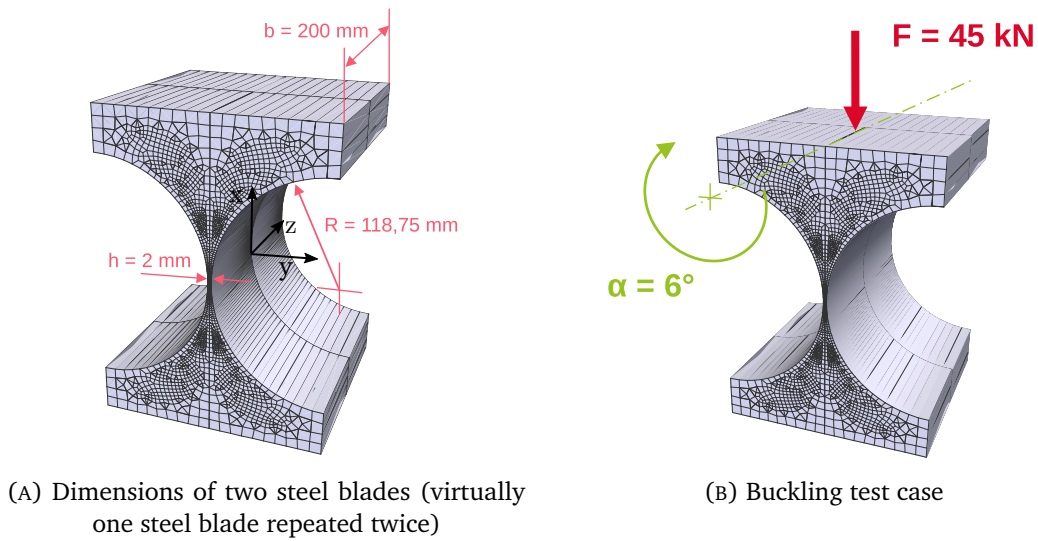


FIGURE 2.12: Design of the steel blades

the coupling between the phenomena occurring in those two different planes. In other words, the effect of the gravity is not considered. In the plane of interest (i.e. in which the loading is applied), the problem is modeled as depicted in figure 2.14.

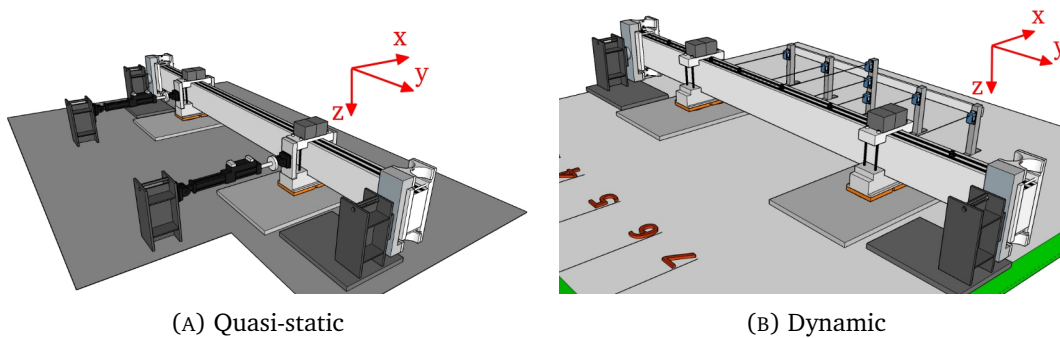


FIGURE 2.13: 3D view of the experimental setups

## 2.5 Loadings

### 2.5.1 Quasi-static loadings

#### 2.5.1.1 QSC1 and QSC2

The goal of QSC1 and QSC2 (figures 2.16a and 2.16b) is to assess the energy dissipated hysteretically for the first two bending vibration modes of the beam using JAM. To this end, the beam has to be deformed according to the 1<sup>st</sup> and the 2<sup>nd</sup> mode shapes. This

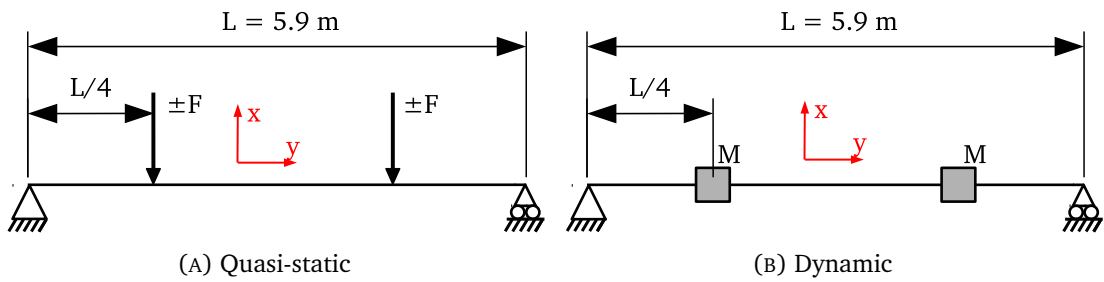


FIGURE 2.14: Beam theory modeling of the experimental setups in quasi-static and dynamic

is the difference between QSC1 and QSC2: the actuators work in-phase for the former while they work in opposition for the latter. The two types of shapes are also comparable thanks to the error criteria of equations (1.125) and (1.126), the comparisons are plotted in figure 2.15.

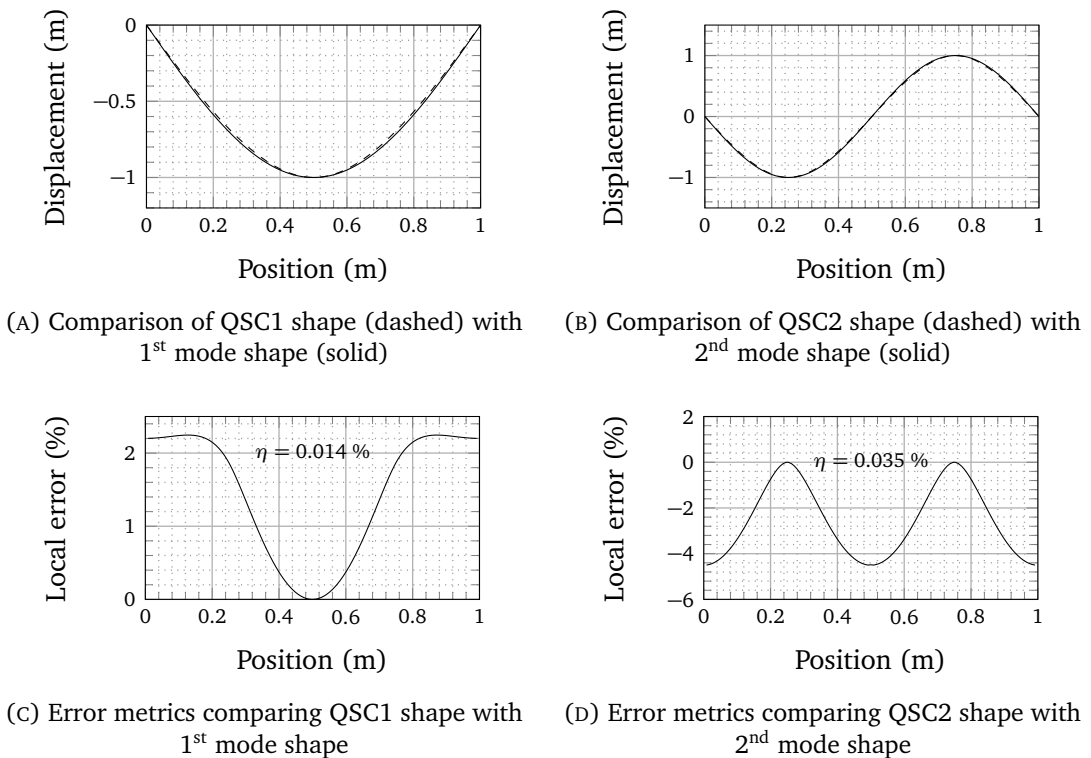


FIGURE 2.15: Comparison of the QSC shapes with the first two eigenmodes

QSC1 and QSC2 are reverse cyclic quasi-static tests. They are both controlled in displacement and consist in successive blocks of three cycles in order to stabilize the damage state of the beam for each displacement amplitude. The tests are performed at a constant velocity of 0.4 mm/s.

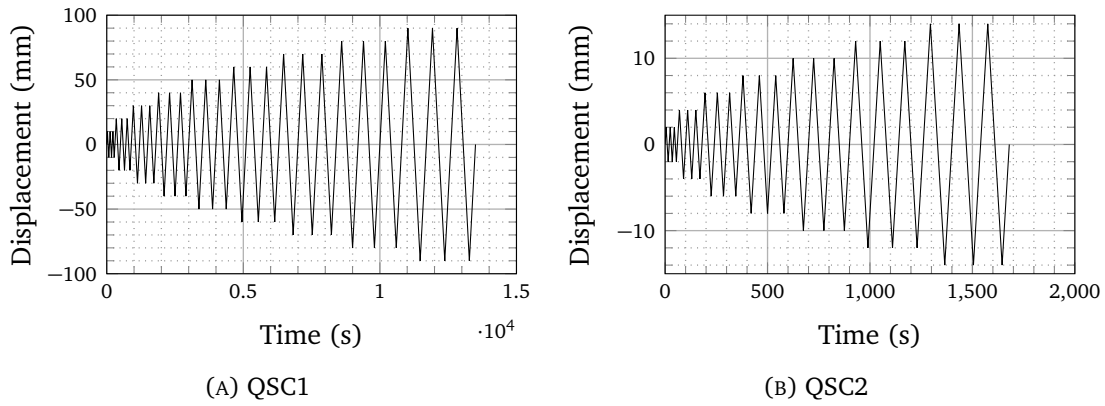


FIGURE 2.16: QSC prescribed actuators displacements

### 2.5.1.2 SPS1 and SPS2

The influence of the strain rate (more precisely the prescribed actuators' velocity) is investigated in these tests. The displacement amplitude is constant during the test (figure 2.17a for SPS1 prescribed displacement). Furthermore, to ensure that no spurious inertial force arises, the velocity is piecewise constant and evolves linearly depending on the maximum acceleration tolerated at velocity changes. This means that the higher is the maximum acceleration tolerated, the higher is the velocity than can be reached.

## 2.5.2 Dynamic loadings

### 2.5.2.1 White noise test (WN)

The white noises labeled WN are high level white noise acceleration signals, meaning that nonlinearities are expected to occur in the beam. The ability of the shaking table to be controlled over several degrees of freedom is used. The first two modes are investigated independently. It is then necessary to be able to excite one mode alone. Theoretically, an acceleration in the  $x$ -direction (see figure 2.18) only activates the symmetric vibration modes with respect to the  $(x, z)$  plane. On the contrary, a rotation around the vertical axis (yaw) only activates anti-symmetric vibration modes with respect to the  $(x, z)$  plane. This is demonstrated later in section 3.1.2.3.

The white noise is generated once, and is then scaled in order to evaluate the dissipation for different acceleration levels. Three different tests are derived from the white noise signal:

- WN1 only in the  $x$ -direction;
- WN2 only around the  $z$ -direction;
- WN12 in the  $x$ -direction and around the  $z$ -direction simultaneously.

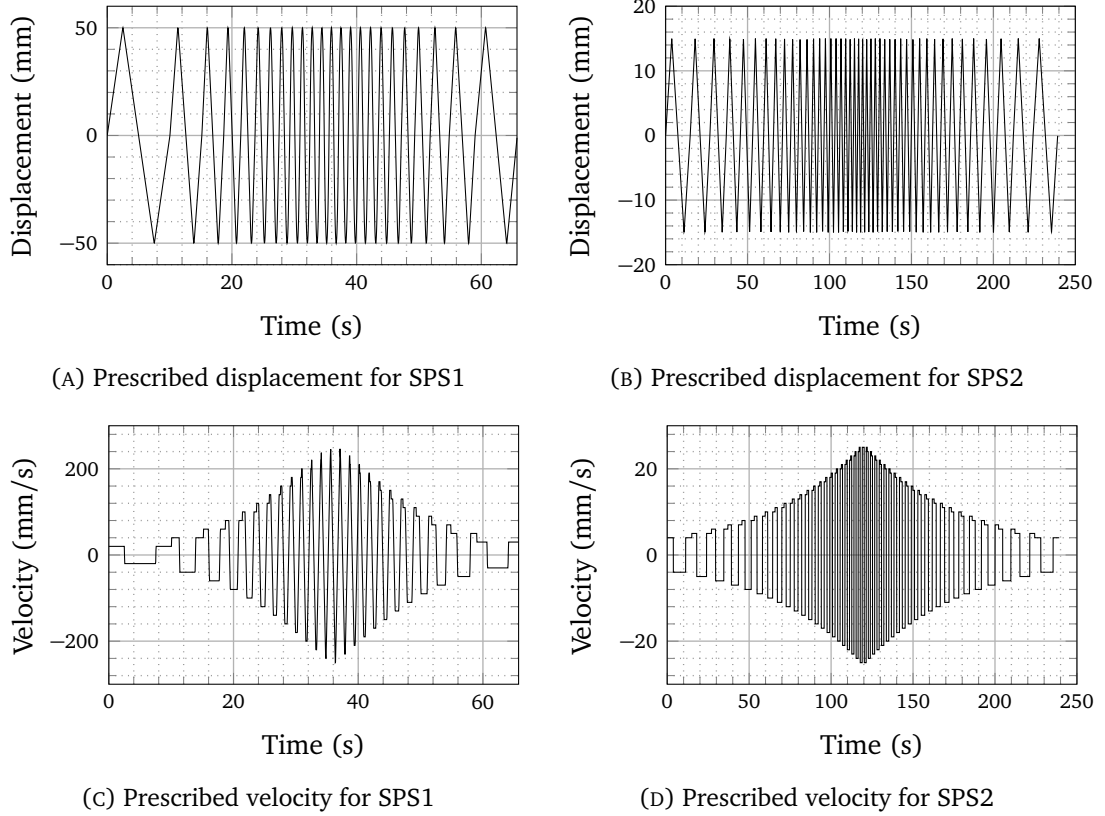


FIGURE 2.17: SPS prescribed actuators displacements

### 2.5.2.2 Band-passed white noise (SC)

In an analogous manner that for QSC1 and QSC2, two signals referred as SC1 and SC2 are generated by the summation of mono-harmonic accelerations with increasing frequencies between  $\omega_a$  and  $\omega_b$  by  $N$  steps and random phase angles:

$$\ddot{u}_{SC1} = \sum_{i=1}^N \ddot{u}_0 \cdot \sin(\omega_i \cdot t + \phi_i) \quad (2.1)$$

$$\text{with } \phi_i \sim U([0, 2 \cdot \pi]) \quad (2.2)$$

$$\text{and } \omega_i = \omega_a + i \cdot \Delta\omega \quad (2.3)$$

with  $\Delta\omega = \frac{\omega_b - \omega_a}{N}$  and  $U([0, 2 \cdot \pi])$  the uniform distribution between 0 and  $2 \cdot \pi$ . SC1/SC2 is intended to activate the 1<sup>st</sup>/2<sup>nd</sup> bending eigenmode of the beam. Since the corresponding frequencies are expected to decrease along with the stiffness degradation, the frequency range excited  $[\omega_a; \omega_b]$  contains the initial aimed frequency  $\omega_1/\omega_2$  but also the fully degraded one (estimated at 0.5 times the initial one) in order to keep the eigenmode activated all along the test. A third signal is designed as the combination of both SC1 and SC2. The shaking table, Azalée allows for choosing the direction of the acceleration. This means that SC1 and SC2 can be performed either in x-direction or around z-axis, and that

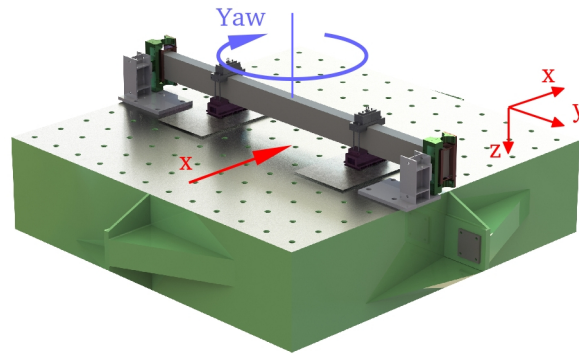


FIGURE 2.18: Degrees of freedom used for the dynamic tests

SC12 can be the combination of SC1 in x-direction and SC2 around z-axis at the same time. The acceleration response spectra are given in figure 2.19.

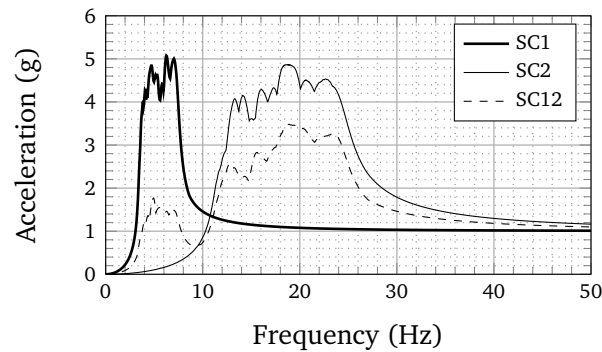


FIGURE 2.19: SC signals spectra

### 2.5.2.3 Decreasing sinus sweep

The decreasing sinus sweep test, consists in successive mono-harmonic acceleration signal with decreasing frequency. Each sinusoid portion lasts for 10 seconds and is followed by a white noise acceleration in order to characterize the changes in the eigenfrequencies and the damping ratios. The decrease in frequency is of 0.5 Hz between two consecutive sinusoids. The amplitude of the sinusoids also decreases proportionally to the inverse of the squared frequency, in order to maintain the displacement demand constant. Under the condition that the viscous damping ratio is small, the displacement response spectrum  $S_d$  is linked to the acceleration response spectrum  $S_a$  by the equation:

$$S_a = \omega^2 \cdot S_d \quad (2.4)$$

with  $\omega$  the angular frequency that is in abscissa of the response spectra. The plot of the accelerogram of signal DSS85 (decreasing sinus sweep from 8 Hz to 5 Hz) is given in figure 2.20.

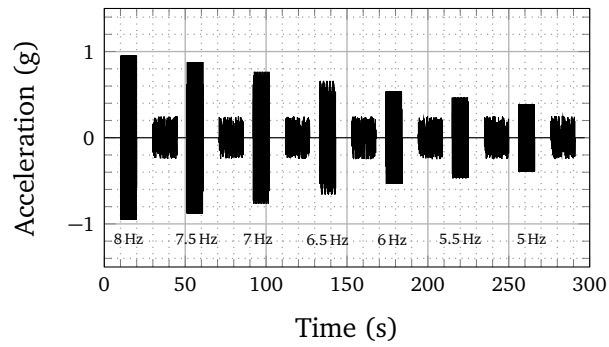


FIGURE 2.20: DSS85 accelerogram

### 2.5.3 Natural seismic signal SS1

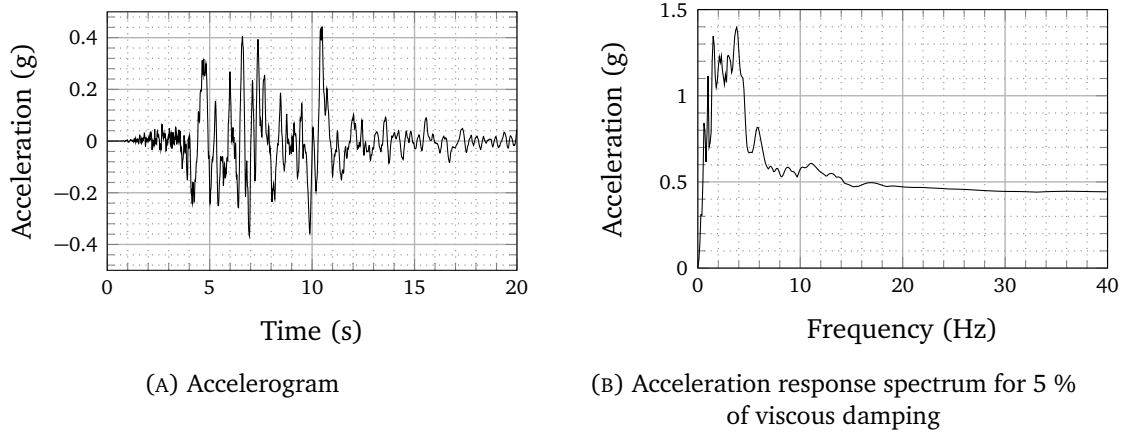


FIGURE 2.21: Accelerogram and acceleration response spectrum of SS1

The natural seismic signal considered is the mainshock of the Niigata-ken Chuetsu Oki Earthquake (NCOE) ground motion transferred to the 3<sup>rd</sup> floor of the Kashiwazaki-Kariwa NPP. The accelerogram and the corresponding response spectrum are given in figure 2.21. The peak ground acceleration (PGA) is 0.47 g and the response acceleration corresponding to the 1<sup>st</sup> eigenfrequency of the beams (around 7 Hz) is about 0.6 g.

### 2.5.4 Summary of the loadings

An exhaustive summary of all the loadings performed during IDEFIX experimental campaign is given in table 2.8 and the detail of loadings performed on each beam are given in table 2.9.

## 2.6 Measurements

### 2.6.1 Positioning

To clarify the labels used to designate the sensors, a number going from 1 to 9 related to the position on the beam is used. A distance of 73.75 cm separates each position. The figure 2.22 gives all the sensors position and their respective labels.

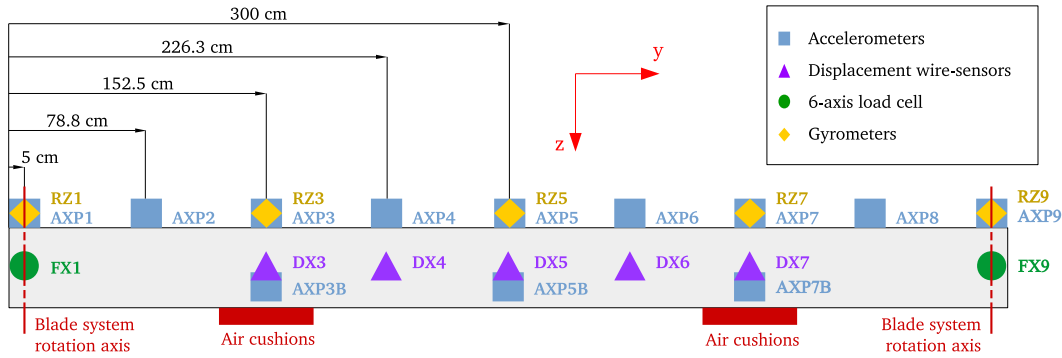


FIGURE 2.22: Sensors positions

### 2.6.2 Displacements

Three types of displacement measurement devices are used. At first, LVDT sensors associated to the actuators (only for quasi-static tests) provide information on the prescribed displacement (channels DXV3 and DXV7). The second one is based on five traditional wire sensors placed periodically between the two additional masses and are referred as DX3 to DX7. The third measurement is a commercial tool called *Videometric*<sup>®</sup> (VDM) which uses the digital image correlation (DIC) technique to assess the displacements of the mean fiber of the beam materialized by the painted stripes seen in figure 2.23. Additional circular targets are placed on the strong floor or the shaking table to deduce the relative displacement between the “ground” and the beam. The system is composed of two cameras mounted on a carbon fiber arm placed in parallel and above the beam at a distance of 13 m. A LED-based lighting system helps to improve the optical contrasts. Depending on the resolution of the pictures taken by camera, the sampling frequency can reach 200 Hz. VDM presents three advantages over the wire-sensors:

- it provides full-field information along the length of the beam, the spatial discretization being chosen by the user and directly related to the noise level (the thinner is the discretization, the higher is the noise). Thirty-one points in the length of the beam (i.e. points spaced by 19.6 cm) proved to be sufficient for all the analyzes performed during this thesis;
- it allows to detect the location of a discontinuity in the rotation of the sections if the spatial discretization is fine enough;
- it can detect out-of-plane displacements thanks to the stereo-correlation.

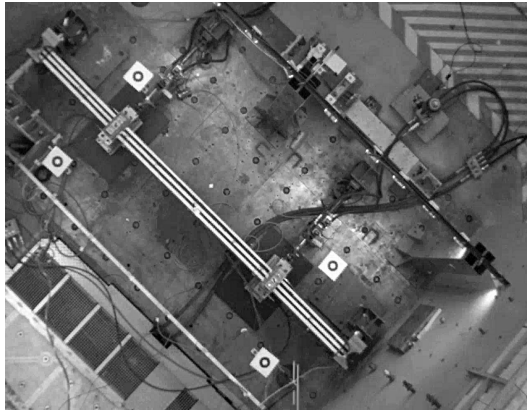


FIGURE 2.23: Snapshot from the Videometric<sup>®</sup> system (right camera)

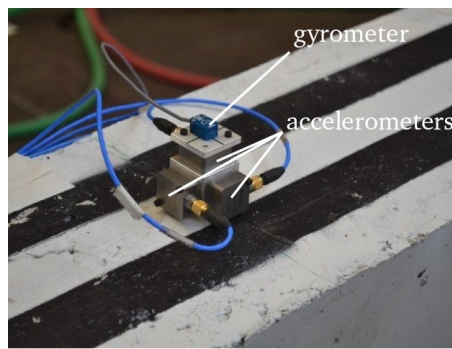


FIGURE 2.24: Three accelerometers and one gyrometer mounted on an aluminium cube glued on the upper surface of the beam

An advanced use of the VDM data is presented in the next chapter, in section 3.1. However, the following points are to be considered:

- the longest test (QSC1) has a duration of more than 13 000 s, the light conditions might change significantly depending on the weather and the time of the day;
- moreover, a flashing mode has been developed for the LED system in order to prevent their overheating when they stay switched on for more than 2 minutes;
- only the displacement of the upper surface of the beam is measured.

Hence, the wire-sensors or any other conventional displacement measurement device stay necessary to guarantee the validity of the VDM measure.

### 2.6.3 Acceleration

Accelerometers are placed all along the beam (from positions 1 to 9). They are either mounted alone (even position numbers for uni-axial measurement) or by three (for three-directional measurement), and represent 19 measurement channels. They are glued on aluminium cubes themselves glued on the beam an picture on figure 2.24.



FIGURE 2.25: Load cells positions

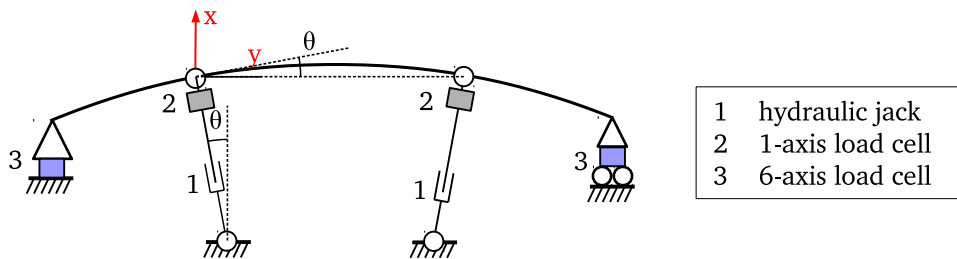


FIGURE 2.26: Rotation of the load cells — 1: hydraulic jacks, 2: 1-axis load cells, 3: 6-axis load cells

#### 2.6.4 Rotational velocity

Gyrometers are placed in positions 1, 3, 5, 7 and 9 in order to measure the vertical rotational velocity (around the bending direction), mounted as on figure 2.24.

#### 2.6.5 Forces

A six-axis load cell (figure 2.25a) connects each beam-end to its support column in order to measure the reaction forces in the x-direction. As emphasized in section 2.4.3, no vertical load is supposed to be applied on the beam-end supports. The load cells allow for checking this hypothesis as well as to check that any unintended force is transmitted through the supports. Also, two uni-axial load cells (figure 2.25b) are mounted on the hydraulic jacks. Therefore, a total of 14 channels is dedicated to the measurement of forces.

The direction of the 6-axis load cells is not supposed to change significantly during the test while the 1-axis load cells follow the direction of the actuators which are affected by the rotation of the beam at the section level (figure 2.26)

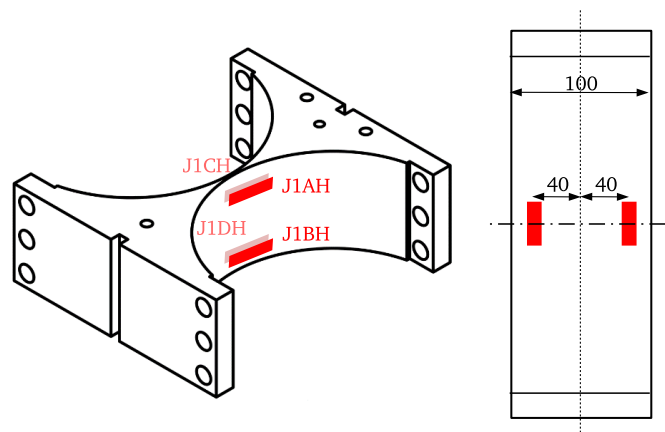


FIGURE 2.27: Positioning of the strain gauges on the steel blades

### 2.6.6 Strains

Strain gauges have been glued on the steel blades (figure 2.27) to ensure the elastic behavior of the latter and to set a safety limit to stop the test automatically when it is exceeded.

## 2.7 Conclusions of the second chapter

The technical aspects of IDEFIX experimental campaign have been presented. A strong attention has been brought to the boundary conditions during the design. The main objective was to design an experimental setup as close as possible to the simply supported beam model. The use of original technical solutions (air cushions for the intermediate supports, steel blades for the beam-end supports) allowed to meet this goal satisfyingly as will show the experimental results presented in the next chapter. In particular, the eigenfrequencies measured via both white noise and hammer shock tests show very good match between the expected theoretical values and the experimental ones (see table 3.7 in chapter 3).

Equipment	Reference	Modes	Description
—	HT	1 and 2	Hammer test
	WN1	1	White noise signal in X-direction (duration 200 s)
	WN2	2	White noise signal around YAW-axis (duration 200 s)
	WN12	1 and 2	White noise signal (combination of WN1 and WN2)
	WN1MTS	1	White noise generated by MTS software
	WND030	1	White noise of table displacement bandpassed between 0 Hz and 30 Hz
	SC1	1	White noise signal in X-direction bandpassed between $0.5 \cdot f_1$ and $1.05 \cdot f_1$ , $f_1$ being the 1 <sup>st</sup> eigenfrequency
	SC2	2	White noise signal in YAW-direction bandpassed between $0.5 \cdot f_2$ and $1.05 \cdot f_2$ , $f_2$ being the 2 <sup>nd</sup> eigenfrequency
	SC2b	2	White noise signal in YAW-direction bandpassed between $0.35 \cdot f_2$ and $1.05 \cdot f_2$ , $f_2$ being the 2 <sup>nd</sup> eigenfrequency
Azalée	SC12	1 and 2	Combination of SC1 and SC2
	SS1	1	Natural seismic signal, transferred at 3 <sup>rd</sup> floor spectrum of Niigataken-Chuetsu-Oki earthquake (NCOE)
	Sinus	1 or 2	Sinusoidal signal in X-direction or around YAW-axis
	DSS $f_1/f_2$	1 or 2	Mono-harmonic signal at constant amplitude, by decreasing frequency steps (from $f_1$ to $f_2$ )
	ISD	1	Step-by-step increasing sinusoidal acceleration following a quadratic law
	BS	1	Continuous linear sinus sweep generated by MTS software
	QSS025	1	Continuous quadratic sinus sweep generated by MTS software
	BiSINUS	1 and 2	Sinusoidal signals consecutively in X, X+YAW and YAW directions
	QSC1	1	Quasi-static reverse cyclic four-point bend test with in-phase actuators
Strong floor	QSC2	2	Quasi-static reverse cyclic 4PB test with actuators in phase opposition
	SPS1	1	Quasi-static reverse cyclic 4PB test with in-phase actuators and increasing velocity
	SPS2	2	Quasi-static reverse cyclic 4PB test with actuators in phase opposition and increasing velocity

TABLE 2.8: Summary of the loadings

Equip.	Reference	Beam tested																			
		1	2	3	4	5	6	7	8	9	10	11	12	13	14	15	16	17	18	19	20
—	HT	•	•	•	•	•	•	•	•	•	•	•	•	•	•	•	•	•	•	•	•
	WN1	•							•	•	•	•	•	•	•	•	•	•	•	•	•
	WN2								•			•									•
	WN12																				
	WN1MTS														•						
	WNDO30													•							
	SC1	•							•												
	SC2	•																			
	SC2b								•												
Azalee	SC12	•																			
	SS1																			•	
	Sinus								•	•											
	DSSftF2									•					•						
	ISD												•								
	BS									•											
	QSS025																				•
	BISINUS																				•
	QSC1	•	•	•	•	•	•	•	•	•	•	•	•	•	•	•	•	•	•	•	•
Strong floor	QSC2	•	•	•	•	•	•	•	•	•	•	•	•	•	•	•	•	•	•	•	•
	SPS1	•	•	•	•	•	•	•	•	•	•	•	•	•	•	•	•	•	•	•	•
	SPS2	•	•	•	•	•	•	•	•	•	•	•	•	•	•	•	•	•	•	•	•

TABLE 2.9: Tests performed on each beam

## Chapter 3

# Experimental results analyses

### 3.1 Identification strategy of the modal damping ratios

#### 3.1.1 Forewords

To reach the objectives regarding the study of the modal damping ratios (section 2.1), the problem has to be expressed in the eigenbasis of the whole experimental setup on Azalée (i.e. considering additional masses and boundary conditions). The way to analyze the experimental data provided by the different sensors in the scope of a modal identification is not straightforward. Since nonlinearities are expected to occur, several hypotheses among which the mode uncoupling are necessary. Furthermore, if the theoretical linear mode shapes of the beam are known (this point is further developed in sections 3.1.2.2 and 3.1.2.3), arbitrary additional mode shapes that would take into account the influence of strong local nonlinearities (e.g. section-crossing cracks or steel yielding) might be added to better describe the discontinuity at the mean fiber level. However, the addition of such non-classical mode shapes, such as the examples provided in figure, proved to be useless for IDEFIX tests that have not shown strong beam shape irregularities. Once in the modal basis, the identification problem can be addressed thanks to the different optimization procedures already implemented in commercial computational tools, such as MATLAB<sup>®</sup>. Indeed, each modal displacement might be considered as the dynamic response of a SDOF damped system (without any assumption on the nature of the said damping), and the damping ratio value — or the parameters of the model that would drive the evolution of the damping ratio — may be identified by minimizing a given objective error function (comparing the experimental modal displacements and the computed SDOF displacement). This procedure is diagrammed in figure 3.2. Two strong hypotheses are made to apply this procedure:

- the bending vibration modes are uncoupled;
- the mode shapes are not modified by the nonlinearities occurring during the dynamic tests.

This section is dedicated to the setup of the theoretical context which is necessary to the development of post-processing tools further described by detailing the different steps playing a role in figure 3.2:

1. projection on the reduced modal basis;

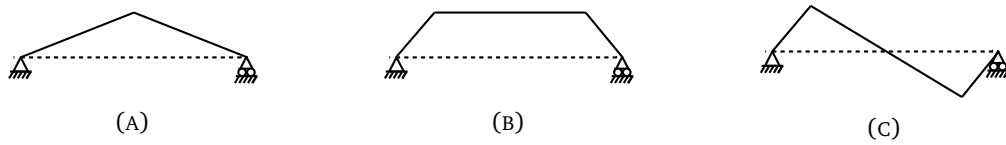


FIGURE 3.1: Examples of arbitrary additional mode shapes to account for strong nonlinearities

2. computation of the  $i^{\text{th}}$  SDOF oscillator response for a set of parameters to identify;
3. evaluation of the error;
4. modification of parameters  $\{p\}$ .

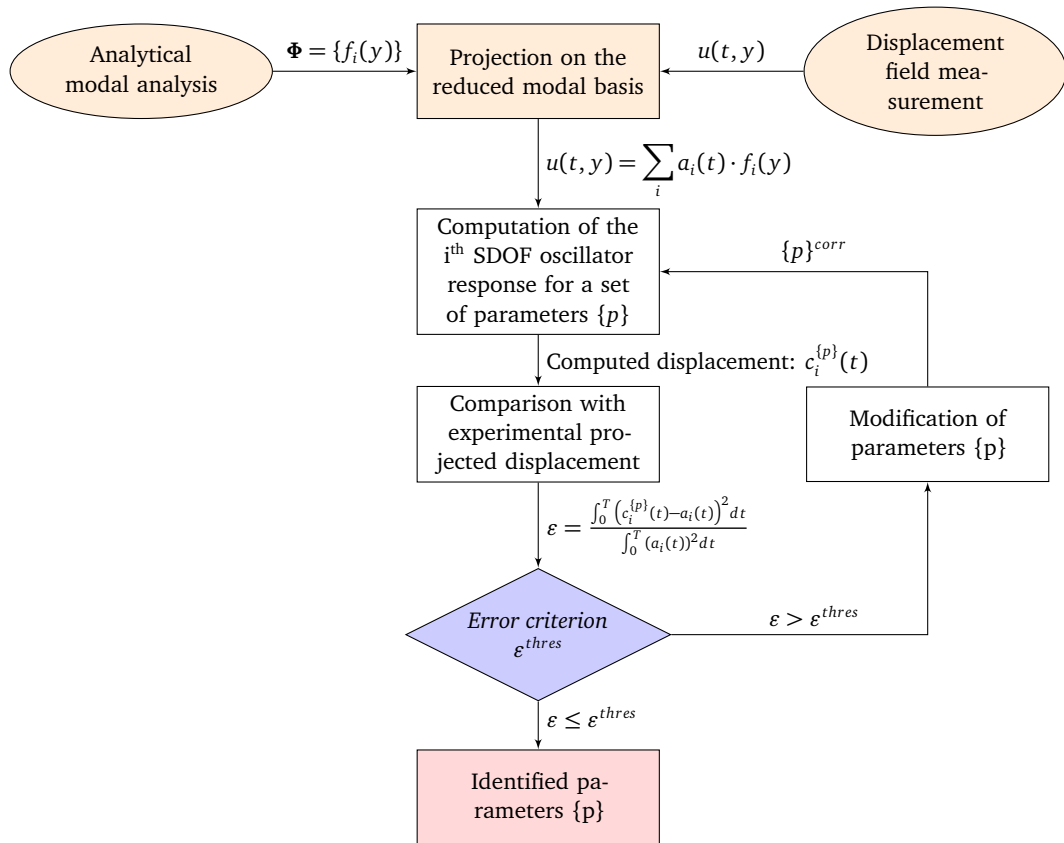


FIGURE 3.2: Flowchart of the SDOF identification procedure with support of the DIC measurements

Finally, the goal of this chapter is not to present an exhaustive study of all the experimental data gathered during the 6-months long experimental campaign but rather to focus on some remarkable results and more particularly the techniques that have been specifically developed to obtain them.

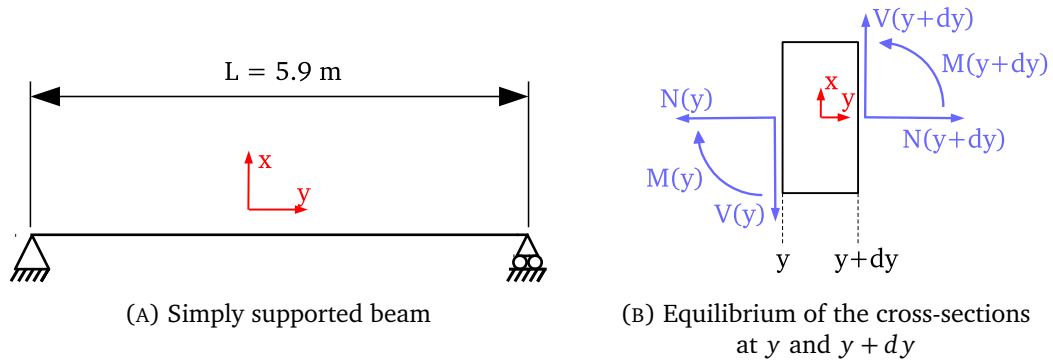


FIGURE 3.3: Beam theory problem

### 3.1.2 Projection on the modal basis

#### 3.1.2.1 Case of a simply supported beam

The study in this section is placed in the linear elastic framework. The dynamic equilibrium equations are written at the section level following the notations given in figure 3.3a and 3.3b:

$$V(y + dy, t) - V(y, t) = \rho \cdot S \cdot dy \cdot \frac{\partial^2 u_x}{\partial t^2}(y) \quad (3.1)$$

$$M(y + dy) - M(y, t) + V(y + dy, t) \cdot dy \approx 0 \quad (3.2)$$

with  $\rho$  the mass density of the beam,  $S$  the cross-section,  $V$  the shear force,  $M$  the bending moment and  $u_x$  the displacement in the  $x$ -direction. The rotational inertial term is neglected in equation (3.2). The following equation is obtained:

$$\frac{\partial^2 M}{\partial y^2}(y, t) + \rho \cdot S \cdot \frac{\partial^2 u_x}{\partial t^2}(y, t) = 0 \quad (3.3)$$

According to the Euler-Bernoulli beam theory:

$$M(y, t) = E \cdot I \cdot \frac{\partial^2 u_x}{\partial y^2}(y, t) \quad (3.4)$$

In this equation,  $E$  is chosen as the Young's modulus of the concrete  $E_c$ , and  $I$  is the moment of inertia of the section around the bending axis ( $z$ -axis for IDEFIX tests). Then, the reinforcement area is taken into account through an equivalent concrete area considering an equivalence coefficient  $\alpha = \frac{E_s}{E_c}$  with  $E_s$  the actual Young's modulus of the steel. This

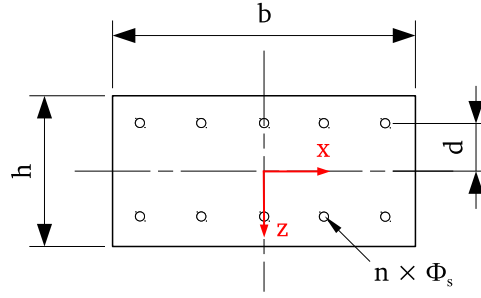


FIGURE 3.4: Notations related to the beam section geometry

equivalence affects the expression of the moment of inertia:

$$I = \underbrace{\frac{b \cdot h^3}{12}}_{\text{Concrete inertia}} + \alpha \cdot \sum_{r=1}^n \left( \underbrace{\frac{\pi \cdot \phi_{s,r}^4}{64}}_{\text{rebars inertia}} + \overbrace{d_r^2 \cdot \frac{\pi \cdot \phi_{s,r}^2}{4}}^{\text{Huygens' theorem}} \right) \quad (3.5)$$

with  $n$  the number of rebars,  $d_r$  the distance between the beam neutral axis and the  $r^{\text{th}}$  rebar's axis, and  $\phi_{s,r}$  the diameter of the  $r^{\text{th}}$  rebar. For IDEFIX beams  $d_r = d$  and  $\phi_{s,r} = \phi_s$  for all rebars since the cross-sections are symmetric (figure 3.4).

Injecting equation (3.4) in equation (3.3):

$$E \cdot I \cdot \frac{\partial^4 u_x}{\partial y^4}(y, t) + \rho \cdot S \cdot \frac{\partial^2 u_x}{\partial t^2}(y, t) = 0 \quad (3.6)$$

which is the wave equation for a beam under bending. The stationary wave solution writes  $u_x(y, t) = f(y) \cdot g(t)$  and allows for writing one equation in time and one equation in space:

$$\begin{cases} \frac{d^2 g}{dt^2}(t) + \omega^2 \cdot g(t) = 0 \\ \frac{d^4 f}{dy^4}(y) + \zeta^4 \cdot f(y) = 0 \\ \omega^2 = \zeta^4 \cdot \frac{E \cdot I}{\rho \cdot S} \end{cases} \quad (3.7)$$

where  $\omega$  and  $\zeta$  correspond respectively to the angular eigenfrequency and the wave number of the beam in bending for the vibration mode considered. The solutions  $f$  and  $g$  are sought in the form:

$$g(t) = A_1 \cdot \cos(\omega \cdot t) + A_2 \cdot \sin(\omega \cdot t) \quad (3.8)$$

$$f(y) = B_1 \cdot \cos(\zeta \cdot y) + B_2 \cdot \sin(\zeta \cdot y) + B_3 \cdot \cosh(\zeta \cdot y) + B_4 \cdot \sinh(\zeta \cdot y) \quad (3.9)$$

with  $A_i$  and  $B_i$  constants to be determined by initial and boundary conditions. For a simply supported beam, the displacement and the moment are null at  $y = 0$  and  $y = L$ :

$u_x(0) = u_x(L) = 0$  and  $M(0) = M(L) = 0$ . These conditions are true for all  $t$ , hence:

$$f(0) = f(L) = 0 \quad (3.10)$$

$$\frac{d^2f}{dy^2}(0) = \frac{d^2f}{dy^2}(L) = 0 \quad (3.11)$$

The only non-null solutions are the ones of the form:

$$f_i(y) = \sin\left(\frac{i \cdot \pi \cdot y}{L}\right) \quad (3.12)$$

$$k_i = \frac{i \cdot \pi}{L} \quad (3.13)$$

$$\omega_i^2 = \left(\frac{i \cdot \pi}{L}\right)^4 \cdot \frac{E \cdot I}{\rho \cdot S} \quad (3.14)$$

### 3.1.2.2 Case of a simply supported beam with additional masses

The problem considered is now the one pictured on figure 2.14b. The presence of the additional masses introduces inertial forces that are included in the wave equation:

$$E \cdot I \cdot \frac{\partial^4 u_x}{\partial y^4}(y, t) + \rho \cdot S \cdot \frac{\partial^2 u_x}{\partial y^2}(y, t) = -M_1 \cdot \delta(y - y_1) \cdot \ddot{u}_x(y_1, t) - M_2 \cdot \delta(y - y_2) \cdot \ddot{u}_x(y_2, t) \quad (3.15)$$

with  $M_1$  the mass added at position  $y_1$ ,  $M_2$  the one added at position  $y_2$ , and  $\delta$  is the Dirac's distribution. The rotational inertia of the masses are neglected because they are mounted close to the mean fiber and the rotational accelerations remain small. The solution displacement field  $u_x(y, t)$  is expressed on the basis  $(f_i)_{i \in \mathbb{N}}$  constituted of the functions given in equation (3.12). In theory,  $(f_i)_{i \in \mathbb{N}}$  has to be of infinite dimension to constitute a basis of the solutions of equation (3.15):

$$u_x(y, t) = \sum_i a_i(t) \cdot f_i(y) \quad (3.16)$$

If equation (3.16) is injected in the wave equation:

$$E \cdot I \cdot \sum_i a_i(t) \cdot \frac{\partial^4 f_i}{\partial y^4}(y) + \rho \cdot S \cdot \sum_i f_i(y) \cdot \frac{\partial^2 a_i}{\partial t^2}(t) = -M_1 \cdot \delta(y - y_1) \cdot \sum_i \ddot{a}_i(t) \cdot f_i(y_1) - M_2 \cdot \delta(y - y_2) \cdot \sum_i \ddot{a}_i(t) \cdot f_i(y_2) \quad (3.17)$$

This equation is multiplied by  $f_j(y)$  and integrated on  $[0; L]$ . This latter operations lead to the matrix form:

$$\mathbf{M} \cdot \ddot{\mathbf{a}}(t) + \mathbf{K} \cdot \mathbf{a}(t) = \mathbf{0} \quad (3.18)$$

where the boldness of the characters denotes non-unidimensional objects (i.e. non-scalars). Using  $i$  and  $j$  indexes to indicate the coefficient at row  $i$  and column  $j$ , there are  $i \times j$  equations:

$$\mathbf{M}_{ij} \cdot \ddot{\mathbf{a}}_j(t) + \mathbf{K}_{ij} \cdot \mathbf{a}_j(t) = 0 \quad (3.19)$$

with:

$$\begin{aligned} \mathbf{M}_{ij} = \delta_{ij} \cdot \int_0^L \rho \cdot S \cdot (f_i(y) \cdot f_j(y)) \cdot dy \\ + M_1 \cdot f_i(y_1) \cdot f_j(y_1) + M_2 \cdot f_i(y_2) \cdot f_j(y_2) \end{aligned} \quad (3.20)$$

and:

$$\mathbf{K}_{ij} = \delta_{ij} \cdot \int_0^L E \cdot I \cdot \frac{\partial^2 f_i}{\partial y^2}(y) \cdot \frac{\partial^2 f_j}{\partial y^2}(y) \quad (3.21)$$

where  $\delta_{ij}$  is the Kronecker delta justified by the mass and stiffness orthogonality properties:

$$f_i \cdot \mathbf{M} \cdot f_j = 0 \quad \text{if } i \neq j \quad (3.22)$$

$$\text{and } f_i \cdot \mathbf{K} \cdot f_j = 0 \quad \text{if } i \neq j \quad (3.23)$$

The modal analysis of equation (3.19) makes possible the evaluation of each vibration mode participation of the beam alone on the modes of the system including the beam plus the additional masses. To simplify the equations, the following notations are introduced where the index  $k$  stands for the position of the additional masses (i.e.  $k = 1$  for  $y = y_1$  and  $k = 2$  for  $y = y_2$ ):

$$m_i = \int_0^L \rho \cdot S \cdot (f_i(y))^2 \cdot dy \quad (3.24)$$

$$\alpha_{ij,k} = f_i(y_k) \cdot f_j(y_k) \quad (3.25)$$

$$k_i = \int_0^L E \cdot I \cdot \left( \frac{\partial^2 f_i}{\partial y^2}(y) \right)^2 \cdot dy \quad (3.26)$$

It is observed that the additional masses introduce a coupling between the eigenmodes through the terms  $M_k \cdot \alpha_{ij,k}$ . When  $M_1$  and  $M_2$  tend to zero, the initial problem is retrieved. Also, the position of the masses has an influence on the coupling: when  $y_k$  corresponds to a zero of  $f_i$ , the couplings between this  $i^{\text{th}}$  mode and the others disappear. The generalized eigenvalue problem associated to equation (3.19) is:

$$(\mathbf{K} - \Omega^2 \mathbf{M}) \cdot \phi = \mathbf{0} \quad (3.27)$$

To determine the eigenvalues  $\Omega$ , the following determinant has to be null:

$$\begin{vmatrix} k_1 - \Omega^2 \cdot (m_1 + M_k \cdot \alpha_{11,k}) & \dots & -\Omega^2 \cdot M_k \cdot \alpha_{1k,k} & \dots \\ \dots & \dots & \dots & \dots \\ -\Omega^2 \cdot M_k \cdot \alpha_{i1,k} & \dots & k_i - \Omega^2 \cdot (m_i + M_k \cdot \alpha_{ii,k}) & \dots \\ \dots & \dots & \dots & \dots \end{vmatrix} \quad (3.28)$$

Then, the eigenvectors  $\phi_i$  associated to the eigenvalues  $\Omega_i$  are obtained by solving:

$$(\mathbf{K} - \Omega^2 \cdot \mathbf{M}) \cdot \phi_i = 0 \quad (3.29)$$

In the context of IDEFIX,  $y_1 = L/4$ ,  $y_2 = 3 \cdot L/4$  and  $M_1 = M_2 = M$ . Hence:

$$M_1 \cdot \alpha_{ij,1} + M_2 \cdot \alpha_{ij,2} = M \cdot \beta_{ij} \quad (3.30)$$

$$\text{where } \beta_{ij} = \alpha_{ij,1} + \alpha_{ij,2} \quad (3.31)$$

To simplify the problem in equation (3.29), the basis  $(f_i)_{i \in \mathbb{N}}$  has to be truncated after the first modes. The sum of the modal participation of the chosen modes should be close to 1. Typically, a 90 % value is often considered as satisfying. For example, if the 8 first eigenmodes are considered, then:

$$(\beta_{ij}) = \begin{pmatrix} 1 & 0 & 1 & 0 & -1 & 0 & -1 & 0 \\ 0 & 2 & 0 & 0 & 0 & -2 & 0 & 0 \\ 1 & 0 & 1 & 0 & -1 & 0 & -1 & 0 \\ 0 & 0 & 0 & 0 & 0 & 0 & 0 & 0 \\ -1 & 0 & -1 & 0 & 1 & 0 & 1 & 0 \\ 0 & -2 & 0 & 0 & 0 & 2 & 0 & 0 \\ -1 & 0 & -1 & 0 & 1 & 0 & 1 & 0 \\ 0 & 0 & 0 & 0 & 0 & 0 & 0 & 0 \end{pmatrix} \quad (3.32)$$

The expression of  $k_i$  is developed:

$$\begin{aligned} k_i &= \int_0^L E \cdot I \cdot \left( \frac{\partial^2 f_i}{\partial y^2}(y) \right)^2 \cdot dy \\ &= \int_0^L E \cdot I \cdot \left( -\frac{i^2 \cdot \pi^2}{L^2} \cdot \sin\left(\frac{i \cdot \pi \cdot y}{L}\right) \right)^2 \cdot dy \\ &= E \cdot I \cdot \frac{i^4 \cdot \pi^4}{L^4} \cdot \int_0^L \sin^2\left(\frac{i \cdot \pi \cdot y}{L}\right) \cdot dy \\ &= E \cdot I \cdot \frac{i^4 \cdot \pi^4}{L^4} \cdot \int_0^L \frac{1 - \cos\left(2 \cdot \frac{i \cdot \pi \cdot y}{L}\right)}{2} \cdot dy \\ &= E \cdot I \cdot \frac{i^4 \cdot \pi^4}{L^4} \cdot \left[ \frac{y - \sin\left(2 \cdot \frac{i \cdot \pi \cdot y}{L}\right)}{2} \right]_0^L \\ &= \frac{E \cdot I \cdot \pi^4}{2 \cdot L^3} \cdot i^4 \end{aligned} \quad (3.33)$$

Hence, the modal stiffness is:

$$k_i = k \cdot i^4 \quad (3.34)$$

$$\text{with } k = \frac{E \cdot I \cdot \pi^4}{2 \cdot L^3} \quad (3.35)$$

Similarly:

$$\begin{aligned}
 m_i &= \int_0^L \rho \cdot S \cdot (f_i(y))^2 dy \\
 &= \int_0^L \rho \cdot S \cdot \sin^2\left(\frac{i \cdot \pi \cdot x}{L}\right) \cdot dy \\
 &= \frac{\rho \cdot S \cdot L}{2}
 \end{aligned} \tag{3.36}$$

This gives the modal mass which is mode independent:

$$m_i = m \tag{3.37}$$

$$\text{with } m = \frac{\rho \cdot S \cdot L}{2} \tag{3.38}$$

In order to normalize the equations, a parameter  $\lambda$  is set such as  $M = \lambda \cdot m$ . The following equation arises for the generalized eigenvalues problem with Einstein's notation:

$$\left( \frac{k}{m} \cdot p^4 \cdot \delta_{pq} - \Omega_{iq}^2 \cdot (\delta_{pq} + \lambda \cdot \beta_{pq}) \right) \cdot \phi_{iq} = 0 \tag{3.39}$$

The number of eigenvectors  $f_i$  (of the beam *without* additional masses) necessary to express the three first eigenmodes of the full structure (i.e. the beam *with* the additional masses) is rather small by studying the convergence of the estimated eigenfrequencies: a relative evolution of less than 1 % is observed for each additional vector above 3 vectors  $f_i$  (table 3.1). This suggests that, in the linear elastic framework, the additional masses do not significantly influence the actual mode shapes of the beam. It is then possible to project with minor error any linear combination of the three first actual eigenvectors (of the beam *with* the additional masses) on a basis constituted of the three first eigenvectors  $f_i$  (of the beam *without* additional masses).

Eigenmode	Number of $f_i$ (and relative variation with left column)			
	3	10	100	1000
1	7.058160	7.057195	7.057122	7.057122
	-	-0.01367 %	-0.00103 %	-0.000001 %
2	24.280797	24.234209	24.231778	24.231774
	-	-0.19187 %	-0.01003 %	-0.00002 %
3	68.031201	67.581519	67.549319	67.549286
	-	-0.66099 %	-0.04765 %	-0.00005 %

TABLE 3.1: Evolution of the eigenfrequencies depending of the number of  $f_i$  vectors considered (example of beam HA12-C1A)

### 3.1.2.3 Seismic loading on shaking table

Two controllable ground motions of the shaking table Azalée are taken into account:

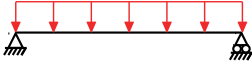
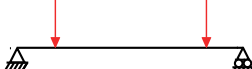
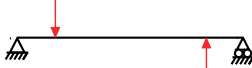
Ground motion	Distributed	Discrete
$\ddot{u}_{g,x}$		
$\ddot{\theta}_{g,z}$		

TABLE 3.2: Loading generated by both ground motions interacting with distributed and discrete masses

- translation in x-direction of amplitude  $\ddot{u}_{g,x}(t)$ ;
- rotation around z-axis (YAW) of amplitude  $\ddot{\theta}_{g,z}(t)$ .

They are pictured on figure 2.18 and act as external loadings through the different masses as illustrated in table 3.2. Hence, their influence on the dynamic equations are independent:

$$\begin{aligned}
 M_{ij} \cdot \ddot{a}_j(t) + K_{ij} \cdot a_j(t) = & \\
 -\ddot{u}_{g,x}(t) \cdot \int_0^L \sum_i f_i(y) \cdot (\rho \cdot S + M \cdot \delta(y - y_1) + M \cdot \delta(y - y_2)) \cdot dy & \\
 -\ddot{\theta}_{g,z}(t) \cdot \int_0^L \sum_i \left(y - \frac{L}{2}\right) \cdot f_i(y) \cdot (\rho \cdot S + M \cdot \delta(y - y_1) + M \cdot \delta(y - y_2)) \cdot dy &
 \end{aligned} \tag{3.40}$$

As it was introduced in section 2.5.2.1, it can be shown in this equation that the forces generated by the symmetric modes (for odd  $i$ ) excited by the rotational acceleration  $\ddot{\theta}_{g,z}(t)$  are null because of the integral. The same is true for the forces generated by antisymmetric modes (for even  $i$ ) excited by the x-direction acceleration  $\ddot{u}_{g,x}(t)$ . Hence, the equation (3.40) can be re-written:

$$M_{ij} \cdot \ddot{a}_j(t) + K_{ij} \cdot a_j(t) = F_i^x(t) + F_i^\theta(t) \tag{3.41}$$

with:

$$F_i^x(t) = \ddot{u}_{g,x}(t) \cdot \int_0^L f_i(y) \cdot (\rho \cdot S + M \cdot \delta(y - y_1) + M \cdot \delta(y - y_2)) \cdot dy \tag{3.42}$$

and:

$$F_i^\theta(t) = \ddot{\theta}_{g,z}(t) \cdot \int_0^L \left(y - \frac{L}{2}\right) \cdot f_i(y) \cdot (\rho \cdot S + M \cdot \delta(y - y_1) + M \cdot \delta(y - y_2)) \cdot dy \tag{3.43}$$

These equations are developed and a viscous damping represented by a matrix  $\mathbf{C}$  is arbitrarily added. The assumption is made that it does not modify the eigenvectors and

that  $\mathbf{C}$  is diagonal in the eigenbasis.

The dynamic problem in the modal basis writes:

$$M_{ij} \cdot \ddot{a}_j(t) + C_{ij} \cdot \dot{a}_j + K_{ij} \cdot a_j(t) = F_i^x(t) + F_i^\theta(t) \quad (3.44)$$

where the modal mass is:

$$M_{ij} = m \cdot \delta_{ij} + M \cdot \beta_{ij} \quad (3.45)$$

$$\text{with } m = \frac{\rho \cdot S \cdot L}{2} \quad (3.46)$$

$$\text{and } M = 360 \text{ kg} \quad (3.47)$$

The modal stiffness is:

$$K_{ij} = k \cdot i^4 \cdot \delta_{ij} \quad (3.48)$$

$$\text{with } k = \frac{E \cdot I \cdot \pi^4}{2 \cdot L^3} \quad (3.49)$$

The modal forces are:

$$F_i^x(t) = \ddot{u}_{g,x} \cdot \left[ \int_0^L \rho \cdot S \cdot f_i(y) \cdot dy \right] + \ddot{u}_{g,x} \cdot M \cdot (f_i(y_1) + f_i(y_2)) \quad (3.50)$$

and:

$$F_i^\theta(t) = \ddot{\theta}_{g,z}(t) \cdot \left[ \int_0^L \left( y - \frac{L}{2} \right) \cdot \rho \cdot S \cdot f_i(y) \cdot dy \right] + \ddot{\theta}_{g,z} \cdot M \cdot \left( f_i(y_1) \cdot \left( y_1 - \frac{L}{2} \right) + f_i(y_2) \cdot \left( y_2 - \frac{L}{2} \right) \right) \quad (3.51)$$

#### 3.1.2.4 Evaluation of the modal displacements using full-field displacement measurement

The data used for the strategy described in this section come from Videometric<sup>®</sup> (section 2.6.2). They are full-field measurements of the displacements along x-direction of the neutral axis of the beam. Let  $u(y, t)$  be the measured displacement field and  $(f_i)_{i \leq N}$  a finite number of eigenvectors as defined in section 3.1.2.1. In this case,  $(f_i)_{i \leq N}$  is a linearly independent set of the bending vibration modes of the beam but does not constitute a complete basis on which it is possible to express  $u(y, t)$ . Thus, a displacement  $v(y, t)$  written as a linear combination of  $(f_i)_{i \leq N}$  is computed as the best-estimate of  $u(y, t)$  by

minimizing the arbitrary functional for each time  $t$ :

$$\eta(a_i(t)) = \int_0^L (u(y, t) - v(y, t))^2 \cdot dy \quad (3.52)$$

$$\Rightarrow \eta(a_i(t)) = \int_0^L \left( u(y, t) - \sum_i a_i(t) \cdot f_i(y) \right)^2 \cdot dy \quad (3.53)$$

The minimization problem writes:

$$\frac{\partial \eta}{\partial a_i(t)}(a_i(t)) = - \int_0^L 2 \cdot f_j(y) \cdot \left( u(y) - \sum_i a_i(t) \cdot f_i(y) \right) \cdot dy = 0 \quad (3.54)$$

then:

$$\int_0^L f_j(y) \cdot u(y) \cdot dy = \sum_i a_i(t) \cdot \int_0^L f_i(y) \cdot f_j(y) \cdot dy \quad (3.55)$$

which can be re-written under the matrix form:

$$\mathbf{B} \cdot \mathbf{a}(t) = \mathbf{b}(t) \quad (3.56)$$

$$\text{with } B_{ij} = \int_0^L f_i(y) \cdot f_j(y) \cdot dy \quad (3.57)$$

$$\text{and } b_i(t) = \int_0^L f_i(y) \cdot u(y, t) \cdot dy \quad (3.58)$$

where the vector  $\mathbf{a}(t)$  contains the sought  $a_i(t)$ . The size of the matrix  $\mathbf{B}$  depends on the number of elements  $N$  in  $(f_i)_{i \leq N}$ . Lower frequencies are expected to be preponderant for IDEFIX beams under seismic motion. For this reason, few vectors  $f_i$  are necessary to express with a satisfying approximation the displacement field  $u(y, t)$ , which allows for less expensive computation because of a reduced size of matrix  $\mathbf{B}$ . Finally, for each time  $t_k$  at which a picture is taken, the best-approximate linear combination of  $(f_i)_{i \leq N}$  is computed as:

$$\mathbf{a}(t_k) = \mathbf{B}^{-1} \cdot \mathbf{b}(t_k) \quad (3.59)$$

An absolute error map is computed at each  $t_k$  by the difference between  $v(y, t_k)$  and  $u(y, t_k)$ :

$$e(y, t_k) = v(y, t_k) - u(y, t_k) \quad (3.60)$$

and constitutes a useful tool to decide whether an enrichment of the subset  $(f_i)_{i \leq N}$  is necessary or not to improve the modal displacements estimation. A relative error map can also be used, however the absolute error map is maybe more intuitive from a user point-of-view.

### 3.1.3 Error evaluation and minimization strategy

To perform the identification by the optimization procedure, an objective functional has to be defined. It constitutes a metric to evaluate how far is the response obtained with

the current set of parameters (i.e. at the current iteration) to the reference response. The said response may be of different natures, such as forces, displacements, velocities, accelerations, etc. A combination of different sources of data can be used. Mathieu *et al.*, 2015 have shown that the simultaneous use of full-field displacements and forces measurements in integrated digital image correlation (I-DIC) can significantly improve the convergence of the optimization algorithm when the sensitivity of one or several parameters is higher for either the force or the displacement.

For the case of IDEFIX, modal displacement data are used in the first place for the objective functional to minimize:

$$\varepsilon_u = \frac{\int_0^T (c_i^{\{p\}}(t) - a_i(t))^2 dt}{\int_0^T (a_i(t))^2 dt} \quad (3.61)$$

where  $c_i^{\{p\}}$  is the computed displacement of the oscillator associated to the  $i^{\text{th}}$  vibration mode for the current test set of parameters  $\{p\}$ . However, the modal forces data might be used as well:

$$\varepsilon_F = \frac{\int_0^T (F_i^{\{p\}}(t) - F_i(t))^2 dt}{\int_0^T (F_i(t))^2 dt} \quad (3.62)$$

where  $F_i(t) = F_i^x(t)$  if  $i$  is *odd* and  $F_i(t) = F_i^\theta(t)$  if  $i$  is *even*.

The method of combination of Mathieu *et al.*, 2015 relies on the assumption that the experimental data are corrupted by a white gaussian noise of standard deviation  $\gamma_u$  and  $\gamma_F$  for the displacement and the force respectively. This allows for the normalization and summation of the objective functions:

$$\varepsilon = (1 - \lambda) \cdot \frac{1}{\gamma_u^2} \cdot \varepsilon_u + \lambda \cdot \frac{1}{\gamma_F^2} \cdot \varepsilon_F \quad (3.63)$$

where  $\lambda$  is an optimization parameter to control the importance given to either the displacement or the force data in the overall objective function. In this case,  $\lambda = 0.5$  would give an equivalent importance to both  $\varepsilon_u$  and  $\varepsilon_F$ . Of course, the overall objective function is not limited to two terms and, as aforementioned, acceleration or velocity-based objective functions could also be added to  $\varepsilon$ .

Regarding the optimization algorithm, multiple choices are arguable. Since the parameters to identify (e.g. viscous damping ratios or eigenfrequency) are physical parameters, upper and lower bounds can be defined to enhance the stability of the optimization. For example, the viscous damping ratio should be positive and lower than 1, otherwise the SDOF system is over-damped (see section 1.3.2.1). Following the recommendations of Mathworks, 2017a and Mathworks, 2017b, the interior-point algorithm is chosen since “it handles large, sparse problems, as well as small dense problems. The algorithm satisfies bounds at all iterations [...]”. An historical review and a description of the interior-point algorithms have been made by Potra & Wright, 2000. A decision table (Mathworks, 2017b) reviewing the functions implemented in MATLAB<sup>®</sup> is given in the software documentation.

### 3.1.4 About parametric and non-parametric identifications

Two strategies are possible for the identification of the parameters gathered in a vector  $\{\mathbf{p}\}$  if they are expected to evolve:

- no assumption on the evolution of the parameters is made, a *non-parametric* identification is performed;
- a model of evolution of  $\{\mathbf{p}\}$  is thought, in this case the parameters of this model are sought in place of the parameters  $\{\mathbf{p}\}$ , a *parametric* identification is performed.

The terms *parametric* and *non-parametric* were originally used by Demarie & Sabia, 2010.

#### 3.1.4.1 Non-parametric identification

The identification is performed on a chosen vibration eigenmode successive time windows of a given duration on which the parameters  $\{\mathbf{p}\}$  are supposed to be constant. Two antagonistic goals have to be reached: the duration as to be long enough to perform the identification on a sufficiently high number of data points to improve the confidence on the identification, but short enough to not force the parameters to stay constant while they should evolve.

The continuity of the different variables between two successive time windows of duration  $T_w$  is imposed. For example, if the viscous damping ratio  $\xi$  and the natural angular frequency  $\omega_0$  are sought, the problem for the chosen modal displacement  $u$  on the  $k^{\text{th}}$  time-window is written as:

$$\begin{cases} \ddot{u}^{(k)}(t) + 2 \cdot \xi^{(k)} \cdot \omega_0^{(k)} \cdot \dot{u}^{(k)}(t) + \omega_0^{(k)2} \cdot u^{(k)}(t) = -\ddot{u}_g(t) \\ \ddot{u}^{(k)}((k-1) \cdot T_w) = \ddot{u}^{(k-1)}((k-1) \cdot T_w) \\ \dot{u}^{(k)}((k-1) \cdot T_w) = \dot{u}^{(k-1)}((k-1) \cdot T_w) \end{cases}, (k-1) \cdot T_w \leq t \leq k \cdot T_w \quad (3.64)$$

where the values of displacement and velocity at the end of the previous time-window are initial conditions for the following one. An additional constraint can be set on the absolute or relative variation between two consecutive sets of parameters  $\{\mathbf{p}\}^{(k)}$  and  $\{\mathbf{p}\}^{(k+1)}$  if the physics suggests it. For example, a relative variation of  $\pm 10\%$  can be imposed:

$$0.9 \cdot \{\mathbf{p}\}^{(k)} \leq \{\mathbf{p}\}^{(k+1)} \leq 1.1 \cdot \{\mathbf{p}\}^{(k)} \quad (3.65)$$

Similarly, a monotonic evolution of a parameter  $p_i$  from the set  $\{\mathbf{p}\}$  can be imposed:

$$p_i^{(k+1)} \leq p_i^{(k)} \quad \text{or} \quad p_i^{(k+1)} \geq p_i^{(k)} \quad (3.66)$$

#### 3.1.4.2 Parametric identification

Because the optimization only allows for identifying parameters that are constant in the time-domain considered, a model is useful to identify the evolution of these parameters throughout the time-history analysis. Thus, the identification is performed on the parameters of the model — that are supposed to be constant — and not on the values of interest sought in the first place. A strong experience of model identification by DIC

methods (integrated-DIC, finite element modeling updating) have been built at the LMT within the eikology team through numerous experimental and numerical studies (Hild & Roux, 2006; Hild *et al.*, 2009a; Hild *et al.*, 2009b; Hild *et al.*, 2015; Mathieu *et al.*, 2012; Mathieu *et al.*, 2015; Bouterf *et al.*, 2013; Bouterf *et al.*, 2014; Bertin *et al.*, 2016b; Bertin *et al.*, 2016a). A “good” model should be able to describe the behavior of the beam throughout the time-history analysis with only one set of parameters (on the contrary of the non-parametric identification). Of course, the limits of applicability of this model should be clearly defined prior to any identification attempt.

## 3.2 Quasi-static tests

The influence of structural and material parameters on the nonlinear range of the behavior of IDEFIX beams is investigated. First, the method used to obtain the capacity curves corresponding to each beam design is presented. Then, a qualitative study of the differences between these capacity curves depending on the type of beam is made. The same procedure is applied on the first and second eigenmodes.

### 3.2.1 Capacity curves

#### 3.2.1.1 Capacity curves deduced from QSC1 tests

##### a Obtaining the capacity curves

The QSC1 quasi-static cyclic reverse tests (see section 2.5.1.1, figure 2.16a) performed on the different beam designs allow for extracting the capacity curves by considering only the envelope of the force-displacement curves. Under the hypothesis that the compressed cracked RC recovers its initial properties when the cracks are closed, the capacity curve obtained is comparable to the one resulting from a pushover analysis. The force considered is the sum of the forces measured on each beam support in X-axis, whereas the displacement is measured at mid-span. Only the positive displacements are considered, i.e. when the actuators push on the beam, by convention. These results are plotted in figure 3.5. For each beam, the nonlinear range begins around 10 kN, with cracks initiation in concrete. In real RC structures steel yielding is not expected in beams but rather at structural joints. Hence, the steel yielding is not investigated during this experimental campaign. The results plotted on figure 3.5 are commented in the next paragraphs.

##### b Concrete influence

Beam HA12-C1B exhibits a lower capacity than HA12-C1A because the measured strength for concrete C1A is 36.9 MPa while the one for C1B is 33.0 MPa (10.6 % lower). More surprisingly, the capacity of HA12-C2 is higher than HA12-C1A in the first 50 mm of prescribed displacement, but is then lower. The difference may not be important enough to conclude about the relative capacities of these two variants. Indeed, only one specimen of each could be tested.

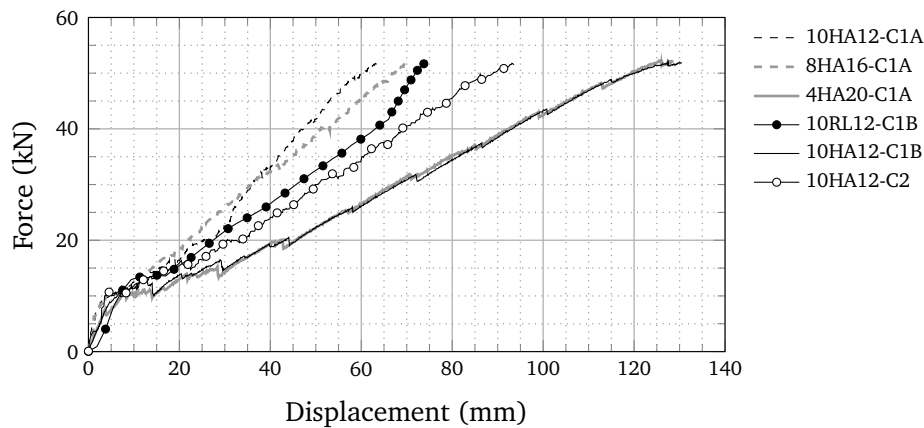


FIGURE 3.5: Capacity curves obtained from QSC1 tests (displacement measured at mid-span)

### c Reinforcement pattern influence

The highest capacity is observed for beam HA16-C1A while the lowest is for beam H20-C1A. The capacity of HA12-C1A is an intermediate between the two previous ones. These results are in accordance with the specific interface surfaces given in table 2.3. This may be a more significant indicator of the beam behavior once in the nonlinear range. Indeed, bond slipping occurs at the steel-concrete interface. The higher the interface specific surface is, the higher the friction force between steel and concrete is.

### d Reinforcement ribs influence

HA12-C1A has classical high adherence steel reinforcement bars, but RL12-C1A has special rebars without ribs. The RL12-C1A capacity was expected to be lower than the one of HA12-C1A, but it is finally not the case. A low confinement of the concrete surrounding the reinforcements may explain this results as stated by Daoud *et al.*, 2013 when comparing the results of a non-confined pull-out test with both smooth and ribbed bars: the ribs play fully their role when the concrete is confined around the rebars.

### e Conclusion regarding the capacity curves (from QSC1)

In conclusion, the capacity curves show interesting tendencies:

- no clear link between concrete strength and the capacity curves has been emphasized, maybe due to an insufficient difference between the studied concretes;
- the reinforcement specific surface (steel-concrete interface surface per unit length) increases the post-yield stiffness of the beam;
- the absence of ribs on the reinforcement bars does not influence the capacity curves (RL12-C1B *versus* HA12-C1B), probably because of a low confinement.

### 3.2.1.2 Capacity curve deduced from QSC2 test

One beam, HA12-C1A-2, was tested first by the loading QSC2 (plotted on figure 2.16b). It is necessary to define the notion of control point when plotting the capacity curve as in figure 3.6. For QSC1 tests, the more “natural” displacement to consider is the highest along the beam, i.e. at mid-span. This means that the displacement of the control point is higher than the one prescribed by the hydraulic jacks. In the case of QSC2, the mid-span displacement is theoretically null. Therefore, the “natural” control point(s) is (are) this time located at the quarter-span(s) and correspond(s) to the hydraulic jacks prescribed displacement. The choice of the control point is arbitrary, but it is important to keep in mind that capacity curves (or force-displacement curves) obtained from QSC1 and QSC2 can be compared only when the same control point is considered. Similarly, several choices are possible for the force to plot in the capacity curve: it can be either the force prescribed by one or both actuators. When the test QSC2 is carried out, the sum of the forces injected by the two actuators cancels itself, but the sum of the absolute values of the forces can also be considered. However, the loading pattern differs between QSC1 (or QSC2) and the dynamic tests since the former are mostly discrete forces while the latter are distributed all along the beam (this point is also discussed in section 3.2.4.2).

The theoretical displacement due to an effort  $F$  (counted as positive) at each quarter-span during a test QSC1 (see figure 2.14a) is given by the beam theory:

$$u_x^{QSC1}(L/2) = -\frac{11 \cdot F \cdot L^3}{384 \cdot E \cdot I} \quad (3.67)$$

$$u_x^{QSC1}(L/4) = -\frac{8 \cdot F \cdot L^3}{384 \cdot E \cdot I} \quad (3.68)$$

and during a test QSC2:

$$u_x^{QSC2}(L/2) = 0 \quad (3.69)$$

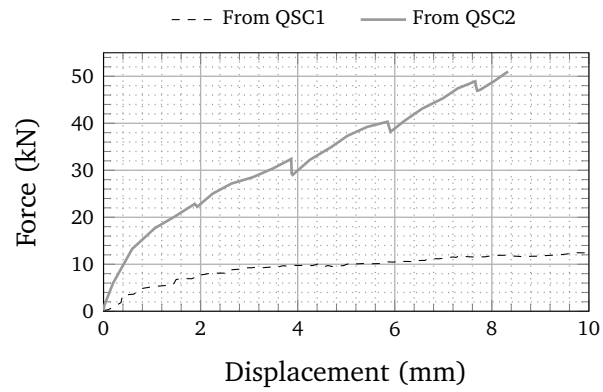
$$u_x^{QSC2}(L/4) = -\frac{F \cdot L^3}{384 \cdot E \cdot I} \quad (3.70)$$

Hence, the apparent stiffness during QSC2 is either 8 times higher than during QSC1.

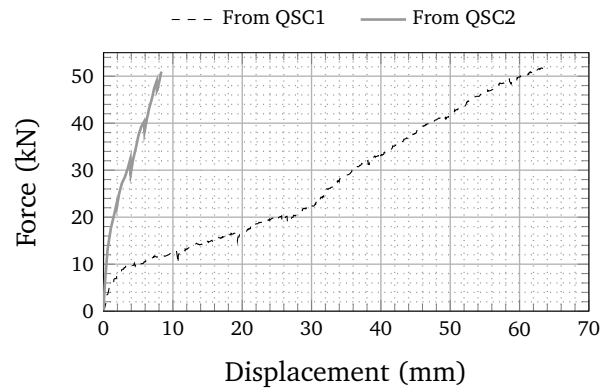
### 3.2.2 Velocity sweep tests (SPS1 and SPS2)

The velocity sweep tests are described in section 2.5.1.2. A focus is made on the beam HA1-C1B-2 which was tested with several SPS1 signals: the displacement amplitude and the peak acceleration are tested at different level. It is recalled that the peak acceleration corresponds to the parabolic transition of displacement when switching the loading direction for smoothing purposes. Starting with an undamaged beam, the test sequence is the following:

1. displacement 20 mm — peak acceleration 0.1 g;
2. displacement 50 mm — peak acceleration 0.1 g;
3. displacement 70 mm — peak acceleration 0.1 g;



(A) Zoomed view



(B) Overall view

FIGURE 3.6: Capacity curves of HA12-C1A-2 obtained from QSC2 versus the one of HA12-C1A-1 obtained from QSC1 considering the same control point at  $y = 3L/4$  (the force is the sum of the absolute values of the forces applied by the hydraulic jacks)

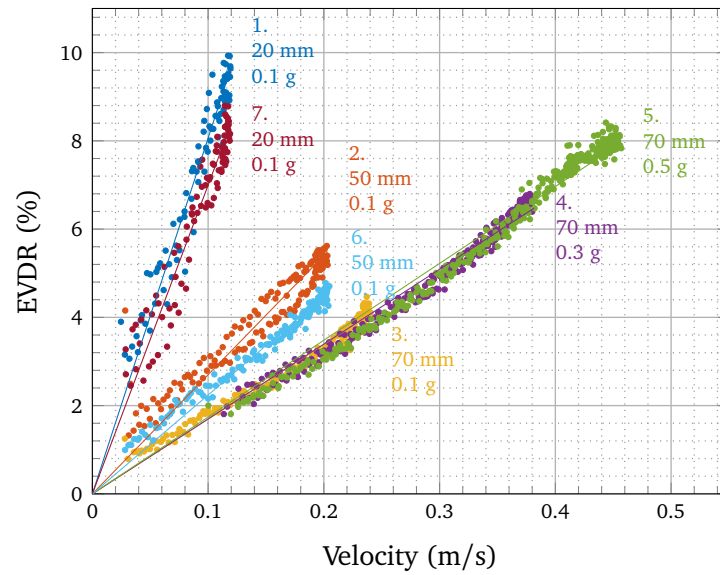


FIGURE 3.7: Sweep velocity influence on the EVDR

4. displacement 70 mm — peak acceleration 0.3 g;
5. displacement 70 mm — peak acceleration 0.5 g;
6. displacement 50 mm — peak acceleration 0.1 g;
7. displacement 20 mm — peak acceleration 0.1 g;

This sequence is plotted on figure 3.7 and four observations are made:

1. the higher is the velocity, the higher is the EVDR;
2. the higher is the prescribed displacement amplitude, the lower is the EVDR;
3. the higher is the damage level, the lower is the EVDR (this effect is light though, see test 1 versus test 7 or test 2 versus test 6 on figure 3.7);
4. the maximum authorized acceleration has no effect on the EVDR (see tests 3, 4 and 5).

The displacement data of a typical SPS1 test are plotted on figure 3.8. On the contrary of the prescribed displacement seen on figure 2.17a, the amplitude is not constant because of the maximum velocity capability of the hydraulic jacks. It is important to take into account this effect that tends to increase with the velocity: it could blur the influence of the velocity and the displacement amplitude.

Now that the influence of the damage state has been shown to be negligible on the EVDR, SPS1 tests are carried out on an already damaged beam HA12-C2-1 after QSC1 and QSC2 tests. This time, more displacement amplitudes are tested: from 10 mm to 70 mm by steps of 10 mm. A linear regression of  $\xi$  versus the velocity is computed, the results are shown on figure 3.9. The slope of the linear regression decreases when the displacement amplitude increases. This effect is studied on figure 3.10 by a curve fitting of the type  $y = a \cdot x^n$ .

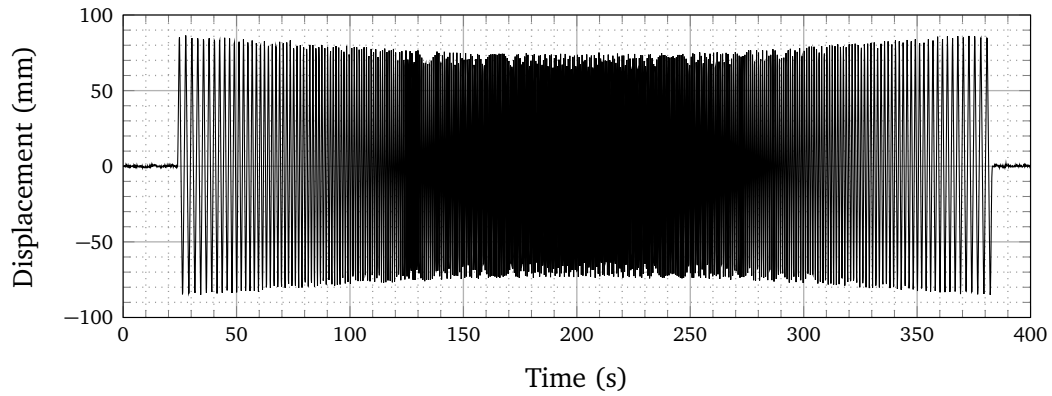


FIGURE 3.8: Mid-span displacement measured with sensor DX5 for SPS1 (run 146) with beam HA12-C1B-2

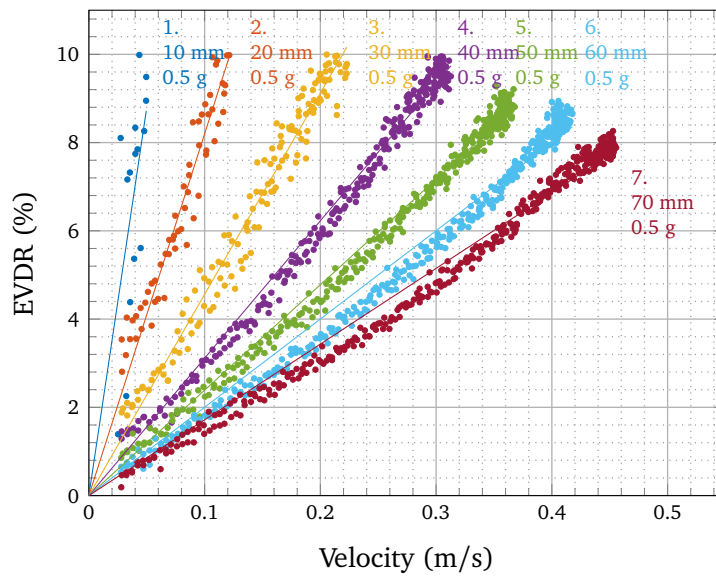


FIGURE 3.9: SPS1 tests on beam HA-12-C2-1

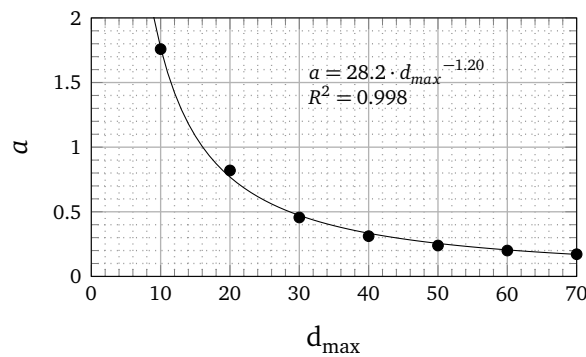


FIGURE 3.10: Linear coefficient  $a$  of the fitted equation of EVDR  $\xi = a \cdot v$  as function of the displacement amplitude  $\delta$

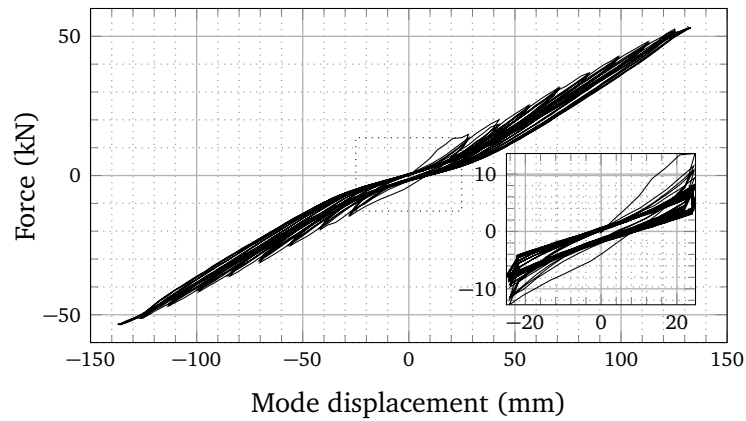


FIGURE 3.11: Force-displacement curve obtained after QSC1 test performed on beam HA20-C1A-1

### 3.2.3 Cyclic quasi-static tests (QSC1 and QSC2)

A post-treatment of the cyclic quasi-static test QSC1 (prescribed displacement plotted on figure 2.16a) performed on the beam HA20-C1A-1 is presented in this section. The force-displacement curve exhibits mainly three phenomena: a stiffness loss, hysteresis loops and a pinching effect. The stiffness loss is essentially due to cracking. Hysteresis have several origins which are not easy to model neither identify. Anyway, crack surfaces friction and bond slipping are supposed to play a major role in this phenomenon. Finally, the so-called pinching effect consists in a stiffness reduction in the neighborhood of the zero-displacement point that explains the reversed S-shape of the load displacement curve in figure 3.11. This effect is still not entirely understood.

Thanks to the DIC device described in section 2.6.2, it is possible to make a projection of the measured transverse displacement field  $u(x, t)$  on the theoretical eigenbasis  $\Phi$ . The resulting error is plotted in figure 3.12 against the position on the beam and the time. Maxima appear at the beam tips (maximum absolute error about 3 mm in this case) due to the presence of the mounting system masking the stripes pattern tracked on the beam. This effect remains local and does not disturb the overall projection error since it stays otherwise as low as a mean absolute value of 0.16 mm for the discretization used in this case (i.e. 201 points distant of 29.5 mm).

In order to study and quantify the dissipations observed during cyclic loadings, the EVDR has been computed. The classical Jacobsen's areas method was originally developed to evaluate the EVDR for nonlinear frictional systems. In practice, several points remain questionable. The stored linear elastic energy is generally supposed to be square-proportional to the displacement (figure 3.14a) but this hypothesis is inexact for a nonlinear behavior, which is the case when pinching occurs for example (figure 3.14b). When the loops are not symmetric, there is no actual reason to pick up the maximum relative displacement rather than the minimum one when assessing the stored elastic energy. For this reason, Kumar *et al.*, 2015 proposed an approach adapted to asymmetric hysteretic behaviors. As depicted in figure 3.14c. A method inspired from this work and more

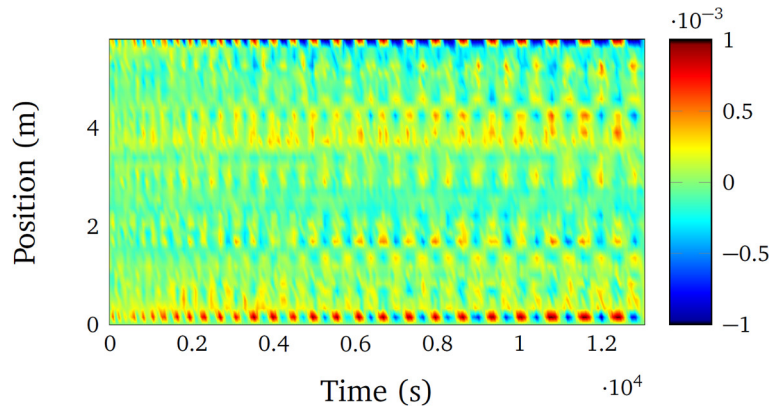


FIGURE 3.12: Spatiotemporal error map after projection on modal basis for QSC1 test (error in meters)

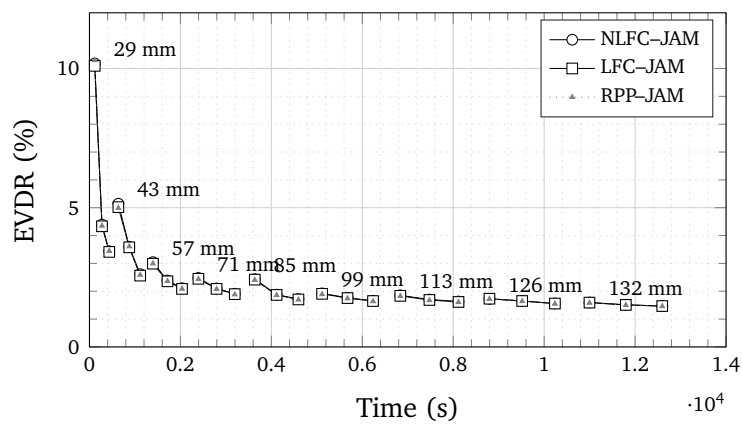


FIGURE 3.13: Evolution of the EVDR during QSC1 for beam HA20-C1A-1

suitable for nonlinear restoring forces is proposed in figure 3.14d. The different methods have been presented in (Heitz *et al.*, 2017b) and (Heitz *et al.*, 2017a).

Jennings, 1968 considered the case of a rigid-perfectly-plastic (RPP) hysteretic model as plotted on figure 3.15 the EVDR is:

$$\zeta_{RPP} = \frac{1}{4 \cdot \pi} \cdot \frac{E_{d,RPP}}{E_{s,RPP}} \quad (3.71)$$

$$= \frac{1}{4 \cdot \pi} \cdot \frac{4 \cdot F_{max} \cdot D_{max}}{\frac{1}{2} \cdot F_{max} \cdot D_{max}} \quad (3.72)$$

which finally gives:

$$\zeta_{RPP} = \frac{2}{\pi} \quad (3.73)$$

which is theoretically the maximum potential EVDR, since no other non-softening hysteretic model dissipates more energy than the RPP model. Then, it is possible to re-write EVDR the ratio of the area within the hysteretic model over the area of the smallest enclosing RPP hysteretic model force-displacement curve:

$$\xi_{eq} = \frac{2}{\pi} \cdot \frac{E_d}{E_{d,RPP}} \quad (3.74)$$

This is illustrated on figure 3.16. Such an expression is considered for example by Dwairi *et al.*, 2007. For the following studies, the method NLFC-JAM of figure 3.14d is used because it is anyway of interest to track the energy stored during the tests.

The energy dissipated during the cracking initiation and propagation should not be included in the EVDR evaluation since it induces unrealistic damping ratio values. This explains why every three cycles, a leap of damping ratio is observed in figure 3.13. When going to the next loading block of cycles of same amplitude (figure 2.16a), the damage state of the beam increases dissipating a large amount of energy for the first cycle. For this reason, only the 3<sup>rd</sup> cycle of each block is used to apply Jacobsen's areas method.

Second degree polynomial functions of the displacement amplitude fit very well both stored and dissipated energy per cycle (figure 3.17): the fitted equation of the dissipated energy is of the form  $y = a \cdot x^2$  while the one of the stored energy is of the form  $y = a \cdot x^2 + b \cdot x$ . As a direct consequence of the classical JAM equation (1.54), the EVDR is proportional to the ratio of the dissipated energy over the stored one. Thus, an inverse function of the form  $y = a + b \cdot x^{-1}$  describes the evolution of the EVDR against the displacement amplitude (figure 3.18). This result is in agreement with several authors (Satake *et al.*, 2003; Li *et al.*, 2002; Liu & Tsai, 2010) who studied the response of slender buildings under dynamic loads and contradicts the hypothesis of a linear viscous damping. Among the expressions proposed by Rodrigues *et al.*, 2011, Priestley *et al.*, 2007 and Kowalsky, 1994, only Kowalsky's equation (1.62) allows for a decreasing EVDR. Despite the fact that experimental data gathered during QSC1 tests do not give information regarding ductility coefficient values lower than 4, the EVDR is expected to increase in the first place until a maximum is reached. However, QSC1 tests do not allow for uncoupling the influences of the displacement amplitude and the displacement ductility levels. This hypothesis has been studied by Heitz *et al.*, 2017b through numerical simulations performed on an hysteretic model calibrated on experimental data. It is shown

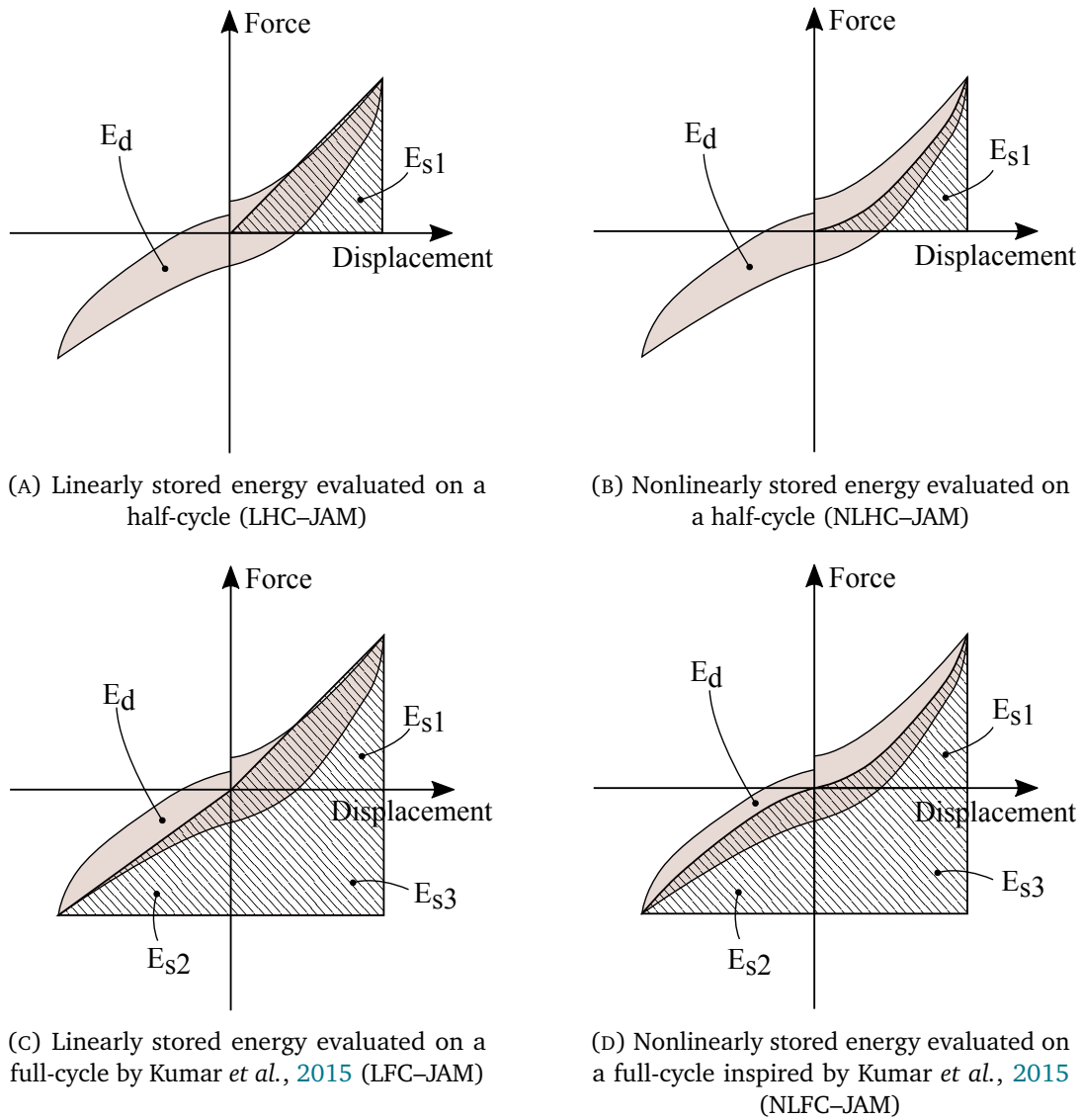


FIGURE 3.14: Different ways to apply areas method derived from Jacobsen, 1960 and Kumar *et al.*, 2015

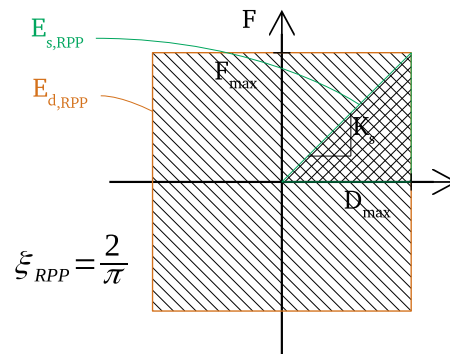


FIGURE 3.15: Rigid-perfectly-plastic hysteretic model EVDR using JAM

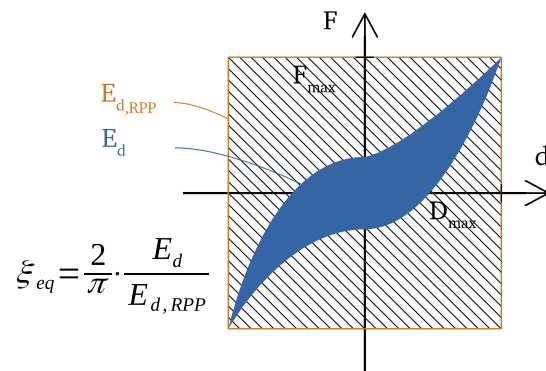
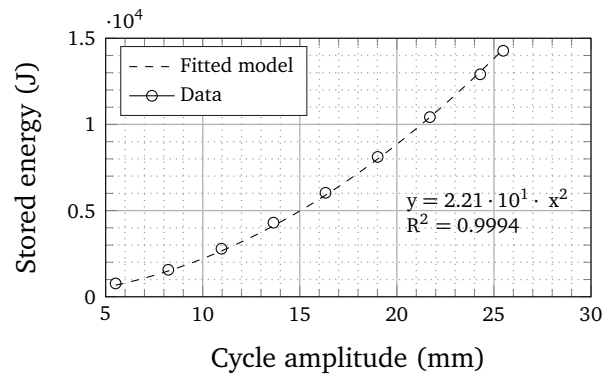
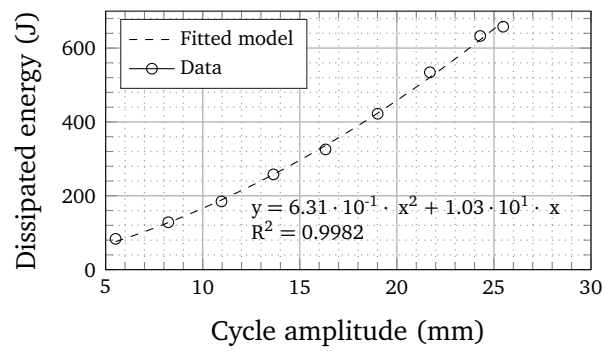


FIGURE 3.16: Example of EVDR evaluated as a ratio of RPP dissipated energy



(A) Stored energy per cycle



(B) Dissipated energy per cycle

FIGURE 3.17: Energies engaged during QSC1 tests

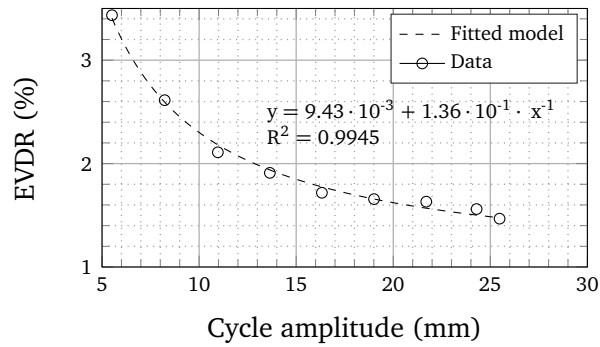


FIGURE 3.18: EVDR values deduced from Jacobsen's areas method

in the same study that the EVDR not only depends on the ductility coefficient but also on the current cycle amplitude of displacement itself. In other words, for an hysteretic model at a given ductility level  $\mu_1$  associated to a maximum historic displacement  $\delta_m$  and submitted to a cyclic prescribed displacement of amplitude  $\delta < \delta_m$ , the EVDR value depends on both  $\mu_1$  and  $\delta$ . This point is further studied in section 3.3.

### 3.2.4 Formulation of a SDOF hysteretic model for the beam behavior

#### 3.2.4.1 Objectives

In order to model the behavior of the beams, a nonlinear oscillator is associated to each vibration eigenmode. To begin with, a model of restoring force is necessary. This model is not intended to be general but rather adapted to the case of IDEFIX tests and provides a useful basis for the numerical experiments carried out on virtual quasi-static tests presented in section 3.3. These numerical experiments investigate the uncoupled influence of both displacement amplitude and ductility level. The model should also make possible dynamic simulations as performed in chapter 4 that help to identify the lacks and gaps to fill regarding damping models for further studies.

#### 3.2.4.2 Modeled phenomena

The formulation of a state potential is driven by the phenomena intended to be modeled. The model presented in this section strongly relies on the work of Moutoussamy, 2014. The cyclic reverse quasi-static tests allow for uncoupling and identify different phases and mechanisms. For small displacements applied at the initial state, the beam in bending has a linear elastic behavior, i.e. has a constant stiffness  $K$  which can be identified. Beyond a limit displacement  $\delta_y$ , the beam starts to exhibit nonlinearities. A stiffness decrease is observed during the unloading phase, this indicates the creation and propagation of cracking and motivates the use of the damage mechanics framework (Lemaître, 1996).

Steel yielding is not observed during the tests and is consequently not taken into account. Nevertheless, hysteresis loops are observed during loading-unloading cycles. It is explained by the existence of friction within the reinforced concrete, e.g. between

cracks surfaces or between the steel reinforcements and the surrounding cracked concrete. Hence, a friction displacement variable  $u^\pi$  is defined. Such a variable has already been proposed by Ragueneau, 1999 or Richard & Ragueneau, 2013.

The unilateral effect is taken into account by splitting each internal variable related to damage in two parts. These parts correspond to two allegedly independent families of cracks on upper or lower half cross-sections of the beam from either side of the neutral axis depending on the direction of deflection.

Finally, the last observed phenomenon is the so-called “pinching” effect which consists in a stiffness reduction in the neighborhood of the zero-displacement point that explains the reversed S-shape of the load displacement curve. The origin of this effect is not clearly understood but different hypotheses exist. Several researchers state that this effect indicates a failure driven by shear (Brown & Jirsa, 1971; Penzien & Celebi, 1973; Bertero & Popov, 1977; Otani, 1980; D’Ambrisi & Filippou, 1999; Vintzileou *et al.*, 2006; Archundia-Aranda *et al.*, 2013). Two explanations are here proposed:

- in the case of a crossing crack, the crack surfaces get into contact when the displacement is high enough (as illustrated on figure 3.19) thus enlarging the virtual cross section of the beam at the crack location;
- the steel-concrete bond failure induces slipping until the adherence is found again at the interface (inter-locking).

Two hystereses have been isolated from two different tests: a dynamic mono-harmonic excitation of beam HA12-C1A-3 at 2.4 Hz and 0.2 g; a static QSC1 test. The idea is to compare the shape of the loops on figure 3.20. Two observations can be made:

- the surface enclosed in the static loop is smaller than the one of the dynamic loop;
- the pinching effect is stronger quasi-static than in dynamics;

Following the observations of the aforementioned authors about the pinching effect, it suggests that the shear is predominant in static and not in dynamic. Indeed, during QSC1, the displacement is prescribed by two hydraulic jacks (i.e. discrete forces) while the dynamic forces are distributed all along the beam. Therefore, at a given level of overall reaction force, the static loading is more kind than the dynamic loading to generate important shear stress where the actuators are mounted. The light pinching effect observed in dynamics might be caused by the presence of the additional masses which act as discrete inertial forces to a lesser extent than with the actuators.

During the bending, each section is divided in two parts: one part in tension, the other in compression. Supposing a linear behavior of concrete in compression, the beam behavior is mainly driven by the tension area (and the associated damage state). Hence, two independent scalar variables  $d_+$  and  $d_-$  are defined depending on the direction of the bending, more precisely on the sign of the displacement  $u$ . The index  $i$  will be used to stand for both direction indexes “+” and “-”.

Isotropic hardening variables  $z_+$  and  $z_-$  are associated to the damage variables because the linear domain expands as long as cracks spread and grow. Similarly, a kinematic hardening variables  $\alpha^\pi$  is associated to the friction displacement  $u^\pi$ .

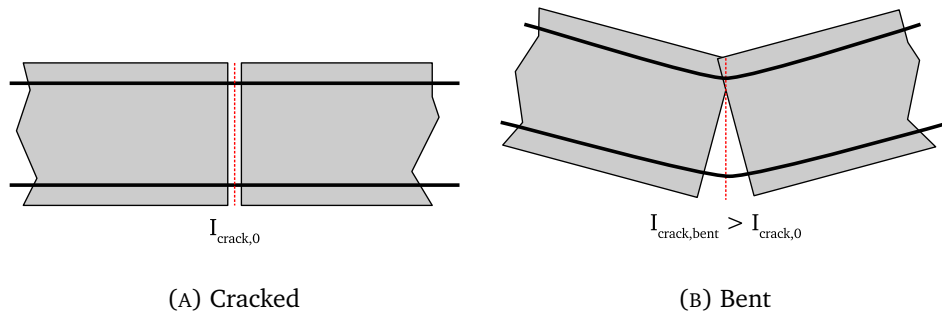


FIGURE 3.19: Illustration of the increase of moment of inertia due to crack closure under bending

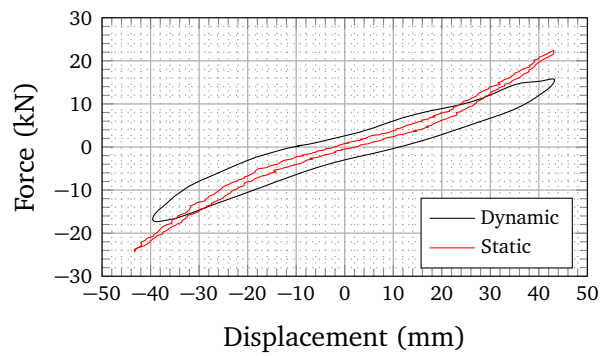


FIGURE 3.20: Beam HA12-C1A-3 under mono-harmonic signal (dynamic) at 2.4 Hz of frequency and 0.2 g of acceleration and another hysteresis loop (quasi-static) of beam HA12-C1A-2 during QSC1

Mechanism	Observable variable	Internal variable
Displacement	$u$	
Damage		$d_i$
Friction		$u^\pi$
Isotropic hardening		$z_i$
Kinematic hardening		$\alpha^\pi$
Crack closure		$\eta$

TABLE 3.3: Internal variables of the model

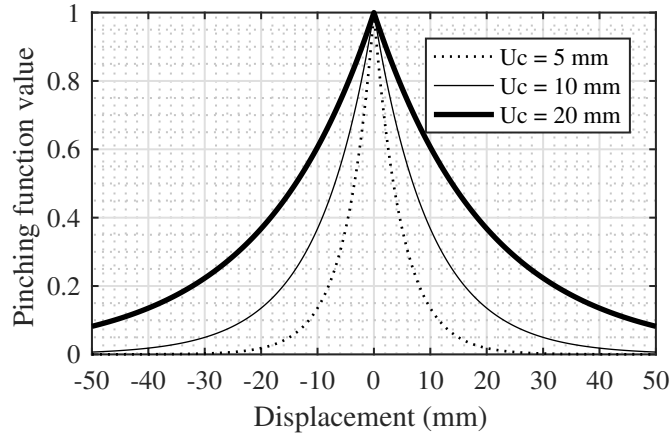


FIGURE 3.21: Plot of the pinching function over displacement for  $d_i = 1$  (0 value corresponds to completely closed cracks)

### 3.2.4.3 State potential

Helmoltz's free energy is chosen as state potential, which is a function of the internal and observable variables summarized in table 3.3:

$$\Psi(u, d_i, u^\pi, z_i, \alpha^\pi, \eta) = \Psi^e(u, d_i, z_i, \eta) + \Psi^\pi(u^\pi, \alpha^\pi, \eta, d_i) \quad (3.75)$$

For a linear elastic behavior:

$$\Psi^e = \frac{1}{2} \cdot K \cdot u^2 \quad (3.76)$$

To take into account the stiffness degradation, the damage variable  $d_i$  is introduced:

$$\Psi^e = \frac{1}{2} \cdot K \cdot (1 - d_i) \cdot u^2 \quad (3.77)$$

The pinching effect only exists along with damage. This is taken into account thanks to a crack closure variable  $\eta$  that evolves from 0 (cracks completely open) to 1 (cracks closed):

$$\eta = d_i \cdot \left[ 1 - \exp\left(-\left|\frac{u}{u_c}\right|\right) \right] \quad (3.78)$$

Hence, the altered stiffness  $K_p$  is defined as follows:

$$K_p(\eta) = K \cdot (1 - \eta) \quad (3.79)$$

which means that the pinching appears progressively with the damage. Examples of "pinching curves" for a fully damages beam (i.e.  $d_i = 1$ ) are given in figure 3.21.

Finally, the isotropic hardening variable associated to damage is introduced through the force  $H(z)$  which leads to:

$$\Psi^e = \frac{1}{2} \cdot K_p(\eta) \cdot (1 - d_i) \cdot u^2 + H(z) \quad (3.80)$$

If the friction state potential is now considered:

$$\Psi^\pi = \frac{1}{2} \cdot K_p(\eta) \cdot d_i \cdot (u - u^\pi)^2 + \frac{1}{2} \cdot b^\pi \cdot (\alpha^\pi)^2 \quad (3.81)$$

To summarize, the overall state potential writes:

$$\Psi = \frac{1}{2} \cdot K_p(\eta) \cdot (1 - d_i) \cdot u^2 + H(z_i) + \frac{1}{2} \cdot K_p(\eta) \cdot d_i \cdot (u - u^\pi)^2 + \frac{1}{2} \cdot b^\pi \cdot (\alpha^\pi)^2 \quad (3.82)$$

#### 3.2.4.4 State laws

The next step is to formulate the state laws, namely:

$$F^e = \frac{\partial \Psi}{\partial u} = K_p(\eta) \cdot (1 - d_i) \cdot u + K_p(\eta) \cdot d_i \cdot (u - u^\pi) \quad (3.83)$$

$$Y_i = -\frac{\partial \Psi}{\partial d_i} = \frac{1}{2} \cdot K_p(\eta) \cdot u^2 - \frac{1}{2} \cdot K_p(\eta) \cdot (u - u^\pi)^2 \quad (3.84)$$

$$Z_i = \frac{\partial \Psi}{\partial z_i} = \frac{Y_0}{\left(1 + \frac{z_i}{d_\infty}\right)^{\frac{1}{q}}} - Y_0 \quad (3.85)$$

$$F^\pi = -\frac{\partial \Psi}{\partial u^\pi} = K_p(\eta) \cdot d_i \cdot (u - u^\pi) \quad (3.86)$$

$$X^\pi = -\frac{\partial \Psi}{\partial \alpha^\pi} = b^\pi \cdot \alpha^\pi \quad (3.87)$$

$$F^\eta = -\frac{\partial \Psi}{\partial \eta} = \frac{1}{2} \cdot K \cdot (1 - d_i) \cdot u^2 + \frac{1}{2} \cdot K \cdot d_i \cdot (u - u^\pi)^2 \quad (3.88)$$

#### 3.2.4.5 Flow rules

The damage and the isotropic hardening are managed in a coupled way and an associative flow rule is assumed. The threshold surfaces for these mechanisms are defined as:

$$f_i^d = Y_i^d - (Y_0 + Z_i) \quad (3.89)$$

where  $Y_i^d$  is the part of energy rate released by damage,  $Y_0$  is an initial energy threshold,  $Z_i$  is the isotropic hardening force.

The choice has been made to not consider the terms proportional to  $\frac{\partial \eta}{\partial u}$  and  $\frac{\partial \eta}{\partial d_i}$  in the expression of  $F^e$  and  $Y_i$  to simplify the formulation of the model. If the final model is not thermodynamically formulated, the experimental identification presented in section 3.2.5 proves that it still adequately represents the hysteretic behavior of the beams. The energy rate is:

$$Y_i^d = \frac{1}{2} \cdot K_p(\eta) \cdot u^2 \quad (3.90)$$

The normality rules are:

$$\dot{d}_i = \lambda_i^d \cdot \frac{\partial f_i^d}{\partial Y_i^d} = \lambda_i^d \quad (3.91)$$

and:

$$\dot{z}_i = \dot{\lambda}_i^d \cdot \frac{\partial f_i^d}{\partial Z_i} = -\dot{\lambda}_i^d \quad (3.92)$$

where  $\lambda_i^d$  is the Lagrange's multiplier. The chosen consolidation function is:

$$H(z_i) = \frac{d_\infty \cdot Y_0}{1 - \frac{1}{q}} \cdot \left(1 + \frac{z_i}{d_\infty}\right)^{1 - \frac{1}{q}} - Y_0 \cdot z_i \quad (3.93)$$

with  $d_\infty \leq 1$  the maximum potential damage (i.e. giving the secant stiffness  $K \cdot (1 - d_\infty)$  for an infinite displacement), and  $q$  a coefficient driving the slope right after the damage initiation in the force-displacement curve. Analytic computations lead to:

$$d_i = d_\infty \cdot \left(1 - \left(\frac{Y_0}{Y_i^d}\right)^q\right) \quad (3.94)$$

$$z_i + d_i = 0 \quad (3.95)$$

For the friction phenomena and the kinematic hardening, the threshold surface is:

$$f^\pi = |F^\pi - X^\pi| \quad (3.96)$$

However, to take into account hysteresis loops that are nonlinear by nature, a non-associative potential of dissipation is used:

$$\Phi^\pi = |F^\pi - X^\pi| + \frac{1}{2} \cdot a^\pi \cdot (\alpha^\pi)^2 \quad (3.97)$$

Then, the flow rules are:

$$\dot{u}^\pi = \dot{\lambda}^\pi \cdot \frac{\partial \Phi^\pi}{\partial F^\pi} = \dot{\lambda}^\pi \cdot \text{sign}(F^\pi - X^\pi) \quad (3.98)$$

and:

$$\dot{\alpha}^\pi = -\dot{\lambda}^\pi \cdot \frac{\partial \Phi^\pi}{\partial X^\pi} = \dot{\lambda}^\pi \cdot \text{sign}(F^\pi - X^\pi) \quad (3.99)$$

### 3.2.4.6 Dissipation

In order to verify the thermodynamical consistency of the model, the positiveness of the dissipation has to be checked. Considering Clausius-Duhem inequality, one get:

$$\begin{aligned} F^e \cdot \dot{u} - \dot{\Psi} \geq 0 &\implies -\frac{\partial \Psi}{\partial V_i} \cdot \dot{V}_i \geq 0 \\ &\implies Y_i \cdot \dot{d}_i + Z_i \cdot \dot{z}_i + F^\pi \cdot \dot{u}^\pi + X^\pi \cdot \dot{\alpha}^\pi + F^\eta \cdot \dot{\eta} \geq 0 \end{aligned} \quad (3.100)$$

where the  $V_i$  are the internal variables of the model. A direct way to verify this inequality is to ensure the positiveness of the variation of the free energy independently for each variable. By definition of the flow rules, the positiveness is verified for the first four terms. Only the last term (i.e.  $F^\eta \cdot \dot{\eta}$ ) of the inequality has to be analyzed.

Name	Description	Unit
$\delta_y$	Yield displacement	m
$K_0$	Initial stiffness	$\text{N}\cdot\text{mm}^{-1}$
$p$	Stiffness loss coefficient	–
$q$	Fragility coefficient	–
$a^\pi$	Hysteresis loops width	N
$b^\pi$	Initial stiffness of the hysteresis loops	$\text{N}\cdot\text{mm}^{-1}$
$U_c$	Crack closure displacement	m

TABLE 3.4: Model parameters

According to its expression,  $F^\eta$  is always positive or nul. Thus, we only need to show the positiveness of  $\dot{\eta}$ .

$$\begin{aligned}\dot{\eta} &= \frac{\partial \eta}{\partial u} \cdot \dot{u} \\ &= -\frac{\text{sign}(u)}{|u_c|} \cdot \dot{u} \cdot \exp\left(-\left|\frac{u}{u_c}\right|\right)\end{aligned}\quad (3.101)$$

With no additional condition, the positiveness of  $\dot{\eta}$  is not always ensured. More particularly, this term is negative for positive displacement and positive increment of displacement or for negative displacement and negative increment of displacement (i.e.  $-\text{sign}[u] \cdot \dot{u} < 0$ ). As this phenomena acts close to zero displacement and that the apparent stiffness is also close to zero due to the pinching, the negative value for this term can not be compensated by other mechanisms of dissipation. Even if this point deserves further investigation, this does not prevent the model from being identified and used with satisfying results in the following sections.

### 3.2.4.7 Model identification strategy

The model identification follows the same principle as the one used for the dynamic parameters described in section 3.1.1. The data used come from QSC1 tests and the objective function is related to the force time-series as in equation (3.62). There are 7 parameters to identify, as summarized in table 3.4.

To facilitate the identification, a sequential procedure is followed:

1. the elastic parameter  $K_0$  is identified either on the 1<sup>st</sup> loading, prior to the 1<sup>st</sup> nonlinearity (expected at the initial value set for  $\delta_y$ ), or is set arbitrarily to match the 1<sup>st</sup> measured eigenfrequency, knowing the associated modal mass. If  $K_0$  influences the whole behavior of the beam, its role is difficult to uncouple from the ones of other parameters in the nonlinear domain while it is straightforward in the linear domain;
2.  $\delta_y$ ,  $p$ ,  $q$  are identified on the capacity curves deduced from QSC1 (section 3.2.1), see figure 3.22;

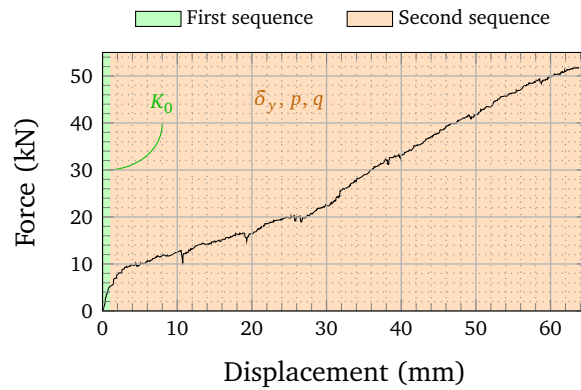
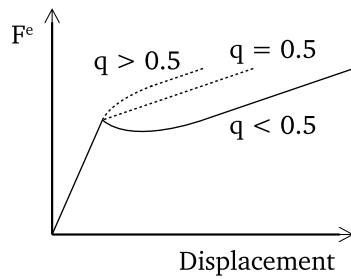
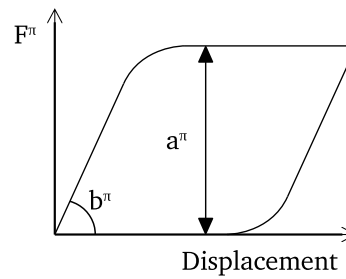


FIGURE 3.22: 1<sup>st</sup> and 2<sup>nd</sup> identification sequences



(A) Parameters influence for a monotonic loading



(B) Parameters influence for a unilateral cyclic loading (without pinching)

FIGURE 3.23: Description of some parameters influence on the model behavior

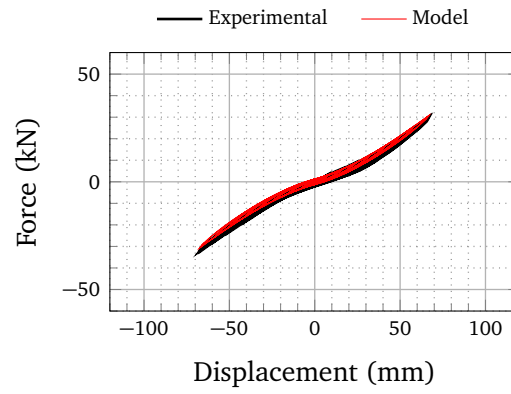
3. the last 3 parameters ( $a^\pi$ ,  $b^\pi$ ,  $U_c$ ) are identified on the full QSC1 force time-history.

The effects of the different parameters are graphically described on figures 3.23 and 3.21.

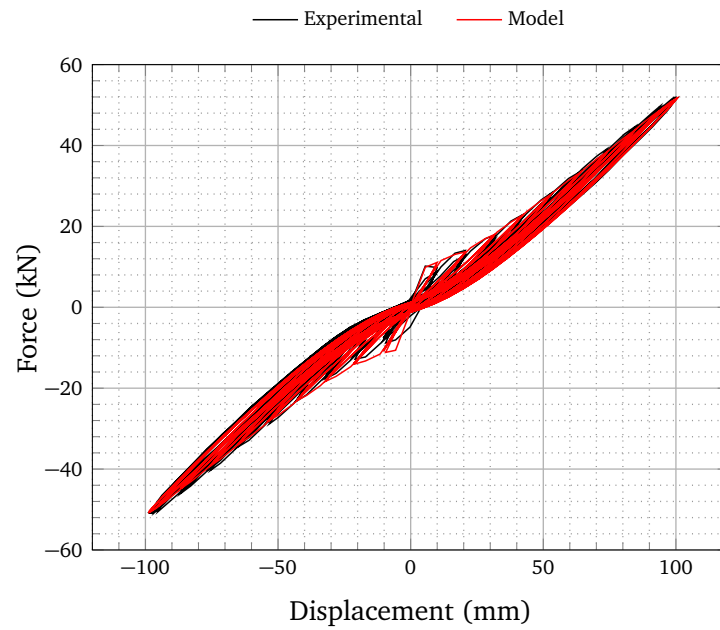
### 3.2.5 IDEFIX identification results

The procedure described in section 3.2.4.7 has been carried out on the different beams tested with QSC1. The results are summarized in table 3.5. In this case the initial stiffness  $K_0$  is set arbitrarily to match the 1<sup>st</sup> eigenfrequency thanks to the equation:  $K_0 = M_{11} \cdot \omega_0^2$ . Two examples of model fitting are given in figure 3.24. The quality of the identification validates the choices made for the macro-element (RC beam) model. The linear correlations between the parameters are also investigated in table 3.6.

The following observations are made:



(A) Beam RL12-C1B-1



(B) Beam HA12-C1B-1

FIGURE 3.24: Identified IDEFIX model for beams RL12-C1B-1 and HA12-C1B-1

Beam ref.	HA12-C1A-1	HA20-C1A-1	RL12-C1A-1	HA12-C1B-1	HA12-C2-1
$\delta_y$	0.0055657	0.0051689	0.0058049	0.0064412	0.0063264
$K$	1763041.8	1765621.09	1889380.99	1883195.13	1889518.99
$p$	0.24219	0.20309	0.18351	0.22765	0.2247
$q$	0.33635	0.31956	0.31253	0.42574	0.40751
$a^\pi$	1156.8729	1341.8764	1640.9566	1480.2864	1525.9361
$b^\pi$	86707.9148	77966.2571	159828.299	74698.0178	61267.6276
$U_c$	0.059838	0.054382	0.075859	0.054224	0.052052
$\xi$	2.56%	2.64%	2.75%	2.54%	2.18%

TABLE 3.5: IDEFIX identification results during QSC1 tests

	$\delta_y$	$K$	$p$	$q$	$a^\pi$	$b^\pi$	$U_c$	$\xi$
$\delta_y$	1	0.836	0.284	0.880	0.516	-0.204	-0.195	-0.560
$K$	0.836	1	-0.278	0.542	0.894	0.241	0.215	-0.285
$p$	0.284	-0.278	1	0.543	-0.668	-0.733	-0.652	-0.543
$q$	0.880	0.542	0.543	1	0.201	-0.626	-0.627	-0.701
$a^\pi$	0.516	0.894	-0.668	0.201	1	0.454	0.391	-0.028
$b^\pi$	-0.204	0.241	-0.733	-0.626	0.454	1	0.992	0.712
$U_c$	-0.195	0.215	-0.652	-0.627	0.391	0.992	1	0.673
$\xi$	-0.560	-0.285	-0.543	-0.701	-0.028	0.712	0.673	1

TABLE 3.6: Correlation between IDEFIX parameters identification HA20-C1A-1 during QSC1 test

- the beams HA12-C1B-1 and H12-C2-1 show slightly better performances, i.e. they have a higher elastic limit and the parameter  $a^\pi$  which drives the width of the hysteresis loops is more important;
- it is difficult to identify the tested beam only from the identified parameters;
- the parameters generally exhibit a light to moderate correlation between each other (i.e. between 0.2 and 0.75), but the couples  $(K, \delta_y)$ ,  $(\delta_y, q)$  and  $(a^\pi, K)$  have a higher correlation (between 0.8 and 0.9) and  $(U_c, b^\pi)$  are strongly correlated (evaluated at 0.992).

### 3.3 Numerical experimentation campaign

#### 3.3.1 Forewords

When practical constraints (for example related to the schedule, the cost, or the available equipment) make impossible to investigate experimentally the influence of different parameters on a quantity of interest, e.g. the dissipated energy or the EVDR, numerical experimentation represents an elegant way to address the problem, under the condition

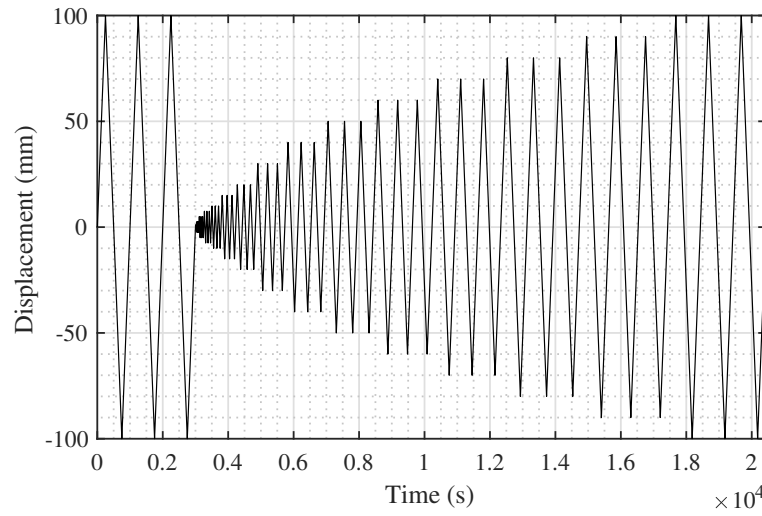


FIGURE 3.25: Loading procedure for the model's parameters sensitivity study (here for a ductility level  $\mu = 14.6$ )

that the numerical model used has been validated experimentally. Considering the ability of the model identified in section 3.2.5 to represent the phenomena taking place during the bending, it can be used as support of virtual quasi-static testing. A focus is made in this section on beam HA20-C1A-1 as an example.

### 3.3.2 Equivalent viscous damping ratio evaluation using Jacobsen's method

Once the thermodynamic model presented in section 3.2.4 is identified, it is possible to compare the EVDR obtained from different methods. One advantage of a virtual experimental study is to avoid spurious dissipation due to external sources. Hence, the validity of the representation of hysteretic dissipation by an equivalent viscous damper is assessed.

To assess the influence of the different model's parameters and of the prescribed displacement, an increasing cyclic quasi-static displacement loading has been designed and is displayed on figure 3.25. Each cycle is repeated three times so the hysteretic behavior in the 2<sup>nd</sup> and 3<sup>rd</sup> cycle can be considered as stabilized and the energy dissipation due to damage initiation is not taken into account. It is important to note that the first three cycles are equal to the last three in order to remain at the same ductility level  $\mu$  of the beam all along the loading. The definition of this ductility level is shown in equation (3.102), where  $\delta_m$  is the maximum displacement in the time-history analysis and  $\delta_y$  is the elastic limit displacement.

$$\mu = \frac{\delta_m}{\delta_y} \quad (3.102)$$

The dependency of the EVDR on the ductility level  $\mu$  is first addressed with a set of parameters identified for the beam HA20-C1A-1 in section 3.2.5 and given in table 3.5.

With the identified set of parameters (line with filled black squares in figures 3.29a to 3.30c), the EVDR exhibits a strong dependency on the displacement amplitude. Starting from zero, it reaches a maximum and then decreases again asymptotically to zero (more or less quickly depending on the model parameters).

The influence of the constitutive model parameters is then studied considering a constant ductility level of  $\mu = 14.6$ .

### 3.3.2.1 Influence of the ductility level $\mu$

The model including damage mechanisms, the maximum elastic energy storage decreases with the ductility level (figure 3.26c). The other important observation is that the energy dissipated does not seem to depend on the ductility level of structures for the present nonlinear model. However, since the equivalent viscous damping ratio depends on the ratio of the dissipated energy over the stored one, the EVDR seems to increase with respect to the ductility level (see figure 3.26a).

### 3.3.2.2 Influence of the hysteresis loops width $a^\pi$ and slope $b^\pi$

The hysteresis loops width, driven by  $a^\pi$ , does not influence significantly the stored energy but highly modifies the dissipated energy per cycle  $E_d$ . When the cycles have a lower amplitude, there is an inversion of dependency between  $E_d$  and  $a^\pi$  because of the kinematic hardening, which explains that the EVDR is higher at low cycle displacements for lower  $a^\pi$  values in figure 3.27a.

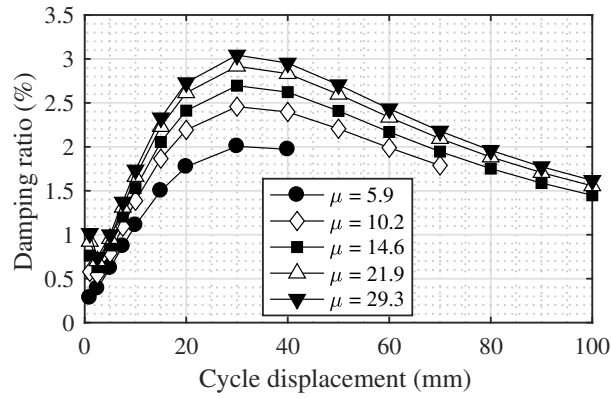
Regarding the dissipated energy per cycle  $E_d$ , the influence of the slope of the hysteresis loops  $b^\pi$  fades out progressively as the latter increases. However, a lower value of  $b^\pi$  can make a major difference due to a drop of energy dissipation (see figure 3.28b).

### 3.3.2.3 Influence of the closure displacement $U_c$

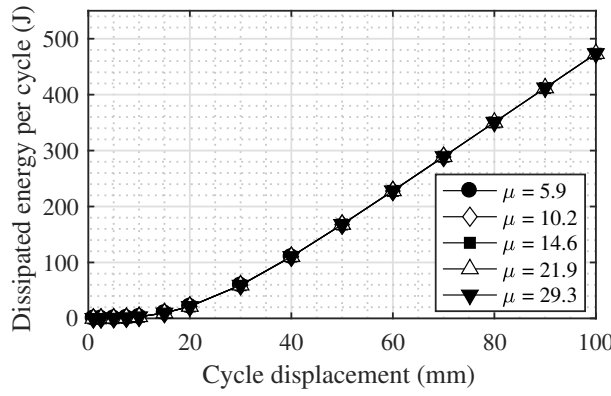
The pinching displacement  $U_c$  defines the domain where the stiffness is influenced by a pinching effect. As plotted on figure 3.29a, the equivalent viscous damping ratio is proportional to the value of  $U_c$ . Regarding the energies involved, the dissipated energy does not depend on this parameter while the stored energy decreased when  $U_c$  increases. This means that the widest the pinching effect is, the less elastic energy can be stored. In agreement with the hypothesis formulated in section 3.2.4.2 regarding the origin of the pinching, this would mean that, for a given constant ductility level  $\mu$ , the more the residual cracks are opened (*i.e.* when no loading is applied), the more prescribed displacement it takes to store the same amount of elastic energy.

### 3.3.2.4 Influence of the fragility coefficient $q$

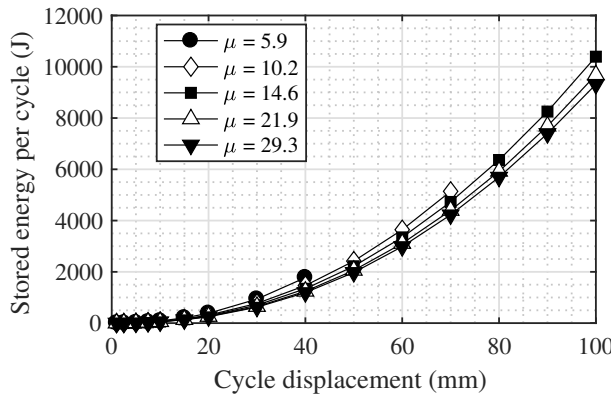
Finally, the fragility coefficient has almost no effect on the dissipated energy per cycle, but tends to lower the stored energy. Thus, the equivalent viscous damping ratio increases with the fragility coefficient (see figures 3.30a, 3.30b and 3.30c).



(A) Influence of the cycle amplitude on the equivalent viscous damping  $\xi_{eq}$  ratio for different ductility levels  $\mu$



(B) Influence of the cycle amplitude on the dissipated energy  $E_d$  per cycle for different ductility levels  $\mu$



(C) Influence of the cycle amplitude on the stored energy per cycle  $E_s$  for different ductility levels  $\mu$

FIGURE 3.26: Influence of the ductility level  $\mu$  over energies and equivalent viscous damping ratio  $\xi_{eq}$  for different cycle amplitudes obtained by Jacobsen's areas method

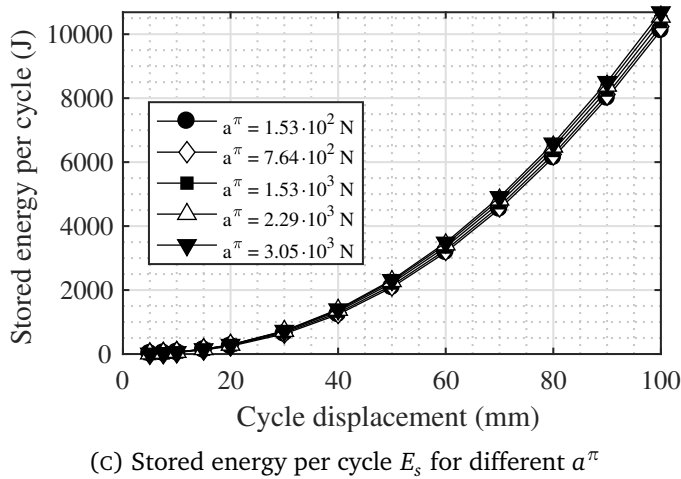
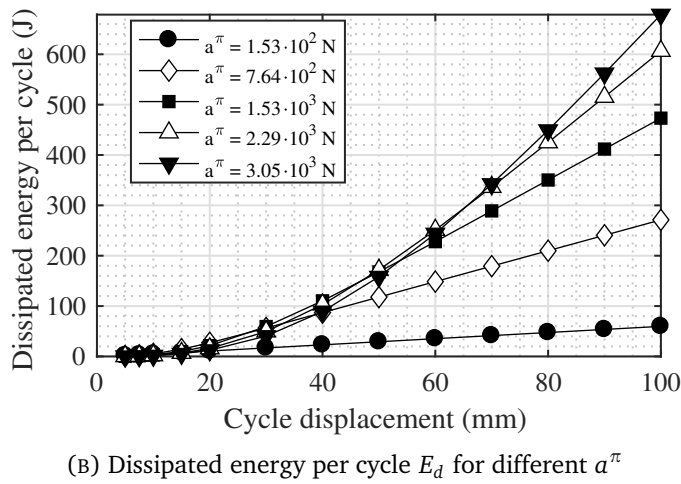
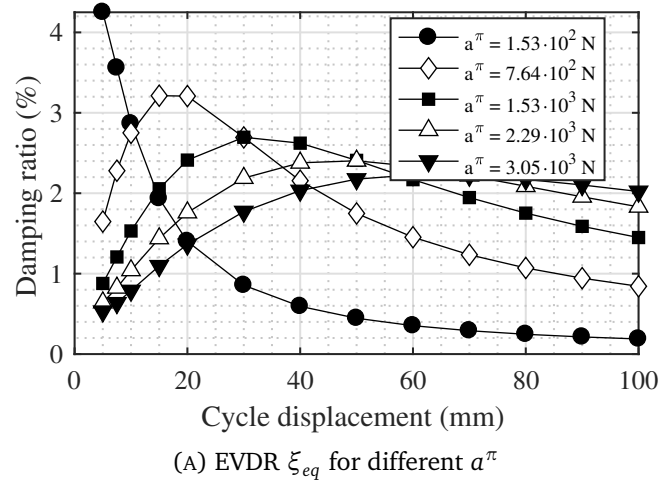
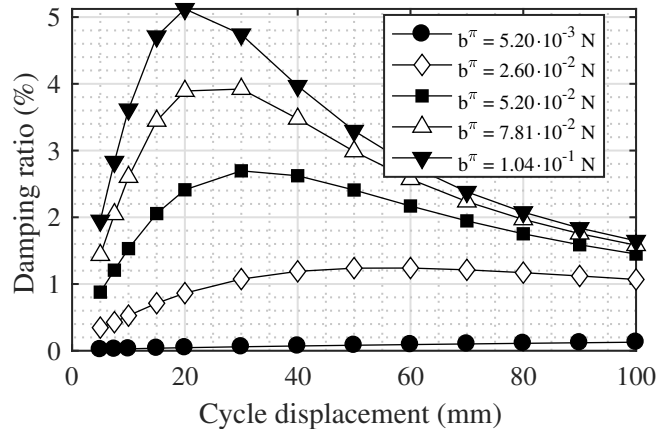
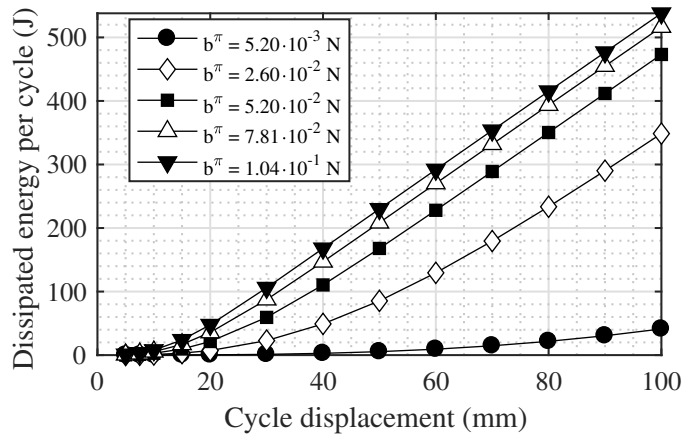


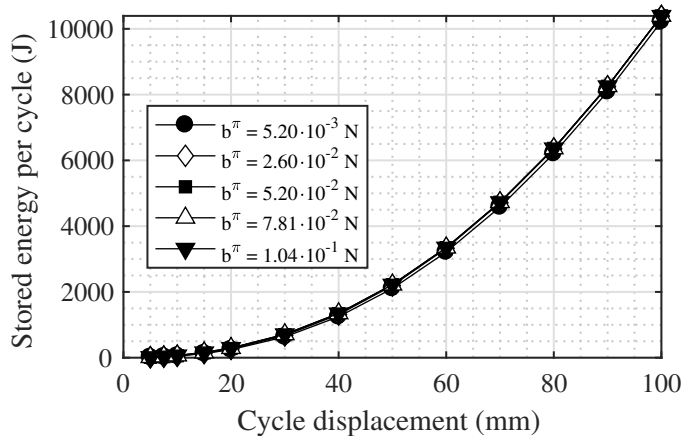
FIGURE 3.27: Influence of the hysteresis loops width  $a^\pi$  and loops slope  $b^\pi$  over energies and equivalent viscous damping ratio  $\xi_{eq}$  for different cycle amplitudes obtained by Jacobsen's areas method



(A) EVDR  $\xi_{eq}$  for different  $b^\pi$

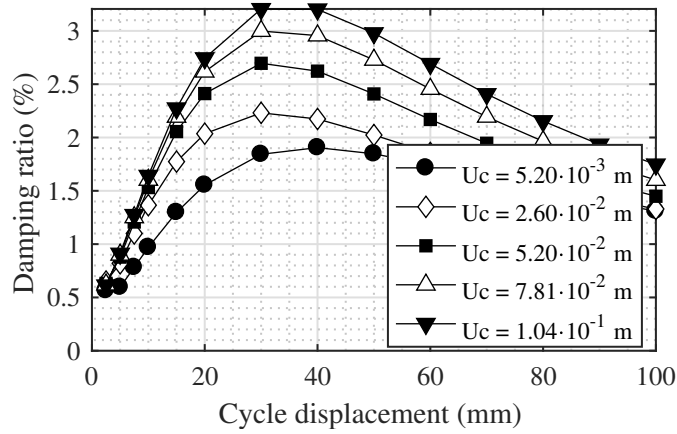


(B) Dissipated energy per cycle  $E_d$  for different  $b^\pi$

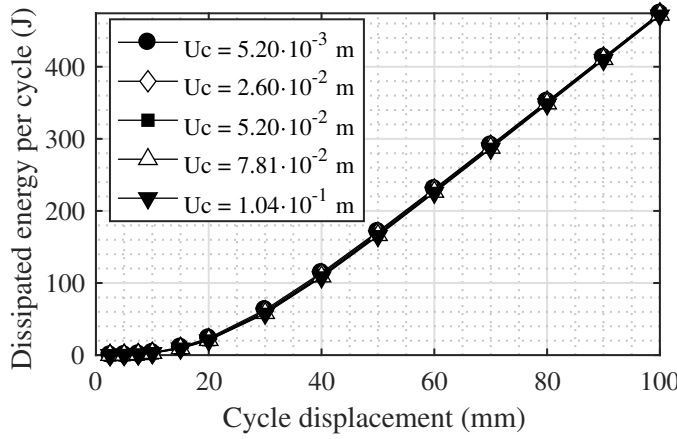


(C) Stored energy per cycle  $E_s$  for different  $b^\pi$

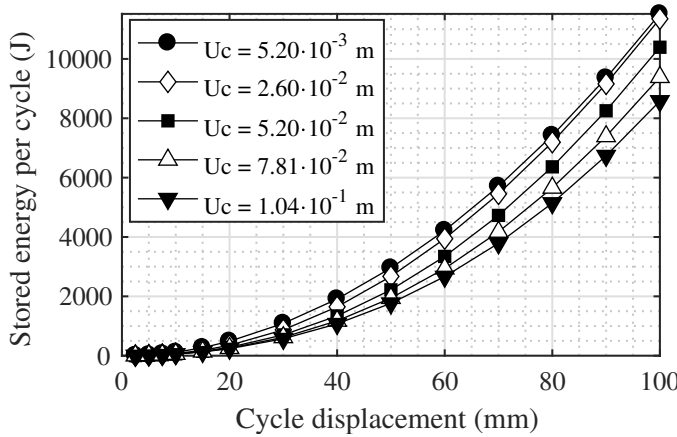
FIGURE 3.28: Influence of the hysteresis loops width  $a^\pi$  and loops slope  $b^\pi$  over energies and equivalent viscous damping ratio  $\xi_{eq}$  for different cycle amplitudes obtained by Jacobsen's areas method



(A) Equivalent viscous damping ratio  $\xi_{eq}$  evaluated by areas method for different  $U_c$

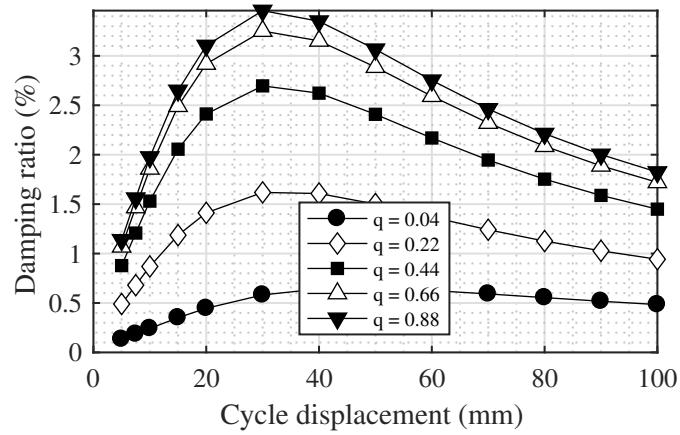


(B) Dissipated energy per cycle  $E_d$  for different  $U_c$

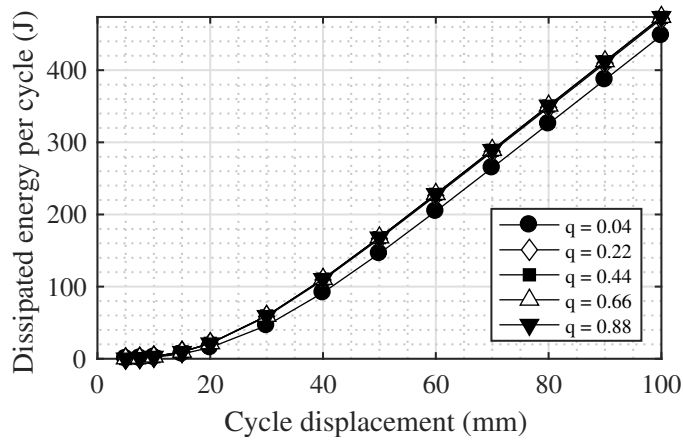


(C) Stored energy per cycle  $E_s$  for different  $U_c$

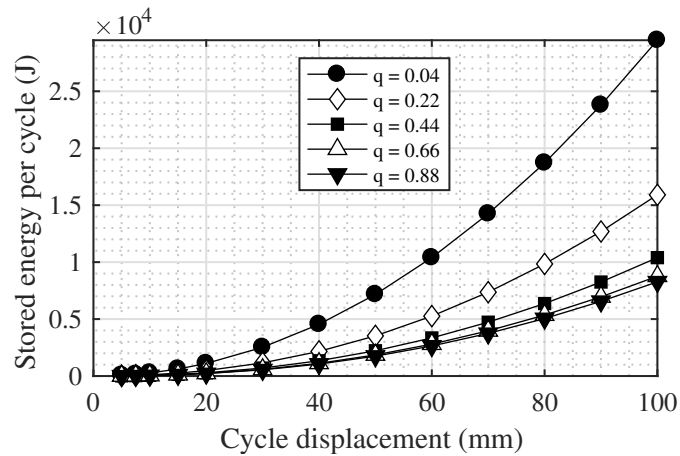
FIGURE 3.29: Influence of the closure displacement  $U_c$  and the fragility coefficient  $q$  over energies and equivalent viscous damping ratio  $\xi_{eq}$  for different cycle amplitudes obtained by Jacobsen's areas method



(A) Equivalent viscous damping ratio  $\xi_{eq}$  evaluated by areas method for different  $q$



(B) Dissipated energy per cycle  $E_d$  for different  $q$



(C) Stored energy per cycle  $E_s$  for different  $q$

FIGURE 3.30: Influence of the closure displacement  $U_c$  and the fragility coefficient  $q$  over energies and equivalent viscous damping ratio  $\xi_{eq}$  for different cycle amplitudes obtained by Jacobsen's areas method

### 3.3.3 Equivalent viscous damping ratio evaluation using logarithmic decrement method

#### 3.3.3.1 Loading procedure

A list of displacement levels  $u_{1 \leq i \leq N}$  is arbitrarily defined. The loading and post-process are performed as follows:

1. a quasi-static cyclic displacement  $u_{1 \leq i \leq N}$  is prescribed to the oscillator in order to make it reach a given ductility level  $\mu$ ;
2. an initial displacement  $u_i$  is prescribed to the beam;
3. the beam is released from the initial displacement value and its free vibrations are simulated by a Newmark implicit algorithm (more details in section 4.2.1) to assess nonlinearities associated to the hysteretic model;
4. the logarithmic decrement method is applied between each consecutive maxima of displacement (see section 1.3.2);
5. perform steps 1 to 4 for all  $i$  between 1 and  $N$ .

#### 3.3.3.2 Comparison with Jacobsen's area method conducted in dynamics

From the different ductility levels, an EVDR is associated to a cycle amplitude of displacement and to a given period (deduced from a measured pseudo-period estimated *via* the time between the two consecutive maxima and the corresponding EVDR). The data obtained are plotted on figures 3.31 to 3.32b. The dependence of the period on the cycle amplitude seen on figure 3.32a is directly due to the pinching effect: the beam stiffness reduction in the neighborhood of the zero-displacement point (i.e. when the cycle amplitude is lower than the closure displacement  $U_c$ ) is accompanied by a period increase. As shown by quasi-static tests using Jacobsen's areas method, the EVDR increases with the ductility level  $\mu$ .

The value of the amplitude of displacement progressively decreases in free vibrations regime because of the energy dissipation. For each pseudo-cycle, the 1<sup>st</sup> maximum of displacement is considered to define the amplitude. Alternatively, the 2<sup>nd</sup> maximum or the mean of the two maxima could have been chosen.

The values obtained for the same ductility level  $\mu = 14.6$  for both QSC1 by JAM and the present free vibrations test by the LDM are in good agreement as depicted in figure 3.33. It can be argued that the areas method gives higher estimates of the EVDR than logarithmic decrement, however, the relative difference remains reasonable at the maximum damping ratio (+3 % of relative difference) and also in mean on the studied cycle amplitude range (+10 % of relative difference).

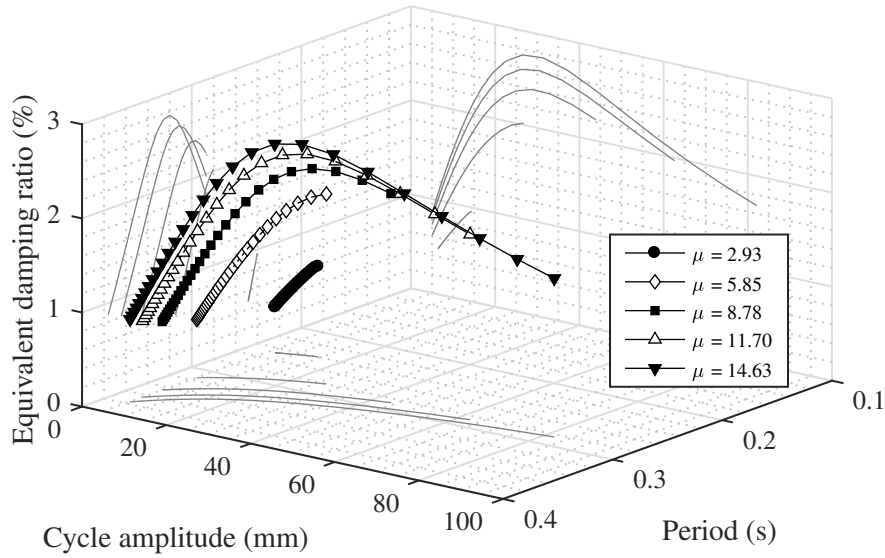


FIGURE 3.31: Equivalent viscous damping ratio *versus* cycle amplitude and measured cycle period for several ductility levels  $\mu$

### 3.3.4 Further investigation on the influence of the ductility level and the displacement amplitude on the EVDR

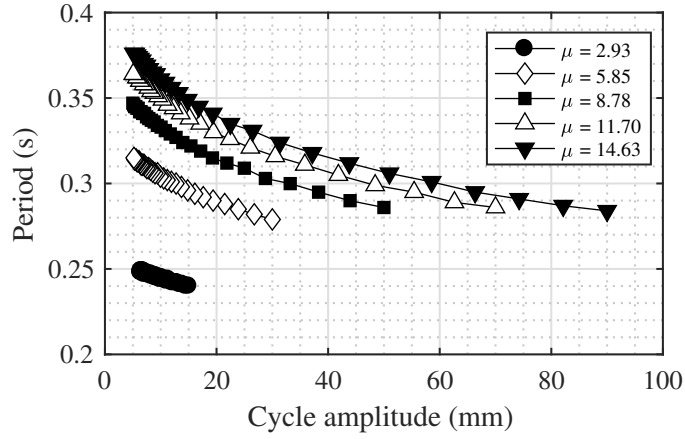
It is clear from the results given in section 3.3 that the ductility level  $\mu$  and the displacement amplitude play a major role in the EVDR. Moreover, these two parameters are model-independent (considering that the displacement ductility level simply indicates the 1<sup>st</sup> nonlinearity, whatever it is). Therefore, further investigation is necessary since the ductility and the displacement amplitude are unilaterally related: the maximum displacement amplitude seen during the NLTHA sets the value of the ductility coefficient  $\mu$ , not the other way around. Following the same numerical loading procedure as in section 3.3.2, it is possible to plot a cloud of points of EVDR depending on both  $\mu$  and displacement amplitude  $\delta$  as on the red dots on figure 3.34.

Then, the highest EVDR point is chosen as the “identification” point of coordinates  $(\mu_{id}, \delta_{id}, \xi_{id})$  for the next steps:

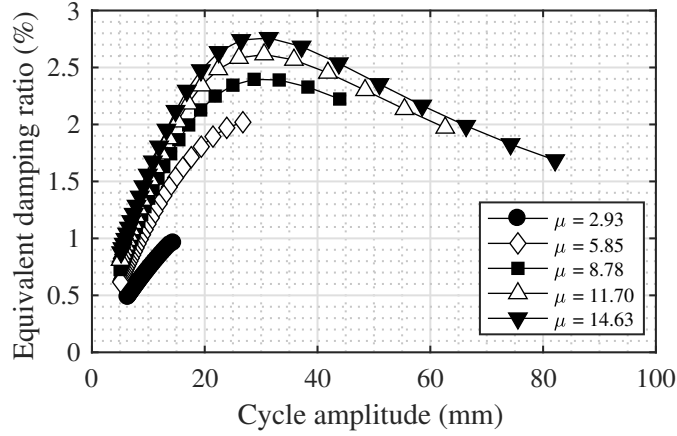
- $\mu = \mu_{id}$  is fixed at this point, and the best-fitting function  $g(\delta)$  is identified;
- $\delta = \delta_{id}$  is fixed at this point, and the best-fitting function  $f(\mu)$  is identified;
- the surface given by equation  $\xi = \alpha \cdot f(\mu) \cdot g(\delta)$  where  $\alpha = \frac{1}{\xi_{id}}$  is a normalization coefficient.

The surface obtained is plotted on figure 3.34, and the so-called “damping surface” fits very well the numerical experiments. The two identified independent functions in the particular case of the numerical experiments carried out on IDEFIX SDOF model identified from QSC1 tests on beam HA20-C1A-1 are:

$$f(\mu) = \frac{0.0479 \cdot \mu + 0.0916}{\mu + 13.9} = \begin{cases} 0.661 \% & \text{if } \mu = 0 \\ 4.79 \% & \text{if } \mu \rightarrow +\infty \end{cases} \quad (3.103)$$



(A) Period versus cycle amplitude (projection of figure 3.31)



(B) Damping ratio versus cycle amplitude (projection of figure 3.31)

FIGURE 3.32: Influence of cycle amplitude, period and ductility level on the equivalent viscous damping ratio evaluated by the logarithmic decrement method

and:

$$g(\delta) = \frac{0.00131 \cdot \delta + 1.67 \cdot 10^{-6}}{\delta^2 - 0.0126 \cdot \delta + 0.000574} = \begin{cases} 0.290 \% & \text{if } \delta = 0 \\ 0 \% & \text{if } \delta \rightarrow +\infty \end{cases} \quad (3.104)$$

where  $\delta$  is in millimeters. The search for an equation of surface in the form of a product of rational functions is motivated by the form of the expression of the EVDR evaluated by JAM as a ratio between two energies, themselves being polynomial functions of  $\mu$  and  $\delta$ . Finally, the expression for the damping surface of the model identified for beam HA20-C1A-1 is:

$$\xi(\mu, \delta) = \underbrace{\frac{1}{0.0391}}_{\alpha} \cdot \underbrace{\frac{0.0479 \cdot \mu + 0.0916}{\mu + 13.9}}_{f(\mu)} \cdot \underbrace{\frac{0.00131 \cdot \delta + 1.67 \cdot 10^{-6}}{\delta^2 - 0.0126 \cdot \delta + 0.000574}}_{g(\delta)} \quad (3.105)$$

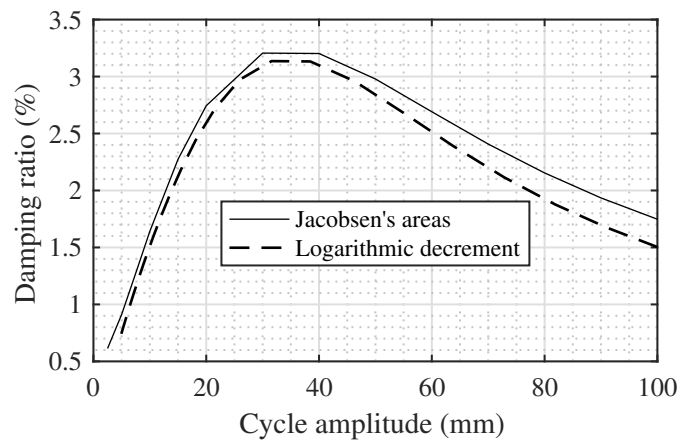


FIGURE 3.33: Comparison of the equivalent viscous damping ratio values obtained by Jacobsen's area method in quasistatic and the logarithmic decrement method in dynamics

### 3.4 Hammer shock tests

As explained in section 1.3.3.1, the Fourier's transform of the hammer excitation is not flat and its content depends particularly on the hammer tip (which should be adapted to the material of the structure) and to the operator expertise (orientation, force, duration of the shock, etc.). To keep the same experimental conditions, the same operator has performed all the 344 hammer shocks that are treated in this section.

Several possibilities exist to get the FRF of the beam. In fact, there is not only one FRF: this depends on input and output locations. To measure the damping on a vibration mode, a favorable signal/noise ratio is preferred. The noise is partially related to the measurement devices but can be reduced by doing several shocks. The signal level can be increased by exciting efficiently the considered vibration mode, and by using a sensor device (an accelerometer in this case) closer to the shock. Because of their symmetry with respect to the middle of the beam, vibration modes 1 and 3 are excited by hitting the beam at the mid-span position associated to accelerometer *axp5* (see figure 3.35). In this case, the 2<sup>nd</sup> vibration mode, which is anti-symmetric, is theoretically not excited because of its zero value for the mode shape at mid-span. On the contrary, to excite the 2<sup>nd</sup> vibration mode, a shock is performed at the quarter-span position since it is where the associated modal displacement is maximal. It will also activate the symmetric modes, but less than shocks at mid-span.

The layout of accelerometers allows for the evaluation of the FRF at different locations for a single hammer shock. Thus, figure 3.36 has been plotted after hammer shocks are performed at *axp3* *before* and *after* QSC1 test. The FRF surface is convenient to visualize the mode shapes (in absolute value) depending on the frequency. The decreasing of the eigenfrequencies and the appearance of new vibration eigenmodes of higher frequencies is observed. Nevertheless, even at the damaged state, the fourth eigenfrequency is above 40 Hz and is out of the excitation range of the shaking table.

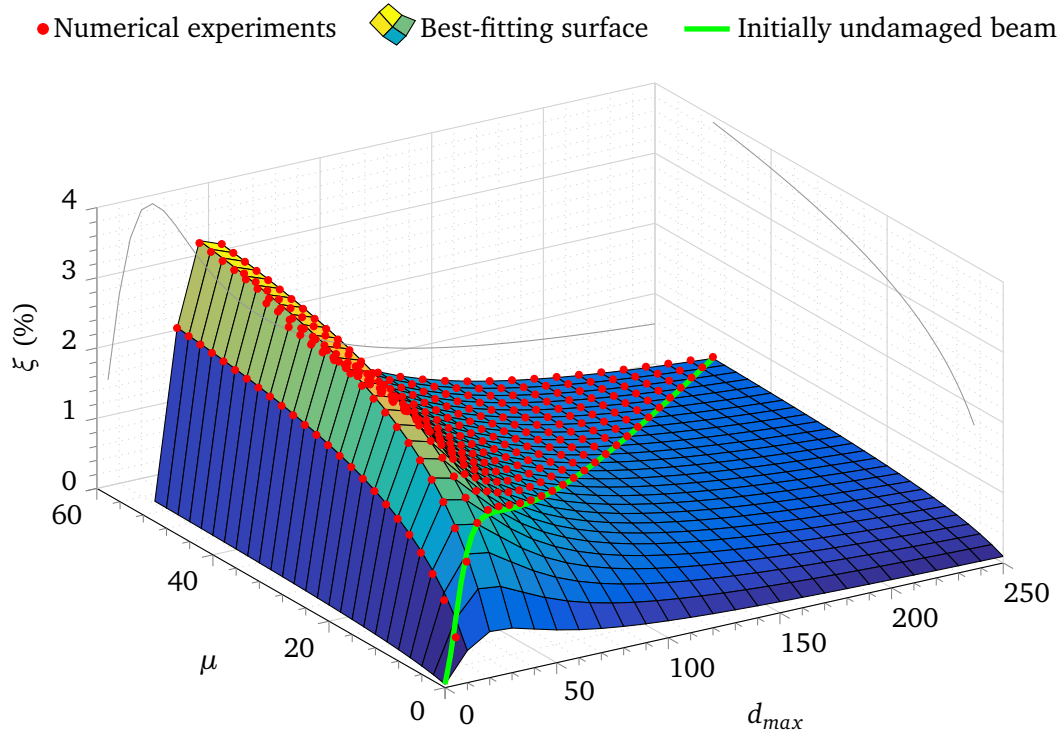


FIGURE 3.34: EVDR surface as a function of displacement amplitude and ductility level

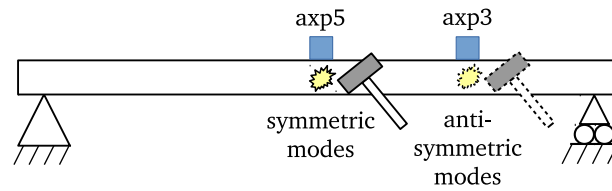


FIGURE 3.35: Hammer shocks layout to measure modal damping ratios depending on the vibration mode considered

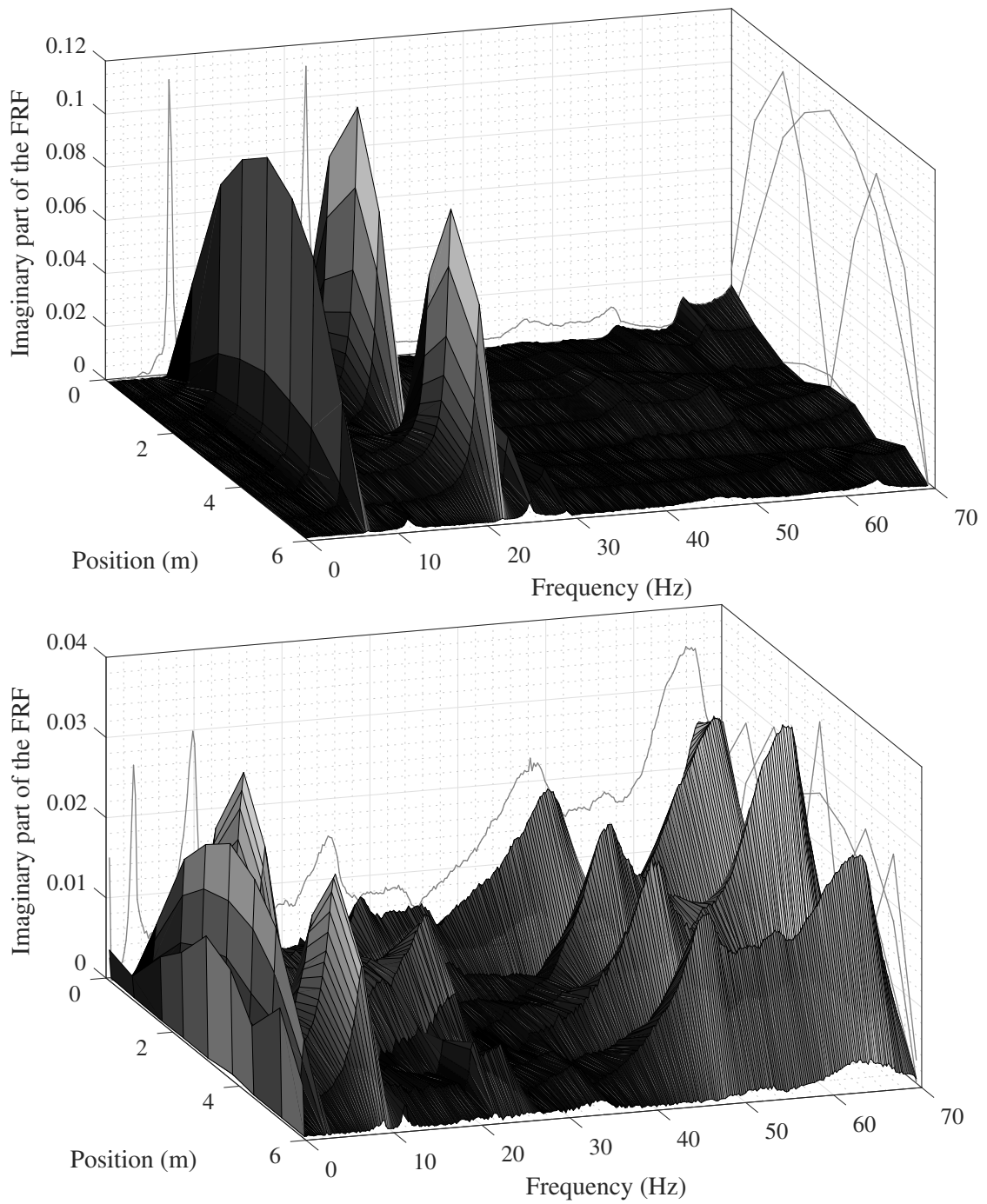


FIGURE 3.36: FRF surfaces obtained by a shock at *axp3* location for beam HA12-C1B-1 *before* and *after* QSC1 test

Beam type	Theoretical			Experimental <sup>1</sup>		
	Mode 1	Mode 2	Mode 3	Mode 1	Mode 2	Mode 3
RL12-C1B	7.20	24.5	70.6	7.13 <sup>-0.97 %</sup>	22.5 <sup>-8.2 %</sup>	58.9 <sup>-16.6 %</sup>
HA12-C1B	7.21	24.5	70.7	6.81 <sup>-5.55 %</sup>	21.5 <sup>-12.2 %</sup>	57.2 <sup>-19.1 %</sup>
HA12-C2	7.22	24.5	70.8	6.84 <sup>-5.26 %</sup>	22.0 <sup>-10.2 %</sup>	57.7 <sup>-18.5 %</sup>
HA12-C1A	6.97	23.7	68.4	7.14 <sup>+2.44 %</sup>	22.5 <sup>-5.06 %</sup>	57.8 <sup>-15.5 %</sup>
HA16-C1A	7.04	23.9	68.9	7.11 <sup>+0.99 %</sup>	23.1 <sup>-3.35 %</sup>	58.2 <sup>-15.5 %</sup>
HA20-C1A	6.99	23.7	68.6	7.16 <sup>+2.43 %</sup>	22.6 <sup>-4.64 %</sup>	57.6 <sup>-16.0 %</sup>

<sup>1</sup> Superscripts are the relative difference between the experimental and the theoretical eigenfrequency.

TABLE 3.7: Comparison between experimental and theoretical eigenfrequencies

The experimental eigenfrequencies are compared in table 3.7 with the theoretical ones obtained as described in section 3.1.2.2 considering an eigenbasis of dimension 3.

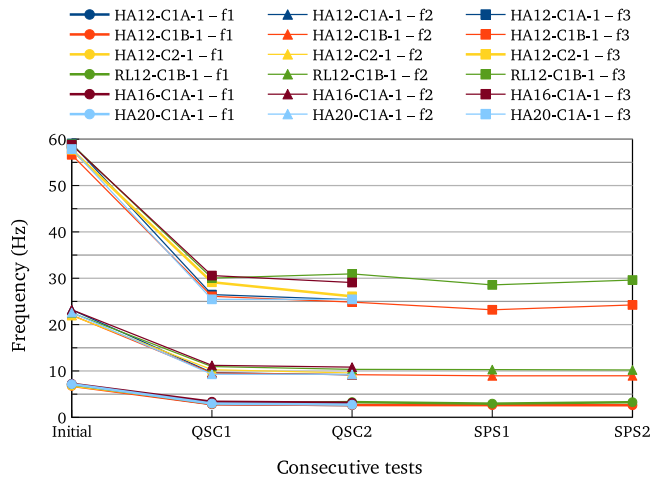
At first, only the loading procedures in the following order are compared: initial, QSC1, QSC2, SPS1, SPS2. The modal frequencies and damping ratios measured with hammer shock tests are given in figures 3.37 and 3.38. Regarding the frequency data, they are all decreasing monotonically along the successive tests (except for the 3<sup>rd</sup> mode of RL12-C1B-1 after test QSC2, but this is probably due to experimental bias). Most of the frequency drop occurs after QSC1, the next tests do not modify significantly the modal stiffnesses. When considering the normalized frequency drop on figure 3.37b, the results for all the beams and all the three vibration modes are comparable. This means that the modal stiffnesses are affected similarly, at least by the 1<sup>st</sup> mode which is responsible for the main degradation.

The same reasoning is not true for the normalized damping ratio on figure 3.38b. The general tendency is an increase of the damping ratios on the 1<sup>st</sup> and 2<sup>nd</sup> eigenmodes (figures 3.37c and 3.37d), but this is not the case for the 3<sup>rd</sup> modal damping ratio which decreases after test QSC2 (figure 3.37e). Moreover, there is no clear link between the normalized modal frequency and its associated modal damping ratio.

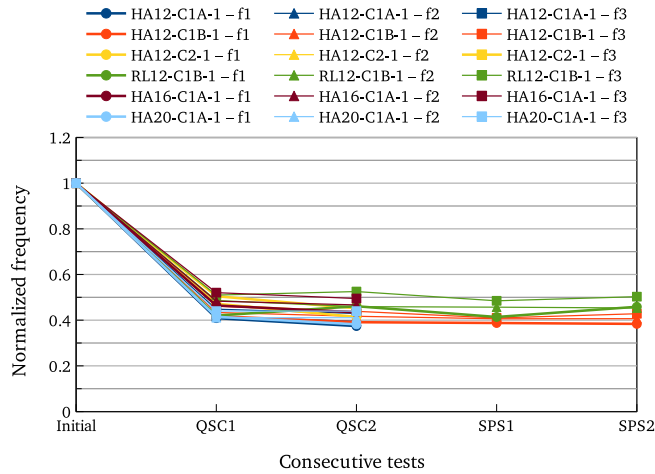
## 3.5 White noise on shaking table

### 3.5.1 General observations

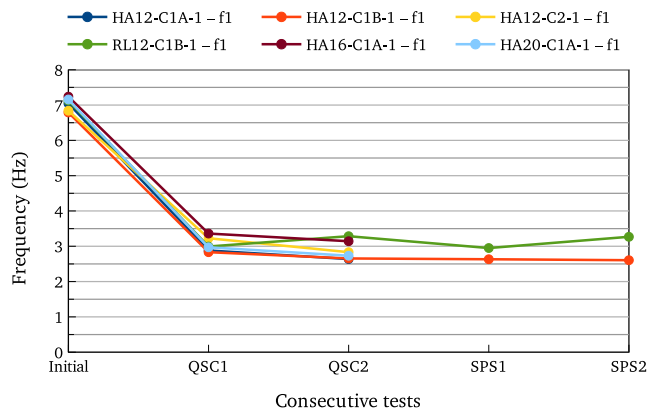
Among the dynamic tests, a focus is made in this section on the white noise signal labeled WN12 sent on *Azalée* shaking table both in x-direction and around yaw-axis. The loading procedure is detailed in table 3.8 in which the so-called historic PGA level refers to the highest peak ground acceleration experienced by the beam in its time-history. Beforehand, the beam is excited by a white noise signal at the reference PGA and then excited by increasing white noise signals for lower PGA (prescribed PGA in x-direction around 0.19 g, 0.20 g, 0.23 g, 0.26 g, 0.31 g, 0.34 g and 0.41 g). The rule given in equation (3.106) is here not strictly followed because of the imperfect online control of the shaking table.



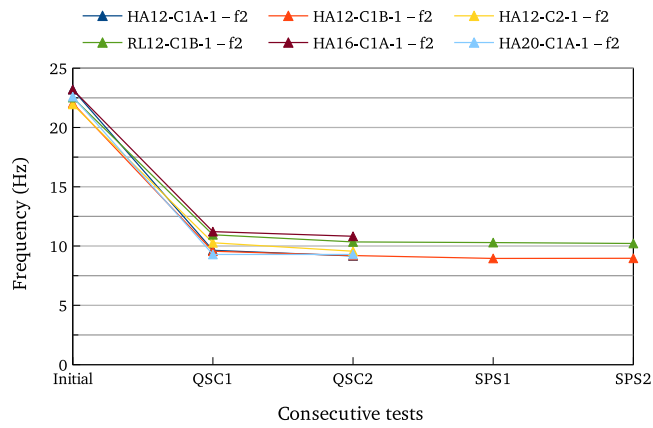
(A) Evolution of the modal frequencies



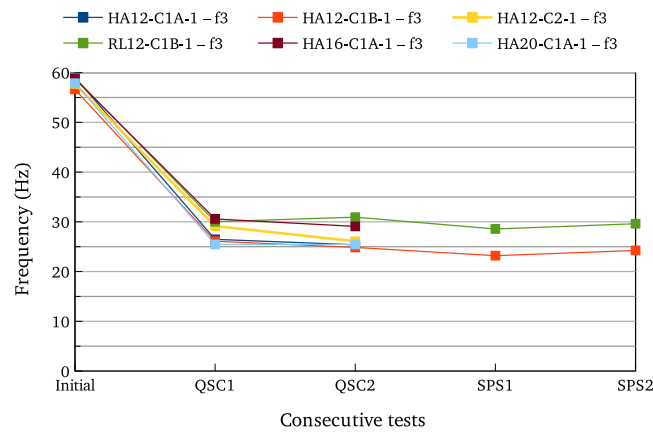
(B) Evolution of the modal frequencies normalized by their respective initial value



(C) Evolution of the 1<sup>st</sup> modal frequencies

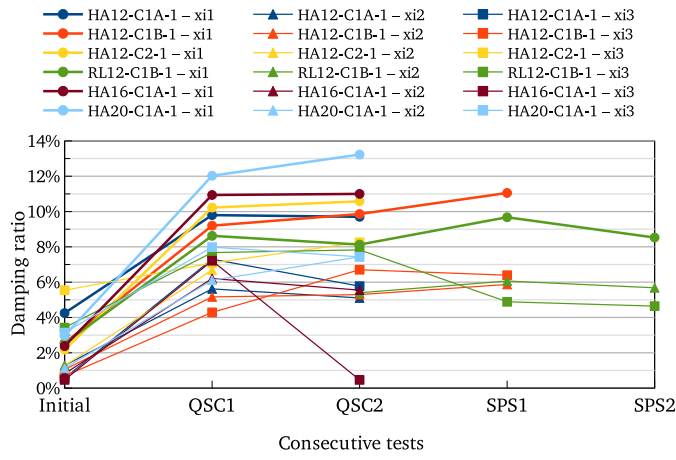


(D) Evolution of the 2<sup>nd</sup> modal frequencies

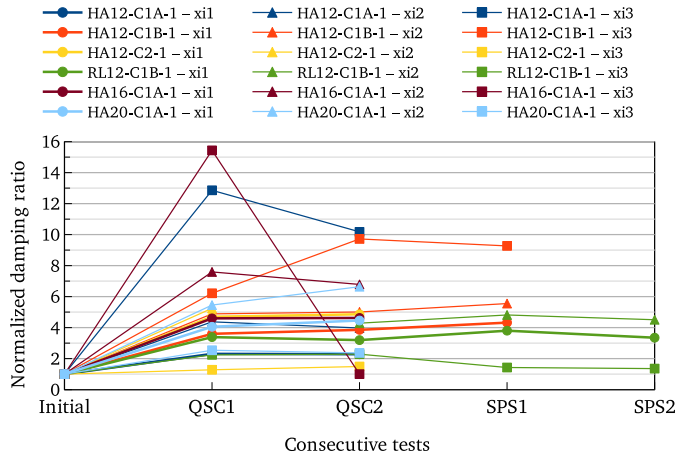


(E) Evolution of the 3<sup>rd</sup> modal frequencies

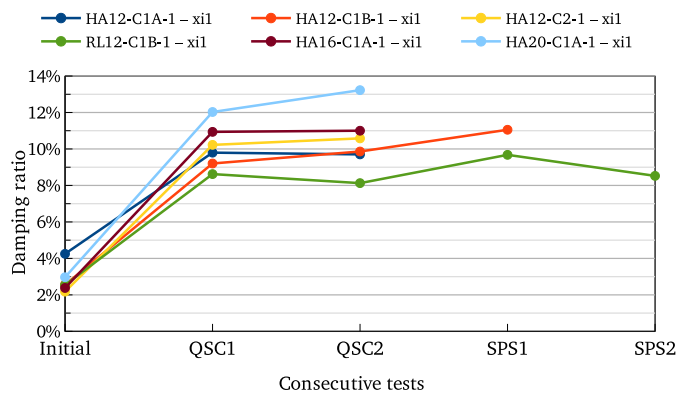
FIGURE 3.37: Evolution of the modal frequencies evaluated during hammer shock tests after consecutive quasi-static tests



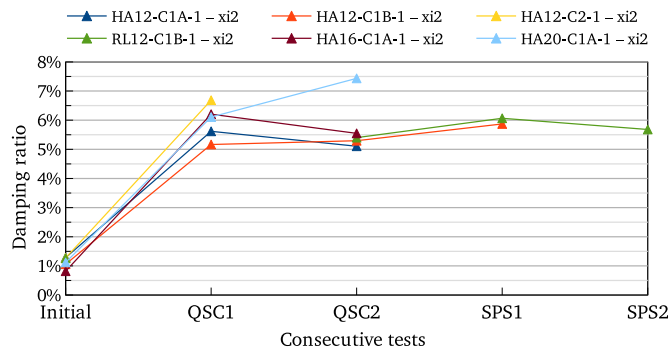
(A) Evolution of all the damping ratios



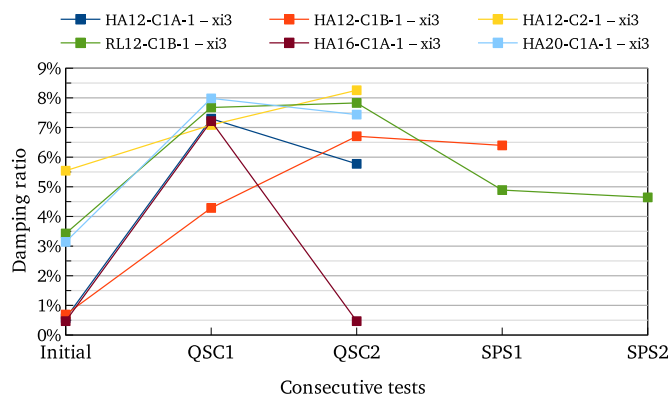
(B) Evolution of all the damping ratios normalized by their respective initial value



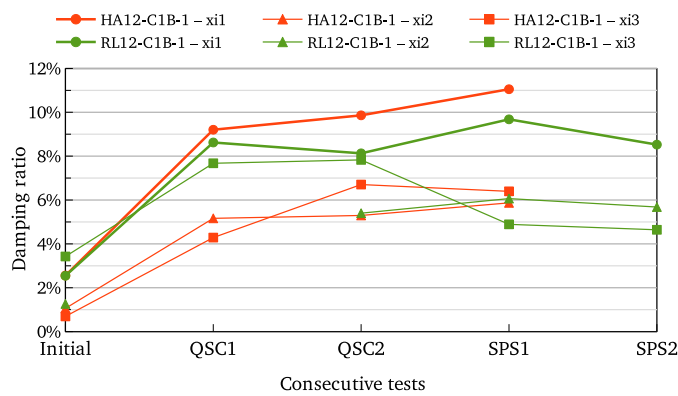
(C) Evolution of the 1<sup>st</sup> modal damping ratios



(D) Evolution of the 2<sup>nd</sup> modal damping ratios



(E) Evolution of the 3<sup>rd</sup> modal damping ratios



(F) Comparison of the evolution of the damping ratios for 2 beams

FIGURE 3.38: Evolution of the damping ratios evaluated by half-bandwidth method during hammer shock tests after consecutive quasi-static tests

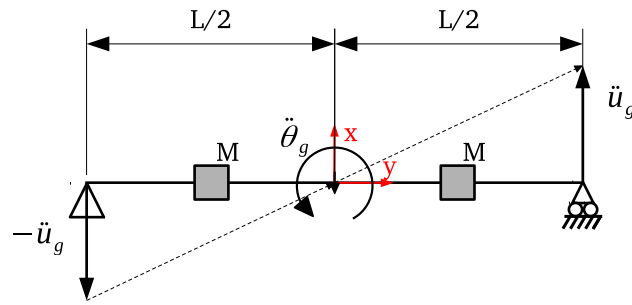


FIGURE 3.39: Equivalence chosen between the shaking table acceleration along x-direction and around z-axis

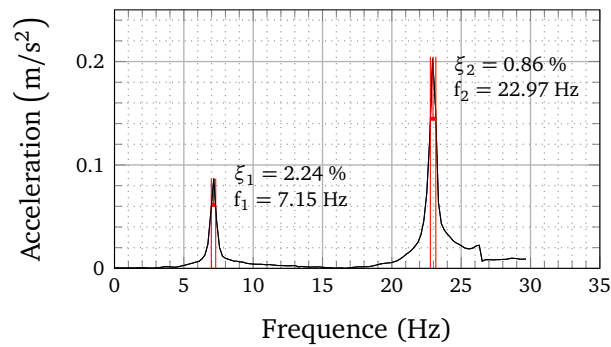


FIGURE 3.40: Half-power bandwidth method applied on hammer shock test performed on beam HA20-C1A-2 prior to WN12

$$\ddot{\theta}_g = \frac{2 \cdot \ddot{u}_g}{L} \quad (3.106)$$

## 3.5.2 Non-parametric identification of WN12 tests

### 3.5.2.1 Forewords

The non-parametric identification process described in section 3.1.4 is applied on the successive white noise tests carried out on beam HA20-C1A-2 and described in sections 2.5.2.1 and 3.5 (see the detailed experimental procedure in table 3.8). A first study is made on the RUN 543, which corresponds to the last WN12 test of the loading procedure. This means that the displacement ductility level is the highest reached during WN12 tests and that it does not evolve during this last test since the damaging test is the RUN 537 previously carried out. The PGA is just below the highest level (0.33 g in x-direction against a maximum of 0.41 g for run 537).

Historic PGA level	1	2	3	4	5	6	7
RUN	516	518	520	523	527	532	538
PGA X (g)	0.17	0.18	0.17	0.18	0.19	0.18	0.27
PGA YAW ( $^{\circ}\cdot s^{-2}$ )	37.8	36.3	35.7	32.8	34.3	33.7	39.3
RUN		517	521	524	528	533	539
PGA X (g)		0.21	0.23	0.22	0.22	0.18	0.18
PGA YAW ( $^{\circ}\cdot s^{-2}$ )		50.9	47.9	48.8	49.4	51.1	52.8
RUN			519	525	529	534	540
PGA X (g)			0.24	0.25	0.28	0.21	0.19
PGA YAW ( $^{\circ}\cdot s^{-2}$ )			64.3	69.9	66.7	62.1	75.7
RUN				522	530	535	541
PGA X (g)				0.25	0.27	0.27	0.24
PGA YAW ( $^{\circ}\cdot s^{-2}$ )				90.8	86.7	83.4	103.4
RUN					526	536	542
PGA X (g)					0.32	0.33	0.28
PGA YAW ( $^{\circ}\cdot s^{-2}$ )					112.3	104.3	120.6
RUN						531	543
PGA X (g)						0.34	0.33
PGA YAW ( $^{\circ}\cdot s^{-2}$ )						122.9	124.6
RUN							537
PGA X (g)							0.41
PGA YAW ( $^{\circ}\cdot s^{-2}$ )							147.1

TABLE 3.8: Loading procedure followed for WN12 tests performed on beam HA20-C1A-2. The first test of the current historic PGA level is the red one. Then, the loading procedure starts from the first row of each column.

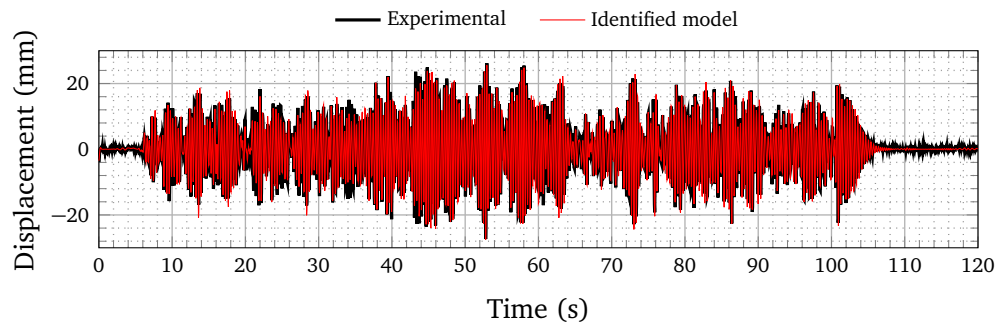
### 3.5.2.2 First vibration mode identification

First, the SDOF oscillator associated to the first vibration mode is considered. The results of the identification are given in figure 3.41. To proceed to the non-parametric identification, a time-window of duration 0.3 s has been chosen, and a maximum relative variation constraint between two successive time-windows of 50 % for the damping ratio and 20 % for the eigenfrequency.

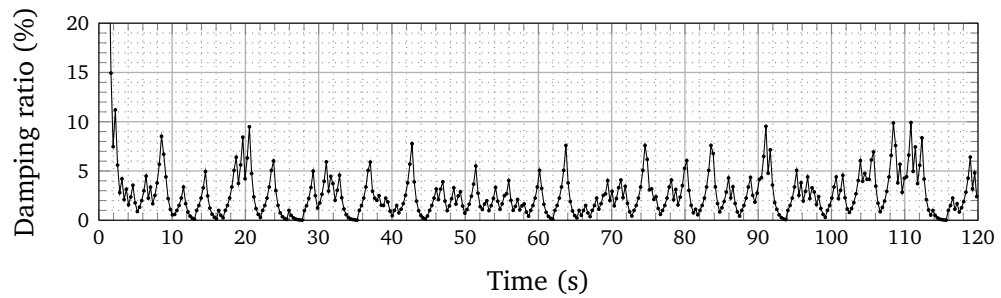
The chosen identification error function is the one given in section 3.1.3. It remains lower than 0.5 when the experimental displacement has an amplitude higher than 10 mm. From the beginning of the signal to 6 s and from 106 s to the end of the signal, an identification error around or beyond 1 indicates that the values identified for the damping ratio and the eigenfrequency are not reliable. This is due to the poor signal/noise ratio in these time domains.

The eigenfrequency is overall constant (figure 3.41c) which confirms that the ductility level does not evolve during this test. The small variations are partially explained by the pinching effect that lowers the stiffness when the displacement amplitude decreases.

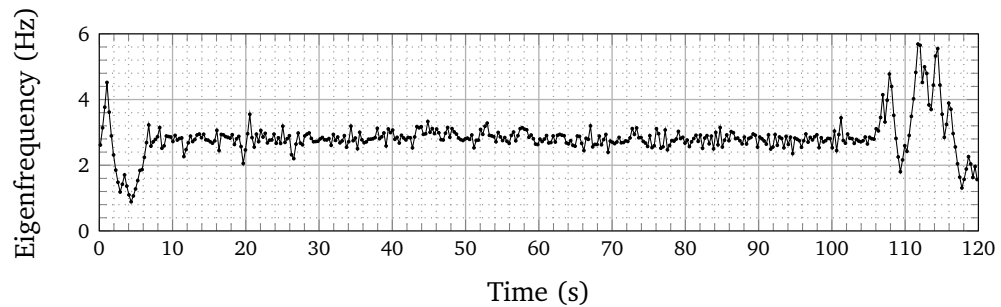
It is also observed that the maxima of damping ratio generally appear when the displacement amplitude is minimal (e.g. at 20 s, 42 s, 64 s or 92 s). This is in agreement with the “damping surface” of figure 3.34 which exhibits a maximum for displacement amplitudes around 25 mm. The same damping surface shows that this effect is exacerbated by a higher displacement ductility level (which is constant here), and the inversion of this effect is expected for the lowest displacement amplitudes.



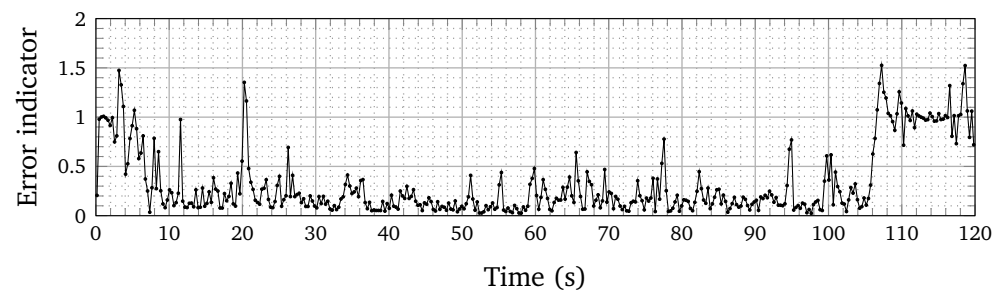
(A) Comparison of the identified model displacement and the experimental displacement



(B) Viscous damping ratio



(C) Eigenfrequency



(D) Identification error

FIGURE 3.41: Non-parametric identification of the viscous damping ratio and the eigenfrequency for WN12 (RUN 543) for the SDOF oscillator associated to the 1<sup>st</sup> vibration mode

### 3.5.2.3 Second vibration mode identification

The SDOF oscillator associated to the 2<sup>nd</sup> vibration mode is now considered. The results of the identification are given in figure 3.42. The time-window duration is shorter (0.2 s) since the eigenfrequency is expected to be higher. Therefore, a shorter duration is sufficient to contain two oscillations. The relative variations of the parameters between two time-windows are still constrained to 50 % for the damping ratio and 20 % for the eigenfrequency.

In this case, the overall behavior of the oscillator seems to reproduce realistically the second vibration mode of the beam on figure 3.42a, but the identification error is higher than for the 1<sup>st</sup> SDOF oscillator (figure 3.41). The first reason for the identification confidence loss is the less favorable signal/noise ratio. The noise corrupting the cameras measurements is the same for both the 1<sup>st</sup> and the 2<sup>nd</sup> projected modal displacements, but the amplitude of the signal is ten times lower for the second mode.

Regarding the eigenfrequency, a constant value slightly higher than 10 Hz arises from the identification. This is in agreement with a standard FRF analysis performed on this white noise test which indicates a second eigenfrequency at 10.6 Hz. Regarding the damping ratio, the identification can be considered as failed since the upper and lower bounds of the research domain are regularly reached.

### 3.5.2.4 Role of the relative variation constraint

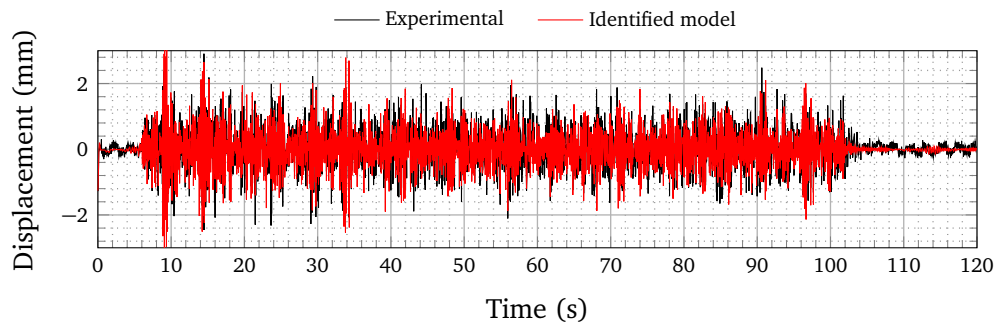
For comparison purposes, the same identification as in section 3.5.2.2 is carried out. The eigenfrequency is still well-identified and is even more stable than the one obtained with the relative variation constraint, but the damping ratio shows a noisy evolution throughout the test. The fact that it often reaches the bounds of the identification domain (i.e. between 0 % and 100 %) indicates the poorer physical relevance of the identified values without the relative variation constraints. Of course, the relevance of the viscous damping model itself is questioned. The looseness of the constraint on the damping ratio gives more stability to the eigenfrequency. This means that the identified eigenfrequency has somehow to compensate the error brought by the impossibility for the damping ratio to reach its optimal value because of the relative variation constraint. Therefore, the identified eigenfrequency values may also be slightly corrupted by the relative variation constraint.

Eventually, a non-parametric identification is arduous in the case of a poor signal/noise ratio. However, the authors cited in section 3.1.4.2 advocate that a parametric identification (e.g. I-DIC) could provide more reliable and physical-wise results in such cases.

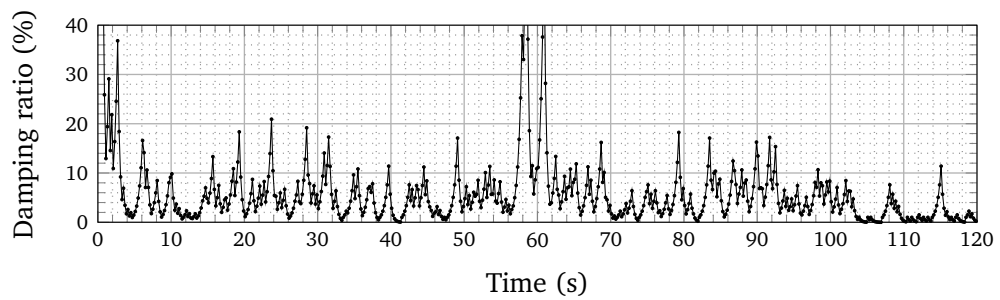
## 3.6 Decreasing sinus sweep on shaking table

### 3.6.1 Non-parametric identification of DSS52 tests

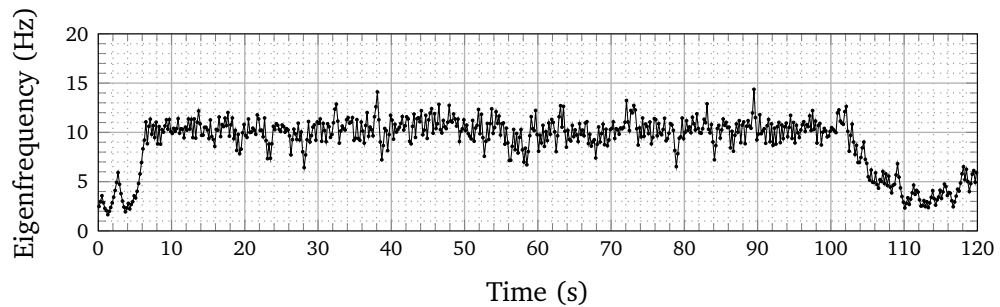
The test used as support of the identification in this case is DSS52 described in section 2.5.2.3 and performed on the beam HA16-C1A-2. The RUNs 423 to 434 have been



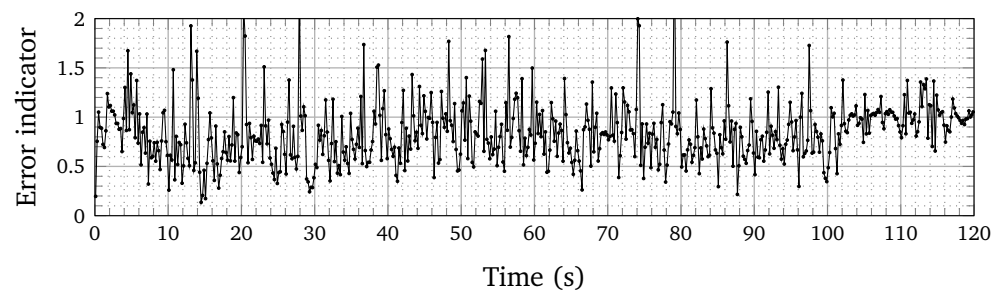
(A) Comparison of the identified model displacement and the experimental displacement



(B) Viscous damping ratio

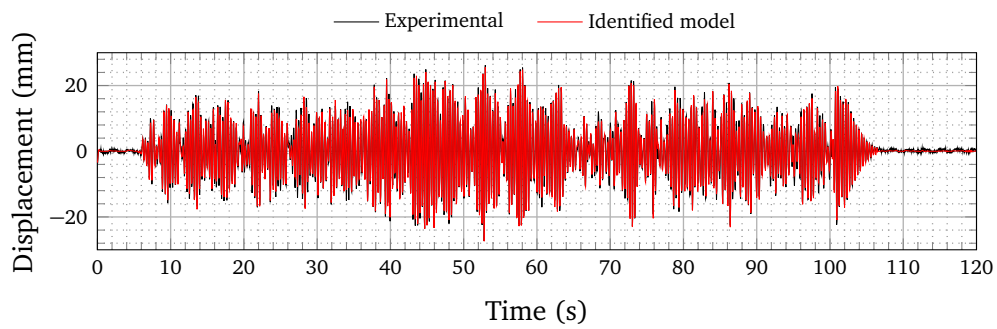


(C) Eigenfrequency

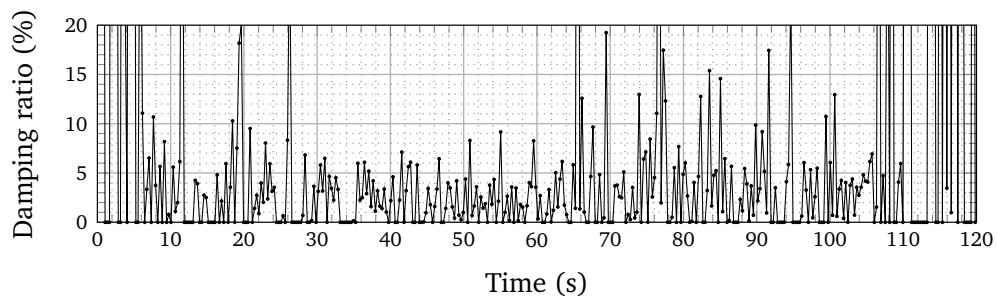


(D) Identification error

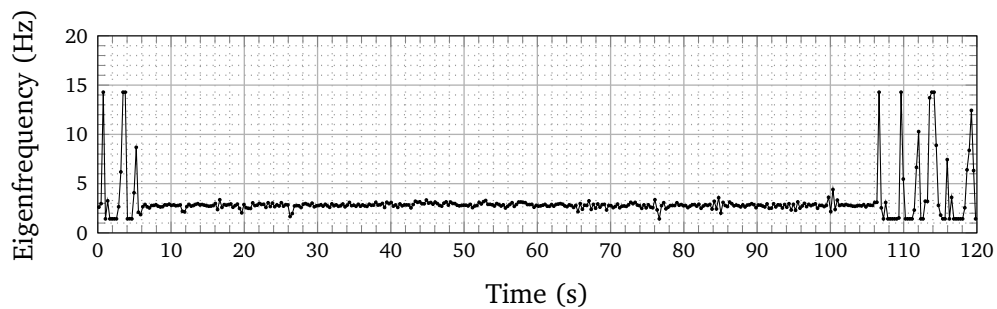
FIGURE 3.42: Non-parametric identification of the viscous damping ratio and the eigenfrequency for WN12 (RUN 543) for the SDOF oscillator associated to the 2<sup>nd</sup> vibration mode



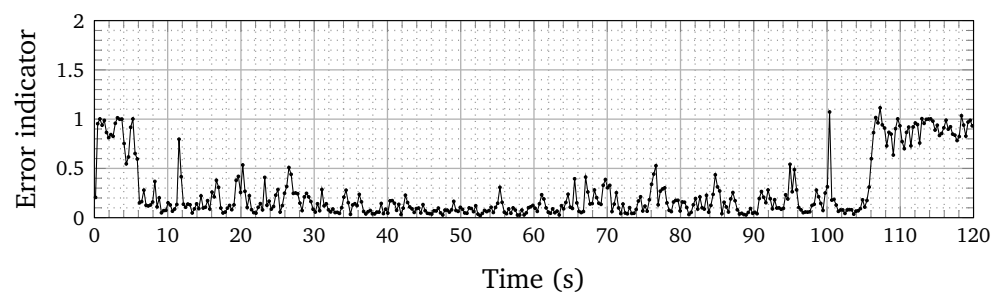
(A) Comparison of the identified model displacement and the experimental displacement



(B) Viscous damping ratio



(C) Eigenfrequency



(D) Identification error

FIGURE 3.43: Non-parametric identification of the viscous damping ratio and the eigenfrequency for WN12 (RUN 543) for the SDOF oscillator associated to the 1<sup>st</sup> vibration mode **without relative variation constraint**

padding and plotted on figure 3.44. The identification error (figure 3.44d) is lower during the sinusoids with higher amplitudes. For a better readability, the values identified with an error criterion lower than 0.2 have been plotted in red. Hence, the frequency decrease through the successive sinusoidal excitations is easily seen on figure 3.44c from 6.3 Hz to 2.6 Hz. It matches well with the frequencies identified by the intermediate low-level white noise tests (respectively 6.3 Hz and 2.7 Hz).

A focus is made on the last four sinusoids of RUN 434 on figure 3.45. The identification error is low during these last four sinusoids. Also, the damping ratio and the eigenfrequency are particularly stable in comparison with previous results: this shows the validity of the viscously damped SDOF oscillator model to describe the behavior of the 1<sup>st</sup> mode of the damaged beam. The excitation frequencies corresponding to these last four sinusoids are 3.5 Hz, 3.0 Hz, 2.5 Hz and 2.0 Hz. The acceleration amplitude decreases as inverse squared of the excitation frequency. The final eigenfrequency is evaluated at 2.6 Hz. Hence, the maximum displacement response is expected for 3.0 Hz or 2.5 Hz but the damping ratio is higher for these two excitation frequencies which could explain why the displacement response is higher at 3.5 Hz. For displacement response amplitudes of 120 mm, 90 mm, 40 mm and 10 mm, the maximum damping ratio is identified at around 1 %, 3 %, 5 % and 15 %.

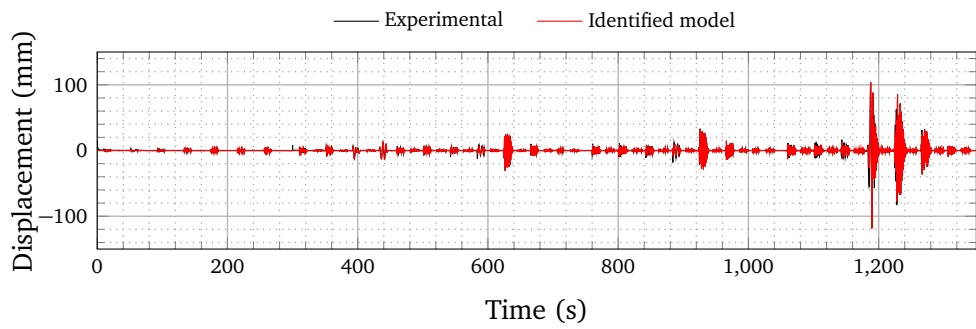
If the damping ratios identified in each time-window are plotted against the corresponding maximum displacement amplitudes, the figure 3.46 is obtained. Only the time-windows on which the identification error is lower than 0.1 are considered. The scattering of the damping ratio decreases with the displacement amplitude.

### 3.7 Conclusions of the third chapter

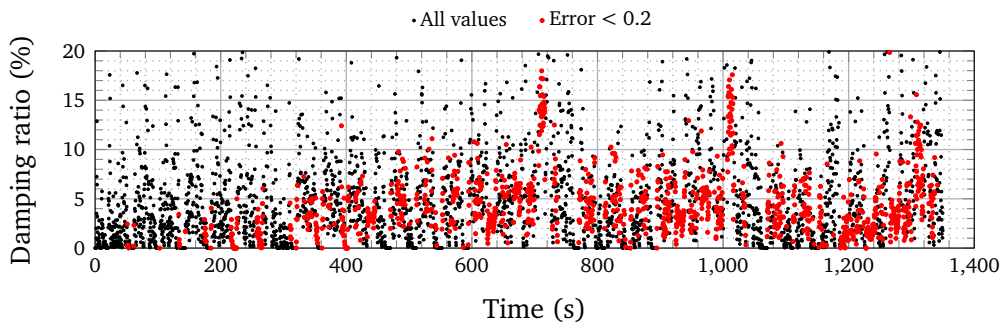
The experimental results have been directly analyzed in this chapter. First, the quasi-static tests support the formulation and the identification of an hysteretic model to assess the internal forces independent on the dynamic effects (section 3.2.4). Damage, friction and pinching have been identified as the main phenomena to drive the energy dissipations during those tests. The hysteretic model, designated as IDEFIX model, has been calibrated for the different beams and accounts for the aforementioned dissipations in a general way (without prejudging from the exact origin of each dissipation, i.e. concrete or steel-concrete bond).

In a second time, a numerical experimental campaign based on IDEFIX nonlinear model has been carried out. The influence of several parameters of the model on the EVDR assessed by JAM has been studied. In particular, the displacement ductility level proved to have an important influence on the EVDR. Hence, four observations have been made:

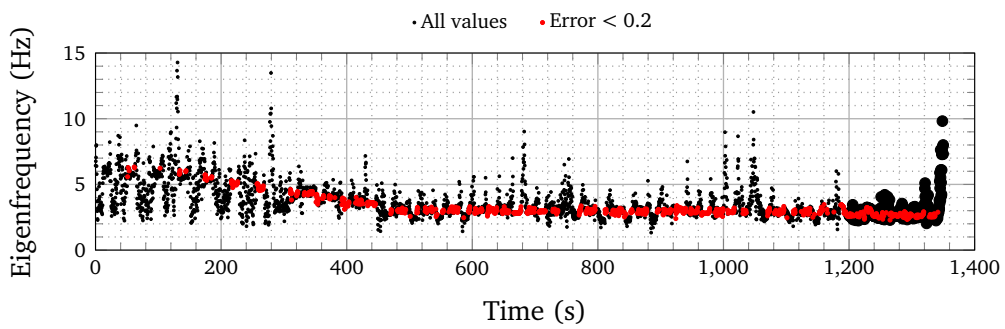
- the higher is the ductility level, the higher is the EVDR;
- this increasing of EVDR is due to a decrease of the energy storing capacity rather than an increase of energy dissipation;
- in agreement with the observation made with the non-parametric identification method, the higher is the displacement amplitude, the lower is the EVDR;



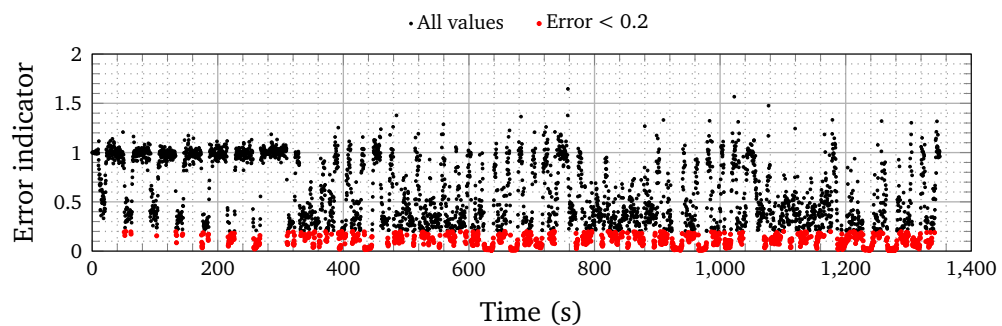
(A) Comparison of the identified model displacement and the experimental displacement



(B) Viscous damping ratio

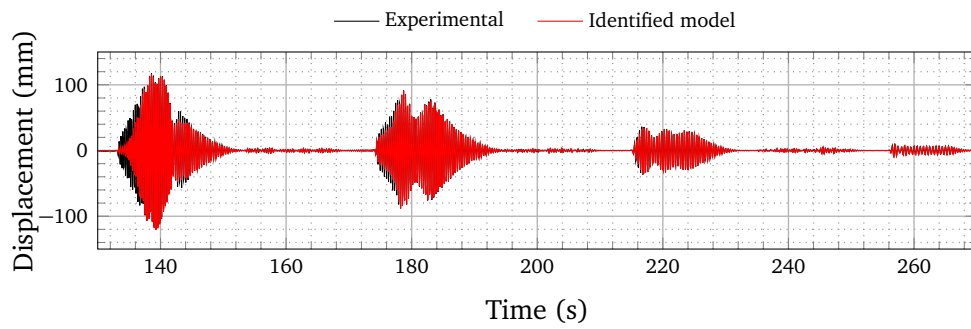


(C) Eigenfrequency

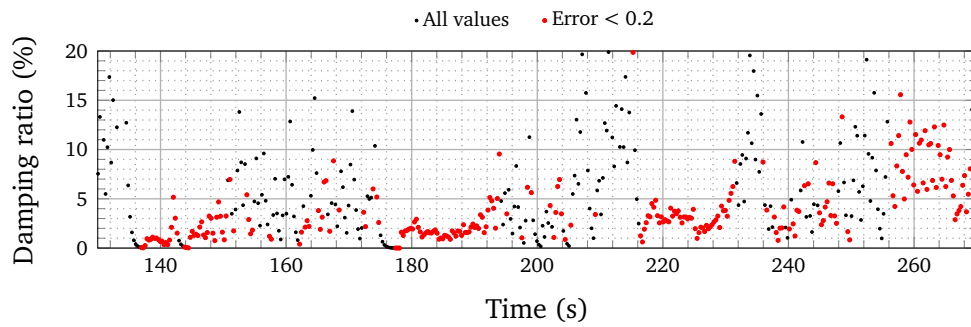


(D) Identification error

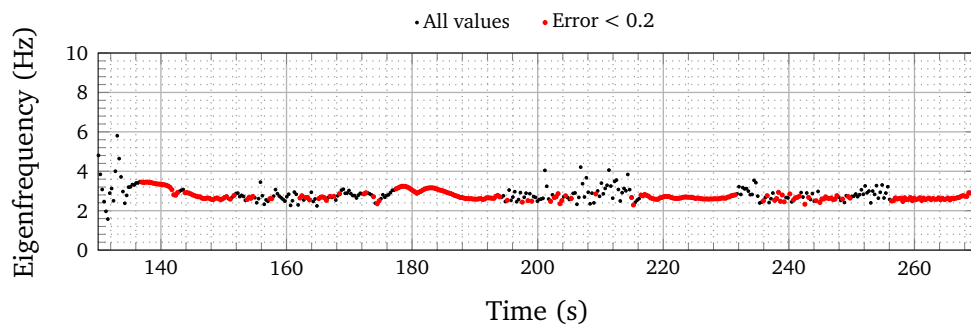
FIGURE 3.44: Non-parametric identification of the viscous damping ratio and the eigenfrequency for DSS52 (RUN 423 to 434 padded) for the SDOF oscillator associated to the 1<sup>st</sup> vibration mode



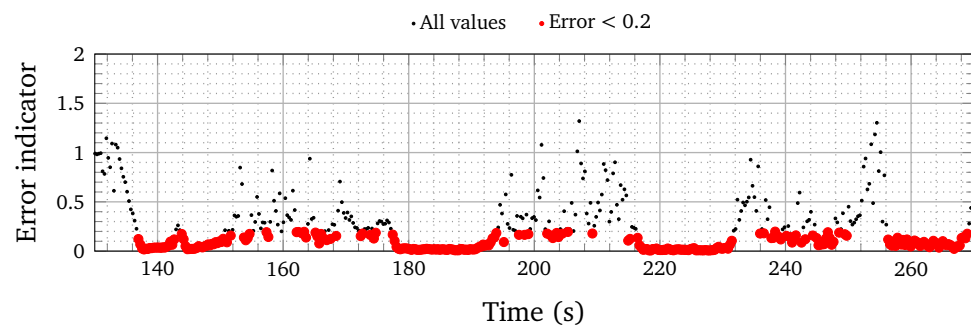
(A) Comparison of the identified model displacement and the experimental displacement



(B) Viscous damping ratio



(C) Eigenfrequency



(D) Identification error

FIGURE 3.45: Non-parametric identification of the viscous damping ratio and the eigenfrequency for DSS52 (RUN 423) for the SDOF oscillator associated to the 1<sup>st</sup> vibration mode, focus on the last four sinusoids

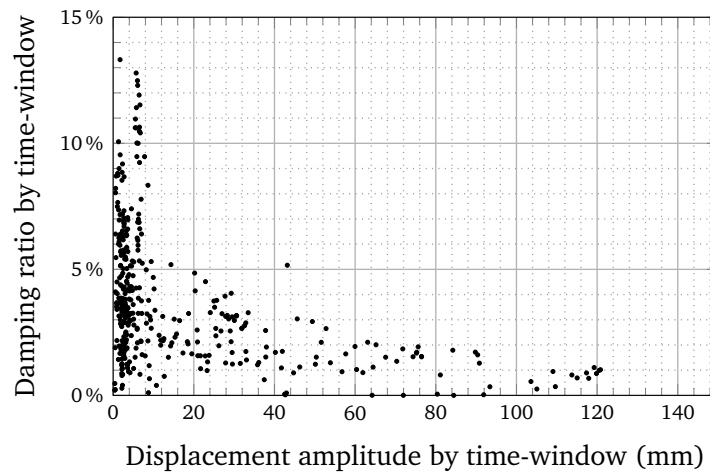


FIGURE 3.46: Values of viscous damping ratio identified depending on the maximum displacement response amplitude of the time-window (duration of 0.3 s) for RUN434, for identification error lower than 0.1

- the pinching effect may partially explain the previous observation (lower stiffness for small displacements implies lower energy storage capacity).

In a third time, the hammer shock tests have been performed and allow for the tracking of the evolution of both the eigenfrequencies and the damping ratio (thanks to the HBM) between the different quasi-static tests experienced by the beams. Particularly, it has been shown that they do not significantly evolve after the first test. Considering the EVDR identified by the HBM, it seems that the 1<sup>st</sup> EVDR ratio is roughly twice higher than the 2<sup>nd</sup> one, and that this ratio is the same for the damaged state. Moreover, either the 1<sup>st</sup> or the 2<sup>nd</sup> EVDR is multiplied by five after the first damaging test (generally QSC1). It is important to emphasize the fact that this EVDR takes into account all the dissipative phenomena.

Then, the WN12 tests were used to carry non-parametric identification. This method has the advantage to give a time-varying information about the eigenfrequencies and EVDR. As previously with HBM, the obtained EVDR value takes into account all the dissipations. However, the validity of the identified values should always be questioned regarding the identification error criterion. The expertise of the user is required to decide the credit to give to such an analysis. The main results are the following ones:

- the EVDR can vary significantly during a tests;
- the EVDR depends on the cycle amplitude recorded during the identification time-window, the higher it is, the lower is the damping ratio;
- in contradiction with the hammer shock tests, the 2<sup>nd</sup> mode EVDR seems higher than the 1<sup>st</sup> one.

A possible explanation for the latter observation is that since WN12 tests have been design to activate at a comparably high level the 1<sup>st</sup> and the 2<sup>nd</sup> mode, the pinching effect should affect equally the both projected modal displacements. The acceleration is high enough to diminish the influence of the pinching on the EVDR. In contrary, in the case of the hammer

Method	EVDR
JAM <sup>1</sup>	2.7 %
LDM <sup>2</sup>	3.1 %
HBM <sup>3</sup>	9 — 12 %
Non-parametric <sup>4</sup>	1 — 3 %

<sup>1</sup> From QSC1 test at  $\mu = 14.6$  and displacement amplitude of 35 mm (beam HA20-C1A-1)

<sup>2</sup> From virtual free vibrations test at  $\mu = 14.6$  and displacement amplitude of 35 mm (beam HA20-C1A-1)

<sup>3</sup> From hammer tests performed on a damaged beam (HA12-C1B for 9 % and HA20-C1A for 12 %)

<sup>4</sup> From DSS52 at  $\mu = 18.6$  and displacement amplitude of 35 mm (beam HA16-C1A-2)

TABLE 3.9: EVDR values identified with different methods

tests, it is more difficult to activate both eigenmodes at the same level and due to a lower displacement amplitude along with the pinching effect, the identified EVDR values are higher with the HBM on hammer tests than with the non-parametric identification on WN12. This may suggest that the nonlinearity introduced by the pinching could make the EVDR obtained from hammer tests sensitive to the force of the shock performed by the operator. The stronger it is, the lower is the EVDR. This effect should be investigated.

Finally, the DSS52 test is also analyzed thanks to the non-parametric identification method. The method proved to be efficient to track the eigenfrequency changes during the test. However, the EVDR values show spurious variations and may not be used directly. Nevertheless, the scatter in the EVDR values increases with higher displacement amplitude, i.e. the method has more probability to identify higher EVDR for a higher displacement amplitude.

Considering only the first mode, the JAM (performed on quasi-static tests) is in agreement with the standard LDM with a maximum of 3 % of EVDR for a cycle amplitude around 35 mm with a fixed displacement ductility level  $\mu = 14.6$ . It is difficult to spot the same configuration (i.e. same ductility level and displacement amplitude) for the non-parametric identification performed on DSS52. However, the value of EVDR identified at time 150 s on figure 3.45b may be considered as close matching: the maximum historic displacement is around 120 mm and the cycle amplitude around 35 mm. This value is somewhere between 1 % and 3 %. Being more precise is not possible since the EVDR varies quickly in a very short period of time due to the pinching effect and the identification error. The hammer tests analyzed thanks to the HBM do not allow for evaluating EVDR for displacement amplitudes as high as 35 mm. For this reason, the EVDR values identified on a damaged beam (after QSC1, see figure 3.38c) vary between 9 % for beam HA12-C1B to 12 % for beam HA20-C1A. Hence, the hammer tests may not be adapted when the EVDR value is intended to be used for a computation where high displacement are expected. These results are summed-up in table 3.9.

The next chapter presents different numerical approaches to simulate the behavior of the beams and their dissipations. The gaps between the experiments and the numerical results will be studied in the scope of the damping modeling.

## Chapter 4

# Numerical simulations using simplified damping modeling

### 4.1 Strategies of numerical modeling

In this chapter, the modeling strategy and the analysis of a RC beam under seismic loading are both presented. Two strategies are considered to simulate the dynamic response of IDEFIX beams subject to one the signal monitored during the Niigataken Chuetsu Oki Earthquake (NCOE):

- an equivalent nonlinear SDOF problem solved thanks to an implicit integration scheme (section 4.2.1);
- a finite element model using Cast3M software (cf. section 4.3).

Because of the nonlinear behavior of the concrete model used in Cast3M for the computation of the beam model, an implicit algorithm is also used. The results provided by both strategies are compared to the experimental measurements in section 4.4. The finite element model represents a predictive approach for the assessment of the beam response because an advanced nonlinear material model is calibrated thanks to the preliminary tests carried out on concrete and steel samples (section 2.3.3). The usual additional viscous damping of 2 % is modeled by a Rayleigh damping proportional to the initial stiffness. This simulation is therefore representative of the state-of-the art for modeling the dynamic response of a RC component and is compared to an alternative strategy (i.e. the nonlinear SDOF oscillator) to attempt to provide clues for the improvement of the modeling of dissipations.

### 4.2 Computation of a SDOF oscillator response

#### 4.2.1 Newmark method

The dynamic balance equation is:

$$m \cdot \ddot{u}_{i+1} + F^D(\dot{u}_{i+1}) + F^S(u_{i+1}) = F_{i+1}^{ext} \quad (4.1)$$

at time-step number  $i + 1$ , where  $F^D$  is the damping force and  $F^S$  is the restoring force. The developments in Taylor's series of the displacement and the velocity give:

$$u_{i+1} = u_i + h \cdot \dot{u}_i + \frac{h^2}{2} \cdot \ddot{u}_i + \frac{h^3}{6} \cdot \dddot{u}_{i+1} + \dots \quad (4.2)$$

$$\dot{u}_{i+1} = \dot{u}_i + h \cdot \ddot{u}_i + \frac{h^2}{2} \cdot \dddot{u}_i + \dots \quad (4.3)$$

with the constant time-step duration  $h = t_{i+1} - t_i$ . These equations are truncated to:

$$u_{i+1} = u_i + h \cdot \dot{u}_i + \frac{h^2}{2} \cdot \ddot{u}_i + \beta \cdot h^3 \cdot \ddot{u}_i \quad (4.4)$$

$$\dot{u}_{i+1} = \dot{u}_i + h \cdot \ddot{u}_i + \gamma \cdot h^2 \cdot \ddot{u}_i \quad (4.5)$$

The assumption that the acceleration is linear is made. Hence:

$$\ddot{u}_i = \frac{\dot{u}_{i+1} - \dot{u}_i}{h} \quad (4.6)$$

Injecting this approximation in equations (4.4) and (4.5):

$$u_{i+1} = u_i + h \cdot \dot{u}_i + \left(\frac{1}{2} - \beta\right) \cdot h^2 \cdot \ddot{u}_i + \beta \cdot h^2 \cdot \dot{u}_{i+1} \quad (4.7)$$

$$\dot{u}_{i+1} = \dot{u}_i + (1 - \gamma) \cdot h \cdot \ddot{u}_i + \gamma \cdot h \cdot \dot{u}_{i+1} \quad (4.8)$$

Equation 4.7 is reversed to obtain:

$$\ddot{u}_{i+1} = \frac{1}{\beta \cdot h^2} \cdot \Delta u_i - \frac{1}{\beta \cdot h} \cdot \dot{u}_i - \left(\frac{1}{2 \cdot \beta} - 1\right) \cdot \ddot{u}_i \quad (4.9)$$

with  $\delta u_i = u_{i+1} - u_i$ . Injecting equation (4.9) in equation (4.8) gives:

$$\dot{u}_{i+1} = \frac{\gamma}{\beta \cdot h} \cdot \Delta u_i - \left(\frac{\gamma}{\beta} - 1\right) \cdot \dot{u}_i - \left(\frac{\gamma}{2 \cdot \beta} - 1\right) \cdot h \cdot \ddot{u}_i \quad (4.10)$$

The case of a constant damping coefficient  $c$  is considered:

$$F^D(u_{i+1}) = c \cdot \dot{u}_{i+1} \quad (4.11)$$

From equations (4.9) and (4.10), the dynamic equilibrium equation (4.1) becomes:

$$\begin{aligned} & \left(m \cdot \frac{1}{\beta \cdot h^2} + c \cdot \frac{\gamma}{\beta \cdot h}\right) \cdot (u_{i+1} - u_i) \\ & - \left(m \cdot \frac{1}{\beta \cdot h} + c \cdot \left(\frac{\gamma}{\beta} - 1\right)\right) \cdot \dot{u}_i \\ & - \left(m \cdot \left(\frac{1}{2 \cdot \beta} - 1\right) + c \cdot \left(\frac{\gamma}{2 \cdot \beta} - 1\right) \cdot h\right) \cdot \ddot{u}_i + F^S(u_{i+1}) = F_{i+1}^{ext} \end{aligned} \quad (4.12)$$

The effective load is defined:

$$\hat{F}_{i+1} = F_{i+1}^{ext} + a_1 \cdot u_i + a_2 \cdot \dot{u}_i + a_3 \cdot \ddot{u}_i \quad (4.13)$$

where:

$$a_1 = m \cdot \frac{1}{\beta \cdot h^2} + c \cdot \frac{\gamma}{\beta \cdot h} \quad (4.14)$$

$$a_2 = m \cdot \frac{1}{\beta \cdot h} + c \cdot \left( \frac{\gamma}{\beta} - 1 \right) \quad (4.15)$$

$$a_3 = m \cdot \left( \frac{1}{2 \cdot \beta} - 1 \right) + c \cdot \left( \frac{\gamma}{2 \cdot \beta} - 1 \right) \cdot h \quad (4.16)$$

and equation (4.12) becomes:

$$a_1 \cdot u_{i+1} + F^S(u_{i+1}) = \hat{F}_{i+1} \quad (4.17)$$

The only unknown in equation (4.17) is  $u_{i+1}$ . Because of the nonlinearity of this equation, a fixed point based solving method should be used (Newton-Raphson or quasi-Newton methods for instance). The solution is generally not found at the first iteration. Hence, at iteration  $j$ , a correction  $\delta u^j$  is sought so that  $u_{i+1}^{j+1} = u_{i+1}^j + \delta u^j$  is the solution of equation (4.17):

$$a_1 \cdot (u_{i+1}^j + \delta u^j) + F^S(u_{i+1}^j + \delta u^j) = \hat{F}_{i+1} \quad (4.18)$$

A first order Taylor series development gives:

$$F^S(u_{i+1}^j + \delta u^j) \approx F^S(u_{i+1}^j) + \frac{\partial F^S}{\partial u}(u_{i+1}^j) \cdot \delta u^j \quad (4.19)$$

The tangent stiffness corresponding to the displacement  $u_{i+1}^j$  is defined as:

$$k_{t,i+1}^j = \frac{\partial F^S}{\partial u}(u_{i+1}^j) \quad (4.20)$$

and can be evaluated with a small perturbation method. Hence:

$$F^S(u_{i+1}^j + \delta u^j) \approx F^S(u_{i+1}^j) + k_{t,i+1}^j \cdot \delta u^j \quad (4.21)$$

and equation (4.18) becomes:

$$\hat{k}_{i+1}^j \cdot \delta u^j = \hat{R}_{i+1}^j \quad (4.22)$$

with the effective stiffness:

$$\hat{k}_{i+1}^j \approx k_{t,i+1}^j + a_1 \quad (4.23)$$

and the residue:

$$\hat{R}_{i+1}^j = \hat{F}_{i+1} - F^S(u_{i+1}^j) - a_1 \cdot u_{i+1}^j \quad (4.24)$$

This means that the sought correction is approximately:

$$\delta u^j \approx \frac{\hat{R}_{i+1}^j}{\hat{k}_{i+1}^j} \quad (4.25)$$

Because of the latter approximation, the procedure has to be repeated until a convergence criterion is reached. Two common criteria are:

- a maximum acceptable load residual  $\Delta R^{crit}$  such as the computation stops when  $\Delta R_i^k \leq \Delta R^{crit}$ ;
- a maximum relative correction  $\varepsilon$  such as the computation stops when  $\frac{\Delta u_i^k}{u_{i+1}^k - u_i^k} \leq \varepsilon$ .

A combination of several criteria is also possible using either AND or OR logical functions. The full algorithm of the Newmark implicit scheme associated to the Newton-Raphson method is given in table 4.1.

Table 4.2 indicates different versions of Newmark methods. Some remarks can be made:

- for  $\gamma > \frac{1}{2}$ , a numerical damping proportional to  $\gamma - 1$  appears;
- the method is conditionally stable if  $\beta > \frac{1}{2}$ ;
- the method is second order accurate if and only if  $\beta \geq \frac{\gamma}{2}$ .

Hilber *et al.*, 1977 state that in many structural dynamics applications, the use of unconditionally stable algorithms is generally preferred over conditionally stable algorithms because only low mode response is of interest. Indeed, a conditionally stable algorithm would require that the size of the time-step employed be inversely proportional to the highest frequency of the discrete model which leads to an unnecessarily high sampling frequency.

#### 4.2.2 Hughes Hilber Taylor (HHT) method

The Hughes Hilber Taylor (HHT) method can be considered as an extension of Newmark algorithm with an additional parameter (often called  $\alpha$ ) that drives an amount of “numerical dissipation”. The Newmark’s approximations of equations (4.4) and (4.5) are still used but the expression of the residual of the dynamic equation is modified and evaluated at time-step number  $i + \alpha$ , i.e. an intermediate time-step between number  $i$  and  $i + 1$ :

$$\hat{R}_{i+\alpha}^j = \hat{F}_{i+1} - F^S(u_{i+\alpha}^j) - a_1 \cdot u_{i+\alpha}^j \quad (4.26)$$

where the intermediate displacement and velocity are:

$$u_{i+\alpha} = (1 - \alpha) \cdot u_i + \alpha \cdot u_{i+1} \quad (4.27)$$

$$\dot{u}_{i+\alpha} = (1 - \alpha) \cdot \dot{u}_i + \alpha \cdot \dot{u}_{i+1} \quad (4.28)$$

Following the same steps than for the Newmark method in section 4.2.1, the iterative problem writes:

$$\hat{k}_{i+\alpha}^j \cdot \delta u_{i+\alpha}^{j+1} = \hat{R}_{i+\alpha}^j \quad (4.29)$$

with:

$$\hat{k}_{i+\alpha}^j = k_{t,i+\alpha} + a_1 \quad (4.30)$$

TABLE 4.1: Implicit Newmark algorithm

<b>1. Initial state</b>	
1.1 Initial state determination:	$F_1^S = F^S(u_1) \quad k_{t,1} = \frac{\partial F^S}{\partial u}(u_1) \quad \ddot{u}_1 = \frac{1}{m} \cdot (F_1^{ext} - c \cdot \dot{u}_1 - F^S(u_1))$
1.2 Set the constants:	$a_1 = m \cdot \frac{1}{\beta \cdot h^2} + c \cdot \frac{\gamma}{\beta \cdot h} \quad a_2 = m \cdot \frac{1}{\beta \cdot h} + c \cdot \left(\frac{\gamma}{\beta} - 1\right)$ $a_3 = m \cdot \left(\frac{1}{2 \cdot \beta} - 1\right) + c \cdot \left(\frac{\gamma}{2 \cdot \beta} - 1\right) \cdot h$
<b>2. For each time-step <math>i</math></b>	
2.1 Set initial state:	$u_{i+1}^1 = u_i \quad F_{i+1}^{S,1} = F^S(u_{i+1}^1) \quad k_{t,i+1}^1 = \frac{\partial F^S}{\partial u}(u_{i+1}^1)$
2.2 Calculate effective load:	$\hat{F}_{i+1} = F_{i+1}^{ext} + a_1 \cdot u_i + a_2 \cdot \dot{u}_i + a_3 \cdot \ddot{u}_i$
<b>3. For each iteration <math>j</math></b>	
3.1 Calculate the residue:	$\hat{R}_{i+1}^j = \hat{F}_{i+1} - F^S(u_{i+1}^j) - a_1 \cdot u_{i+1}^j$
3.2 Check the convergence criterion. If reached go to step 4., else continue to 3.3.	
3.3 Calculate the effective stiffness:	$\hat{k}_{i+1}^j \approx k_{t,i+1}^j + a_1$
3.4 Calculate the correction:	$\delta u^j = \hat{R}_{i+1}^j / \hat{k}_{i+1}^j$
3.5 Apply correction:	$u_{i+1}^{j+1} = u_{i+1}^j + \delta u^j \quad F_{i+1}^{S,j+1} = F^S(u_{i+1}^{j+1}) \quad k_{i+1}^{j+1} = \frac{\partial F^S}{\partial u}(u_{i+1}^{j+1})$
3.6 Iterate and go back to step 3.1: $j \leftarrow j + 1$	
<b>4. Deduce velocity and acceleration</b>	
	$\dot{u}_{i+1} = \frac{\gamma}{\beta \cdot h} \cdot (u_{i+1} - u_i) + \left(1 - \frac{\gamma}{\beta}\right) \cdot \dot{u}_i + \left(1 - \frac{\gamma}{2 \cdot \beta}\right) \cdot h \cdot \ddot{u}_i$ $\ddot{u}_{i+1} = \frac{1}{\beta \cdot h^2} \cdot (u_{i+1} - u_i) - \frac{1}{\beta \cdot h} \cdot \dot{u}_i - \left(\frac{1}{2 \cdot \beta} - 1\right) \cdot \ddot{u}_i$
<b>5. Go to next time step <math>i \leftarrow i + 1</math> and repeat steps 2. to 4.</b>	

Method's name	$\gamma$	$\beta$	Stability
Centered difference	1/2	0	Conditionally
Fox Goodwin	1/2	1/12	Conditionally
Linear acceleration	1/2	1/6	Conditionally
Mean acceleration	1/2	1/4	Unconditionally

TABLE 4.2: Newmark methods

defined in an analogous way as with Newmark implicit scheme in table 4.1. Once the solution of this iterative problem ( $u_{i+\alpha}, \dot{u}_{i+\alpha}, \ddot{u}_{i+1}$ ) is found, the values of the displacement and the velocity at time-step number  $i + 1$  using equations (4.27) and (4.28):

$$u_{i+1} = \frac{u_{i+\alpha} - (1 - \alpha) \cdot u_i}{\alpha} \quad (4.31)$$

$$\dot{u}_{i+1} = \frac{\dot{u}_{i+\alpha} - (1 - \alpha) \cdot \dot{u}_i}{\alpha} \quad (4.32)$$

The following observations are made:

- $\alpha = 1$  corresponds to the Newmark method;
- the choice of  $\beta$  and  $\gamma$  is free, but the following expression ensure that the method is unconditionally stable and second order accurate if  $\frac{2}{3} \leq \alpha \leq 1$ :  $\beta = \frac{(2-\alpha)^2}{4}$  and  $\gamma = \frac{3}{2} - \alpha$ ;
- the smaller is  $\alpha$ , the greater is the numerical damping.

The numerical damping may prove to be useful when noise affects the inputs data. For example, if a ground motion record is affected by noise and that no displacement is observed in reality, the computed response of an undamped SDOF linear system is not null if no numerical damping is added. The drawback is that even if the level of numerical damping is controllable, the frequencies damped are not. Hence, it is difficult to associate it with the physical damping matrix  $\mathbf{C}$  in a manner that the corresponding total damping matches with the actual dissipations desired. For these reasons, the non-dissipative Newmark's mean acceleration algorithm is used (also called "trapezoidal rule" with  $\beta = \frac{1}{4}$  and  $\gamma = \frac{1}{2}$ ).

### 4.2.3 Influence of the integration scheme on the identified damping

#### 4.2.3.1 Reference problem

The system considered is the one modeled by the following system of equations:

$$\begin{cases} \ddot{u}(t) + 2 \cdot \xi \cdot \omega_0 \cdot \dot{u}(t) + \omega_0^2 \cdot u(t) = -\ddot{u}_{g,0} \cdot \sin(\omega_0 \cdot t) \\ u(0) = 0 \\ \dot{u}(0) = 0 \end{cases} \quad (4.33)$$

where  $\ddot{u}_{g,0}$  is the ground acceleration amplitude and  $\omega_0 = \sqrt{\frac{k}{m}}$  is the natural angular frequency of the SDOF system and is set at 12.6 rad/s (corresponding to a frequency of 2 Hz). The analytical solution of equation (4.33) is recalled equation (4.34).

$$u(t) = \frac{m \cdot \ddot{u}_{g,0}}{2 \cdot \xi \cdot k} \cdot \left[ \exp(-\xi \cdot \omega_0 \cdot t) \cdot \left( \cos(\omega_d \cdot t) + \frac{\xi}{\sqrt{1 - \xi^2}} \cdot \sin(\omega_d \cdot t) \right) - \cos(\omega_0 \cdot t) \right] \quad (4.34)$$

TABLE 4.3: Implicit HHT algorithm

<p>1. <b>Initial state (same as in table 4.1)</b></p> <p>1.1 Initial state determination</p> <p>1.2 Set the constants</p> <p>2. <b>For each time-step <math>i</math></b></p> <p>2.1 Set initial state:</p> $u_{i+1}^1 = u_i \quad F_{i+1}^{S,1} = F^S(u_{i+1}^1) \quad k_{t,i+1}^1 = \frac{\partial F^S}{\partial u}(u_{i+1}^1)$ <p>2.2 Calculate effective load:</p> $\hat{F}_{i+1} = F_{i+1}^{ext} + a_1 \cdot u_i + a_2 \cdot \dot{u}_i + a_3 \cdot \ddot{u}_i$ <p>3. <b>For each iteration <math>j</math></b></p> <p>3.1 Calculate the residue:</p> $\hat{R}_{i+\alpha}^j = \hat{F}_{i+1} - F^S(u_{i+\alpha}^j) - a_1 \cdot u_{i+\alpha}^j$ <p>3.2 Check the convergence criterion. If reached go to step 4., else continue to 3.3.</p> <p>3.3 Calculate the effective stiffness:</p> $\hat{k}_{i+\alpha}^j \approx k_{t,i+\alpha}^j + a_1$ <p>3.4 Calculate the correction:</p> $\delta u^j = \hat{R}_{i+\alpha}^j / \hat{k}_{i+\alpha}^j$ <p>3.5 Apply correction:</p> $u_{i+\alpha}^{j+1} = u_{i+\alpha}^j + \delta u^j \quad F_{i+\alpha}^{S,j+1} = F^S(u_{i+\alpha}^{j+1}) \quad k_{i+\alpha}^{j+1} = \frac{\partial F^S}{\partial u}(u_{i+\alpha}^{j+1})$ <p>3.6 Iterate and go back to step 3.1: <math>j \leftarrow j + 1</math></p> <p>4. <b>Calculate velocity at time <math>i + \alpha</math> and deduce solution at time <math>i + 1</math></b></p> $\dot{u}_{i+\alpha} = \frac{\gamma}{\beta \cdot h} \cdot (u_{i+\alpha} - u_i) + \left(1 - \frac{\gamma}{\beta}\right) \cdot \dot{u}_i + \left(1 - \frac{\gamma}{2 \cdot \beta}\right) \cdot h \cdot \ddot{u}_i$ $u_{i+1} = \frac{u_{i+\alpha} - (1 - \alpha) \cdot u_i}{\alpha}$ $\dot{u}_{i+1} = \frac{\dot{u}_{i+\alpha} - (1 - \alpha) \cdot \dot{u}_i}{\alpha}$ $\ddot{u}_{i+1} = \frac{1}{\beta \cdot h^2} \cdot (u_{i+1} - u_i) - \frac{1}{\beta \cdot h} \cdot \dot{u}_i - \left(\frac{1}{2 \cdot \beta} - 1\right) \cdot \ddot{u}_i$ <p>5. <b>Go to next time step <math>i \leftarrow i + 1</math> and repeat steps 2. to 4.</b></p>
---

with  $\omega_d = \omega_0 \cdot \sqrt{1 - \xi^2}$ . This analytical solution offers a reference to evaluate the performance of the integration method used.

The intrinsic quality of the Newmark algorithm is not studied in this section since this kind of study is found in many papers, e.g. by Newmark, 1959; Hilber *et al.*, 1977.

This first study focuses on the damping ratio evaluated on a numerically computed solution using Newmark algorithm. The prescribed damping ratio is 10 % and this value should be found by JAM (section 1.3.1.2).

#### 4.2.3.2 Validation of the numerical implementation of JAM

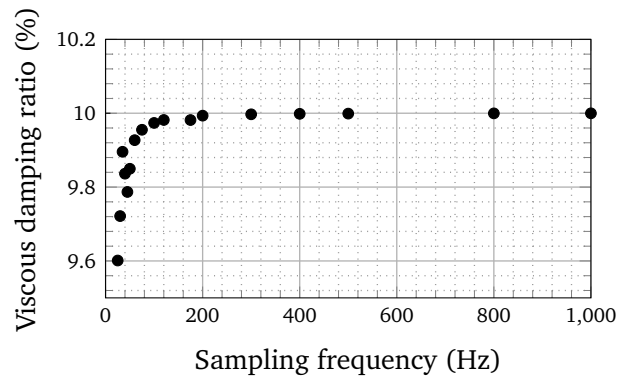
To validate the numerical implementation of JAM in MATLAB<sup>®</sup>, the damping ratio is first evaluated on the analytical solution computed at different time-steps depending on the sampling frequencies  $f_s$ . The results are plotted on figure 4.1. The JAM result depends on the sampling frequency and always underestimate the viscous damping ratio. The relative error remains small, mostly considering a sampling frequency greater than five times the excitation frequency since it remains within a 0.2 % error margin. The underestimation is due to the fact that the discretized loops of force-displacement are enclosed within the analytic loops because of their concavity (see figure 4.2). Therefore, the dissipated energy is underestimated, which leads to smaller damping ratios. When the sampling frequency is increased, the round shape of the loop is better reproduced, which provides higher damping ratios.

#### 4.2.3.3 Newmark parameters influence on the computation error

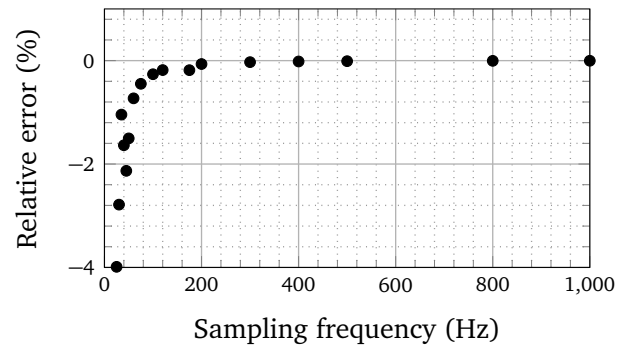
Now that the accuracy of the JAM implemented in MATLAB<sup>®</sup> has been demonstrated (under the condition that the sampling frequency is high enough), the influence of the Newmark parameters ( $\beta$  and  $\gamma$ ) is studied. To this end, a parametric study is carried out: a JAM identification is performed on dynamic responses generated by different couples of values of  $\beta$  and  $\gamma$ . First, the viscous damping ratio is plotted as a function of the Newmark parameters as on figure 4.4. The right value of viscous damping is obtained for  $(\gamma, \beta)$  on the red line, the mean acceleration scheme for  $\gamma = \frac{1}{2}$  and  $\beta = \frac{1}{4}$  gives almost the right value: the relative error on  $\xi$  is -0.07 %, which mean that the damping ratio is slightly underestimated.

#### 4.2.4 Application of the Newmark implicit algorithm to the Niigata-ken Chuetsu Oki Earthquake (NCOE)

The NCOE is described in section 2.5.3. For numerical testing purposes, this signal is scaled and padded three times. The PGA for the three NCOE are increasing: 0.18 g, 0.27 g et 0.56 g. The displacement and the acceleration response spectra are plotted on figure 4.5. The dynamic response to the NCOE of the equivalent nonlinear SDOF identified on HA12-C1B IDEFIX beams (parameters given in table 3.5) is assessed thanks to a Newmark implicit scheme as described in section 4.2.1. Newmark parameters are set at  $\beta = \frac{1}{4}$  and  $\gamma = \frac{1}{2}$ . The linear viscous damping ratio associated to the SDOF oscillator is set at 5 % since it



(A) Viscous damping ratio



(B) Relative error

FIGURE 4.1: Viscous damping ratio identified by JAM from analytic results and relative error with respect to the prescribed viscous damping ratio of 10 %, for different sampling frequencies

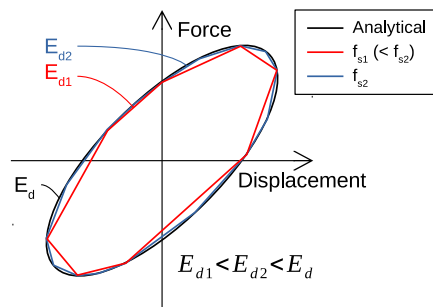


FIGURE 4.2: Schematic representation of the influence of the sampling frequency on the dissipated energy

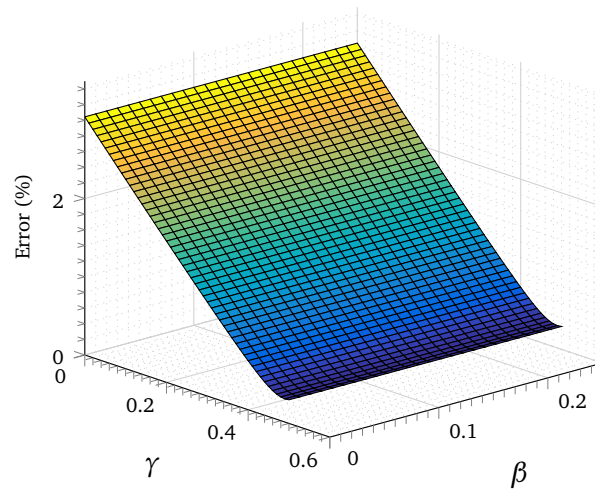


FIGURE 4.3: Overall error defined as in equation (1.126) between the analytical displacement and the Newmark computed displacement with parameters  $\beta$  and  $\gamma$

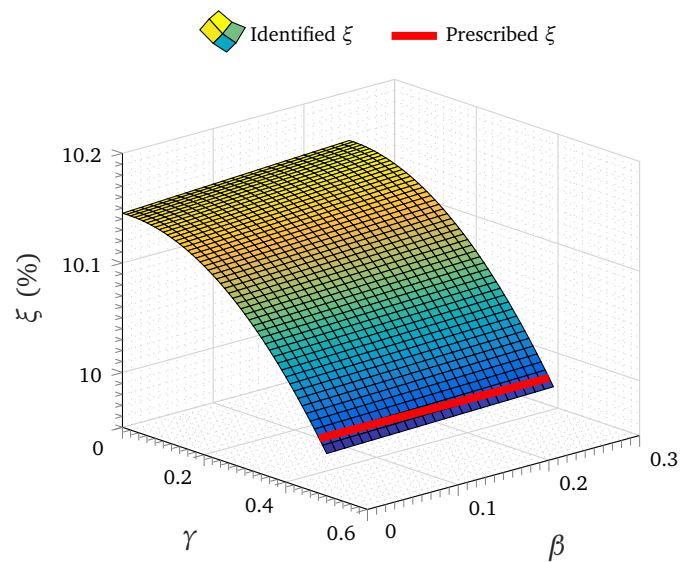
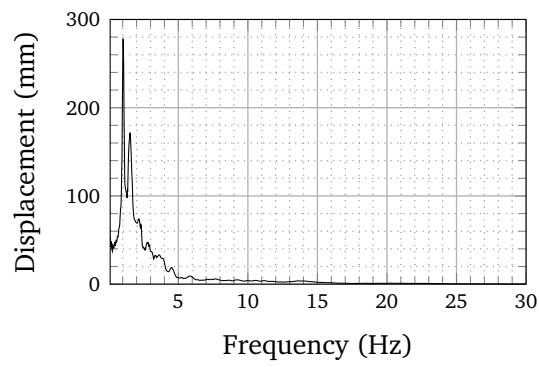
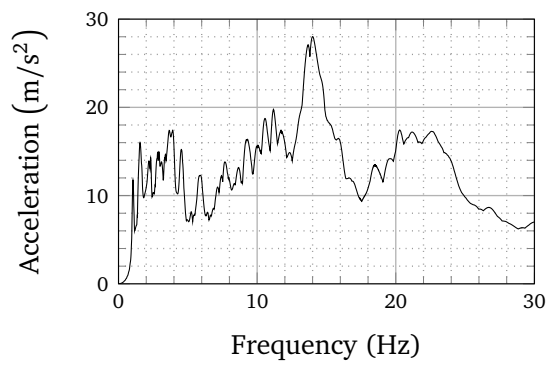


FIGURE 4.4: Viscous damping ratio identified by JAM depending on Newmark's parameters



(A) Acceleration response spectrum



(B) Displacement response spectrum

FIGURE 4.5: Response spectra for the three successive NCOEs and a viscous damping ratio of 2 %

seems to be an intermediate value between the initial state and the damaged state as it can be seen on figures 3.44 and 3.45 with the non-parametric identification and on figure 3.38 with the hammer-shocks tests. The associated viscous damping coefficient is set constant at:

$$c = 2 \cdot \xi \cdot m \cdot \omega_1(t = 0) \quad (4.35)$$

where  $\omega_1(t = 0)$  is the initial angular eigenfrequency. The SDOF oscillator response is plotted on figure 4.6 for the identified set of parameters. An overall displacement error indicator is used as reference:

$$\varepsilon_u = \frac{\int_0^T (u(t) - u_{exp}(t))^2}{\int_0^T u_{exp}(t)^2} \quad (4.36)$$

where  $u(t)$  is the computed displacement and  $u_{exp}(t)$  is the experimentally measured displacement. The model succeed to reproduce the response to the second NCOE, while the first one is slightly overdamped compared to the reference. However, the last NCOE response is too low. The SDOF oscillator eigenfrequency remains constant during the time-history analysis (except for the slight decrease at the very end) and this explains why the last NCOE displacement response is lower than the one observed experimentally: the stiffness has not decreased enough during the second NCOE earthquake.

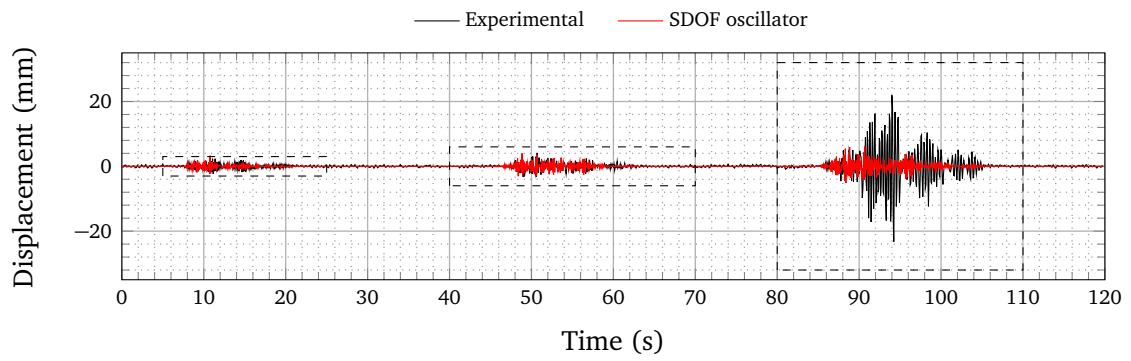
As an attempt to improve the displacement response of the SDOF oscillator, a second identification is performed in order to find a better matching elastic displacement. This time, the displacement is used as support for the error criterion comparing the numerical simulation and the experiments. Consequently, the elastic limit displacement  $\delta_y$  is changed from 6.7 mm to 3.0 mm. This modification proves to be efficient to produce a more satisfying SDOF oscillator response as plotted on figure 4.7.

By reducing the elastic limit, the first Niigataken Chuetsu Oki earthquake (NCOE) has a moderate displacement demand to initiate damage and start reducing the stiffness. This effect makes the SDOF oscillator closer to the observed experimental coefficient. Indeed, intermediate low-level white noise tests showed that the first eigenfrequency follows the evolution given in table 4.4. The quick variations of eigenfrequency on figure 4.7b are due to the pinching effect that makes the secant stiffness vary in the neighborhood of zero displacement.

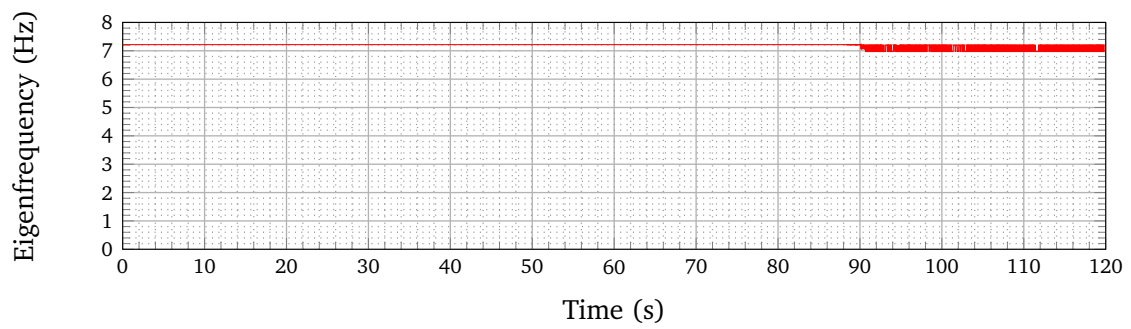
<b>Exp.:</b>	6.8 Hz	0.18 g	6.6 Hz	0.27 g	5.2 Hz	0.56 g	2.9 Hz
	→	1 <sup>st</sup> NCOE	→	2 <sup>nd</sup> NCOE	→	3 <sup>rd</sup> NCOE	
<b>Num.:</b>	7.2 Hz		6.7 Hz		5.9 Hz		2.5 Hz

TABLE 4.4: Evolution of the experimental eigenfrequency assessed by low-level white noise tests compared to the numeric one obtained with the adapted SDOF oscillator

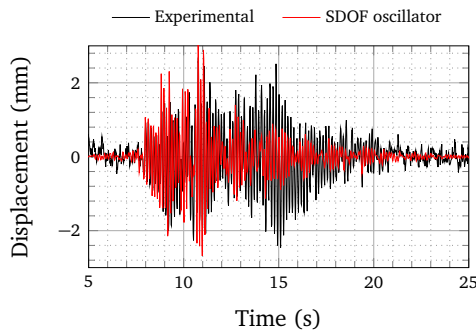
The fast Fourier transforms (FFT) of the displacements and the accelerations of the both versions of the SDOF oscillator (i.e. initial and adapted) are compared to the experimental ones on figure 4.8. The improvements brought by the modification of the SDOF oscillator model are particularly visible on the displacement FFTs on figure 4.8a. The four peaks mostly visible on the acceleration FFTs on figure 4.8b correspond to the four different



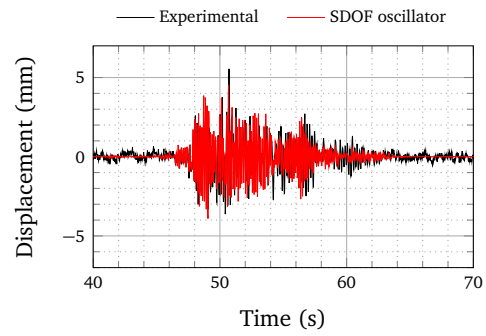
(A) Overall



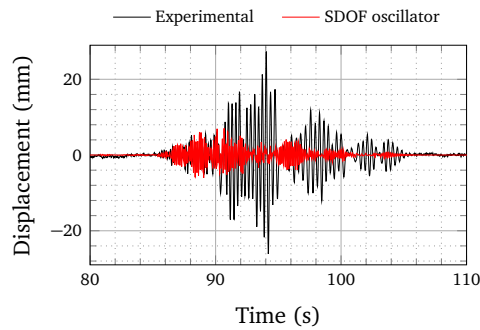
(B) Evolution of the eigenfrequency



(C) Zoom 1

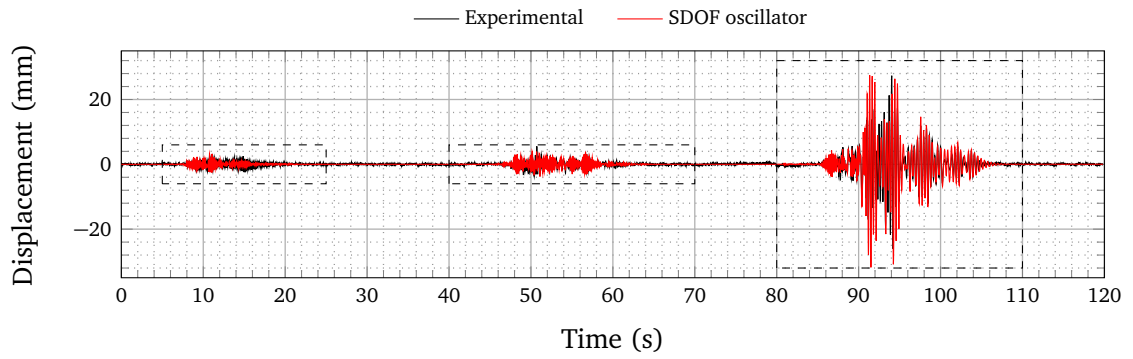


(D) Zoom 2

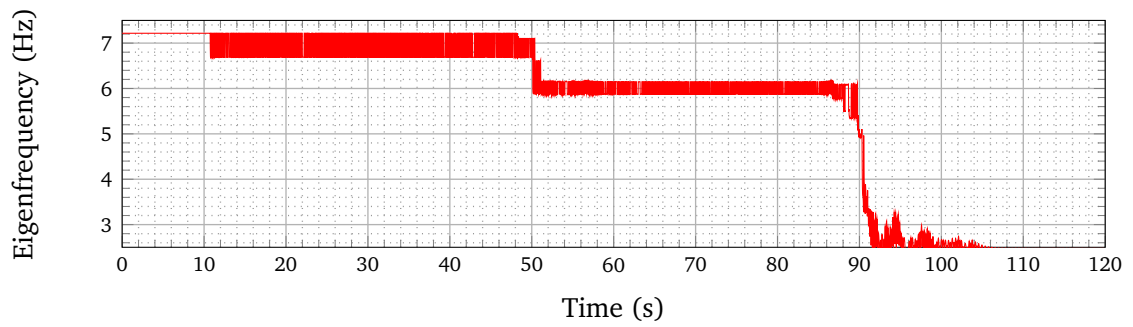


(E) Zoom 3

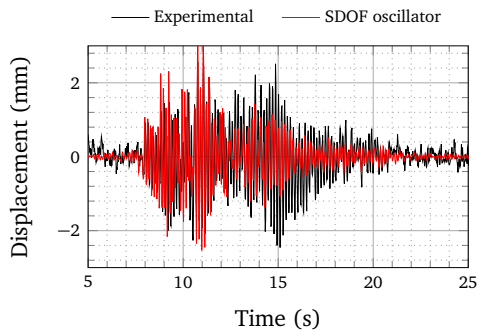
FIGURE 4.6: Comparison between the experimental 1<sup>st</sup> mode displacement and the computed equivalent SDOF nonlinear oscillator displacement for successive scaled NCOE and for the parameters identified for HA12-C1B (overall error indicator: 3.01 of equation (4.36))



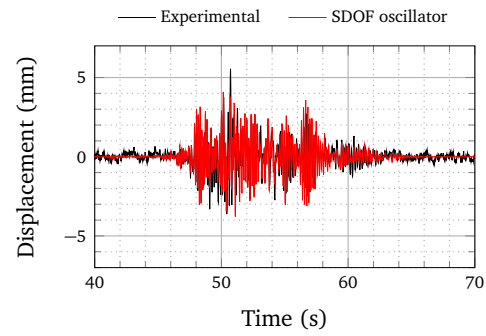
(A) Overall



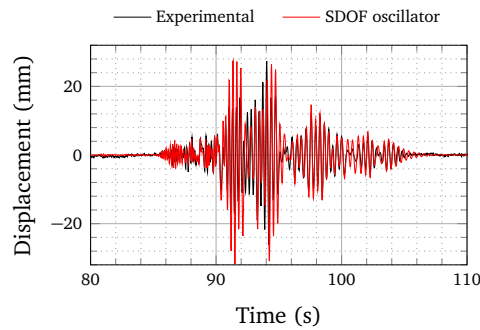
(B) Evolution of the eigenfrequency



(C) Zoom 1

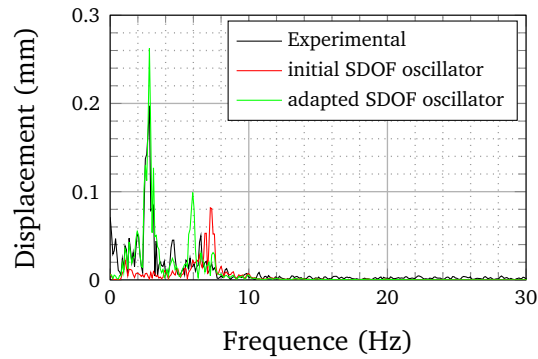


(D) Zoom 2

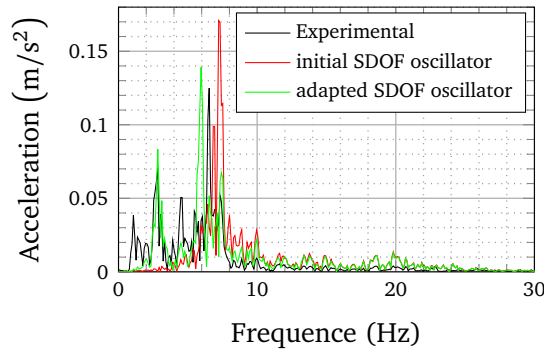


(E) Zoom 3

FIGURE 4.7: Comparison between the experimental 1<sup>st</sup> mode displacement and the computed equivalent SDOF nonlinear oscillator displacement for successive scaled NCOE and for adapted parameters (overall error indicator: 0.74 of equation (4.36))



(A) Displacement FFTs



(B) Displacement FFTs

FIGURE 4.8: Comparison between the experimental and SDOF oscillators FFTs

stabilized states of degradation given in table 4.4. As observed on the temporal data, the initial SDOF oscillator only exhibits one peak corresponding to the initial state because almost no damage occurs.

One reason why the initially identified SDOF model requires a modification is that the confidence in this identification is relatively low since only one test on one beam is used. Unfortunately, more tests were not possible for practical reason. The elastic limit is a critical parameter, especially when considering the case of aftershocks, because it could make the structure more sensitive to low frequency contents as illustrated in this case with the second and the third NCOE.

The assumption of a constant damping coefficient is questionable regarding the results of the non-parametric identification in section 3.5.2 that suggest that the damping ratio depends on the displacement amplitude. Moreover, a damping proportional to the tangent stiffness is generally a more satisfying model than a constant damping as stated by several authors (see section 1.2.2.3).

As a perspective, the solving of the thermodynamic drawbacks of the model described in section 3.2.4 would allow for a physical-wise study of the dissipated energy uncoupling the different phenomena involved. Some of them could alternatively be modeled by an

evolving equivalent viscous damping. If this approximation proves to be satisfying, the extension of such an evolution law could be extended to the case of the predictive finite element method computation thanks to the development of calibration techniques of this evolution law with respect to material and structural parameters.

## 4.3 Finite element modeling

### 4.3.1 Forewords

It has been shown in section 1.2.1 that it is still of interest to reduce the computational cost through the use of simplified finite elements (FE). Sorted according to their geometrical complexity, one can cite three types of elements:

- multifiber or multilayer elements;
- generalized beam or shell elements;
- macro-elements.

The equivalent SDOF oscillator developed in chapter 3 might be sorted in the macro-element type, since it does not represent the physical structure itself but only its behavior. This chapter rather focuses on multifiber elements which model the IDEFIX beams explicitly. The difference between the multifiber and the generalized beam model is discussed in the next section (4.3.2).

### 4.3.2 Multifiber elements

The main differences between multifiber beam elements and generalized beam elements concern the cross-section behavior. In the former, the classical Euler-Bernoulli (or Timoshenko) beam kinematics are associated with more local material constitutive laws at the section scale. Hence, for Euler-Bernoulli kinematics, a constitutive matrix  $\mathbf{C}$  is formulated at the initial state as:

$$\mathbf{C} = \begin{bmatrix} C_{11} & 0 & C_{13} & C_{14} \\ 0 & C_{22} & 0 & 0 \\ C_{13} & 0 & C_{33} & C_{34} \\ C_{14} & 0 & C_{34} & C_{44} \end{bmatrix} \quad (4.37)$$

where:

$$\begin{aligned} C_{11} &= \int_S E \cdot dS & C_{13} &= \int_S E \cdot z \cdot dS & C_{14} &= -\int_S E \cdot y \cdot dS \\ C_{22} &= \int_S G \cdot (y^2 + z^2) \cdot dS & C_{33} &= \int_S E \cdot z^2 \cdot dS \\ C_{34} &= -\int_S E \cdot y \cdot z \cdot dS & C_{44} &= \int_S E \cdot y^2 \cdot dS \end{aligned}$$

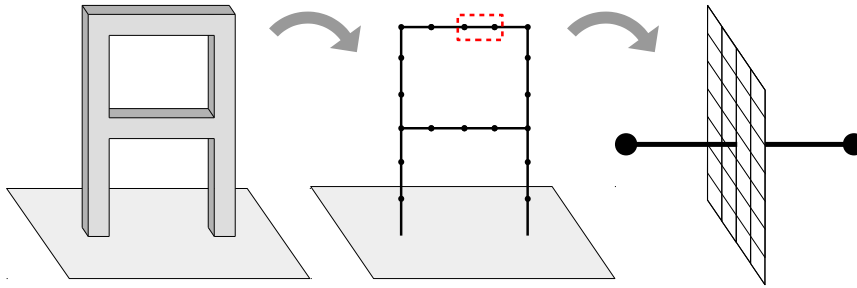


FIGURE 4.9: Multifiber beam formulation (inspired from Davenne *et al.*, 2003)

with  $E$  and  $G$  the Young's and shear moduli which may vary in the section. At the cross-section level, this matrix links the generalized stress  $\mathbf{s}$  with the generalized strain  $\mathbf{e}$ :

$$\mathbf{s} = \begin{pmatrix} N \\ M_x \\ M_y \\ M_z \end{pmatrix} \quad \text{and} \quad \mathbf{e} = \begin{pmatrix} \varepsilon \\ \theta_x \\ \chi_y \\ \chi_z \end{pmatrix} \quad (4.38)$$

through the relationship:

$$\mathbf{s} = \mathbf{C} \cdot \mathbf{e} \quad (4.39)$$

Knowing the generalized strain  $\mathbf{e}$ , the local strain can be computed for each element of the cross section with the assumption that plane sections remain plane. The stress is then computed with respect to the constitutive law. The detailed implementation of the multifiber beam model depicted on figure 4.9 is given by Davenne *et al.*, 2003. Multifiber elements allow the explicit modeling of the reinforcements since each element in the cross-section can have its own material properties. In its original implementation, the adherence between each fiber is ensured. This latter point prevents a satisfying modeling of steel-concrete bond slipping. Further developments have been investigated recently to enlarge the capabilities of multifiber models, such as taking into account the warping under torsion loading (Capdevielle *et al.*, 2016), or the effect of the confinement on the concrete in the steel frames (Khoder *et al.*, 2017). Nevertheless, the multifiber formulation that does not include the aforementioned improvements is used in this numerical study.

### 4.3.3 IDEFIX numerical multifiber beam model

#### 4.3.3.1 Discretization

##### a Axial discretization

The software used for the numerical simulations presented in this section is Cast3M (CEA, 2017). First, nodes are created at each position corresponding to a sensor, as described in section 2.6.1 and on figure 2.22. Hence, 10 nodes are placed. Then, beam elements are created connecting the neighbor nodes. The beam elements 1 and 10 on figure 4.10 only support the inertial load of the beam itself since the boundary conditions

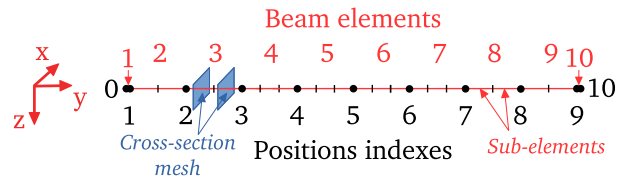


FIGURE 4.10: FE discretization of IDEFIX beam in the axial direction

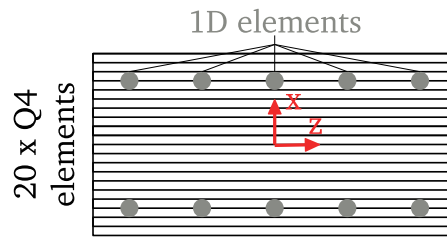


FIGURE 4.11: FE discretization of IDEFIX beam in the cross-section

are put on nodes 1 and 9 and no external load is applied outside the beam-end supports. Because of this and because of the small length of these two beam elements, 1 sub-element is sufficient to describe the behavior of the whole beam on these two beam elements. The other beam elements are discretized into 2 or 3 sub-elements. For beam elements 4, 5, 6 and 7, three sub-elements are used because the bending moment is maximum in this area. For elements 2, 3, 8 and 9, two sub-elements are used. This discretization is thought to optimize the computational cost. Overall, 23 sub-elements are created.

#### b Cross-section discretization

The only studied loading is the bending of the beam around the  $z$ -axis. Hence, for the sake of computational efficiency, only 1 element is required in the  $z$ -direction (see figure 4.11). To have a better description of the damage progress in the concrete, 20 elements are used in the  $x$ -direction. Regarding the steel reinforcements, only the longitudinal rebars are modeled by 1D elements, i.e. a point in the cross-section. Each 1D element is placed at the position of the center of the corresponding rebar. A section and a moment of inertia are associated to each element. As mentioned in section 4.3.2, a perfect adherence is supposed between the steel bars and the surrounding concrete. The FE mesh finally obtained is represented on figure 4.12 on which only the cross-sections of the 23 sub-elements are represented (for HA12-C1A beam type as an example).

#### 4.3.3.2 Boundary conditions

The boundary conditions are supposed perfect, they are given in table 4.5. A more realistic modeling would be provided by considering elastic stiffness for the beam-end supports.

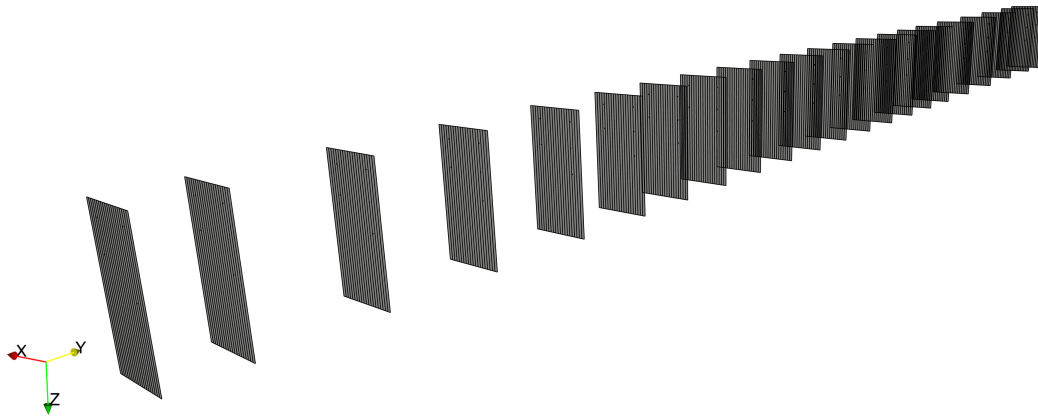


FIGURE 4.12: Multifiber beam mesh of a HA12-C1A beam

However, it will be shown in section 4.3.4 that the perfect boundary condition hypothesis is satisfactory.

DOF	P1	P3	P7	P9
UX	0	1	1	0
UY	0	1	1	1
UZ	0	0	0	0
RX	0	0	0	0
RY	0	1	1	0
RZ	1	1	1	1

TABLE 4.5: Blocked (0) and freed (1) DOFs for nodes P1, P3, P7 and P9 depicted on figure 4.10 — U corresponds to a translation and R corresponds to a rotation

#### 4.3.3.3 Additional masses

The additional masses of 360 kg each are lumped at nodes at positions 3 and 7 (figure 4.10). The rotational inertias are not considered for the computation because the masses are placed close to the mean fiber of the beam and because the rotational accelerations of the sections remain low. This is verified by differentiating the rotational velocities provided by the gyrometers (section 2.6.4).

#### 4.3.3.4 Additional viscous damping

An additional viscous damping formulated as a Rayleigh damping is considered. It is formulated as explained in section 1.2.2.2 so that the viscous damping ratio is equal to 2 % at the 1<sup>st</sup> and the 2<sup>nd</sup> eigenfrequencies, following equation (1.10).

#### 4.3.3.5 Materials models

##### a Concrete

The model used for the concrete is the one proposed by Richard & Ragueneau, 2013 and called RICBET in Cast3M. It has been formulated for the cyclic loading of quasi-brittle materials. The features of this model are:

- an asymmetric behavior in traction and in compression;
- an unilateral effect;
- permanent strains;
- hysteretic effects.

Therefore, this model is adapted for a proper description of the behavior of the concrete under seismic loading. The model has been adapted for the multifiber formalism in Cast3M under the name RICBET\_UNI. The parameters have been identified thanks to the cyclic compressive tests described in section 2.3.3.1 and whose full results are given in appendix A.1. An illustration of the cyclic reverse behavior of this model associated to a fiber of unit dimensions is given in figure 4.13.

Symbol	Parameter	C1A	C1B	C2	Unit
$E$	Young's modulus	26.2	28.1	28.2	GPa
$\nu$	Poisson's ratio	0.2	0.2	0.2	–
$f_t$	Tensile strength	2.09	2.22	2.09	MPa
$A_d$	Fragility coefficient in traction	0.006	0.006	0.006	m <sup>3</sup> /J
$\gamma$	Kinematic hardening modulus 1	3.0	3.0	3.0	GPa
$\alpha$	Kinematic hardening modulus 2	8.0	8.0	8.0	MPa <sup>-1</sup>
$\sigma_f$	Mean closure stress	-3.0	-3.0	-3.0	MPa
$f_c$	Compressive strength	27.8	25.0	45.2	MPa
$\alpha_f$	Plastic surface modulus	1.0	1.0	1.0	–
$\alpha_\phi$	Plastic pseudo potential modulus	1.0	1.0	1.0	–
$a_R$	Plastic hardening modulus 1	28.1	28.1	28.1	GPa
$b_R$	Plastic hardening modulus 2	550	650	550	–
$\sigma_U$	Asymptotic compressive stress	10.0	10.0	10.0	MPa

TABLE 4.6: Parameters identified for the concrete model

##### b Steel

If a numerical study taking into account plasticity of the rebars were to be carried out, it would be suggested to use the model commonly designated as Menegotto–Pinto model. It was originally proposed by Giuffrè, 1970 (and Pinto) and used by Menegotto, 1973 (with Pinto). It has then been modified by Monti & Nuti, 1992 to take into account the buckling of the reinforcing bars.

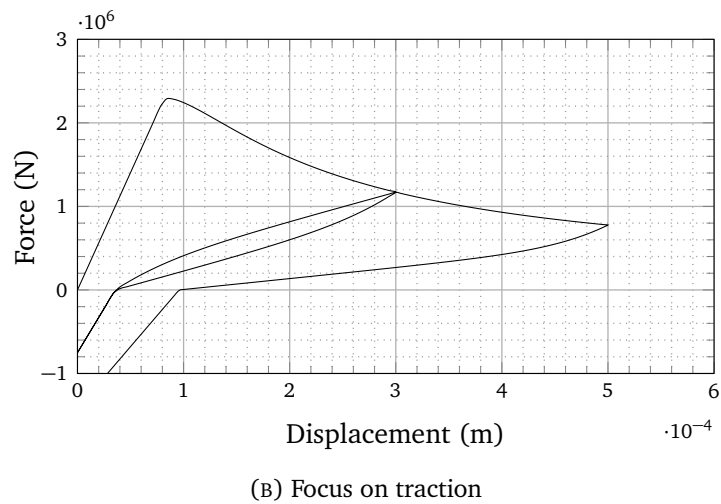
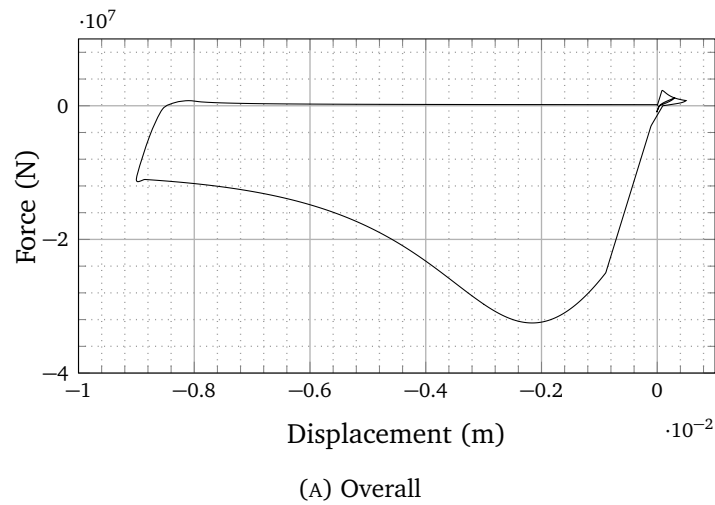


FIGURE 4.13: Reverse cyclic behavior of a fiber of unitary dimensions associated to C1B concrete model (traction counted as positive)

However, an elastic behavior is supposed for the reinforcing bars because no steel yielding has been observed during IDEFIX tests. The Young's Modulus is taken equal to 210 GPa and the Poisson's ratio to 0.3.

#### 4.3.4 Validation of the FE model

##### 4.3.4.1 Eigenfrequencies

A first validation is made by comparing experimental and numerical vibration modes. Only the three first eigenfrequencies are considered.

The eigenfrequencies are well-predicted but the ones of HA12-C1B and HA12-C2 are slightly over-estimated. Moreover, they are experimentally lower than the ones of the

Symbol	Parameter	Value	Unit
$E$	Young's modulus	210	GPa
$\nu$	Poisson's ratio	0.3	–

TABLE 4.7: Parameters used for the steel model

Beam type	Experimental (Hz)			Numerical (Hz) <sup>1</sup>		
	Mode 1	Mode 2	Mode 3	Mode 1	Mode 2	Mode 3
HA12-C1A	7.14	22.5	57.8	7.13 <sup>-0.11 %</sup>	24.2 <sup>+7.50 %</sup>	69.3 <sup>-19.9 %</sup>
HA12-C1B	6.81	21.5	57.2	7.36 <sup>+8.04 %</sup>	25.0 <sup>+16.3 %</sup>	71.5 <sup>-25.1 %</sup>
HA12-C2	6.84	22.0	57.7	7.37 <sup>+7.75 %</sup>	25.0 <sup>+13.9 %</sup>	71.6 <sup>-24.0 %</sup>
RL12-C1A	7.13	22.5	58.9	7.13 <sup>+0.07 %</sup>	24.2 <sup>+7.44 %</sup>	69.3 <sup>-17.7 %</sup>
HA16-C1A	7.11	23.1	58.2	7.23 <sup>+1.65 %</sup>	24.6 <sup>+6.72 %</sup>	70.1 <sup>-20.5 %</sup>
HA20-C1A	7.16	22.6	57.6	7.11 <sup>-0.66 %</sup>	24.1 <sup>+6.64 %</sup>	69.1 <sup>-19.4 %</sup>

<sup>1</sup> Superscripts are the relative difference between the numerical and the experimental eigenfrequency.

TABLE 4.8: Comparison between numerical and experimental eigenfrequencies

beams that are made of C1A concrete while the numerical ones are on the contrary higher. Cracking related to the shrinkage of concrete may have occurred during the drying for concretes C1B and C2 and could explain this lower frequency. Indeed, it is recalled that it has been observed that the measures from hammer tests are sensitive to cracks when there is a pinching effect. The concretes have a relatively high water/cement ratio (respectively 0.60 and 0.65, see the delivery forms in figures C.1 and C.2). The first cast of concrete C1 (C1A) seemed to contain less water than the second one (C1B) based on its consistence. This point could not be verified, but a less important cracking related to shrinkage could explain a part of the shift in eigenfrequencies.

#### 4.3.4.2 Dissipated energy

To assess the ability of RICBET\_UNI model to dissipate the right amount of energy, a comparison is made for the last cycle of a quasi-static test QSC1 on figure 4.14. The pinching effect is represented adequately, meaning that the responsible phenomena are taken into account in the model. As mentioned in section 3.2.3, this observation consolidates the idea that the unilateral effect is a good candidate as a responsible of the pinching effect.

## 4.4 Numerical results

The results of the FE simulation are compared on figure 4.16 with the results obtained with the equivalent nonlinear SDOF oscillator previously presented in section 4.2.4. The SDOF oscillator displacement and the FE 1<sup>st</sup> mode displacement are very close from each other. It is interesting to note that the FE computation took about 5 hours on a computer

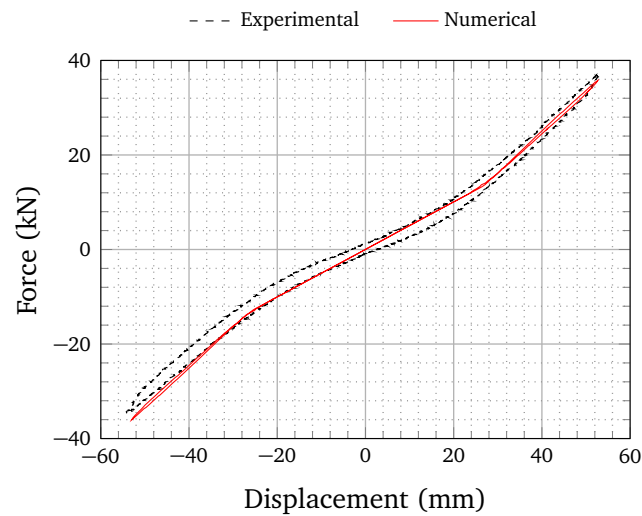


FIGURE 4.14: Comparison of numerical (Cast3M) and experimental last cycle of QSC1 test carried out on beam HA16-C1A-1

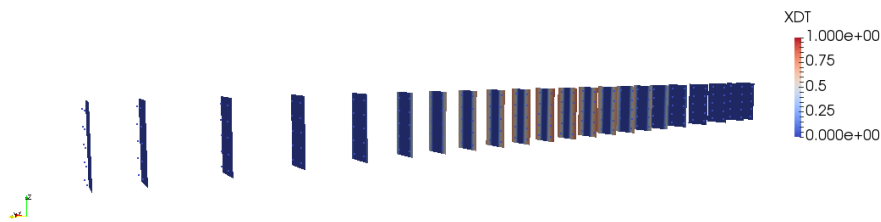
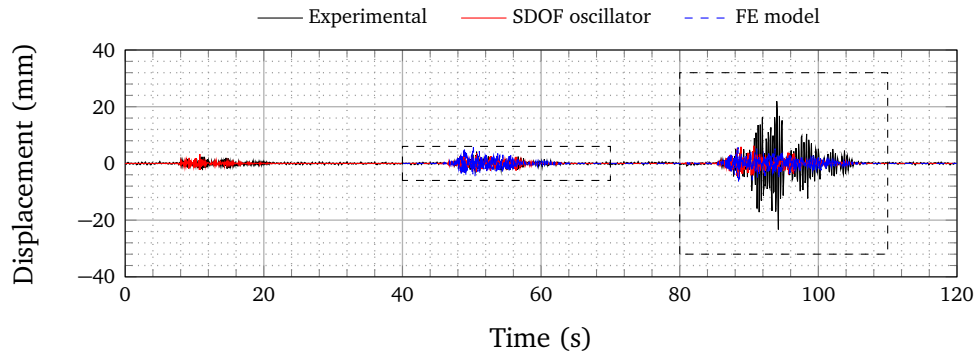


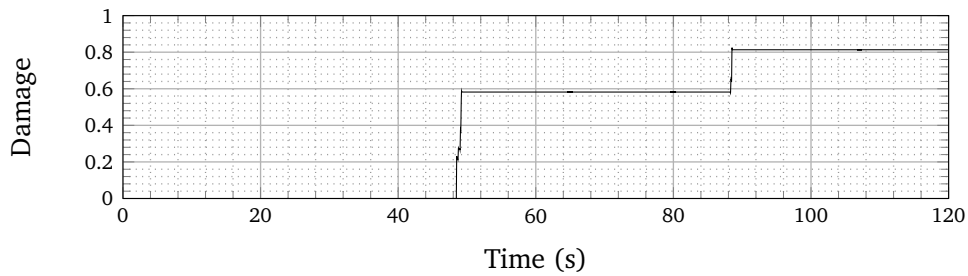
FIGURE 4.15: Final damage state of the FE model (maximum at 0.82)

equipped with a Intel<sup>®</sup> Xeon<sup>®</sup> CPU E5-2650 v2 at 2.60 GHz (8 cores) and 32 Go of RAM while the SDOF oscillator computation took less than 5 seconds. The Cast3M computation has been carried out only from the second NCOE for computational cost reasons and because the damage during the first NCOE is either very low or nonexistent.

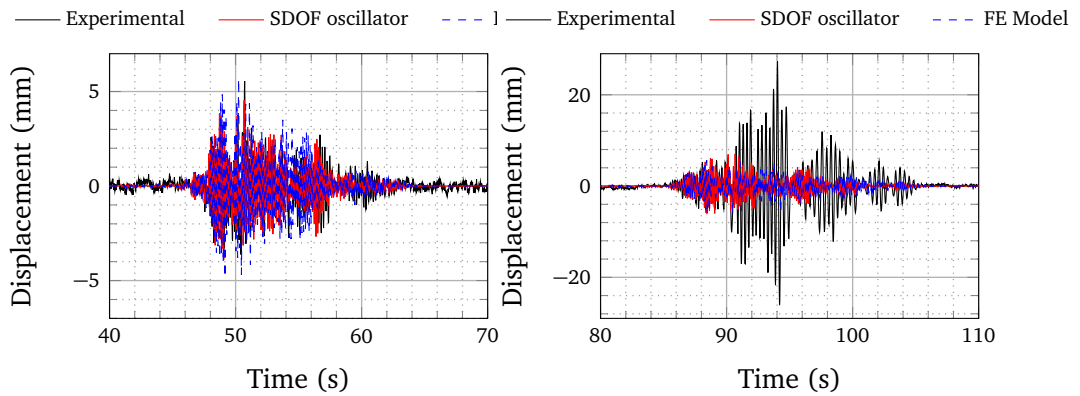
The final damage state of the FE model is presented on figure 4.15 and reaches a maximum of 0.82 (see figure 4.16b) at lower and upper fibers at the mid-span. The beam has not reached its maximum damage capacity because the larger damage value is lower than 1 and the elements closer to the mean fiber are not damaged. The damage pattern is constant in the z-direction because only one element has been considered in the cross section in this direction. The numerical deformed shape of the beam is projected on the eigenbasis in the same way as it has already been done with Videometric<sup>®</sup> measured displacement field (section 3.1.2.4), and the projection error remains small. An overestimation of the damping in the damaged state due to the use of an initial stiffness proportional Rayleigh damping has been thought as a candidate to explain the over-damped displacement response. However, the anticipation of this degradation by choosing the degraded first eigenfrequency as the first damping setting frequency ( $\omega_a$  in



(A) Overall



(B) Damage evolution of the upper fiber of the beam at the mid-span during the NCOE Cast3M simulations



(C) Zoom 1

(D) Zoom 2

FIGURE 4.16: Comparison between the experimental 1<sup>st</sup> mode displacement, the computed equivalent SDOF nonlinear oscillator displacement and the FE computed 1<sup>st</sup> mode displacement for successive scaled NCOE and for the parameters identified for HA12-C1B

section 1.2.2.2) has not fixed the problem.

## 4.5 Concluding remarks

Numerical tools to simulate the dynamic response of the IDEFIX beams have been presented in this chapter. Basically, two approaches are compared with each other: the equivalent SDOF oscillator modeling and the FE modeling. None of both methods succeeds to model adequately the dynamic response with a constant damping ratio (2 % in this case) in case of the strongest earthquake accelerogram. In fact, even a zero damping ratio provides an over-damped response — not to mention that, in this case, spurious vibrations that are numerically induced appear. A correction of the hysteretic model of the SDOF oscillator allows for a better agreement between numerical and experimental results, but the physical relevance of an arbitrary correction brought to a model that has been identified on experimental results is questionable and might not be fully justified. However, the quality of the identification performed on the QSC1 quasi-static tests is itself questionable and it should be kept in mind that no definitive conclusion can be drawn on this single basis. The performance of the nonlinear corrected model suggests that a good representation of the hysteretic behavior is sufficient to compute with a satisfying precision the dynamic response of the beam. The fact that the external dissipations are well-controlled experimentally because of the technological solutions selected for the boundary conditions is probably a reason why an additional viscous damping seems unnecessary.

A less biased approach would have been to propose a different damping model. Indeed, as suggested by the results presented in chapter 3, the damping ratio depends on the cycle amplitude. This dependence may have a significant influence on the dynamic response. In particular, the EVDR decreases with higher displacement amplitude and this could finally increase the displacement response amplitude. This effect is nonlinear (auto-dependent) and requires further investigations.

Nonetheless, the nonlinear SDOF oscillator model identified on the quasi-static tests provides a reliable displacement response for light to moderate intensity earthquakes and a better identification procedure (based on more specimens) would have probably considerably improved the results in case of higher intensity earthquakes. The additional viscous damping seems not to be necessary when the spurious dissipation sources are well-controlled or absent as it is the case with IDEFIX experiments (e.g. friction between elements, non-structural elements, etc.). A light viscous damping may also be useful for the sake of numerical stability though. This damping could be added in the SDOF oscillator model, or implicitly accounted by the use of a HHT algorithm (cf. section 4.2.2).



## Conclusions and perspectives

Surprisingly, finding a satisfying definition of the term “damping” on the Internet may prove to be quite difficult. At the time this thesis is written, even Wikipedia has not a dedicated page (the closer match being “damping ratio”). However, Google™ provides the following definition which is rather precise: “a reduction in the amplitude of an oscillation as a result of energy being drained from the system to overcome frictional or other resistive forces” (“*damping definition*” search)<sup>1</sup>. Google™ also provides another interesting statistic: the occurrence rate of the term “damping” in the Google™ Books database plotted on figure 4.17 (“*damping definition*” search). Of course, these data are more a qualitative than a quantitative metric of the popularity of the study of damping in the context of mechanical engineering since no distinction is made depending on the context of each usage of the word “damping”. Nevertheless, the usage of the word “damping” reached its climax in the 1960’s and has decreased since then but remains quite popular. This maximum matches with the publication of Jacobsen, 1960. Indeed, Jacobsen proposed a computationally efficient way to model the damping in structures through an equivalent damping ratio evaluated from experimental evidence. The appearance of more advanced techniques such as finite element methods associated to nonlinear constitutive laws have probably diminished the interest of scientists and engineers on the EVDR and equivalent SDOF modeling. Still, the work carried out in this thesis have shown that in the particular context of the structure assimilable to a nonlinear SDOF oscillator and for low to moderate intensity earthquakes, such a model is much more computationally efficient than a FE model. However, it has also been regularly emphasized in this thesis that the equivalent viscous damping models lack physical evidence.

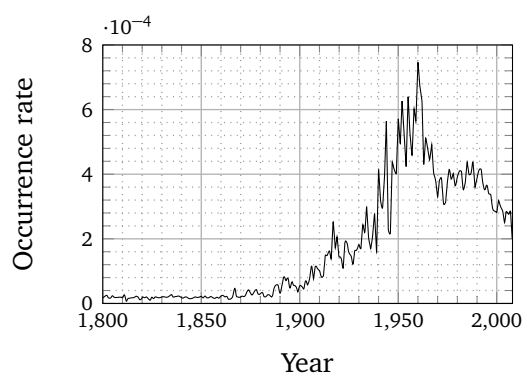


FIGURE 4.17: Occurrence rate of the term “damping” through years in Google™ Books database (obtained by typing “damping” in the search bar)

<sup>1</sup>This definition is limited since it does not take into account the case of a damped system initially at rest and subjected to a harmonic force: the oscillations increase until the permanent regime is reached.

In the first chapter, different sources of dissipation have been presented and sorted as it is commonly made in two categories: external and internal dissipations. The external dissipations are not studied in this work, but the use of an equivalent viscous damping to model them seems to be justified since they remain generally lower than the internal dissipations and because some of them actually show viscous characteristics. The technical solutions used for the boundary conditions allow to reduce drastically the said external dissipations. The focus is rather made on the so-called internal dissipations. Various damping models have been presented. Since the publication of Jacobsen, 1960, various attempts to improve the standard viscous damping model and to extend it to multi-degree-of-freedom systems have been made. The emergence of the finite element methods has boosted even more the use of the proportional damping approaches (also called Rayleigh damping, section 1.2.2.3). If a general formulation is given by Caughey's damping matrix, the two most used versions are probably the initial stiffness proportional and the tangent stiffness proportional damping matrix. The main advantage of these two damping models (tangent or secant stiffness proportional) is that their formulation and implementation is straightforward. Jehel *et al.*, 2014 state that it is possible to control the damping throughout the inelastic time-history analysis with both models, even if it is more convenient with the tangent one. Nevertheless, the said control is often limited to keep the damping ratios constant and the question of the way the damping ratio should evolve remains open. Thus, a better knowledge on the variation of damping during the nonlinear time-history analysis is required. The IDEFIX experimental campaign aims to enrich this knowledge.

The second chapter presents the design of the experimental campaign thought to study the evolution of the damping throughout the degradation of the beams on different modes, depending on various material and structural parameters. Original technical solutions have been used and allow for reducing the gap between the simply supported beam model and the experimental setup. The boundary conditions are well-handled thanks to specially-designed elastic blades and air-cushion devices. Azalée shaking table also allows for a more uncoupled vibration eigenmode study by its controllable 6 degrees of freedom. The experimental campaign is divided into two parts: quasi-static tests and dynamic tests. The fact that the same real scale components are tested in both dynamic and quasi-static with comparable boundary conditions is a novelty. It allows for comparing the different strategies of identifying the EVDR.

The third chapter does not pretend to exploit the whole experimental data obtained during the 642 tests carried out but rather to highlight remarkable results. For example, it is observed that the dissipations are higher in dynamics than in quasi-static (figure 3.20). An hysteretic model accounting for various mechanisms (damage, hardening, friction, unilateral effect, pinching) has been formulated to compute the cyclic reverse quasi-static behavior of the beams. This model allowed for extensive numerical experiments in order to assess the influence of various parameters on the EVDR evaluated by Jacobsen's areas method (JAM). If the influence of the model parameters have been investigated, the ductility level and the displacement amplitude have been identified as of first importance on the EVDR value. The link between the ductility level and the EVDR has been explained and modeled in many ways since a long time (depending on the hysteretic model considered as presented in table 1.1), but the influence of the displacement amplitude is generally not taken into account. The pinching effect is also an important factor in this phenomenon: it reduces the energy storage capacity for the lower displacement amplitudes, thus increasing

the EVDR for small displacement amplitudes. The pinching effect is only observed on cracked beams. This means that cracks due to a normal life cycle of the RC structure may be beneficial for the damping of small amplitude vibrations. It would also indicate that there is a risk that the values of damping ratios obtained from low-level dynamic excitation (e.g. hammer shocks or ambient noise) are over-estimated if used directly for the simulation of seismic loadings. In particular, the hammer shock tests could be very sensitive to the force of the shock which is difficult to control for the operator. This effect should be investigated in order to check the relevance of the EVDR identified by this mean.

Regarding the simulations, it might be advised to activate the additional viscous damping only beyond a given displacement amplitude and to use a value lower than the one deduced from the low-level level excitations. A test consisting in a high-level dynamic signal makes it possible to assess more confidently the damping ratios for high amplitude input signals, but such tests are destructive and difficult to perform in-situ. For these reasons, only mock-ups such as CAMUS (SEMT/EMSI/RT/98-066A, 1998), SMART 2008 (Richard *et al.*, 2016a), SMART 2013 (Richard *et al.*, 2016b) or IDEFIX (Heitz *et al.*, 2017a) would allow for such studies.

Numerical experiments provide a useful tool for the evaluation of EVDR for higher displacement and ductility levels. Furthermore, it helps for plotting the damping surface of figure 3.34 that would otherwise require many tests and specimens to be evaluated. Criticisms may be formulated about the definition of the displacement ductility level being model-dependent and mostly, difficult to assess since it requires preliminary computations to predict the elastic limit displacement. A more arbitrary definition of another displacement ductility might be based on a relative deflection expressed as a ratio of the span for beam components similarly to what is done in *Eurocode 2: Design of concrete structures – Part 1-1: General rules and rules for buildings 2005* clauses 7.4.1 and 7.4.2 regarding the deflection limit at service limit state (SLS). A limit is set at  $\delta_{SLS} = \frac{L}{250}$ ,  $L$  being the span of the beam. In this case, this limit is equal to 23.6 mm. Hence, another possible definition of the displacement ductility level might be:

$$\mu = \frac{\delta_m}{\delta_{SLS}} \quad (4.40)$$

with  $\delta_m$  the maximum seen displacement. Nevertheless, even if this definition is model-independent, the influence of the structural and material parameters on the EVDR should be taken into account anyway through a modification of the damping surface.

The last chapter presents first numerical developments for the modeling of IDEFIX tests. When using a relatively low constant viscous damping ratio (i.e. 2 %), the single-degree-of-freedom oscillator associated to the nonlinear restoring force model identified in the previous chapter is able to model adequately the dynamic response of the beam to the Niigata-ken Chuetsu Oki earthquake (NCOE) after some modifications brought to the set of parameters identified in quasi-static. Without these changes, the nonlinear model does not provide satisfying results for the highest amplitudes. This modification is difficult to justify from a physical point of view though: are the quasi-static tests not representative of the dynamic hysteretic behavior or is the quasi-static identification biased for experimental reasons? Due to practical reasons, an identification based on several versions of the same specimen was not possible and this question remains open. The nonlinear finite element computation performed with Cast3M code did not succeed to

provide realistic results despite several sets of material model parameters tested. It should be noted that the SDOF model and the FE model give very similar responses, but the former is much more faster from a computation point of view (of the order of one second versus one hour). The improvement of the SDOF model would make it a very efficient tool to assess the displacement demand of a component. In such a case, it may be possible to do without any additional viscous damping to model realistically (and physically) the dynamic response of the beam.

If further investigations are still necessary regarding the IDEFIX experimental campaign, several major results about the damping arise:

- the higher is the ductility level, the higher is the EVDR;
- this increasing of EVDR is due to a decrease of the energy storing capacity rather than an increase of energy dissipation;
- in agreement with the observations made with the non-parametric identification method, the higher is the displacement amplitude, the lower is the EVDR (at a given ductility level);
- the pinching effect may partially explain the previous observation (lower stiffness for small displacements implies lower energy storage capacity).

Also, several methods show promising results:

- the identification of an hysteretic restoring force allows for numerical experiments;
- the numerical experiments allow for the assessment of the influence of model and loading parameters on the dissipations;
- the damping surface obtained consequently to the numerical experiments may be used as an abacus that provides the EVDR corresponding to a displacement amplitude and a ductility level (requires an iterative process);
- different versions of the JAM were compared, the ones that have the widest applicability domain are the RPP and the NLFC-JAM (figures 3.15 and 3.14 respectively);
- the non-parametric identification gives an estimation of the EVDR throughout the nonlinear time-history analysis and consolidates the observations made with JAM carried out on quasi-static tests that the EVDR depends on the displacement amplitude and on the ductility level.

These results provide improvement possibilities for the modeling of the damping in RC structures. The “damping surface” constitutes the first step in the formulation of an EVDR evolution law that could be implemented in a first place in the SDOF oscillator computed with the implicit Newmark scheme (section 4.2.1). Adjustments are necessary to prevent the double counting of hysteretic dissipations that are also included in the EVDR evaluated by JAM during the numerical experiments. This could be done by explicitly separating the restoring force in two contributions. This is already the case with IDEFIX model that has a

damage-related force and a friction-related force (section 3.2.4):

$$F = F^e + F^\pi \quad (4.41)$$

$$\text{with } F^e = \frac{\partial \Psi}{\partial u} = K_p \cdot (1 - d_i) + K_p \cdot d_i \cdot (u - u^\pi) \quad (4.42)$$

$$\text{and } F^\pi = -\frac{\partial \Psi}{\partial u^\pi} = K_p \cdot d_i \cdot (u - u^\pi) \quad (4.43)$$

The former contribution dissipates energy only when the damage grows, which does not happen when the JAM is used on stabilized cycles. Hence, the EVDR is rather calibrated to replace the friction-related force. Eventually, the friction-related contribution could be deleted or modified to be replaced by the EVDR evolution law deduced from the damping surface. The deletion of the friction contribution in RICBET\_UNI model (in Cast3M) is also of interest because the associated local complexity introduced may lead to a less robust global computation (i.e. problems of convergence, slower computation). The suggested modification of the SDOF oscillator model may provide a first validation step to reach this second goal regarding the FE computation.

The problematics of the damping in RC structures during seismic events represent a vast field of challenges that has still to be tackled. The amount of tests and experimental results consecutive to IDEFIX experimental campaign certainly contains many other interesting results. As part of SINAPS@ project ([SINAPS@](#)), an important work of storage, formatting, classification and communication is necessary to make these data available and exploitable by the scientific community. A parametric identification of a damping evolution law is a promising pursuit encouraged by the identification of the damping surface obtained in this thesis thanks to numerical experiments (section 3.3.4). Indeed, the identification of the parameters of such a damping surface depending on structural and material properties is a highly motivating task.



## Appendix A

# Experimental results

### A.1 Cyclic compressive tests results

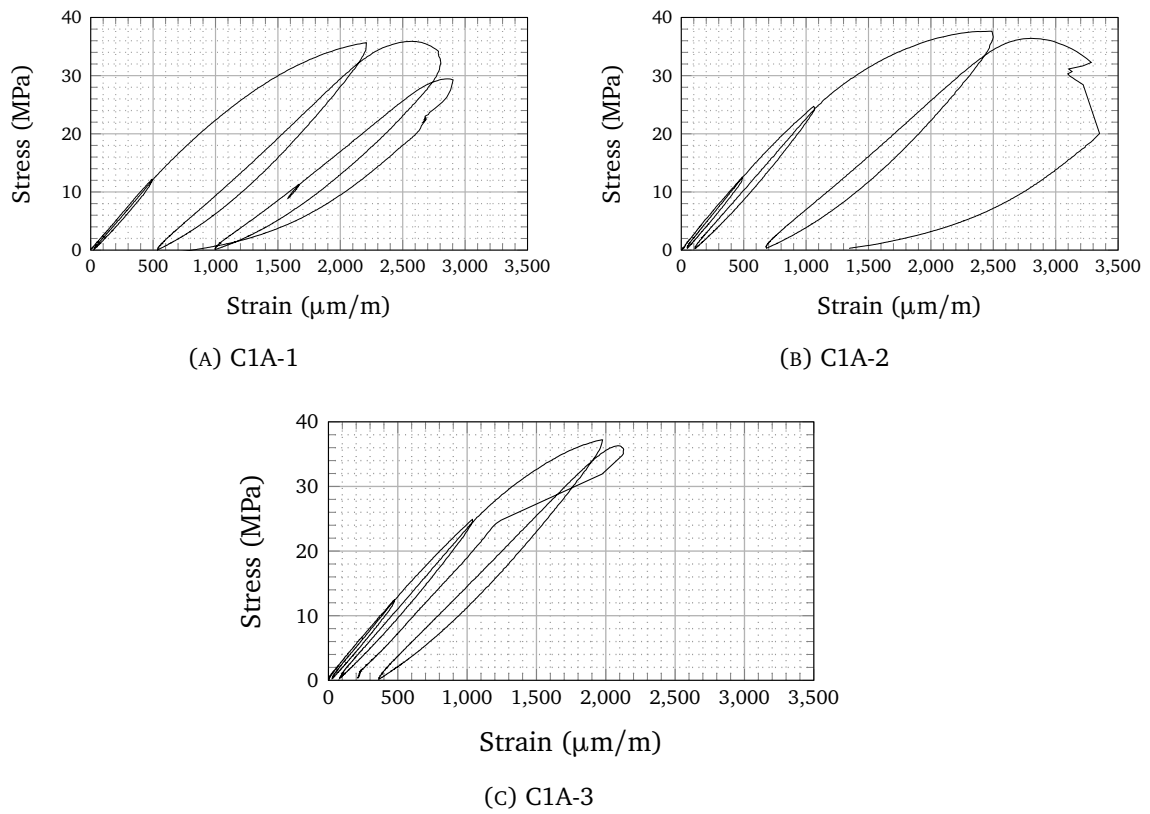


FIGURE A.1: Cyclic compression test of C1A

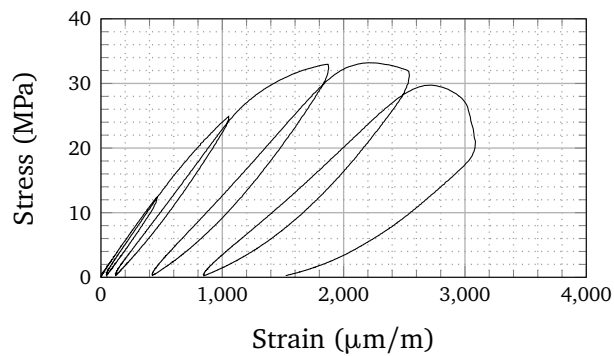
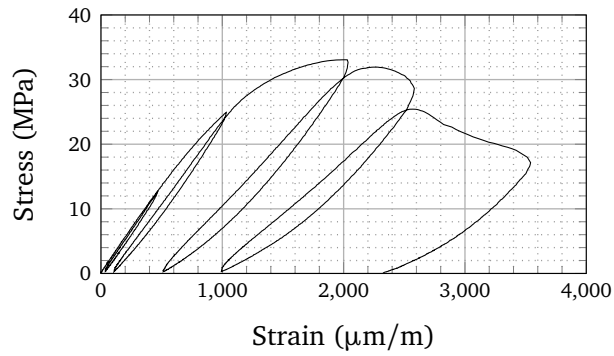
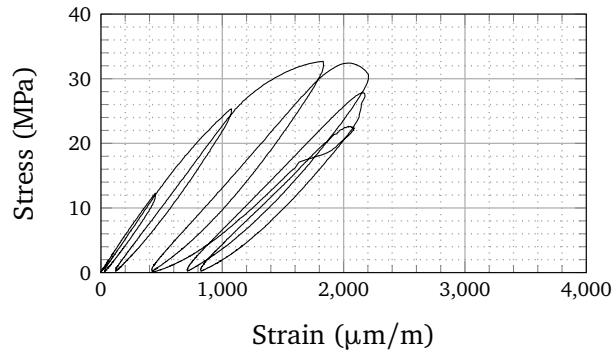
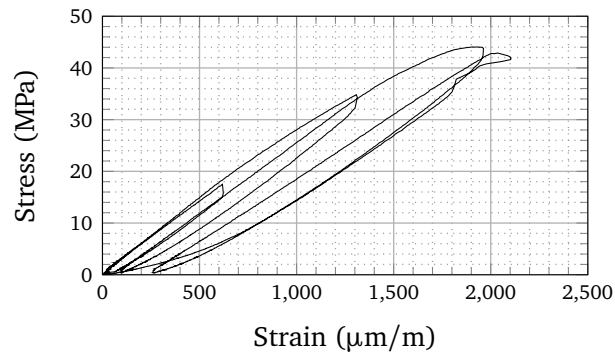
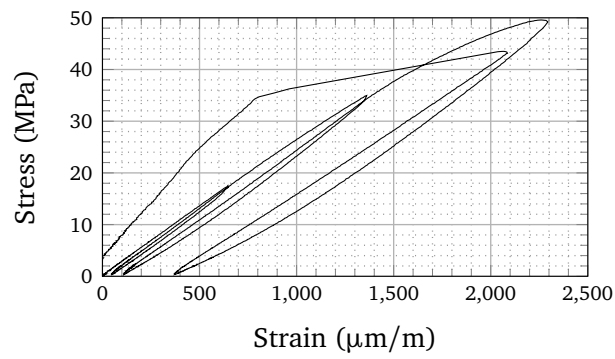


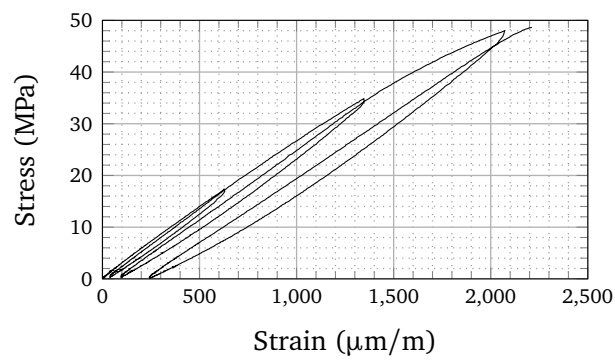
FIGURE A.2: Cyclic compression test of C1B



(A) C2-1



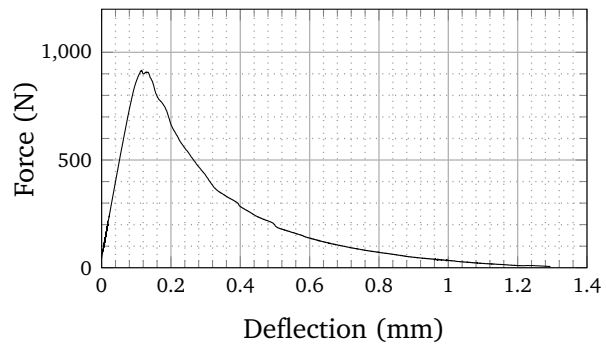
(B) C2-2



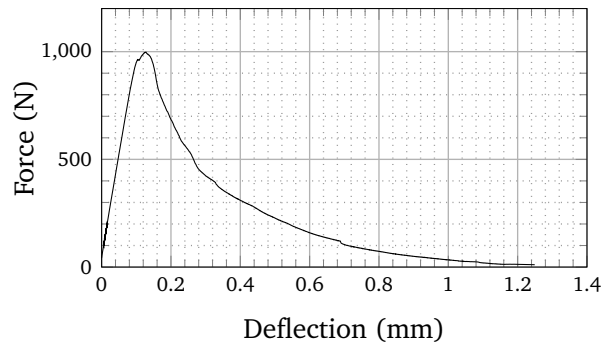
(C) C2-3

FIGURE A.3: Cyclic compression test of C2

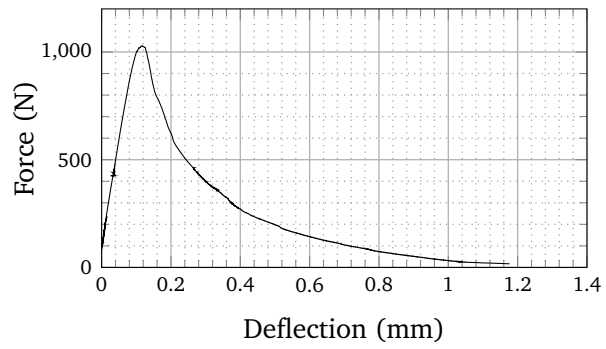
## A.2 Fracture energy measurement tests



(A) C1A-1

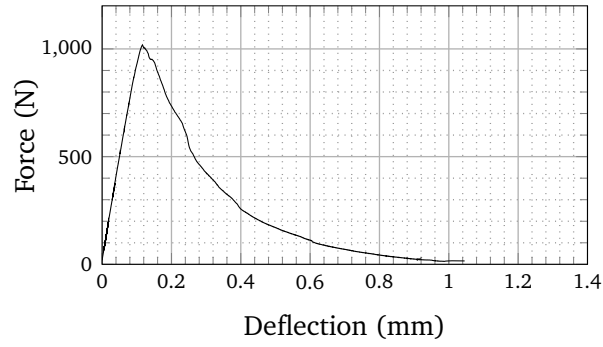


(B) C1A-2

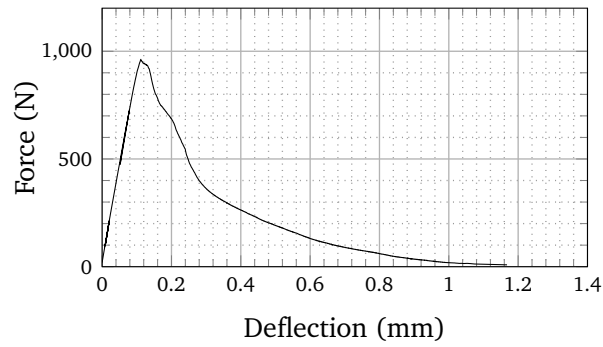


(C) C1A-3

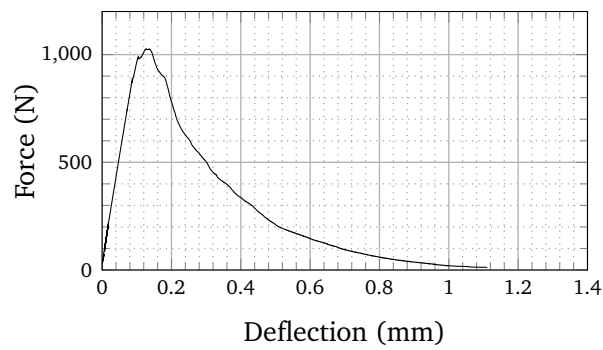
FIGURE A.4: Fracture energy measurement of C1A



(A) C1B-1

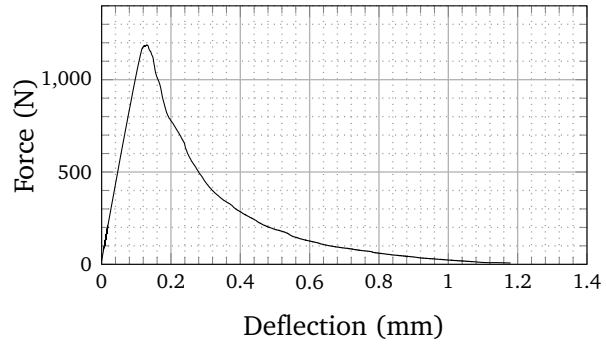


(B) C1B-2

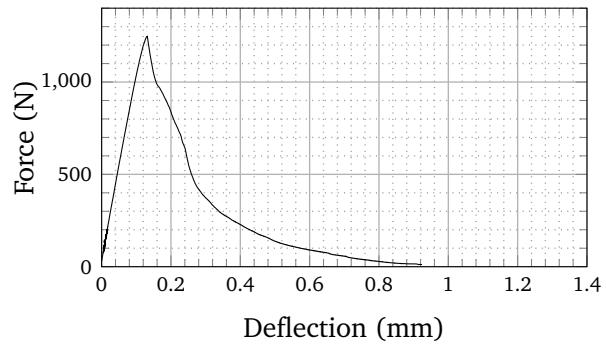


(C) C1B-3

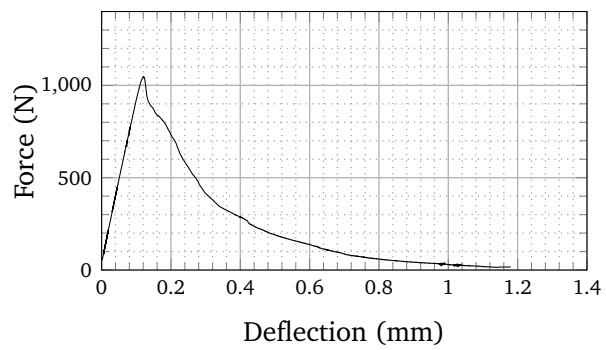
FIGURE A.5: Fracture energy measurement of C1B



(A) C2-1



(B) C2-2



(C) C2-3

FIGURE A.6: Fracture energy measurement of C2

### A.3 Pull-out tests

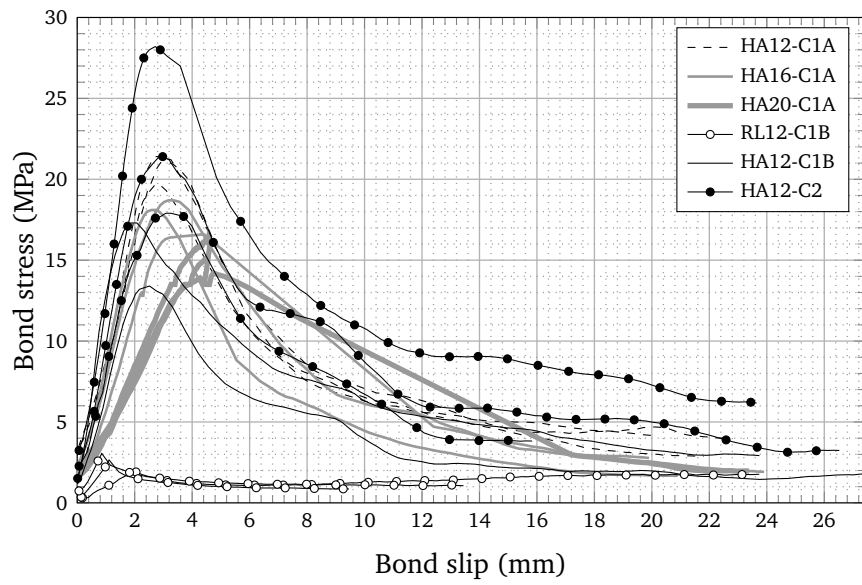


FIGURE A.7: Pull-out tests results



## **Appendix B**

# **Plans**

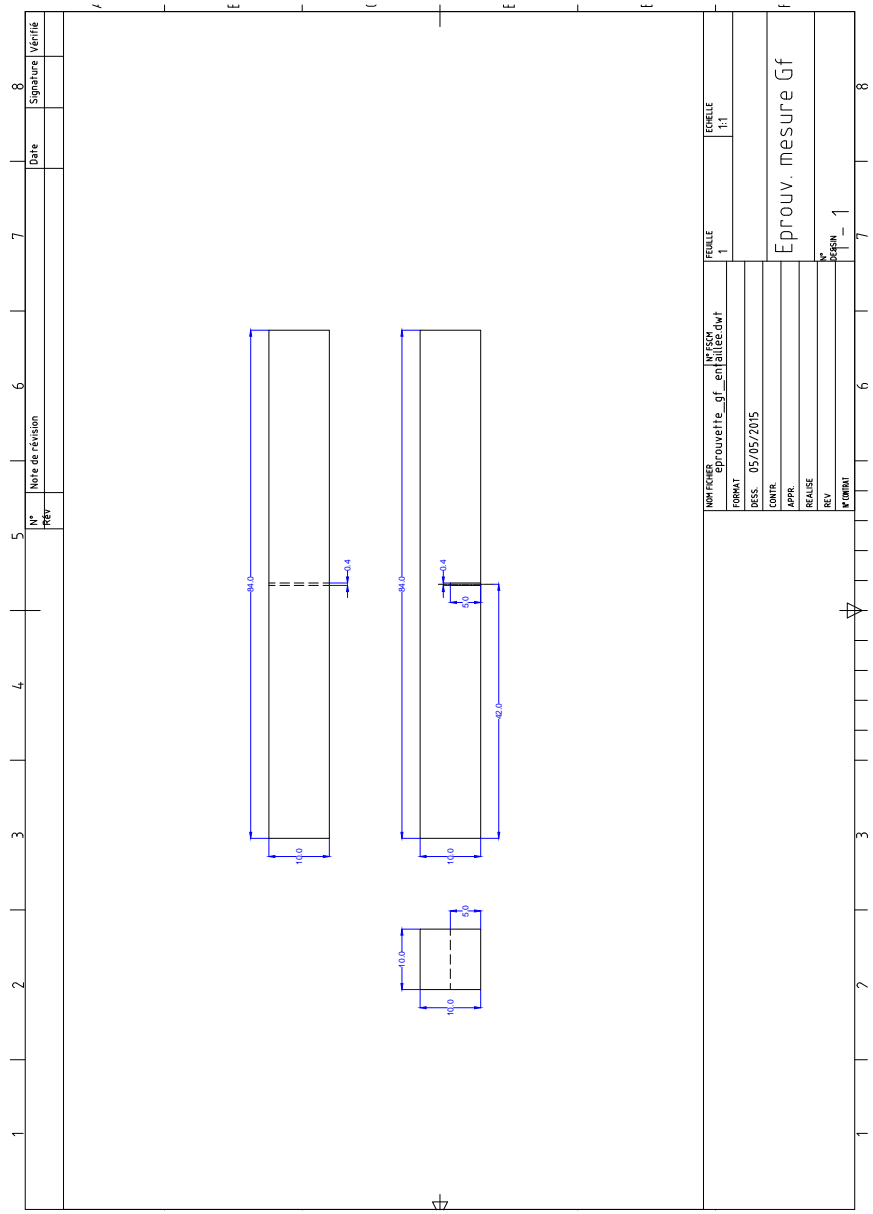


FIGURE B.1: Fracture energy measurement sample

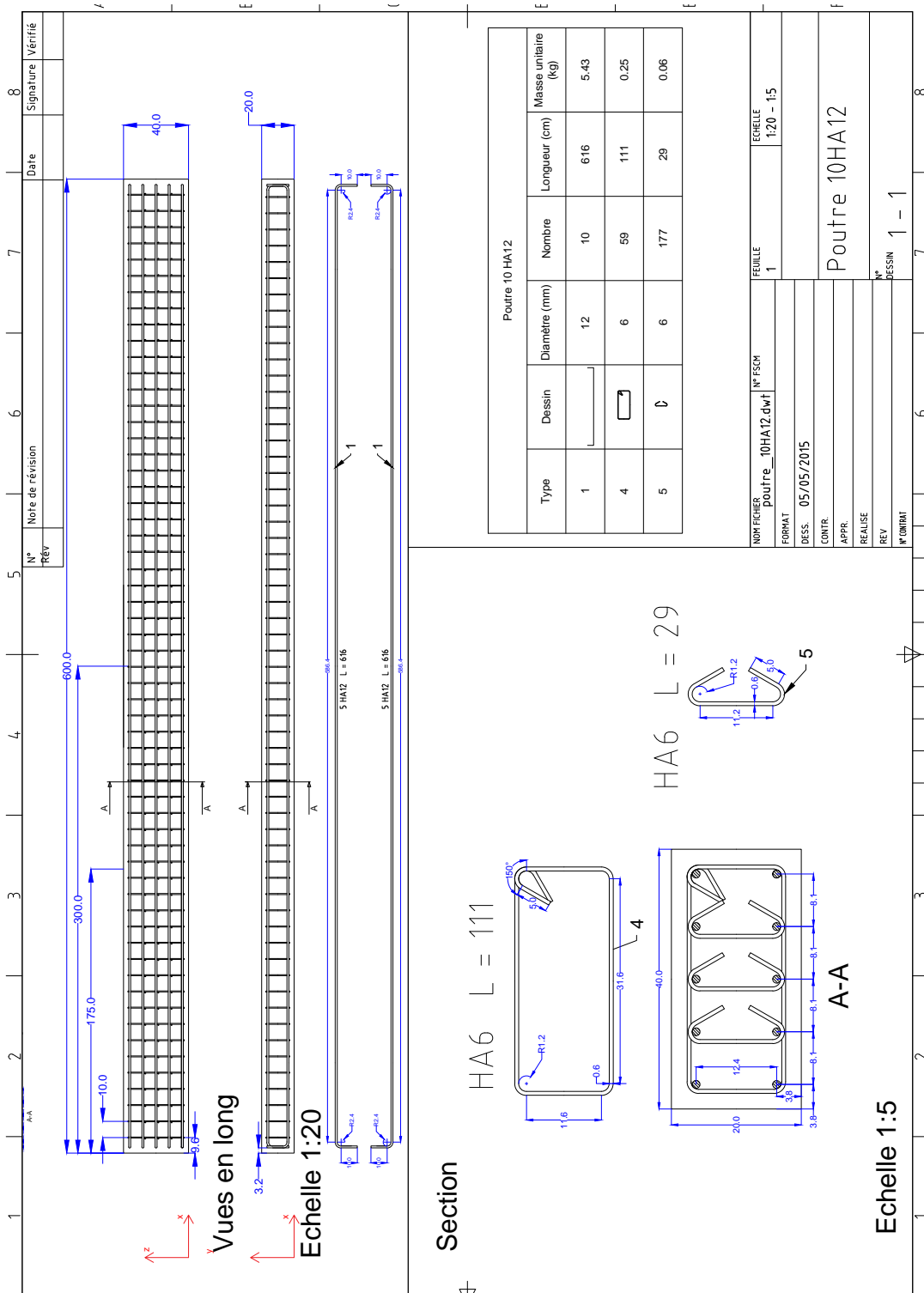


FIGURE B.2: 10HA12 beam

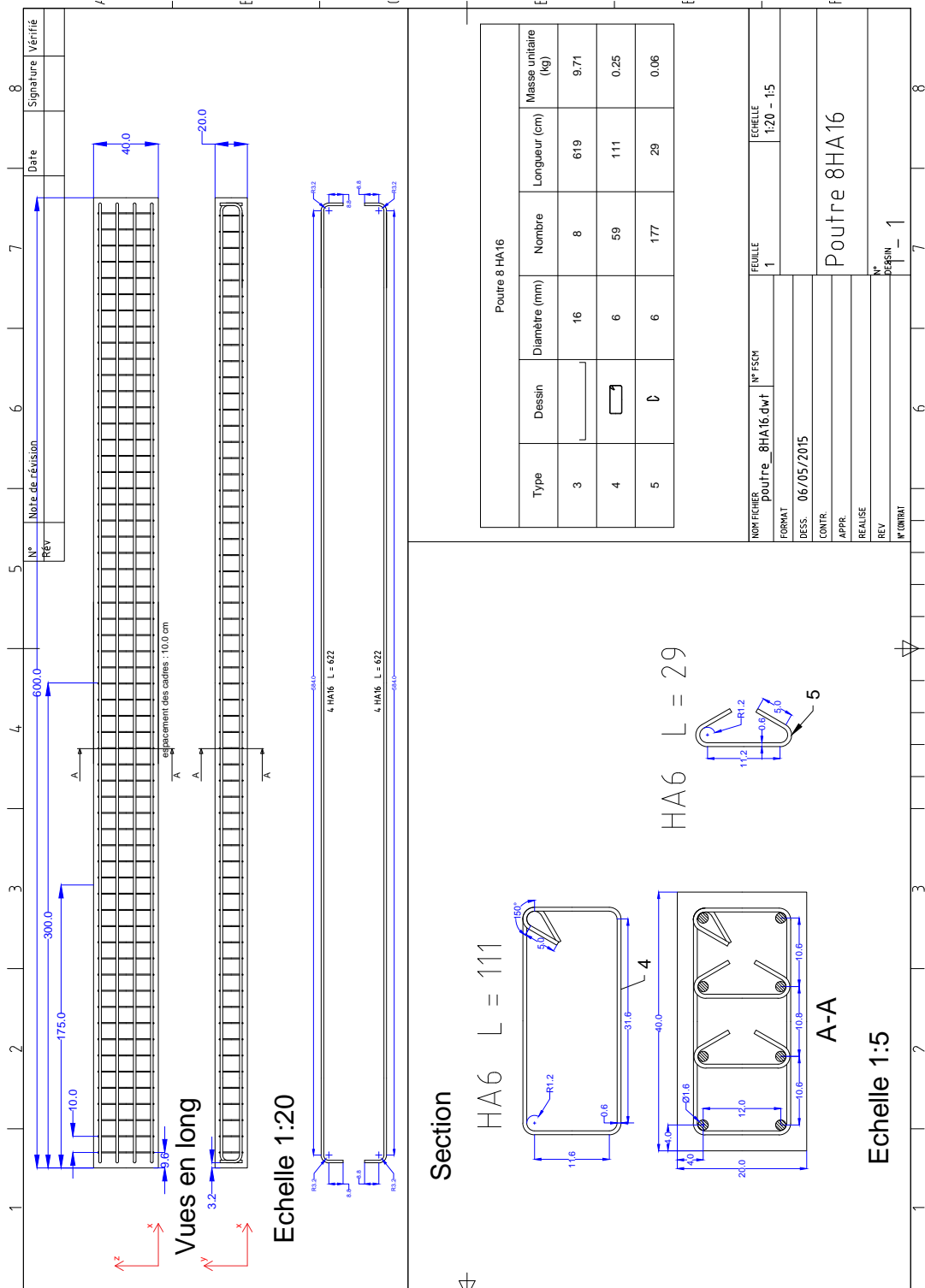


FIGURE B.3: 8HA16 beam

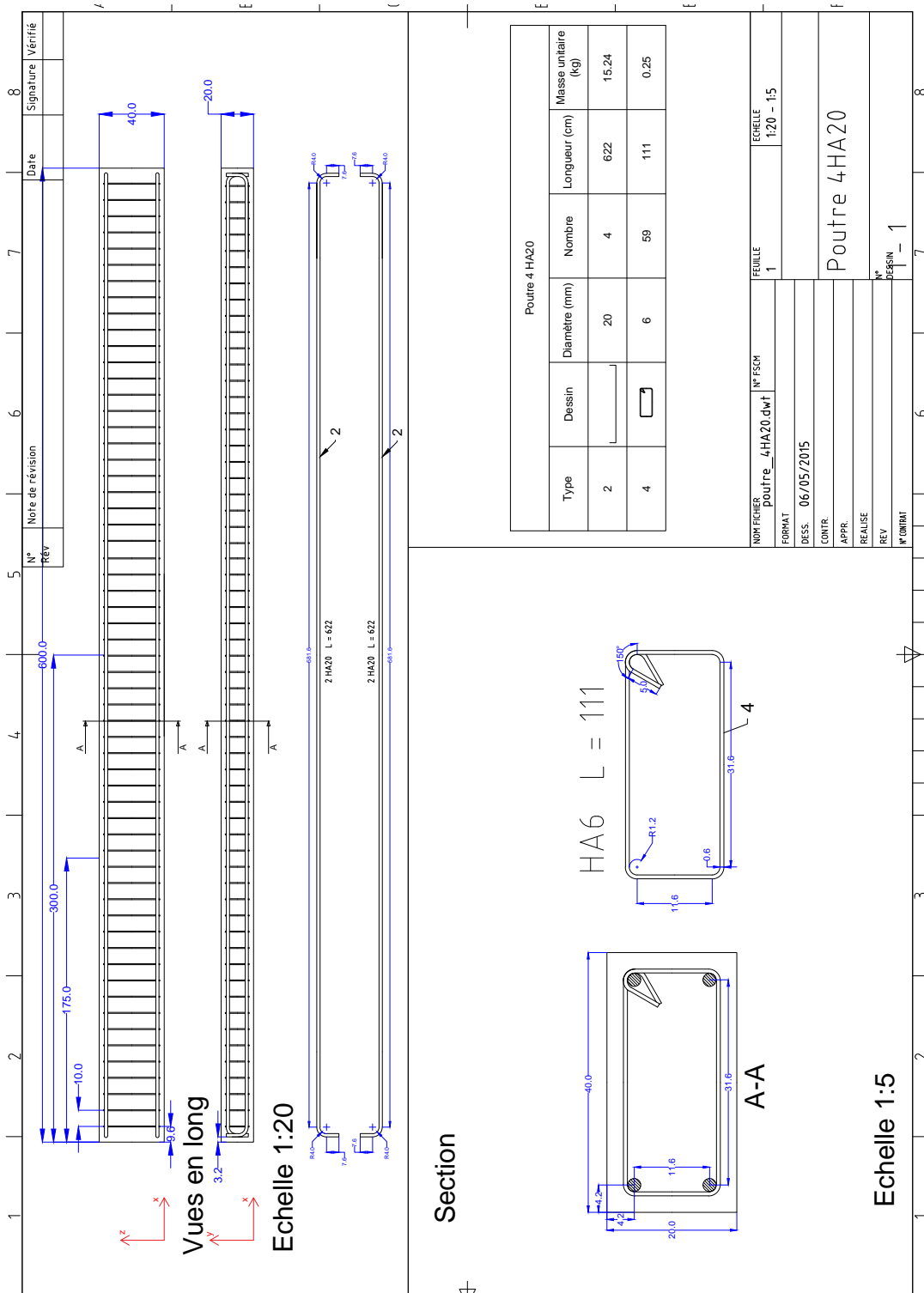


FIGURE B.4: 4HA20 beam



## Appendix C

# Miscellaneous



### FORMULE

Edition du : 09/12/15

BDF Ile de France

Page 1 / 1

Centrale : Port Victor J084

Produit / Formule		Chantier	
Code produit	308855	Client	SPBT.BET
Libellé commercial	CXB RETARDÉ C25/30 XC1 G1	Chantier	SACLAY
Numéro alternative	02	Type ouvrage	CEA
Désignation de norme	BPS NF EN 206-1	Partie d'ouvrage	
Classe d'exposition	XC1	Complément d'information	20007014 / 226842
Classe de Résistance	C25	Option(s) Commerciale(s)	
Caract. Complémentaire (s)	-	Option 1	
Classe granulaire / Dmax	G1 / 10	Option 2	
Consistance	S3	Option 3	
Classe de chlorure	CL040	Option 4	
Dosage spec.client kg/m3		Option 5	
Spécification Complément.		Option 6	

Détail formule					
Code MP	Libellé MP	Fournisseur	Origine	Qtité (Kg)	Qtité (%)
24317	GA 4/10 SLX MCVDS 77MAROLLES	MCVDS	MAROLLES-SUR-SEINE	1022	
28101	ST 0/4 SLS CEMEX 27VALDEREU	CEMEX	VAL-DE-REUIL	732	
2982	CEM II/A-L 42,5 R CE CP2 NF	CALC	GARGENVILLE	249	
1531	V SURC 57123 UPPC CARLING	SURC	CARLING	107	
2081	ISORETARD 180 L	ISOL		1.07	0.30
2801	ISOFLECX 771	ISOL		2.13	0.60
161	EAU D'APPORT	EAU		200	

Caractéristiques de la formule					
Caractéristiques normatives - Valeurs limites en fonction de la classe d'exposition (tableau NA.F.1 norme NF206 -1)					
Commentaires					
Eeff/(C+kA) maxi	0.65	A/(A+C) maxi	0.20		
Liant équivalent mini NF EN 206-1 (Kg/m3)	286	Classe de résistance minimale (MPa)	20.0		
Caractéristiques techniques					
Commentaires					
Eau Totale (Kg)	203	Eeff/(C+KA)	0.59	Masse volumique (kg/m3)	2313
Eau Efficace (Kg)	168	A/(A+C) %	0.20	Taux de chlorure (%)	0.08
Liant équivalent (Kg/m3)	286	Addition correcteur (kg)	44	Temps malaxage (s)	55

FIGURE C.1: Delivery form of concretes C1A and C1B



## FORMULE

Edition du : 08/01/16

BDF Ile de France

Page 1 / 1

Centrale : 

Produit / Formule		Chantier	
Code produit	324768	Client	SPBT
Libellé commercial	CXB GÉNIE CIVIL C45/55 XF1 G1 CEM II SC6	Chantier	SACLAY
Numéro alternative	02	Type ouvrage	CEA
Désignation de norme	BPS NF EN 206-1	Partie d'ouvrage	
Classe d'exposition	XF1	Complément d'information	20198577/263154
Classe de Résistance	C45	<b>Option(s) Commerciale(s)</b>	
Caract. Complémentaire (s)	- C2 - SC6 -	Option 1	
Classe granulaire / Dmax	G1 / 10	Option 2	
Consistance	S3	Option 3	
Classe de chlorure	CL040	Option 4	
Dosage spec.client kg/m3		Option 5	
Spécification Complément.		Option 6	

Détail formule					
Code MP	Libellé MP	Fournisseur	Origine	Qté (Kg)	Qté (%)
24317	GA 4/10 SLX MCVDS 77MAROLLES	MCVDS	MAROLLES-SUR-SEINE	911	
28101	ST 0/4 SLS CEMEX 27VALDEREU	CEMEX	VAL-DE-REUIL	651	
2982	CEM II/A-L 42,5 R CE CP2 NF	CALC	GARGENVILLE	400	
1531	V SURC 57123 UPPC CARLING	SURC	CARLING	150	
2081	ISORETARD 180 L	ISOL		1.65	0.30
2945	ISOFLOW 857	ISOL		4.4	0.80
161	EAU D'APPORT	EAU		196	

Caractéristiques de la formule			
<b>Caractéristiques normatives</b> - Valeurs limites en fonction de la classe d'exposition (tableau NA.F.1 norme NF206 -1)			
Commentaires			
$E_{eff} / (C+KA)$ maxi	0.60	$A / (A+C)$ maxi	0.20
Liant équivalent mini NF EN 206-1 (Kg/m3)	308	Classe de résistance minimale (MPa)	25.0

Caractéristiques techniques					
Commentaires					
Eau Totale (Kg)	201	$E_{eff} / (C+KA)$	0.37	Masse volumique (kg/m3)	2314
Eau Efficace (Kg)	170	$A / (A+C)$ %	0.20	Taux de chlorure (%)	0.06
Liant équivalent (Kg/m3)	460	Addition correcteur (kg)	50	Temps malaxage (s)	55

FIGURE C.2: Delivery form of concrete C2

# Bibliography

- Angela Salzmann S. Fragomeni, Y. C. Loo (2003). “The Damping Analysis of Experimental Concrete Beams under Free-Vibration”. In: *Advances in Structural Engineering* 6.1, pp. 53–64. ISSN: 13694332.
- Archundia-Aranda, Hans I., Arturo Tena-Colunga & Alejandro Grande-Vega (2013). “Behavior of reinforced concrete haunched beams subjected to cyclic shear loading”. In: *Engineering Structures* 49, pp. 27–42. ISSN: 01410296.
- Asmussen, J. C. (1997). “Modal analysis based on the random decrement technique: application to civil engineering structures”. PhD thesis. Aalborg Universitet.
- Autorité de sûreté nucléaire (2006). *ASN/GUIDE/2/01*.
- Baghiee, Neda, M. Reza Esfahani & Kazem Moslem (2009). “Studies on damage and FRP strengthening of reinforced concrete beams by vibration monitoring”. In: *Engineering Structures* 31.4, pp. 875–893. ISSN: 01410296.
- Bažant, Z. P. (1999). “Size effect on structural strength: a review”. In: *Archive of Applied Mechanics (Ingenieur Archiv)*. ISSN: 0939-1533.
- Bazant, Zdenek P (1983). “Fracture in concrete and reinforced concrete”. In: *Preprints. Qf William Prager Symposium. QD. Mechanics. Qf Geomaterials: ~. Concretes*.
- Bažant, Zdeněk P (1984). “Size effect in blunt fracture: concrete, rock, metal”. In: *Journal of Engineering Mechanics* 110.4, pp. 518–535.
- Bažant, Zdeněk P (1997). “Fracturing truss model: size effect in shear failure of reinforced concrete”. In: *Journal of Engineering Mechanics*.
- Bertero, V.V. & E.P. Popov (1977). “Seismic Behavior of Ductile Moment-Resisting Reinforced Concrete Frames”. In: *Special Publication* 53, pp. 247–292.
- Bertin, Morgan, François Hild, Stéphane Roux, Florent Mathieu, Hugo Leclerc & P. Aimedieu (2016a). “Integrated digital image correlation applied to elastoplastic identification in a biaxial experiment”. In: *Journal of Strain Analysis for Engineering Design* 51.2, pp. 118–131. ISSN: 03093247.
- Bertin, Morgan, François Hild & Stéphane Roux (2016b). “Optimization of a Cruciform Specimen Geometry for the Identification of Constitutive Parameters Based Upon Full-Field Measurements”. In: *Strain* 52.4, pp. 307–323. ISSN: 14751305.
- Bouterf, A., S. Roux, F. Hild, J. Adrien, E. Maire & S. Meille (2014). “Digital volume correlation applied to X-ray tomography images from spherical indentation tests on lightweight gypsum”. In: *Strain* 50.5, pp. 444–453. ISSN: 14751305.

- Bouterf, Amine, Stéphane Roux, François Hild, E. Maire, S. Meille, X. Brajer & G. Vivier (2013). "Identification d'une loi d'endommagement de plâtre à partir de mesures de champs de déplacements". In: *21ème Congrès Français de Mécanique*.
- Brown, Russell H. & James O. Jirsa (1971). "Reinforced Concrete Beams Under Load Reversals". In: *ACI Journal Proceedings* 68.5, pp. 380–390. ISSN: 0002-8061.
- Capdevielle, Sophie, Stéphane Grange, Frédéric Dufour & Cédric Desprez (2016). "A multifiber beam model coupling torsional warping and damage for reinforced concrete structures". In: *European Journal of Environmental and Civil Engineering* 20.8, pp. 914–935. ISSN: 1964-8189.
- Capozucca, Roberto (2009). "Static and dynamic response of damaged RC beams strengthened with NSM CFRP rods". In: *Composite Structures* 91.3, pp. 237–248. ISSN: 02638223.
- Carneiro, J.O. O, F.J.Q. J Q deMelo, S. Jalali, V. Teixeira & M. Tomás (2005). "The use of pseudo-dynamic method in the evaluation of damping characteristics in reinforced concrete beams having variable bending stiffness". In: *Mechanics Research Communications* 33.5, pp. 601–613. ISSN: 00936413.
- Carpinteri, Alberto & Bernardino Chiaia (1995). "Multifractal nature of concrete fracture surfaces and size effects on nominal fracture energy". In: *Materials and Structures* 28.8, pp. 435–443. ISSN: 1871-6873.
- Carpinteri, Alberto & Giuseppe Ferro (1994). "Size effects on tensile fracture properties: a unified explanation based on disorder and fractality of concrete microstructure". In: *Materials and Structures* 27.10, pp. 563–571. ISSN: 1871-6873.
- Caughey, T K (1960). "Classical normal modes in damped linear dynamic systems". In: *Journal of Applied Mechanics* 27.2, pp. 269–271.
- CEA (2017). *Cast3M*. URL: <http://www-cast3m.cea.fr/>.
- Celik, Ozan Cem & Bruce R. Ellingwood (2010). "Seismic fragilities for non-ductile reinforced concrete frames – Role of aleatoric and epistemic uncertainties". In: *Structural Safety* 32.1, pp. 1–12. ISSN: 01674730.
- Charney, Finley a. (2008). "Unintended Consequences of Modeling Damping in Structures". In: *Journal of Structural Engineering* 134.4, pp. 581–592. ISSN: 0733-9445.
- Chopra, Anil K. (2007). *Dynamics of structures - theory and applications to earthquake engineering, third edition*. Vol. 23. 2, pp. 491–492. ISBN: 0-13-156174-X.
- Clough R.W., Penzien J. (2003). *Dynamics of structures*. Ed. by Computers and Structures. 2nd edition. Berkeley, CA.
- Cole, Henry A. Jr. (1973). *On-line failure detection and damping measurement of aerospace structures by random decrement signatures*. Tech. rep. NASA.
- Comité Européen de Normalisation (2005a). "EN 10080 - Steel for the reinforcement of concrete — Weldable reinforcing steel — General". In:
- Comité Européen de Normalisation (2005b). "Eurocode 2: Design of concrete structures - Part 1-1: General rules and rules for buildings". In: February 2015.

- Comité Européen de Normalisation (2005c). “Eurocode 8 Design of structures for earthquake resistance Part 1: General rules, seismic actions and rules for buildings”. In:
- Comité Européen de Normalisation (2012). *NF-EN-12390-1: Testing hardened concrete. Shape, dimensions and other requirements for specimens and moulds*. ISBN: 978-0-580-76920-7.
- Correia, António A., João P. Almeida & Rui Pinho (2013). “Seismic energy dissipation in inelastic frames: Understanding state-of-the-practice damping models”. In: *Structural Engineering International: Journal of the International Association for Bridge and Structural Engineering (IABSE)* 23.2, pp. 148–158. ISSN: 10168664.
- Crambuer, R., B. Richard, N. Ile & F. Ragueneau (2013). “Experimental characterization and modeling of energy dissipation in reinforced concrete beams subjected to cyclic loading”. In: *Engineering Structures* 56, pp. 919–934. ISSN: 01410296.
- Crouse, C. B. & Jeff McGuire (2001). “Energy Dissipation in Soil-Structure Interaction”. In: *Earthquake Spectra* 17.2, pp. 235–259. ISSN: 8755-2930.
- Cruz, Cristian & Eduardo Miranda (2016). “Evaluation of Damping Ratios for the Seismic Analysis of Tall Buildings”. In: *Journal of Structural Engineering*, p. 04016144. ISSN: 0733-9445.
- D’Ambrisi, Angelo & Filip C. Filippou (1999). “Modeling of Cyclic Shear Behavior in RC Members”. In: *Journal of Structural Engineering* 125.10, pp. 1143–1150. ISSN: 0733-9445.
- Daoud, Atef (2003). “Etude expérimentale de la liaison entre l’acier et le béton autoplaçant - Contribution à la modélisation numérique de l’interface”. PhD thesis. Institut National des Sciences Appliquées de Toulouse.
- Daoud, Atef, Olivier Maurel & Christian La Borderie (2013). “2D mesoscopic modelling of bar-concrete bond”. In: *Engineering Structures* 49, pp. 696–706.
- Davenne, L., F. Ragueneau, J. Mazars & A. Ibrahimbegovic (2003). “Efficient approaches to finite element analysis in earthquake engineering”. In: *Computers and Structures* 81.12, pp. 1223–1239. ISSN: 00457949.
- Demarie, G. V. & D. Sabia (2010). “Non-linear damping and frequency identification in a progressively damaged R.C. Element”. In: *Experimental Mechanics* 51.2, pp. 229–245. ISSN: 00144851.
- Dunand, François (2005). “Pertinence du bruit de fond sismique pour la caractérisation dynamique et l’aide au diagnostic sismique des structures de génie civil”. PhD thesis. Université Joseph Fourier - Grenoble I.
- Dutta, Sekhar Chandra & Rana Roy (2002). “A critical review on idealization and modeling for interaction among soil–foundation–structure system”. In: *Computers & Structures* 80.20, pp. 1579–1594. ISSN: 00457949.
- Dwairi, H. M., M. J. Kowalsky & J. M. Nau (2007). “Equivalent damping in support of direct displacement-based design”. In: *Journal of Earthquake Engineering* 11.4, pp. 512–530. ISSN: 1363-2469.

- Eligehausen, R., E. P. Popov & V. V. Bertero (1982). *Local bond stress-slip relationships of deformed bars under generalized excitations*. Tech. rep.
- Elmenschawi, Abdelsamie & Tom Brown (2009). “Hysteretic energy and damping capacity of flexural elements constructed with different concrete strengths”. In: *Engineering Structures* 32.1, pp. 297–305. ISSN: 01410296.
- Eurocode 2: Design of concrete structures – Part 1-1: General rules and rules for buildings* (2005). Tech. rep. CEN.
- Franchetti, P. C. Modena & M. Q. Feng (2009). “Nonlinear damping identification in precast prestressed reinforced concrete beams”. In: *Computer-Aided Civil and Infrastructure Engineering* 24.8, pp. 577–592. ISSN: 10939687.
- Giuffrè, A (1970). “Il comportamento del cemento armato per sollecitazioni cicliche di forte intensità”. In: *Giornale del Genio Civile*.
- Google. “damping definition” search. URL: <https://www.google.fr/search?q=damping+definition>.
- Gulkan, Polat & Mete A Sozen (1974). “Inelastic responses of reinforced concrete structure to earthquake motions”. In: *Journal Proceedings*. Vol. 71. 12, pp. 604–610.
- Gutierrez Soto, Mariantonieta & Hojjat Adeli (2013). “Tuned Mass Dampers”. In: *Archives of Computational Methods in Engineering* 20.4, pp. 419–431. ISSN: 1134-3060.
- Hall, John F. (1988). “The dynamic and earthquake behaviour of concrete dams: review of experimental behaviour and observational evidence”. In: *Soil Dynamics and Earthquake Engineering* 7.2, pp. 58–121. ISSN: 02677261.
- Hall, John F. (2006). “Problems encountered from the use (or misuse) of Rayleigh damping”. In: *Earthquake Engineering and Structural Dynamics* 35.5, pp. 525–545. ISSN: 00988847.
- Heitz, T, A Le Maoult, B Richard, C Giry & F Ragueneau (2017a). “Dissipations in reinforced concrete components: static and dynamic experimental identification strategy”. In: *Engineering Structures* Under review.
- Heitz, Thomas, Cédric Giry, Benjamin Richard & Frédéric Ragueneau (2017b). “How are the equivalent damping ratios modified by nonlinear engineering demand parameters?” In: *6th International Conference on Computational Methods in Structural Dynamics and Earthquake Engineering*. Rhodes Island.
- Hilber, Hans M., Thomas J. R. Hughes & Robert L. Taylor (1977). “Improved numerical dissipation for time integration algorithms in structural dynamics”. In: *Earthquake Engineering & Structural Dynamics* 5.3, pp. 283–292. ISSN: 00988847.
- Hild, F. & S. Roux (2006). “Digital Image Correlation: from displacement measurement to identification of elastic properties - A review”. In: *Strain* 42, pp. 69–80. ISSN: 00392103.
- Hild, François, Stéphane Roux, Renaud Gras, Néstor Guerrero, Maria Eugenia Marante & Julio Flórez-López (2009a). “Displacement measurement technique for beam kinematics”. In: *Optics and Lasers in Engineering* 47.3-4, pp. 495–503. ISSN: 01438166.

- Hild, François, Stéphane Roux, Renaud Gras, Néstor Guerrero, Maria Eugenia Marante & Julio Flórez-López (2009b). “Displacement measurement technique for beam kinematics”. In: *Optics and Lasers in Engineering* 47.3, pp. 495–503. ISSN: 01438166.
- Hild, François, Amine Bouterf & Stéphane Roux (2015). “Damage measurements via DIC”. In: *International Journal of Fracture* 191.1-2, pp. 77–105. ISSN: 15732673.
- Hill, R. (1963). “Elastic properties of reinforced solids: Some theoretical principles”. In: *Journal of the Mechanics and Physics of Solids* 11.5, pp. 357–372. ISSN: 00225096.
- Hilloulin, Benoit, Yuxiang ZHANG, Odile Abraham, Frédéric Grondin, Ahmed Loukili, Olivier Durand & Vincent TOURNAT (2014). “Closed Crack Detection in Concrete with Coda Wave Non-Linear Modulation”. In: *EWSHM - 7th European Workshop on Structural Health Monitoring*. Ed. by Vincent Le Cam, Laurent Mevel & Franck Schoefs. Nantes, France.
- Iwan, Wilfred D. & Nathan C. Gates (1979). “The effective period and damping of a class of hysteretic structures”. In: *Earthquake Engineering and Structural Dynamics* 7.3, pp. 199–211. ISSN: 10969845.
- Jacobsen, Lydik S. (1930). “Steady forced vibration as influenced by damping”. In: *Transactions of ASME* 52, pp. 169–181.
- Jacobsen, Lydik S. (1960). “Damping in composite structures”. In: *Proceedings of the 2nd world conference on on earthquake engineering* 2, pp. 1029–1044.
- Jehel, Pierre (2014). “A critical look into Rayleigh damping forces for seismic performance assessment of inelastic structures”. In: *Engineering Structures* 78, pp. 28–40. ISSN: 01410296.
- Jehel, Pierre, Pierre Léger & Adnan Ibrahimbegovic (2014). “Initial versus tangent stiffness-based Rayleigh damping in inelastic time history seismic analyses”. In: *Earthquake Engineering and Structural Dynamics* 43, pp. 467–484.
- Jennings, P. C. (1968). “Equivalent Viscous Damping for Yielding Structures”. In: *Journal of the Engineering Mechanics Division* 94.1, pp. 103–116.
- Kareem, A. & K. Gurley (1996). “Damping in structures: its evaluation and treatment of uncertainty”. In: *Journal of Wind Engineering and Industrial Aerodynamics* 59, pp. 131–157. ISSN: 01676105.
- Kareem, A, T Kijewski & Y Tamura (1999). “Mitigation of motions of tall buildings with specific examples of recent applications”. In: *Wind and structures*.
- Khoder, N., S. Grange & Y. Sieffert (2017). “Enhancement of multifiber beam elements in the case of reinforced concrete structures for taking into account the lateral confinement of concrete due to stirrups”. In: *International Symposium on Defects and Material Mechanics*. Lyon.
- Kowalsky, M. J. (1994). *Displacement based design: a methodology for seismic design applied to RC bridge columns*. Tech. rep. San Diego, California: University of California.

- Kumar, Shiv Shankar, Murali Krishna & Arindam Dey (2015). "Cyclic Response of Sand Using Stress Controlled Cyclic Triaxial Tests". In: *50th INDIAN GEOTECHNICAL CONFERENCE* December.
- La Borderie, Christian (1991). "Crack closure effect in continuum damage mechanics: Modelling and application to concrete structure analysis". PhD thesis. Université Pierre et Marie Curie (Paris VI).
- Lee, Sang Hyun, Kyung Won Min, Jae Seung Hwang & Jinkoo Kim (2004). "Evaluation of equivalent damping ratio of a structure with added dampers". In: *Engineering Structures* 26.3, pp. 335–346. ISSN: 01410296.
- Léger, Pierre & Serge Dussault (1992). "Seismic-energy dissipation in MDOF structures". In: *Journal of Structural Engineering* 118.5, pp. 1251–1269.
- Lemaître, Jean (1996). *A course on damage mechanics*. Second. Berlin, Heidelberg: Springer Berlin Heidelberg. ISBN: 978-3-540-60980-3.
- Lestuzzi, Pierino & Hugo Bachmann (2007). "Displacement ductility and energy assessment from shaking table tests on RC structural walls". In: *Engineering Structures* 29.8, pp. 1708–1721. ISSN: 01410296.
- Li, Q. S., K. Yang, N. Zhang, C. K. Wong & A. P. Jeary (2002). "Field measurements of amplitude-dependent damping in a 79-storey tall building and its effects on the structural dynamic responses". In: *The Structural Design of Tall Buildings* 11.2, pp. 129–153. ISSN: 1062-8002.
- Liu, Kun Sung & Yi Ben Tsai (2010). "Observed natural frequencies, damping ratios, and mode shapes of vibration of a 30-story building excited by a major earthquake and Typhoon". In: *Earthquake Spectra* 26.2, pp. 371–397. ISSN: 87552930.
- Livaoğlu, R. & A. Doğançün (2006). "Simplified seismic analysis procedures for elevated tanks considering fluid–structure–soil interaction". In: *Journal of Fluids and Structures* 22.3, pp. 421–439. ISSN: 08899746.
- Lou, Menglin, Huaifeng Wang, Xi Chen & Yongmei Zhai (2011). "Structure–soil–structure interaction: Literature review". In: *Soil Dynamics and Earthquake Engineering* 31.12, pp. 1724–1731. ISSN: 02677261.
- Luco, J Enrique & Armando LANZI (2017). "Optimal Caughey series representation of classical damping matrices". In: *Soil Dynamics and Earthquake Engineering* 92, pp. 253–265. ISSN: 0267-7261.
- Matallah, M, M Farah, F Grondin, A Loukili & E Rozière (2013). "Size-independent fracture energy of concrete at very early ages by inverse analysis". In: *Engineering Fracture Mechanics* 109, pp. 1–16. ISSN: 0013-7944.
- Mathieu, Florent, François Hild & Stéphane Roux (2012). "Identification of a crack propagation law by digital image correlation". In: *International Journal of Fatigue* 36.1, pp. 146–154. ISSN: 01421123.
- Mathieu, Florent, Hugo Leclerc, François Hild & Stéphane Roux (2015). "Estimation of elastoplastic parameters via weighted FEMU and integrated-DIC". In: *Experimental Mechanics* 55.1, pp. 105–119. ISSN: 17412765.

- Mathworks (2017a). *Choosing the algorithm*. URL: <https://ch.mathworks.com/help/optim/ug/choosing-the-algorithm.html>.
- Mathworks (2017b). *Optimization decision table*. URL: <https://ch.mathworks.com/help/optim/ug/optimization-decision-table.html>.
- Menegotto, M. (1973). “Method of analysis for cyclically loaded RC plane frames including changes in geometry and non-elastic behavior of elements under combined normal force and bending”. In: *Proc. IABSE symposium on resistance and ultimate deformability of structures acted on by well defined repeated loads*, pp. 15–22.
- Michel, Clotaire, Philippe Guéguen & Pierre-Yves Bard (2008). “Dynamic parameters of structures extracted from ambient vibration measurements: An aid for the seismic vulnerability assessment of existing buildings in moderate seismic hazard regions”. In: *Soil Dynamics and Earthquake Engineering* 28.8, pp. 593–604. ISSN: 02677261.
- Mikael, Ali (2011). “Évaluation des paramètres physiques des bâtiments : amortissement, fréquences et modes de comportement des structures de génie civil : approche expérimentale”. PhD thesis. Université de Grenoble.
- Monti, Giorgio & Camillo Nuti (1992). “Nonlinear cyclic behavior of reinforcing bars including buckling”. In: *Journal of Structural Engineering* 118.12, pp. 3268–3284.
- Moutoussamy, Laurent (2014). “Essais hybrides en temps réel sur structures de Génie Civil”. PhD thesis. Ecole Normale Supérieure de Cachan.
- Ndambi, J.M., B. Peeters, J. Maeck, J. De Visscher, M.A. Wahab, J. Vantomme, G. De Roeck & W.P. De Wilde (2000). “Comparison of techniques for modal analysis of concrete structures”. In: *Engineering Structures* 22.9, pp. 1159–1166. ISSN: 01410296.
- Newmark, Nathan M (1959). “A method of computation for structural dynamics”. In: *Journal of the Engineering Mechanics Division* 85.3, pp. 67–94.
- O’kelly, M E J & T K Caughey (1965). “Classical normal modes in damped linear dynamic systems”. In: *Journal of Applied Mechanics* 32.3, pp. 583–588.
- Otani, Shunsuke (1980). “Nonlinear dynamic analysis of reinforced concrete building structures”. In: *Canadian Journal of Civil Engineering* 7, pp. 333–344. ISSN: 0315-1468.
- Ozdemir, Z., M. Souli & Y.M. Fahjan (2010). “Application of nonlinear fluid–structure interaction methods to seismic analysis of anchored and unanchored tanks”. In: *Engineering Structures* 32.2, pp. 409–423. ISSN: 01410296.
- Papagiannopoulos, George A & George D Hatzigeorgiou (2011). “On the use of the half-power bandwidth method to estimate damping in building structures”. In: *Soil Dynamics and Earthquake Engineering* 31.7, pp. 1075–1079. ISSN: 0267-7261.
- Penzi, J. & M. Celebi (1973). “Experimental Investigation into the Seismic Behavior of Critical Regions of Reinforced Concrete Components as Influenced by Moment and Shear”. In: *Earthquake Engineering Research Center, Report* 73-4.
- Perera, Ricardo, Consuelo Huerta & Juan Manuel Orquín (2007). “Identification of damage in RC beams using indexes based on local modal stiffness”. In: *Construction and Building Materials* 22.8, pp. 1656–1667. ISSN: 09500618.

- Petrini, Lorenza, Claudio Maggi, M. J. Nigel Priestley & G. Michele Calvi (2008). "Experimental verification of viscous damping modeling for inelastic time history analyzes". In: *Journal of Earthquake Engineering* 12.S1, pp. 125–145.
- Potra, Florian A. & Stephen J. Wright (2000). "Interior-point methods". In: *Journal of Computational and Applied Mathematics* 124.1-2, pp. 281–302. ISSN: 03770427.
- Priestley, M. J. N., G. M. Calvi & M. J. Kowalsky (2007). "Displacement-based seismic design of structures". In: *NZSEE Conference*. Vol. 23. 33, pp. 1453–1460. ISBN: 8861980007.
- Priestley, M J Nigel (2003). *Myths and fallacies in earthquake engineering, revisited*. IUSS press.
- Ragueneau, Frédéric (1999). "Fonctionnement dynamique des structures en béton - Influence des comportements hystérétiques locaux". PhD thesis. École Normale Supérieure de Cachan.
- Reynolds, P. & A. Pavic (2000). "Impulse hammer versus shaker excitation for the modal testing of building floors". In: *Experimental Techniques* 24.3, pp. 39–44. ISSN: 0732-8818.
- Richard, Benjamin & Frédéric Ragueneau (2013). "Continuum damage mechanics based model for quasi brittle materials subjected to cyclic loadings: Formulation, numerical implementation and applications". In: *Engineering Fracture Mechanics* 98.1, pp. 383–406. ISSN: 00137944.
- Richard, Benjamin, Paolo Martinelli, François Voldoire, Thierry Chaudat, Salim Abouri & Nicolas Bonfils (2016a). "SMART 2008: Overview, synthesis and lessons learned from the International Benchmark". In: *Engineering Structures* 106, pp. 166–178. ISSN: 01410296.
- Richard, Benjamin, Stefano Cherubini, François Voldoire, Pierre-Etienne Charbonnel, Thierry Chaudat, Salim Abouri & Nicolas Bonfils (2016b). "SMART 2013: Experimental and numerical assessment of the dynamic behavior by shaking table tests of an asymmetrical reinforced concrete structure subjected to high intensity ground motions". In: *Engineering Structures* 109, pp. 99–116. ISSN: 01410296.
- RILEM TCS (1985). "Determination of the fracture energy of mortar and concrete by means of three-point bend tests on notched beams". In: *RILEM Recommendations for the testing and use of constructions materials* 18.106, pp. 285–290.
- Rodrigues, Hugo, Humberto Varum, António Arêde & Aníbal Costa (2011). "A comparative analysis of energy dissipation and equivalent viscous dampung of RC columns subjected to uniaxial and biaxial loading". In: *Engineering Structures* 35, pp. 149–164. ISSN: 01410296.
- Rosenblueth, E. & I. Herrera (1964). "On a kind of hysteretic damping". In: *Journal of Engineering Mechanics* 90, pp. 37–48.
- Salzmann, Angela (2002). "Damping characteristics of reinforced and prestressed normal and high strength concrete beams". PhD thesis. Griffith University.

- Satake, Naoki, Ken-ichi Suda, Toshiharu Arakawa, Atsushi Sasaki & Yukio Tamura (2003). “Damping evaluation using full-scale data of buildings in Japan”. In: *Journal of Structural Engineering* 129.4, pp. 470–477. ISSN: 0733-9445.
- SEISM Paris-Saclay Insitute. *De la faille à la structure*. URL: <http://www.institut-seism.fr/en/>.
- SEISM Paris-Saclay Institute. *SINAPS@*. URL: <http://www.institut-seism.fr/en/projects/sinaps/>.
- SEMT/EMSI/RT/98-066A (1998). *CAMUS International benchmark – Report 1, Mock-up and loading characteristics*. Tech. rep. CEA Saclay.
- Skinner, R., A. J. Heine & R. Tyler (1977). “No Title”. In: *6th World Conference on Earthquake Engineering*. New Delhi, pp. 1319–1324.
- Smyrou, Eleni, M. J. Nigel Priestley & Athol J. Carr (2011). “Modelling of elastic damping in nonlinear time-history analyses of cantilever RC walls”. In: *Bulletin of Earthquake Engineering* 9, pp. 1559–1578.
- Torre-Casanova, A., L. Jason, L. Davenne & X. Pinelli (2013). “Confinement effects on the steel–concrete bond strength and pull-out failure”. In: *Engineering Fracture Mechanics* 97, pp. 92–104. ISSN: 00137944.
- Videometric. *Videometric*. URL: <http://www.videometric.com/en/>.
- Vintzileou, Elizabeth, T. P. Tassios & M. Chronopoulos (2006). “Experimental validation of seismic code provisions for RC columns”. In: *Engineering Structures* 29.6, pp. 1153–1164. ISSN: 01410296.
- Wang, Ivan (2011). “An analysis of higher order effects in the half power method for calculating damping”. In: *Journal of Applied Mechanics* 78.1, p. 14501.
- Zembaty, Zbigniew, Marcin Kowalski & Stanislav Pospisil (2006). “Dynamic identification of a reinforced concrete frame in progressive states of damage”. In: *Engineering Structures* 28.5, pp. 668–681. ISSN: 01410296.

**Titre :** Comportements non-linéaires locaux et modélisation numérique de l'amortissement dans les structures de génie civil en dynamique

**Mots clefs :** amortissement, béton armé, séisme, SINAPS@

**Résumé :** Le programme de recherche (Projet d'Investissement d'Avenir) SINAPS@ a été lancé en 2014 et regroupe les acteurs majeurs de l'ingénierie parasismique, tant académiques qu'industriels. L'objectif principal de ce projet, s'adossant à l'architecture de l'Institut SEISM, consiste à développer les outils de modélisation permettant d'apprécier les effets de séismes, de la rupture de la faille jusqu'au comportement vibratoires des structures et équipements. Ce travail de thèse s'inscrit dans les volets 3 et 5 du projet dédiés aux comportements des structures et des équipements, et aux contributions expérimentales respectivement. Pour des raisons de coût de calcul et de difficultés de modélisation des dissipations issues des non-linéarités au sein des structures de génie civil en dynamique, un amortissement visqueux additionnel est souvent utilisé pour représenter les dissipations non prises en compte par le modèle constitutif. Ainsi, un coefficient d'amortissement visqueux équivalent est calibré afin de dissiper la quantité d'énergie nécessaire par un champ de forces visqueuses. Cette thèse vise à étudier et à comparer différentes méthodes d'évaluation de l'amortissement visqueux équivalent, ainsi que l'influence de paramètres matériaux et structuraux. Une campagne expérimentale reposant sur des essais quasi-statiques et dynamiques sur table vibrante est mise en place et décrite dans ce manuscrit. Les analyses spécifiquement développées pour ces essais et les résultats significatifs sont présentés. Notamment, une dépendance entre amortissement, demande en déplacement, et niveau de déplacement maximal historique a été identifiée.

**Title:** Nonlinear local behaviors and numerical modeling of damping in civil engineering structures in dynamics

**Keywords:** damping, reinforced concrete, earthquake, SINAPS@

**Abstract:** The research project (Projet d'Investissement d'Avenir) SINAPS@ has started in 2014 and gathers the main participants of the seismic engineering, both from academics and industry. The main goal of this project relying on SEISM Institute is to improve modeling tools allowing one to evaluate the effects of an earthquake from the failure to the vibration behavior of the structures and amenities. The work carried out in this thesis falls within work packages 3 and 5 of the project dedicated to the behaviors of structures and equipments, and to experimental contributions, respectively. Because of the numerical cost and the difficulties associated to the modeling of dissipations generated by nonlinearities within civil engineering structures in dynamics, an additional viscous damping is often used to account for the dissipations not taken into account by the constitutive model. Hence, an equivalent viscous damping coefficient is calibrated in order to dissipate the required amount of energy through a viscous forces field. This thesis studies and compares different assessment methods of the equivalent viscous damping, and the influence of material and structural parameters. An experimental campaign consisting in quasi-static and dynamic tests on shaking table is set up and described in this manuscript. Specifically developed analyses and significant results are presented. In particular, a relationship between displacement demand and maximum time-history displacement has been identified.

